GaN Radiation Detectors for Particle Physics and Synchrotron Applications

James Paul Grant

UNIVERSITY
of
GLASGOW

Department of Physics and Astronomy

Thesis submitted for the degree of Doctor of Philosophy in the subject of physics

September 4, 2007

ProQuest LLC.
789 East Eisenhower Parkway
P.O. Box 1346
Ann Arbor, MI 48106 – 1346

To my family

Abstract

In this thesis the work will focus on the development of wide band gap radiation detectors for radiation hard, biological and monitoring applications. Gallium nitride (GaN) was investigated as a radiation hard particle detector and as an UV light detector while the properties of single crystal diamond as a soft x-ray beam position monitor were assessed.

Photolithographic processes were used to produce Schottky pad detectors of 1 mm diameter on three epitaxial GaN wafers grown on a sapphire substrate. Two of the wafers were obtained from Tokushima University, Japan and had an epitaxial thickness of 2.5 μm while the third GaN wafer was grown by Lumilog, France and had an epitaxial thickness of 12 μm. Devices were irradiated with 24 GeV/c protons and neutrons (1 MeV equivalent) to fluences of 10^{14}, 10^{15}, 2x10^{15}, 5x10^{15} and 10^{16} particles cm^{-2} and the macroscopic properties characterised through current-voltage (I-V), capacitance-voltage (C-V) and charge collection efficiency measurements using alpha particles. The leakage currents of the irradiated GaN detectors were in some cases orders of magnitude smaller than the unirradiated devices. This phenomenon has also been observed in other irradiated wide band gap semiconductors, SiC and diamond. The maximum CCE of the thin epitaxial GaN detector was 97% while the thicker epitaxial GaN detector exhibited a maximum CCE of 53%. Irradiation with protons and neutrons led to a dramatic reduction

in the CCE of the GaN detectors. For example, the CCE of one of the thin epitaxial GaN detectors dropped from 97% pre-irradiation to 40% after irradiation to 10^{16} neutrons cm^{-2} and 13% after irradiation to 10^{16} protons cm^{-2}. The drop in CCE of the thicker epitaxial material was less pronounced however the devices irradiated to the highest fluences, 10^{16} neutrons cm^{-2} and 10^{16} protons cm^{-2} exhibited CCEs of only 17% and 25% respectively.

Attempts were made at identifying and understanding the microscopic as-grown and radiation-induced defects that determine the macroscopic characteristics of the GaN detectors. The microscopic properties of unirradiated and irradiated GaN detectors were evaluated using photoluminescence (PL), contact photoconductivity (CPC) and thermally stimulated current (TSC) techniques. Both PL and CPC measurements of the irradiated devices revealed a substantial increase in non-radiative recombination. In particular the intensity of the yellow band PL peak is significantly reduced after irradiation to 10^{16} particles cm^{-2}. TSC measurements of the GaN detectors revealed several competing complicated transport mechanisms. Thermal activation energies of 0.16-0.2, 0.27-0.32, 0.36-0.45 and 0.73-0.74 eV were extracted from neutron irradiated thin epitaxial GaN detectors.

Dry etching of various GaN materials was done in a inductively coupled plasma (ICP) machine. The GaN samples were etched in order to produce ohmic contacts to the n-GaN buffer layers and to realise a parallel plate capacitor detector geometry. From the current-voltage and capacitance-voltage characteristics of the etched devices the ideality factor, Schottky barrier height and carrier concentration were extracted. The parallel plate capacitor geometry of the etched devices resulted in an increase in charge collection efficiency compared to the unetched devices. This is attributed to better definition of the electric field within the etched devices resulting in

significantly improved charge transport.

Metal-Semiconductor-Metal (MSM) UV detectors were fabricated on four GaN wafers and one AlGaN wafer. Two MSM device geometries; one with a finger spacing/width of 5 μm and one with a finger spacing/width of 10 μm, were investigated. The optimal GaN material, MSM geometry and metalisation contact scheme was established via current-voltage and spectral response measurements and a 46 channel diode GaN array detector fabricated. This position sensitive GaN array detector was to be used in an energy dispersive Circular Dichroism (CD) experiment at Daresbury Laboratory. The CD spectra of a protein may be used to establish the conformation it adopts - i.e. how the protein folds. Neuro-degenerative diseases are thought to occur when proteins fold incorrectly. The channels of the GaN array detector exhibited significant priming destroying the CD measuring capability. This priming is attributed to photo-generated carriers filling defect traps in the semi-insulating GaN material resulting in an increase of the device photoconductivity with time.

Further MSM devices with semi-transparent contacts were fabricated using e-beam lithography. These devices had increased responsivities compared to the full-metal contact devices, showing that semi-transparent contacts should be employed where possible. The CD spectrum of camphorsulphonic acid (CSA) was measured using a semi-metal GaN photodiode array detector and compared to the spectrum obtained with a Hamamastu Si photodiode. The typical CSA CD spectrum of a minimum at 192.5 nm and a maximum at 290.5 nm was not recorded by the semi-metal 45GaN device. This is again attributed to the priming of the semi-insulating GaN materials which destroys the CD measuring capability.

Finally, single crystal chemical vapour deposition (CVD) diamond was

assessed for its suitability as an in-situ soft x-ray semi-transparent beam position monitor. The fabricated detector exhibited low leakage currents up to an applied field of 0.6 V/μm and $\sim$ 100% CCE at an applied reverse bias of 50 V. X-Ray measurements at the ESRF showed the excellent uniform response over the full area of the diamond device. These preliminary investigations indicate that single crystal diamond shows great promise as an in-situ semi-transparent position beam monitor.

Acknowledgements

I would firstly like to thank my supervisors Val O'Shea and Richard Bates for their help and guidance over the past 3 and a half years. I must also thank them for their willingness to read and re-read the chapters in this thesis. I do realise how painful it is reading and correcting a 250 page thesis! Thanks also to PPARC and the CCLRC for funding my PhD. Spyros Manolopoulos, my CCLRC supervisor, also deserves a mention for his help and assistance.

If I was to pick out three people who have aided me the most over the course of my PhD I would have to name Keith Mathieson, Liam Cunningham and Andrew Blue. Whether it be answering my (often silly) questions, showing me new techniques, discussing my results or just chatting about the merits of a 4-4-2 versus a 5-3-2 these guys were always available to help. I've never come across a person as helpful, considerate, patient, kind and intelligent (no I dont fancy him!) as Keith. He won't like me for saying this but he is an inspiration not only to me but to several other members of the detector development group. Shame he supports Aberdeen and Inverness. Liam also is no doubt sick and tired of me knocking on his door and asking, "Have you got a minute?" or "Are you busy?". It's to his credit that I can only remember one instance where he actually replied "No" to the former question. Once again many thanks to Keith, Liam and Andy.

Fred Doherty, Lena Haddad, John Melone, and Fiona McEwan also helped

with their technical expertise and top quality banter (Fiona excluded ;)) over the past three years. Special thanks to John for having the patience to bond and re-bond my numerous GaN devices - I didn't break that many bonds.....honest! The technicians in the electrical engineering department also deserve a mention; Fiona (before she was poached by physics), Susan, Helen, Eve, Davie M, Linda, Davie G and Tam thank you all. Perhaps one day we'll figure out why the crystal in the Plassys evaporator continually failed when I was using it!

A large part of the work in this thesis was done in collaboration with Vilnius University and I was lucky enough to visit Vilnius twice. Thanks to Professor Juozas Vaitkus and Dr. Eugenijus Gaubas (his coffee is by far the worst I have ever tasted) for discussing some of my more confusing results and proposing equally confusing solutions. The students I worked with during my two stays in Vilnius were extremely friendly and hospitable. Vidmantas Kalendra deserves a special mention for taking me under his wing and acting as translator and guide. We had many good days together performing TSC measurements while listening to Lithuanian radio and drinking Russian coffee (thankfully his coffee was better than Gaubas'). The conversation we had about Vidmantas' love for tractors and nuclear power plants will live long in my memory. Many Svturys beers were also shared with Zenius, Marius, Paulus and Karolis. Good times.

Thanks also to Debbie Gunning for putting up with my whinging about how hard all this writing up was. She also deserves a medal for all the friendly banter/abuse I gave her over these three and a half years. Thanks also to Keith, Dave D, Andy, Liam, Celeste and Dave P for being excellent office mates. One day I'll tidy my desk!

Craig "The Ginge" Brownlie has not only been a great source of enter-

tainment over the years but also a good friend. Both being Hamiltonians (someone from Hamilton) we would often travel into work together either in his black panther Fiesta (hairdresser car) or in my Vauxhall Corsa (another hairdresser car). Monday morning car trips were always eventful where Craig would regale his weekend stories that typically involved alcohol, women, and The Garage. It's definitely your turn to drive Craig.....

Thanks to all the uni guys who played five-a-sides on Mondays and Thursdays. A special mention to MPL, JJ and Hibee for arranging the games and not getting too annoyed when someone had to pull out at the last minute. All the guys in my 11-a-side team, Westwoodhill, deserve a mention for giving me a reason to get up at 8 am on a Saturday morning to play football. They are all a great bunch of lads especially Chris, Davechenko, McGinty and Spiersy (who one day will give me a pass).

Cheers to my brother Jonathan, Iain "Bertie" Lickerish and Gary for all the memorable Friday nights out at Hamilton Palace, or as it is more commonly known, "la Palais". Also thanks to all my school mates who I don't see enough of these days; Walker, Kingy, Derek Mc, Arvind, Hazel and Mary.

I'd also like to thank all of my family - Mum, Dad, Jonathan, my gran, my late grandfather, aunts, uncles and cousins for everything over the years. Words cant express how grateful I am in particular to Mum, Dad and Jonathan. Jonathan is not only my twin brother, he is my best friend and I would not be the person I am today without him. Thank you J dud/J Rod and big hugs (Too far?)! Finally thanks to Fiona for being so kind, caring, understanding and thoughtful (basically for being you - very cheesy I know). Most importantly, thank you Fi for laughing at all my terrible jokes!

Declaration

Except where explicit reference is made to the work of others, this dissertation is the result of my own work. None of this material has been submitted for any other degree at the University of Glasgow or any other institution.

James Paul Grant

Contents

List of Figures

List of Tables

Chapter 1

Introduction

Semiconductors have been studied in laboratories since 1830 [1]. The first materials investigated were a group of elements and compounds that were poor electrical conductors. Shining light on them generated an electric current that would pass through the material. The first major application of semiconductors were as detectors in radios, used in a device called a "cat's whisker" [2]. These devices were somewhat troublesome, however, requiring the operator to move a small tungsten filament (the whisker) around the surface of a galena (lead sulfide) or carborundum (silicon carbide) crystal until it suddenly started working. The "cat's whisker" is a primitive example of a special type of diode still popular today; a Schottky diode. One of the most significant inventions of the 20th century was the fabrication of the solid-state transistor by Bardeen, Brattain, and Shockley which stimulated increased interest in semiconductors. In the past three decades, integrated circuits have allowed the manufacture of millions of transistors onto a single semiconductor crystal. This has led to an explosion in the electronics sector transforming it into a multi trillion pound industry. Nowadays semiconductor devices are used in computers, mobile phones, lasers and digital cameras,

to name only a few applications.

Silicon is the most widely used and well known semiconductor material. It is the second most abundant element on earth and exhibits excellent semiconducting properties. Recently more exotic semiconductors such as GaAs, GaN, SiC, CdZnTe and diamond have been studied for applications where silicon performs poorly or is not suitable. Three such applications where other semiconductors may outperform Si are: as radiation hard tracking detectors; ultra-violet (UV) light detectors; and in-situ soft (5 - 25 keV) x-ray beam position monitors at third generation synchrotron light sources. This thesis examines the compound semiconductor gallium nitride (GaN) as a radiation hard tracking detector and UV light detector as well as studying single crystal chemical vapour deposition (CVD) diamond as an in-situ soft x-ray beam position monitor.

1.1 GaN as a Radiation Hard Detector

Over the past thirty years experiments at particle colliders, such as the Large Electron Positron (LEP) collider at CERN, have been used to rigorously test the standard model of particle physics. In pursuit of new physics, the total collisional energy of the particles has increased during this time placing huge demands on designers of tracking detectors. Modern tracking detectors, such as those at the ATLAS [3] experiment on the Large Hadron Collider (LHC) [4] beam line, are made from solid state semiconductors and are typically used in a pixel or strip configuration. The LHC, due to be switched on in 2008, will collide protons at a centre of mass energy of 14 TeV. The time between proton bunch crossings will be 25 ns and the tracking detectors are positioned only a few centimetres from the interaction point in order to observe short

lived particles. Over the 10 year operational lifetime of the LHC these Si tracking detectors will experience high levels of radiation damage resulting in a severe degradation of tracking capability.

The proposed upgrade of the LHC, the Super LHC (SLHC), which will operate at an anticipated design luminosity of 10^{35} $cm^{-2}s^{-1}$, will require tracking detectors that can withstand a radiation environment that is 10 times more hostile than the LHC. Figure 1.1 shows the accumulated hadron fluences expected in the SUPER-ATLAS inner detector after 5 years operation [5]. At these anticipated SLHC fluences the radiation damage is so great

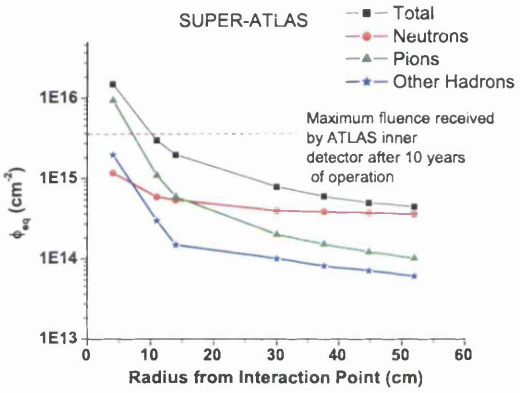

Figure 1.1: Hadron fluences expected in the SUPER-ATLAS inner detector after 5 years of operation. ϕ_{eq} is the 1 MeV neutron equivalent fluence [5].

that with the currently available Si technology the tracking detectors would need to be replaced every few years [6]. Substantial research is currently being conducted within the framework of the CERN RD48 [7] and CERN RD50 [8] collaborations to find tracking detectors that are significantly more radiation hard. The vast majority of research has focussed on the defect engineering of Si [5] and on 3D detectors [9] where, instead of employing the more

typical planar detector structure [10], the electrodes penetrate the detector bulk with the advantage of minimising the charge collection distance. Also investigated within these collaborations is the use of semiconductors other than Si as a tracking detector material. Diamond and 4H-SiC have received particular attention, however the reported results have not been as promising as first anticipated. GaN is another so called wide band gap semiconductor that is thought to be potentially more radiation hard than Si.

GaN is not found naturally on earth and was first synthesised by Juza and Hahn in 1938 [11]. However the first growth of large area GaN epilayers on sapphire substrates was not achieved until 1969 [12]. Table 1.1 shows the various properties of GaN and other semiconductors commonly used as radiation detectors, namely Si, Ge, GaAs, 4H-SiC and diamond. GaN's

Property	Si	GaN	4H-SiC	Diamond	Ge	GaAs
Z	14	31/7	14/6	6	32	31/33
E_g (eV)	1.12	3.39	3.3	5.5	0.66	1.42
Density (g/cm^3)	2.3	6.15	3.2	3.5	5.32	5.32
μ_e (cm^2/Vs)	1450	1000	800-1000	1800-2200	3900	9200
μ_h (cm^2/Vs)	450	30	50-115	1200-1600	1800	320
Dielectric constant	11.9	8.9	9.7	5.7	16.2	12.4
e-h pair creation energy (eV)	3.6	8.9	8.4	13.1	2.96	4.35
e-h pairs/μm (eV)	81	$\sim$ 65	51	36	247	130
Displacement (eV)	13-25	10-20	20-35	43	28	10
Radiation length χ_0 (cm)	9.36	2.56	8.7	12.15	2.30	2.3

Table 1.1: Properties of various semiconductors [5]. The e-h pairs/μm value is for a Minimum Ionising Particle (MIP). Electrons with an energy greater than a few MeV are relativistic and are said to be MIPs.

wide band gap should result in detectors with lower leakage currents than an equivalent Si detector. A further possible advantage of using GaN as a tracking detector is that its displacement energy may be larger than Si resulting in it being more intrinsically resistant to radiation damage. Two limitations of GaN compared to Si are its lower hole mobility and lower signal per incident ionising particle.

The radiation hardness of three semi-insulating epitaxial GaN wafers was investigated in this thesis. All three of these wafers had an epitaxial thickness of either 2.5 μm or 12 μm and were grown on sapphire substrates. Unintentionally doped GaN is n-type, however by selecting certain growth conditions (i.e. temperature, pressure, precursor gas flow rates etc.) it is possible to realise semi-insulating GaN. Pad and guard ring structures were fabricated and devices irradiated with 24 GeV/c protons and 1 MeV equivalent neutrons to fluences of 10^{14} particles cm^{-2}, 10^{15} particles cm^{-2}, 2x10^{15} particles cm^{-2}, 5x10^{15} particles cm^{-2} and 10^{16} particles cm^{-2}. The effects of the various irradiations were evaluated and the radiation hardness of GaN assessed.

Chapter 2 describes the lithography and dry etching techniques used to produce the detectors while Chapter 3 outlines the fundamental semiconductor physics theory and principles of radiation detection necessary for understanding of the results in subsequent chapters. Chapters 4, 5 and 6 evaluate the radiation hardness properties of the three GaN wafers and should be used to complement each other. Specifically, Chapter 4 details the macroscopic properties, namely the current-voltage (I-V), capacitance-voltage (C-V) and charge collection efficiency (CCE) characteristics, of the irradiated GaN detectors. Chapter 5 describes the inductively coupled plasma (ICP) dry etching of the three GaN materials for the purpose of forming ohmic contacts and improving the detector geometry. The macroscopic properties

of these etched devices are also presented in this chapter. Chapter 6 looks at the as-grown and radiation induced defects of the GaN detectors through photoluminescence (PL), contact photoconductivity (CPC) and thermally stimulated current (TSC) measurements. GaN is noted as having a high density of as grown defects and dislocations that can significantly affect device performance.

1.2 GaN as a UV Detector

The direct, wide band gap of GaN also makes it an attractive material for the detection of UV light. It can be seen from Equation 1.1 [13] that the band gap (E_g) of GaN, which is approximately 3.39 eV at 300 K, corresponds to a cut-off wavelength (λ_C) of 365 nm.

$$\lambda_C = \frac{1.24}{E_g} = \frac{1.24}{3.39\text{eV}} = 365\text{nm} \tag{1.1}$$

Therefore any detector fabricated on GaN should, theoretically, exhibit no photoresponse to light with a wavelength greater than 365 nm i.e. GaN is an intrinsic rejector of visible light. This presents a significant advantage over Si, the currently preferred material for UV detection. Visible and infra-red filters have to be used with Si UV photodetectors, increasing both expense and complexity. An additional benefit of GaN is that by adding varying fractions of Al, forming the ternary alloy AlGaN, the cut-off wavelength may be tuned between 365 nm and 200 nm (see Table 1.2).

GaN and AlGaN detectors are currently being developed for UV space applications under the umbrella of the BOLD (Blind to Optical Light Detectors) initiative [14]. The BOLD initiative was established primarily to develop radiation hard UV and extreme detectors for the ESA solar orbiter [15], due to be launched in 2015.

$Al_xGa_{1-x}N$	E_g (eV)	λ_c (nm)
x = 0	3.39	365
x = 0.23	3.88	320
x = 0.25	4.0	310
x = 0.35	4.28	290
x = 1	6.2	200

Table 1.2: Band gaps (E_g) and cut-off wavelengths (λ_c) of AlGaN materials with varying Al molar fraction

A biological application that uses detector technology developed by physicists is the measurement of circular dichroism (CD). CD is defined as the difference in absorption between left hand and right hand circularly polarised light as it passes through a solution of an optically active molecule. Proteins are optically active molecules and CD may be used to determine how various proteins fold and the time taken for a protein to adopt a certain configuration. Neuro-degenerative diseases such as Alzheimer's and Creutzfeldt-Jakob disease occur when certain proteins in the brain do not fold in the conventional way. By establishing how different proteins fold it may be possible to design drugs to treat diseases such as Alzheimer's.

Traditionally the CD spectrum of a particular protein is measured using a photomultiplier tube and lock-in amplifier. However this method is time consuming and an improved approach, utilising solid state position sensitive semiconductor detectors, has been proposed by scientists at the Rutherford Appleton and Daresbury Laboratories [16]. This novel technique requires a position sensitive 46 channel diode array detector that is efficient at detecting light in the 180-240 nm wavelength range.

One of the main aims of this thesis was to produce a 46 channel diode

array detector on GaN to be used in a CD experiment at Daresbury Laboratory. Five different GaN/AlGaN materials, three metal-semiconductor-metal (MSM) diode geometries and two different contact schemes were investigated and the optimal material, diode geometry and contact scheme established. Several multi-channel GaN array detectors were fabricated and the device that exhibited the maximum responsivity was used in a CD experiment at Daresbury Laboratory.

Chapter 2 details the lithography techniques used to produce the various test devices and array detectors. The current-voltage (I-V) and spectral response characteristics of the test structures are given in Chapter 7. Chapter 8 outlines the CD station experimental set-up at Daresbury Laboratory and evaluates the CD data of camphorsulphonic acid (CSA) obtained using both a Si photodiode array and a MSM GaN array detector.

1.3 Single Crystal Diamond as a Beam Position Monitor

Diamond is another material that has been extensively investigated over the past decade for use as a radiation hard particle tracking detector [17]. Its large band gap, large displacement energy and excellent charge transport characteristics (see Table 1.1) lends it to being intrinsically more resistant to radiation damage than the current tracking detector material of choice, silicon. Until recently only polycrystalline diamond material has been commercially available. However, the emergence of single crystal diamond, with its more uniform response than its polycrystalline rival, has stimulated increased interest. Diamond is now being investigated for wider applications, such as an X-ray beam position monitor [18].

Third generation synchrotron X-ray beams may nowadays be focussed to a precision of less than 1 μm and devices with similar spatial precision are required to monitor the beam position or provide real-time information for position control. The properties of single crystal diamond makes it an excellent material for an in-situ beam position monitor over the soft X-ray energy range of 5-25 keV. A further advantage of diamond is that, as illustrated in Figure 1.2, its lower atomic number compared to silicon results in less attenuation of the incident X-ray beam.

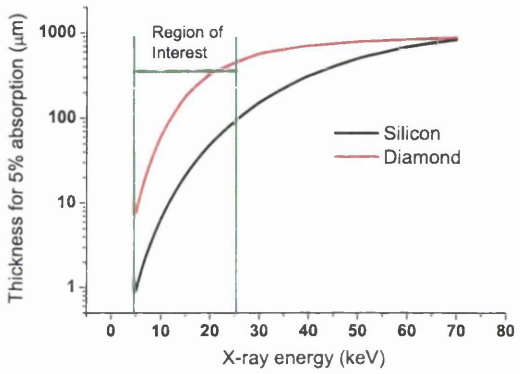

Figure 1.2: Plot comparing the thickness for 5% absorption versus x-ray energy between diamond and silicon

In this thesis, the suitability of single crystal CVD diamond as an in-situ soft X-ray beam position monitor is assessed. The dark current, charge collection and X-ray response properties of a single crystal diamond pad detector are given in the latter half of Chapter 8. The chapter concludes with descriptions and images of two mask designs that will be used to produce single crystal diamond beam position monitors with various device configurations.

Material	Grower	Epi thickness (μm)	Rad. Hard	UV	Label
GaN	Lumilog	12	Yes	Yes	12GaN
GaN	Tokushima	2.5	Yes	Yes	36GaN
GaN	Tokushima	2.5	Yes	Yes	45GaN
GaN	Emcore	2.5	No	Yes	Emcore GaN
AlGaN	Emcore	2.5	No	Yes	AlGaN

Table 1.3: Properties of the four GaN wafers and one AlGaN wafer studied in this thesis. Details are also given whether the material was used for radiation hardness studies (Rad. Hard) or Ultraviolet light detection studies (UV). The final column gives the naming convention used for each material

1.4 Labelling of GaN Devices

Four GaN wafers and one AlGaN wafer were studied in this thesis. Table 1.3 gives some properties of these wafers and also the naming convention that is used throughout this thesis for the different materials . The radiation hardness of the Emcore GaN material has previously been assessed [19].

Publications

Main Author

- J. Grant et. al., "GaN as a Radiation Hard Particle Detector", Nucl. Instr. Meth. A, 576, 60-65, 2007
- J. Grant et. al., "GaN UV Detectors for Protein Studies", Nucl. Instr. Meth. A, 563, 27-30, 2006
- J. Grant et. al., "Wide Bandgap Semiconductor Detectors for Harsh Radiation Environments", Nucl. Instr. Meth. A, 546, 213-217, 2005

Named Author

- J. Morse et. al., "Single Crystal Diamond as an X-Ray Beam Monitor", Dia. and Rel. Mat., 16, 1049-1052, 2007
- A. Blue et. al., "GaN UV Detectors for Synchrotron Based Protein Studies", Nucl. Instr. Meth. A, 546, 131-134, 2005

Chapter 2

Fabrication Techniques

2.1 Introduction

This chapter discusses the techniques used to process the GaN and diamond material into radiation detectors. These techniques include photolithography, electron beam lithography and metal lift-off to define contacts and alignment markers. Also described in this section is the dry etching process for semiconductor devices. In order to understand the mechanisms of dry etching a brief description of plasma physics is also given. The detector fabrication was carried out in the James Watt Nanofabrication Clean room facility at the University of Glasgow. The information in this chapter is broadly referenced from three sources, "The Science and Engineering of Microelectronic Fabrication" by Stephen A. Campbell [20], "Semiconductor Devices: Physics and Technology" by S.M. Sze [13] and "E-Beam Lithography" course notes by Dr. Stephen Thoms[21].

2.2 Lithography

Lithography is defined in the online Oxford English Dictionary as; "the process of printing from a flat metal surface treated so as to repel the ink except where it is required for printing." In this work the word lithography is used to define a process for transferring a pattern onto the surface of a semiconductor via an intermediate radiation sensitive polymer called a resist. Radiation sources used in lithography techniques range from optical (ultraviolet, deep ultraviolet and extreme ultraviolet) to non-optical (electron beam and X-ray). Each radiation exposure tool has its own advantages and disadvantages. The performance of an exposure tool is determined by three parameters: resolution, registration and throughput. Resolution is the minimum feature size that can be transferred with high fidelity to a resist on a semiconductor sample. Registration is a measure of how accurately patterns on successive masks can be aligned, or overlaid, with respect to the previously aligned patterns on the semiconductor sample. Throughput is the number of samples that can be exposed per hour for a given mask.

2.2.1 Photolithography

Photolithography uses ultra-violet (UV) light as the radiation source to transfer the pattern onto an intermediate compound called a photoresist or simply a resist. A mask is positioned between the UV light source and the resist that is to be patterned. The only areas of resist exposed to the UV light are those beneath the transparent sections of the mask. Exposure to the UV light changes the chemical structure of the resist so that it either becomes more soluble or insoluble (depending on the type of resist used) in a developer solution. This development stage leaves the remaining resist on the sample

either in the shape of the mask design or in the negative shape of the mask design (again this is dependent on the type of resist used).

There are two main types of mask aligners used in photolithography pattern transfer; the contact printer mask aligner and the projection printer mask aligner. The differences between the two are shown in Figure 2.1.

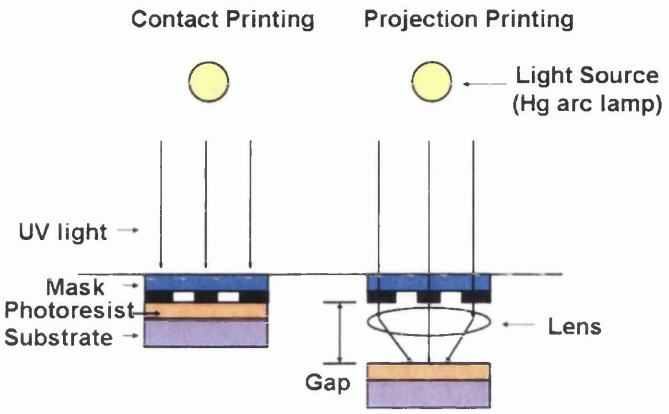

Figure 2.1: Contact and projection printing

The main difference between contact printing and projection printing lies in the positioning of the mask plate. In contact printing the mask is in intimate contact with the sample whereas for projection printing there is a gap between the mask and the sample. In projection printing a lens system is used to focus the UV light onto the substrate. The optics for a projection printing system are more complex than the optics for a contact printer and the mask has to be scaled very precisely to take the projection effects into account. In projection printing the features on the mask are not directly transferred to the resist but undergo a change in scale. Contact printing has good resolution without the need for expensive optics or scaling of the mask features that are associated with projection printing. However, with contact

printing there is greater possibility of mask contamination. Also, uneven layers of resist result in broadening of the features that are patterned and hence resolution is limited. Projection printing is mainly used in industry where is it critical that there is no mask contamination, as one mask is used to pattern thousands of wafers. A state of the art projection printer can pattern 100 or more 200 mm diameter wafers per hour with a resolution of 80 nm [21]. The photolithographic processing used for this thesis was carried out using a Karl-Suss MA6 contact printing mask aligner. The registration size of this aligner is ~ 5 μm with a resolution of ~ 1 μm.

Photoresist

A photoresist is made up of three main components: a resin or base material, a photo-active compound (PAC) and an organic solvent. The organic solvent controls the mechanical properties, such as the viscosity of the base, keeping it in a liquid state. All photoresists are polymeric coatings that are designed to change properties upon exposure to light. For positive resists, the PAC acts as an inhibitor before exposure, slowing the rate at which the resist will dissolve when placed in a developing solution. Upon exposure to UV light, a chemical process occurs by which the inhibitor becomes a sensitiser, increasing the dissolution rate of the resist. The exposed resist will be removed by the developer solution whereas the unexposed regions of the resist will remain on the substrate. The mask, therefore, is an exact copy of the pattern which is to remain on the resist. Negative resists behave in the opposite manner. Exposure to the UV light causes the negative resist to become polymerised (cross linked), and therefore more difficult to dissolve. The negative resist remains on the surface wherever it is exposed, and the developer solution removes the unexposed portions. Negative resists are developed in an organic

solvent rather than in an aqueous solution. Masks used for negative photoresists, therefore, contain the inverse (or photographic "negative") of the pattern to be transferred. Figure 2.2 shows the difference between positive and negative resists after development.

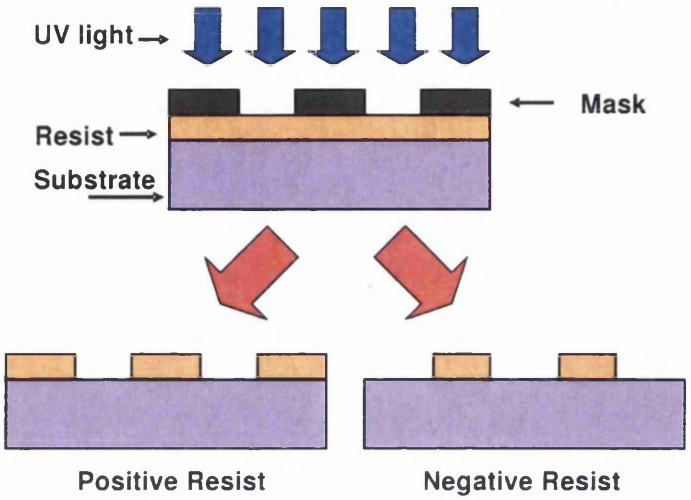

Figure 2.2: Positive and negative resist profiles after development

A disadvantage of negative resists is that their exposed portions swell as their unexposed areas are dissolved by the developer. This swelling phenomenon limits the resolution of negative resist processes. The unexposed regions of positive resists do not exhibit swelling and distortions to the same extent as the exposed regions of negative resists. This results in positive resists achieving a better image resolution than negative resists. Positive resists were used exclusively throughout this thesis.

Mask production for photolithography

The masks used for photolithography were produced using an electron beam writer. In order to produce a mask with the required pattern a design file

is created in a CAD package such as Wavemaker (WAM) or Tanner L-Edit, which was the CAD package used in this work. In L-Edit a hierarchy layout file is produced that is made up of a number of different individual cells. This layout file is transferred to be written by the electron beam writer onto the mask plate. The mask plates are coated with 100 nm of chrome, which allows 0.1 % transmission of ultraviolet light through the covered areas. The mask plates can then be copied using contact lithography onto ferric oxide covered plates. These ferric oxide plates have the advantage of allowing partial light transmission enabling more accurate registration of samples with an optical mask aligner. The mask copying process results in a slight loss of resolution, but this is not significant for the large features discussed in this work.

Sample Processing Using Photolithography

The steps involved in simple photolithographic processing are: sample cleaning, resist application, soft bake, exposure and finally resist development. These fabrication steps are carried out in a cleanroom, where the temperature, humidity and density of dust particles can be controlled. The cleanliness of a cleanroom is defined by the number of 0.5 μm dust particles per cubic foot. The lower the number of 0.5 μm dust particles the more clean the cleanroom. The James Watt Nanofabrication Cleanroom has areas that have cleanliness classes of 1000, 100 and 10.

Table 2.1 shows the standard process steps for producing a pattern in Shipley S1818 resist (a positive tone resist). Usually the last two digits in the photoresist name give its thickness when spun at 4000 rpm for 30 seconds. These process steps were used to pattern the pad and guard ring structures on the 12 GaN, 36 GaN, 45 GaN and to pattern the various structures on the diamond material.

Step	Process
Substrate surface clean	Sequential solvent cleans in opticlear, acetone and IPA (isopropyl alcohol)
Sample dry	Dry sample using N_2 gun
Spin resist	Spin S1818 resist at 4000 rpm for 30 seconds. This will give a resist thickness of 1.8 μm
Soft bake	Bake for 30 minutes at 90°C to remove solvents from the resist
Exposure	Expose for $\sim$ 4 seconds using Karl Suss MA6 mask aligner
Development	S1818 resist developed in a solution of 1:1 reverse osmosis water: Microposit developer for 75 seconds at room temperature
Sample dry	Dry sample using N_2 gun

Table 2.1: Photolithography process steps using S1818 resist

Before application of the resist it is essential to ensure that the surface of the substrate is clean of debris and dust particles. If this is not done there will be a degradation in the quality of pattern that is transferred which may lead to device failure. Surface debris and dust particles are removed from the sample by placing it in beakers of organic solvents. The sample is first placed into a beaker of opticlear which has been heated to 60°C for 10 minutes. The beaker is transferred to the ultrasonic water bath and is agitated for a further 10 minutes. These processes are repeated using beakers of acetone and IPA (isopropyl alcohol) and the sample is finally blown dry using an N_2 gun. After the solvent cleaning stage the substrate is placed onto a vacuum chuck in order to apply the photoresist. An HDMS (hexamethyldisilazane) based

primer coating is sometimes spun onto the substrate in order to promote adhesion between the substrate and the resist. Primer is used when there is oxide formation on the surface of the substrate. The HDMS reacts with the oxide on the surface forming a strong bond and the remaining free bonds readily react with the photoresist, enhancing adhesion. In this thesis primer was rarely used as there proved to be no adhesion problems between the various substrates and the photoresist. The photoresist is applied to the surface of the substrate using a syringe with a 0.1 μm filter and then spun at the required speed for a set time. When spinning S1818 resist onto small substrates it is essential to deposit the correct amount of resist. Deposit too little resist and the resist will not cover the entire area of the substrate, deposit too much and the resist will accumulate at the edges of the sample. Both situations are severely detrimental to the quality of the pattern transfer. Once the resist has been spun, the sample is placed in an oven held at a temperature of 90°C for 30 minutes to remove solvents from the resist. The sample is then exposed for the required time using the MA6 Karl Suss contact aligner. It is then developed in the appropriate developer solution for the required time and is finally blown dry using an N_2 gun.

Figure 2.3 shows the process steps for S1818 resist. The exposed areas of resist are removed after development leaving features with sharp, clean edges. Underexposure or underdevelopment of resist leads to incomplete resist removal. Overexposure or overdevelopment of the resist results in broadening of patterned features. Diffraction effects, which occur as a result of the mask not being in intimate contact with the sample, also lead to the broadening of features or incomplete exposure of the resist. Broadening of features, while undesirable, rarely leads to complete failure of the device.

In this work S1818 was the most commonly used photoresist however a

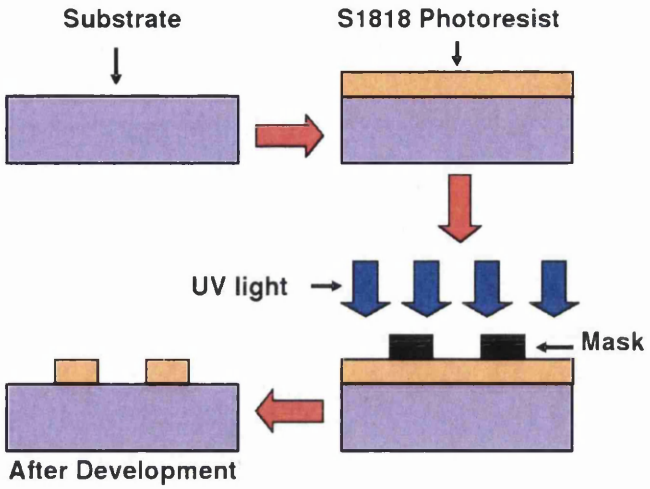

Figure 2.3: Substrate patterning using photolithography

second positive photoresist called AZ4562 was also used. AZ4562 is more resilient to dry etch damage than S1818 and so it was used to pattern the 12GaN, 36GaN and 45GaN samples for subsequent etching. Table 2.2 shows the process steps used for patterning the samples with AZ4562. The hard bake step is required to reduce the sensitivity of the resist to etch damage.

2.2.2 Electron Beam Lithography

Direct write electron beam (e-beam) lithography is the other method used in this thesis for pattern transfer to a substrate. An electron beam is used to directly pattern an electron sensitive resist - there is no mask involved. This electron sensitive resist is similar to photoresist. Using e-beam lithography it is possible to write features that are as small as 3 nm [21]. The minimum feature size of a projection system is determined by Rayleigh's criterion [13],

$$W_{min} = k\frac{\lambda}{NA} \tag{2.1}$$

Step	Process
Substrate surface clean	Sequential solvent cleans in opticlear, acetone and IPA (isopropyl alcohol)
Sample dry	Dry sample using N_2 gun
Spin resist	Spin AZ4562 resist at 1500 rpm for 30 seconds. This will give a resist thickness of $\sim$ 15 μm
Soft bake	Bake for 30 minutes at 90°C to remove solvents from the resist
Exposure	Expose for $\sim$ 30 seconds using Karl Suss MA6 mask aligner
Development	AZ4562 resist developed in a solution of 4:1 reverse osmosis water: AZ400K developer for 4 minutes at room temperature
Sample dry	Dry sample using N_2 gun
Hard bake	Bake for 30 minutes at 120°C

Table 2.2: Process steps for photolithography using AZ4562 resist

where W_{min} is the minimum feature size, k is a constant related to resist sensitivity, λ is the wavelength of the radiation source and NA is the numerical aperture of the projection system. The minimum feature size is determined by the wavelength of the incident radiation and by the numerical aperture of the system. The wavelength of multi kV electrons is much shorter than the wavelength of UV light and so smaller features may be written using e-beam lithography.

Physical Parts of the Electron Beam Machine

The e-beam writer used for this work was a Leica EBPG5 HR100. Figure 2.4

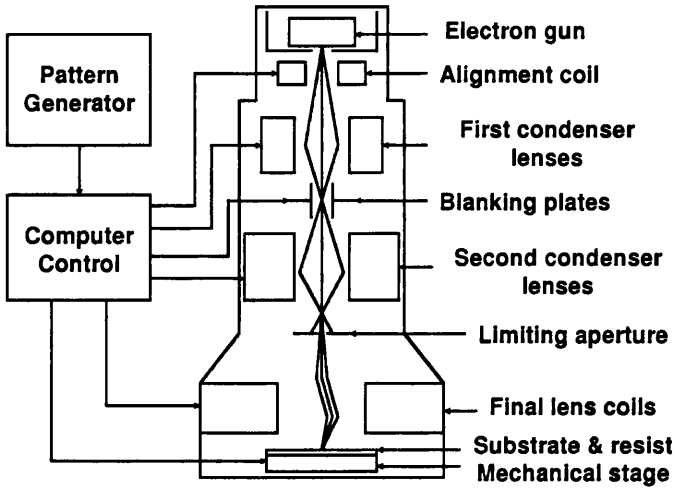

Figure 2.4: Schematic diagram of an e-beam writer

shows the main components of an electron beam writer. Typically electron beam writers use two scanning methods; vector scanning and raster scanning. In vector scanning the electron beam only travels over the regions that are to be patterned, whereas in raster scanning the electron beam scans the entire substrate and is switched on where the pattern is desired and switched off, or blanked, for the other areas. The EBPG5 HR100 uses vector scanning which is more accurate and faster than raster scanning. The electrons are generated by a thermionic electron gun at the top of the column. All electron beam writing systems have in common the need for an electron source with a high intensity, high uniformity, small spot size, good stability and a long life. The electron gun is made of a material that can emit a suitable current density of electrons such as a tungsten filament or a single crystal of Lanthanum Bromide (LaB_6). The EPG5 HR100 has a LaB_6 filament that is typically changed every 3 months. The condenser lenses are formed with electromagnets. The first set of condenser lenses are used to focus the beam

onto a blanking plate, which controls the direction of the beam electrostatically and can direct it to a beam stop when required. The second set of condenser lenses are used to focus the beam onto the limiting aperture. The limiting aperture is variable in size and controls the spot size (the current density) of the beam. A smaller aperture results in a smaller spot size of the electron beam. Large areas are best patterned using a large spot size whereas small areas are best patterned using a small spot size. Spot sizes of the EBPG5 HR100 range from 12 nm to 200 nm. The final beam coils are used to move the position of the beam relative to the sample that is to be patterned. The EBPG5 HR100 writes blocks of 800 μm. Patterns that are larger than 800 μm are written by moving the sample on the mechanical stage and stitching the 800 μm blocks together. Shapes that are written on block boundaries may be written incorrectly as a small error may occur in the alignment of adjacent blocks.

Sample Processing Using Electron Beam Lithography

The resist most commonly used in e-beam lithography is PMMA (polymethyl methacrylate). It adheres to almost any surface and gives very reproducible results but has poor dry etch resistance. PMMA is a long chain homopolymer compound which is acid and alkali resistant. In PMMA the rate of dissolution is much higher than the rate of cross-linking. The polymer chains break into fragments (chain scission) when exposed to the electron beam. These fragments have a reduced molecular weight and are readily dissolved in the developing fluid MIBK (methyl isobutyl ketone).

The fabrication techniques used for e-beam lithography are similar to those used for photolithography. The process steps used to pattern a typical e-beam resist such as PMMA are shown in Table 2.3. In this work e-beam

lithography was used to pattern the MSM structures on the various GaN materials and to pattern the masks used for photolithography.

Step	Process
Substrate surface clean	Sequential solvent cleans in opticlear, acetone and IPA (isopropyl alcohol)
Sample dry	Dry sample using N_2 gun
Spin resist	Spin PMMA resist at 5000 rpm for 60 seconds
Soft bake	Bake for 60 minutes at 180^{o}C to remove solvents from the resist
Exposure	Expose using electron beam writer. Spot size, dose and write time are dependent on resist type and features to be patterned
Development	Developed in solution of 2:1 MIBK:IPA for 45 seconds at 23^{o}C
Sample dry	Dry sample using N_2 gun

Table 2.3: Process steps for e-beam lithography using PMMA resist

Photolithography Versus E-Beam Lithography

The obvious advantage of e-beam lithography compared to photolithography is that smaller features can be written. Using photolithography the minimum feature size that can be produced is 1 μm whereas features as small as 3 nm can be written using e-beam lithography. Also, registration precision of e-beam lithography is a factor of 100 times better than photolithography. Using e-beam lithography it is possible to align two layers with 50 nm accuracy whereas using photolithography it is difficult to align two layers with 5 μm accuracy. A further advantage of e-beam lithography is that more densely

packed features may be successfully produced.

The major disadvantage of e-beam lithography is that it has a much lower throughput than photolithography. E-beam lithography is a serial process, i.e. each section of the desired pattern is written sequentially whereas photolithography is a parallel process, i.e the entire pattern is written in one exposure. Another difficulty with e-beam lithography arises from the fact that due to the thin nature of the resists used they are less suitable for some types of processing, such as dry etching. Both e-beam lithography and photolithography complement each other since in general, features <1 μm are patterned utilising e-beam lithography and features ≥ 1 μm are patterned using photolithography.

2.3 Metal Deposition of Thin Films and Lift Off

Often is is desirable to deposit metal onto substrates that have been patterned using lithography techniques (e.g. to form Ohmic or Schottky contacts to semiconductors). This section describes the metal evaporation technique used in this work and the subsequent lift-off process.

Metals can be deposited onto a substrate using either evaporation or sputtering techniques. During evaporation the source metal is heated in a vacuum using either a high current passing through a tungsten wire or using a focused electron beam. The two variations are called thermal and e-beam evaporation respectively. In both cases atoms are removed from the solid metal source, diffuse across the vacuum chamber and are deposited onto the sample that sits on a holder some distance away.

In this work thin metal layers were deposited onto samples by evaporation

using a focused electron beam to heat the metal. A schematic diagram of an electron beam metal evaporator is shown in Figure 2.5. The temperature

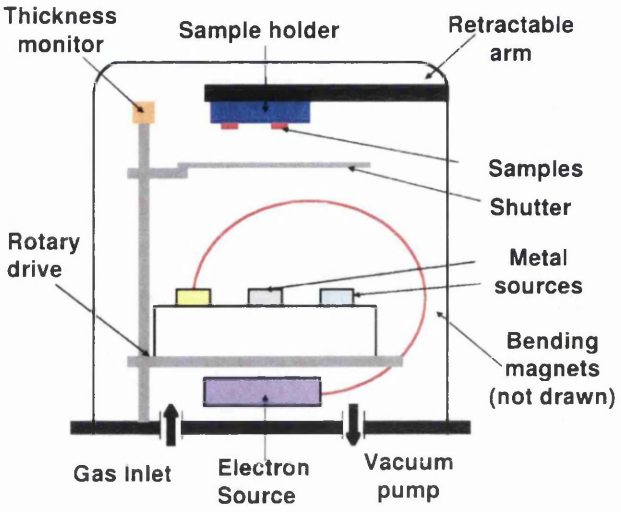

Figure 2.5: Schematic of an e-beam evaporator

required to achieve evaporation is mainly a function of the metal and the chamber pressure. To achieve evaporation at reasonably low temperatures and to minimise possible contamination, electron beam evaporators are operated at a pressure of $\sim 1\text{x}10^{-6}$ mbar. The electrons produced by the electron gun are refracted by a strong magnetic field through 270^{o} and are incident on the surface of the metal target. Usually more than one metal layer is required to be deposited without exposing the sample to the atmosphere. Therefore a rotary drive is fitted that allows the crucible to be rotated and different metals selected while the sample remains under vacuum. There are two shutters, one below the substrate and one above the crucible where the metals are located. The substrate shutter masks the sample until the required deposition rate is achieved and is also used to stop the deposition of the metal onto the sample when the required thickness is achieved. A quartz

crystal thickness monitor is used to measure the thickness of the deposited metal in real time. Metal deposition by evaporation is a low energy process and because the sample sits at a long distance away from the metal source, a sharp metal/semiconductor interface will be created without disruption to the semiconductor interface. However significant thermal stress may occur because the metal ions have a high temperature on arrival at the sample surface. Typical deposition rates of the Plassys MEB 450 electron beam evaporator used in this work range from 0.3 to 1 nm/s.

2.3.1 Metal Lift-Off & Techniques to Improve Lift-Off

After metal deposition it is necessary to remove the unwanted areas of metal. This is done in a process called metal lift-off (see Figure 2.6).

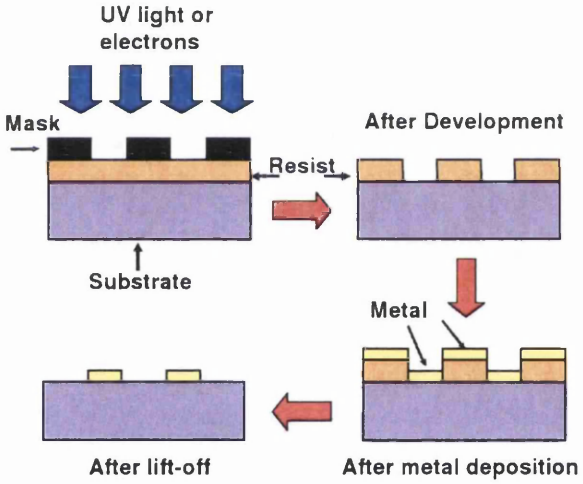

Figure 2.6: Metal lift-off process

The metalised sample is placed in a beaker of hot acetone (heated to 60°C) and the remaining resist is removed along with the metal on top of it. For a positive resist, this leaves only the areas that were exposed during the

lithography process with the deposited metal. The metal ions evaporated travel perpendicular to the surface of the sample with very little horizontal spread therefore the success or failure of lift-off depends on the resist profile after the pattern development.

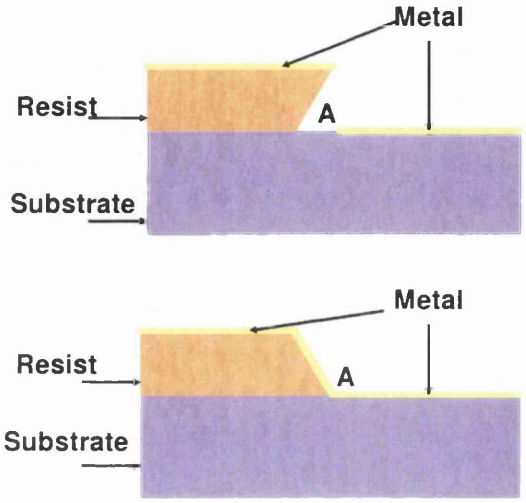

Figure 2.7: Resist profiles after development. Top diagram shows the resist profile desired for successful lift-off. Bottom diagram shows the resist profile that results in lift-off failure

Figure 2.7 shows two cases of resist profile after development. If the angle, A, between the resist and the substrate is $<90^o$ then the side of the resist remains uncovered by metal, creating an opening for solvents (top diagram of Figure 2.7). This opening enables the acetone to reach the resist and lift-off is successful. If the angle, A, between the resist and the substrate is $>$ 90^o then during deposition the side of the resist is coated with metal and the path for solvents to attack the resist is closed (bottom diagram of Figure 2.7) and failure of the lift-off process. Figure 2.8 shows an image taken using a scanning electron microscope (SEM) of a gold layer prior to lift-off. Lift-off

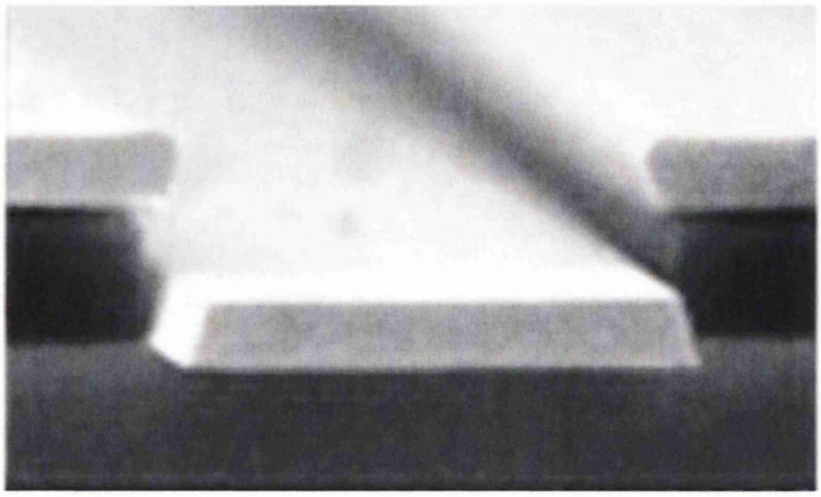

Figure 2.8: SEM image of Au layer prior to lift-off [21]

is more prone to failure if small, densely packed features are to be metalised.

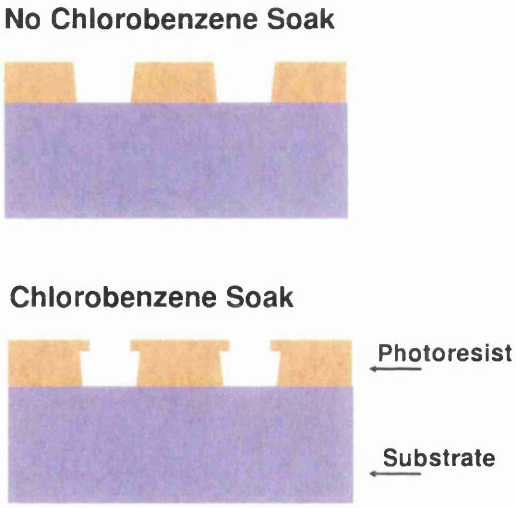

Figure 2.9: Effects of CBZ soak on the resist profile

There are various techniques that can be used to improve lift-off. A technique used to improve lift-off when photoresist is used is a chlorobenzene

(CBZ) soak. The photolithography process follows the steps described in Table 2.1 except that between the exposure and development steps the sample is placed in a solution of CBZ for 15 minutes. The chlorobenzene has the effect of hardening the top surface of the resist. During the development stage the dissolution rate of these hardened regions is much slower and so an overhang in the resist is produced (see Figure 2.9). When a CBZ soak is used the development time of the resist is increased by 50%.

A second approach to improve lift-off is to use a bi-layer (or sometimes even a tri-layer) of e-beam resists. A first layer of resist with a low molecular weight is spun onto the substrate and baked at 180°C for one hour. A second layer of resist with a higher molecular weight is spun on top of this first layer and the substrate is again baked at 180°C for one hour. The first layer spun onto the substrate, due to its lower molecular weight, is more sensitive to electrons than the second layer. This creates an overhang in the resist profile aiding metal lift-off.

2.4 Etching of Semiconductors

The etching of semiconductors was developed to allow the selective removal of material from the semiconductor surface. The ability to create mesas in semiconductors is necessary for many applications such as the isolation of surfaces by silicon trench etching [13] and forming 3D pixel detectors by etching vias in silicon [9]. The etching of semiconductors can be achieved through either chemical etching (known as wet etching), physical etching (known as dry etching) or more typically by using a combination of chemical and physical etching. The appropriate figures of merit associated with etching are:

- Etch rate
- Selectivity
- Etch rate uniformity
- Anisotropy

The primary figure of merit is the etch rate of the semiconductor material, which has dimensions of depth per unit time. A high etch rate is desirable. Too high an etch rate, however, may render a process difficult to control. Selectivity is quantified as the ratio of the etch rate of the semiconductor material and the etch rate of the mask layer. Etch rate uniformity is measured in terms of the percentage variation of the etch rate across the sample. The anisotropy is a measure of the lateral extent of the etch under the mask. Anisotropy, A is given by:

$$A = 1 - \frac{R_L}{R_V} \tag{2.2}$$

where R_L and R_V are the lateral and vertical etch rates respectively. A process is said to be perfectly anisotropic ($A = 1$) if the lateral etch rate is zero. On the other hand an anisotropy of zero would imply that the lateral and vertical etch rates are identical leading to a homogeneous etch.

Wet etching (see Figure 2.10) is typically used for a wide range of non-critical tasks where anisotropy and process control are of less importance. Since the reactive species is normally present in an etchant solution, wet chemical etching consists of three processes; movement of the etchant species to the surface of the sample, a chemical reaction with the exposed material that produces soluble by-products, and the movement of the reaction products away from the surface of the sample.

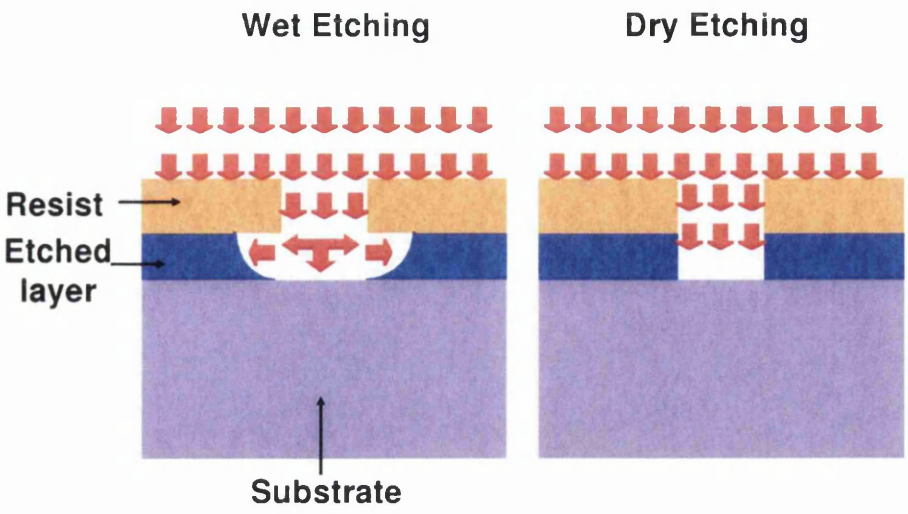

Figure 2.10: Dry and wet etching profiles

A second approach to etch a semiconductor is to use dry etching techniques. Dry etching is synonymous with plasma assisted etching, which denote several techniques that use a plasma in the form of low pressure discharges. Plasma can be defined as a partially or wholly ionised gas with a roughly equal number of positively and negatively charged particles and a different number of unionized molecules. Plasmas are used in many applications; ranging from fluorescent tubes, to tissue culturing in biological studies [23]. Plasmas are also used in various semiconductor processes, such as reactive ion etching (RIE), in chemical vapour deposition and in sputtering. Plasmas can be used in place of high temperatures to crack molecules and hence drive reaction chemistry. They may also be used to create and accelerate ions. The types of processes that may occur in the most common method of plasma generation, DC glow discharge, are shown in Table 2.4.

A small fraction of a plasma contains dissociated atoms or molecules called radicals or ions in the form of charged atoms or molecules. Radi-

Type of Process	Reaction
Dissociation	$e^* + XY \rightleftharpoons X + Y + e$
Atomic excitation	$e^* + X \rightleftharpoons X^* + e$
Molecular excitation	$e^* + XY \rightleftharpoons XY^* + e$
Atomic ionisation	$e^* + X \rightleftharpoons X^+ + e + e$
Molecular ionisation	$e^* + XY \rightleftharpoons XY^+ + e + e$

Table 2.4: Processes that occur in DC glow discharge (denotes an atom or molecule in an excited state, $^+$ denotes a charged atom or molecule)*

cals have an incomplete bonding state and are extremely reactive. Ions are charged atoms or molecules, such as X^+ and XY^+ in Table 2.4. It is these charged atoms and molecules that perform the removal of material from the sample either through physical sputtering or, along with the radicals, through chemical reactions. In a typical plasma, radicals and charged species account for 1% and 0.01% respectively, of the total plasma [20].

2.4.1 Plasma Theory

Plasma theory is an extensive and complex area of physics. A brief description of the fundamentals of plasma theory as related to the application of plasma etching of semiconductors is presented here. A more complete and thorough treatment may be found in, "Industrial Plasma Engineering" volumes 1 and 2 by J. Reece Roth [24], [25]. These references cover all aspects of the generation, development and evolution of plasma discharges.

A plasma can be generated when a DC bias is applied between two electrodes in the presence of a gas contained at a low pressure. Figure 2.11 shows a simple plasma reactor. Two parallel electrodes are contained in a vacuum

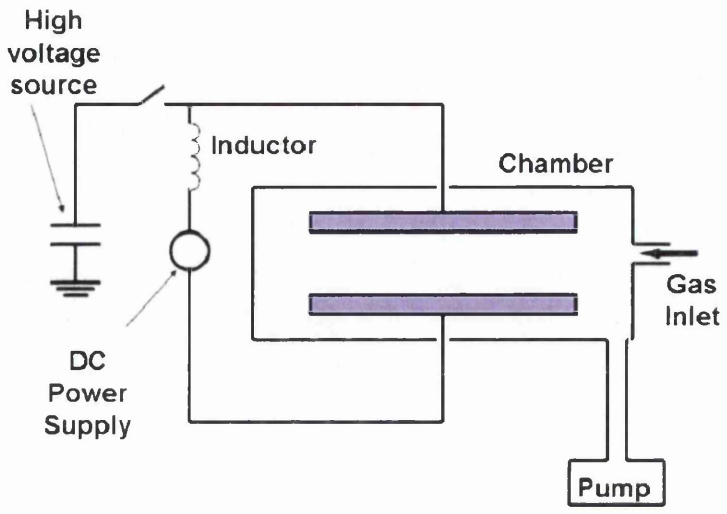

Figure 2.11: A simple parallel plate plasma reactor

system and are attached to a DC power supply through vacuum feedthroughs. A high voltage source, typically a charged capacitor, is connected momentarily to initiate the plasma. The inductor protects the DC power supply from the high voltage arc. Until the arc is struck, the gas will not conduct current since it acts as an insulator. If the voltage is high enough the field in the reactor will exceed the breakdown field of the gas and a high voltage arc will pass between the two electrodes. The arc will create a large number of ions and free electrons. Due to the electric field in the chamber the electrons will be accelerated toward the positively charged anode, while the ions will be accelerated toward the negatively charged cathode. The small mass of the electrons means they will be accelerated much more rapidly than the slowly moving ions. The ions travel across the tube and eventually strike the cathode. When they do, they release a cloud of secondary electrons from the material in the cathode. These secondary electrons are accelerated back toward the anode. If the DC voltage across the electrodes is large enough, then

the electrons have sufficient kinetic energy to collide inelastically with neutral ions within the plasma. Collisions between these high energy electrons and neutral atoms create more ions. In this way the process of secondary electron release and ion generation sustains the plasma.

The requirement for moderate energy electrons precludes optical emission near each of the electrodes. These regions are called dark spaces. These dark spaces are illustrated in Figure 2.12. The anode is a sink for electrons and

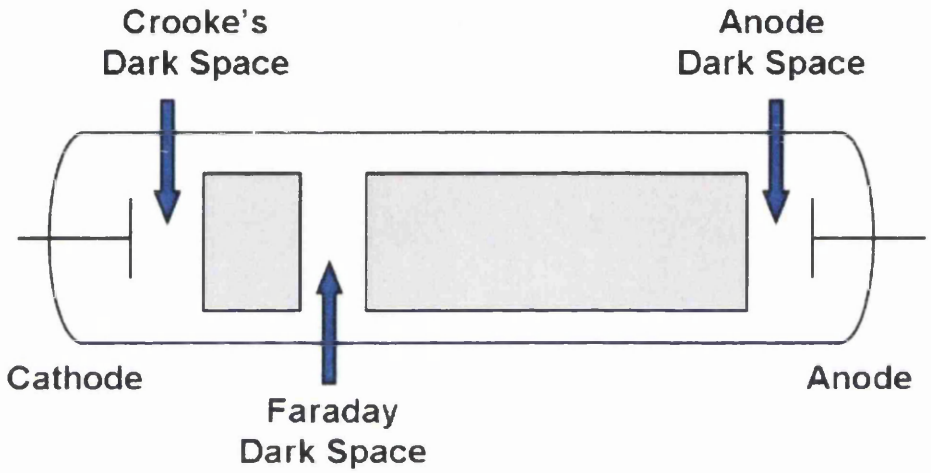

Figure 2.12: Regions of a DC plasma

so the electron density just above the anode is too small for appreciable light emission. This dark space is called the Anode dark space. The region just above the cathode where most of the electrons have very low energy is called Crooke's dark space. The Faraday dark space is located above the cathode where the electrons have been accelerated to very high energies, leading to ionisation. In this region there are few electrons that have energies appropriate for the emission of light.

Plasma etching proceeds in five steps. The etchant species is generated

in the plasma; the reactant is then transported by diffusion through a stagnant gas layer to the surface of the sample; the reactant is adsorbed on the surface; a chemical reaction, along with physical effects such as ion bombardment, follows to form volatile compounds; the compounds are desorbed from the surface, diffused into the bulk gas and pumped out by the vacuum system. The chemistry of plasma etching is highly complex and not completely understood [26] and will not be discussed further.

In physical etching, positive ions bombard the surface at high speed. Small amounts of negative ions formed in the plasma cannot reach the surface of the sample and therefore play no direct role in plasma etching. In chemical etching, neutral reactive species generated by the plasma interact with the surface of the material to form volatile products. Physical and chemical etch mechanisms have different characteristics. Physical etching can yield anisotropic profiles but is associated with low etch selectivity and high ion bombardment induced damage. Chemical etching exhibits a high etch rate, can have good selectivity and produce low ion bombardment induced damage but has poor anisotropy. Combinations of physical and chemical etching can give anisotropic etch profiles, reasonably good selectivity and only moderate ion bombardment induced damage. An example which combines both methods of etching is Reactive Ion Etching (RIE).

2.4.2 Reactive Ion Etching (RIE)

In many cases the material on one or more of the electrodes is insulating. As ions strike the surface of an insulating material (e.g. a photoresist) and secondary electrons are emitted, the surface of the material becomes charged. The charge accumulates on the surface of the sample and the field is reduced until the plasma is ultimately extinguished. To overcome this problem, the

plasma can be driven by an AC signal. Figure 2.13 shows a schematic diagram of an RIE setup. The plasma is generated by applying a 13.56 MHz radio frequency (RF) signal to the reactive gas flowing between two parallel planar electrodes.

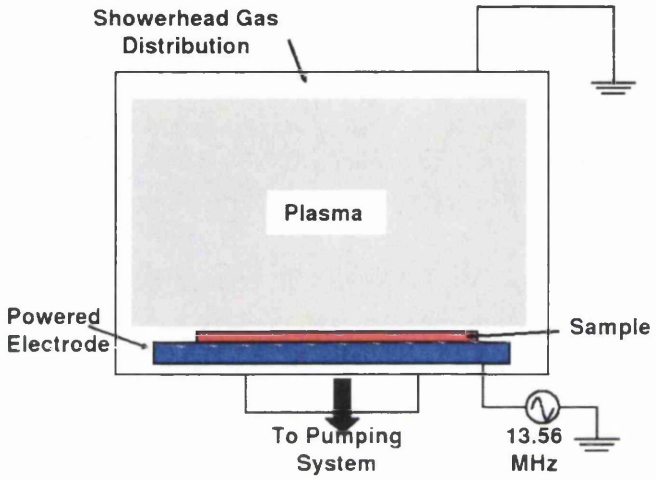

Figure 2.13: Schematic of a Reactive Ion Etching (RIE) reactor

At low frequencies the plasma follows the excitation and the width of the dark space regions pulse with the applied signal. When the excitation rate is greater than 10 kHz, the electrons in the plasma are rapidly accelerated, whereas the relatively slow ions are unable to follow the voltage change. During alternate half cycles, electrons strike the surface of each electrode, giving both a negative charge with respect to the plasma. This results in there being dark space at each electrode. Due to electron depletion at the electrode a large voltage drop exists between the plasma and the electrodes. The potential drop between the plasma and each electrode is related by the ratio of the areas of the respective electrodes. For a parallel plate reactor the

potential drops are related by:

$$\frac{V_1}{V_2} = \left(\frac{A_2}{A_1}\right)^q \tag{2.3}$$

where V_1, V_2, A_1, A_2 denote the voltage drop of the powered electrode, the voltage drop of the grounded electrode, the area of the powered electrode and the area of the grounded electrode respectively. The exponent, q, in the equation varies from 1 to 2.5. To maximise the voltage difference between the powered electrode and the plasma, and therefore the ion bombardment energy on the powered electrode, it is desirable to increase the area of the grounded electrode. This is done by connecting the grounded electrode to the walls of the chamber. Now the effective area of the grounded electrode is the sum of the areas of the actual electrode and the walls of the chamber. Due to the mostly vertical delivery of reactive ions, reactive ion etching can produce very anisotropic etch profiles, which contrast with the typically isotropic profiles of wet chemical etching. Etch conditions in an RIE system are highly dependent on the system's many process parameters such as pressure, gas flow and RF power.

2.4.3 Inductively Coupled Plasma (ICP) Etching

A variation of standard RIE is to increase the density of ion species by using a high density plasma (HDP) source. One way to increase the density of a plasma is to use inductively coupled plasmas (ICP). ICP plasmas are formed in a dielectric vessel encircled by an inductive coil into which RF power is applied. A schematic diagram of an ICP etch system is shown in Figure 2.14.

When a time-varying electric current is passed through the coil, it creates a time-varying magnetic field around it, which in turn induces azimuthal electric currents in the gas, leading to gas break down and the formation of

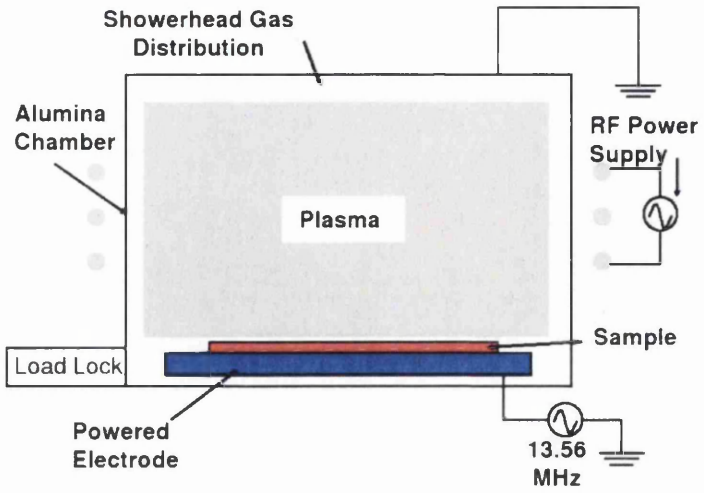

Figure 2.14: Schematic of an Inductively Coupled Plasma (ICP) reactor

a plasma. The neutrality of the ICP plasma and the lack of DC currents means that the ions have no acceleration toward the sample surface. This allows a large RF power to be applied creating a much denser plasma than could be produced in a conventional RIE setup. A second RF source is used to power the table on which the sample is placed. This sets up a capacitive discharge between the sample and the ICP generated plasma which results in a potential drop and hence a stream of ions is attracted toward the sample. Since ion energy and plasma density are effectively decoupled, uniform density and energy distributions are transferred to the sample while keeping the ion energy low. Etching using ICP is faster than unassisted RIE etching due to the fact that larger plasma densities can be achieved. This is particularly important when studying etching of III-V semiconductors, such as GaN. The large binding energy of GaN (8.9 eV/atom [27]) and its wide bandgap results in it being difficult to etch. The GaN samples in this work were etched using an ICP etching system.

Chapter 3

Semiconductor Theory and Radiation Detection

3.1 Introduction

The aim of this chapter is to introduce basic semiconductor principles which will allow an understanding of the work in the subsequent chapters. The concepts of crystal structure, energy bands, carrier transport, carrier generation and recombination, carrier trapping and metal-semiconductor contacts, specifically Schottky contacts, are discussed. The physics of radiation detection within a semiconductor will also be discussed. Much of the information covered in this chapter can be found in the following books; "Semiconductor Devices: Physics and Technology" by S.M. Sze [13], "Metal Semiconductor Contacts" by E.H. Rhoderick [28], "GaN and Related Materials II" by S. J. Pearton [29] and "Radiation Detection and Measurement" by G.F. Knoll [30].

3.2 Solid State Theory

3.2.1 Crystal Structure

The crystalline structure of a semiconductor determines much of its properties. The majority of semiconductors that have been studied as radiation detection media are of the single crystal variety. The atoms of a single crystal semiconductor are arranged in a three dimensional periodic structure called a lattice. For any crystal, there is a unit cell that is representative of the entire lattice. The lattice can be generated by repeating the unit cell throughout the crystal. Figure 3.1 shows three basic cubic crystal unit cells; simple cubic (sc), body-centred cubic (bcc) and face-centred cubic (fcc).

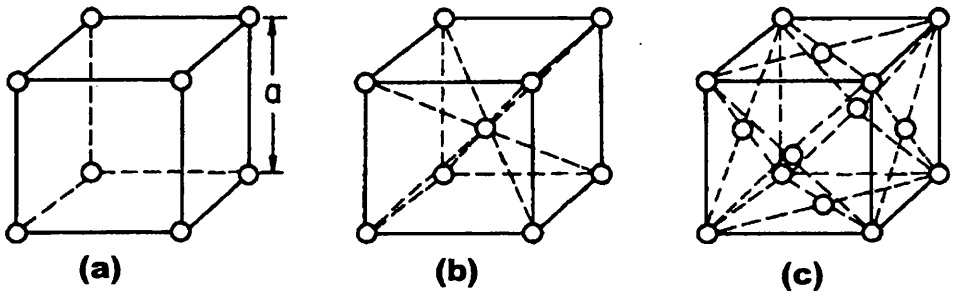

Figure 3.1: The (a) simple cubic, (b) body-centred cubic and (c) face-centred cubic lattice structures [31]

Semiconductors such as silicon, germanium, diamond, GaAs and GaN have a more complex crystal structure. The elemental semiconductors, silicon and germanium, have a diamond lattice structure as shown in Figure 3.2(a). The diamond structure belongs to the fcc crystal family and can be visualised as two interpenetrating fcc lattices with one sublattice displaced from the other by one quarter of the distance along the body diagonal of the cube.

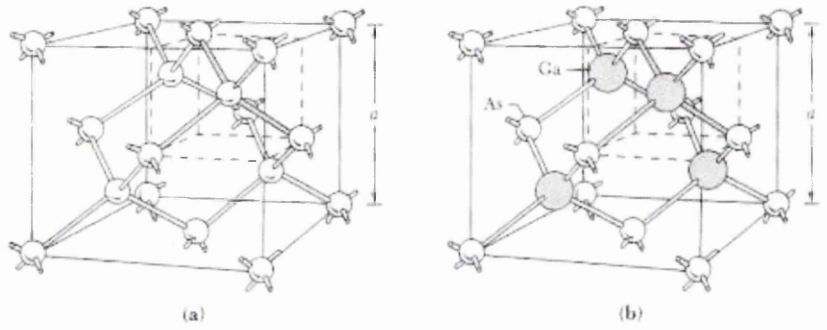

Figure 3.2: The diamond and zincblende lattice structures respectively [13]

The majority of the III-V semiconductors (e.g. GaAs) have a zincblende lattice structure as shown in Figure 3.2(b). The zincblende lattice is identical to the diamond lattice with the exception that one fcc sublattice has group III atoms and the other fcc sublattice has group V atoms.

GaN, the predominant semiconductor studied in this work, can be grown in zincblende and wurtzite form (see Figure 3.3). Wurtzite is the hexagonal close packed (hcp) analogue of zincblende. The wurtzitic structure consists of two interpenetrating hcp sublattices, one sublattice of Ga and one sublattice of N, offset along the c axis (see Figure 3.3) by five eighths of the cell height. For both the zincblende and wurtzite structures each Ga atom has four nearest neighbour N atoms and similarly each N atom has four nearest neighbour Ga atoms. The wurtzite structure is energetically preferable for GaN compared to the zincblende structure, although this energy difference is small (9.88 meV/atom [32]). The zincblende structure of GaN may be

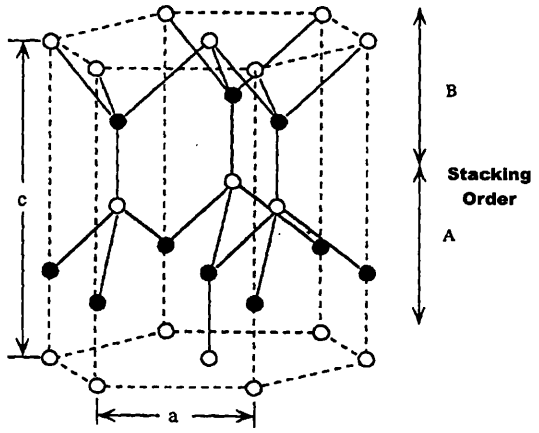

Figure 3.3: Unit cell of the wurtzite GaN structure [29]

grown on crystal planes of cubic structures where the innate tendency to form the wurtzite structure is overcome by topological compatibility. The lattice constants for wurtzite GaN are a = 3.19 $\AA$ and c = 5.19 $\AA$, while a = 4.52 $\AA$ for zincblende GaN. The bonding of elemental semiconductors, such as silicon, is completely covalent. For compound semiconductors there is an additional small ionic contribution as a result of an electrostatic attractive force between the two different elements. In the case of GaN there is an attractive force between each Ga^+ atom and its four neighbouring N^- atoms and between each N^- atom and its four neighbouring Ga^+ atoms.

3.3 Energy Bands

An isolated atom has well defined quantised energy levels in which orbiting electrons can exist. For example, the discrete energy levels of an isolated hydrogen atom are given by the Bohr model [13]:

$$E_H = \frac{m_o q^4}{8\epsilon_o^2 h^2 n^2} = \frac{-13.6}{n^2} eV \tag{3.1}$$

where m_o is the mass of a free electron, q is the electronic charge, ϵ_o is the permittivity of free space, h is the Planck constant and n the principal quantum number which takes the value of a positive integer. For the ground state, when $n = 1$, an electron will occupy the energy level E = -13.6 eV. For the first excited state, when $n = 2$, the electron will occupy the energy level E = -3.6 eV. When two identical atoms are separated by a large distance, they have no influence on each other and their electrons exist in their degenerate states. As the atoms are brought closer together the energy levels are split in two due to the interaction between the atoms. If N atoms are considered instead of two, then as the N atoms are brought closer together to form a solid, the orbits of the outer electrons of different atoms overlap and interact with each other. This interaction results in a shift of the energy levels, as in the case of two identical interacting atoms. However, instead of two discrete levels, N separate but closely spaced levels are formed. These closely spaced levels can essentially be considered as a continuous band of energy. The changes the atomic levels of silicon undergo as it forms a diamond structure with other silicon atoms are shown in Figure 3.4.

At large distances between the N atoms there are two discrete energy levels where electrons can exist. As the distance between the atoms is reduced, interactions between electrons occur and the allowed energy states cease to be distinct. As the atoms move closer the bands merge and become one. The atoms feel a repulsive force (between like charges) which counteracts the attractive force (between opposite charges) and settle into an equilibrium position which determines the lattice spacing. The position of this equilibrium determines whether the solid is a metal, insulator or semiconductor. At closer lattice spacings, the bands then split into two allowed energy states for electrons; the valence band and the conduction band. Between the va-

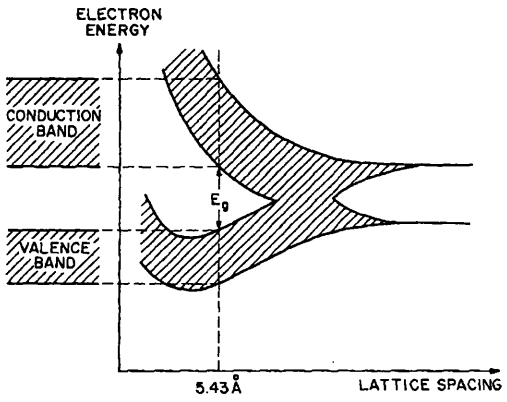

Figure 3.4: The energy levels of silicon atoms in a diamond structure [13]

lence and the conduction band there is a forbidden region where no electrons can exist. The energy difference between the top of the valence band and the bottom of the conduction band is known as the band gap and is an important parameter in semiconductor physics.

The energy band structures for a metal, an insulator and a semiconductor are shown in Figure 3.5. In a metal the conduction band is either partially filled or overlaps the valence band so that there is no band gap. The electrons in the partially filled conduction band or electrons at the top of the valence band may move to the next higher available energy level when they gain kinetic energy. In an insulator the valence electrons form strong bonds between neighbouring atoms. These bonds are extremely difficult to break and consequently at room temperature there are no free electrons that may participate in conduction. In an insulating material, the electrons occupy all the energy levels in the valence band while all energy levels in the conduction band are empty. Thermal or kinetic energy is insufficient to raise an electron from the top of the valence band to the bottom of the conduction band. In

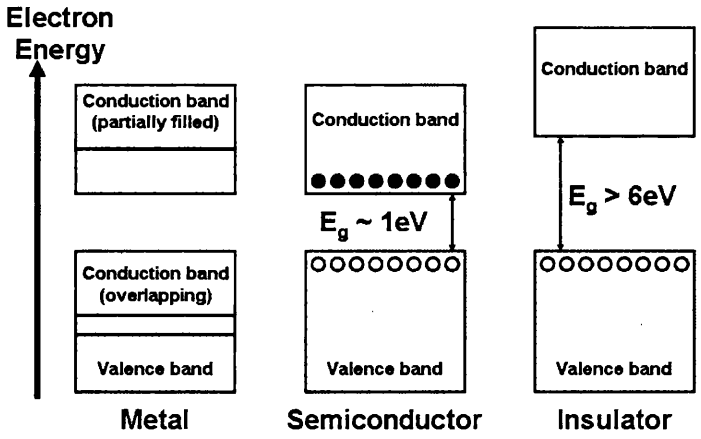

Figure 3.5: Energy bands of a metal, an insulator and a semiconductor

a semiconductor at a temperature of 0 K all the electrons are in the valence band and there are no electrons in the conduction band. Hence semiconductors are poor conductors at low temperatures. At increased temperatures, e.g. room temperature, there is enough thermal energy to break the bonds and an electron can be excited from the valence band to the conduction band. When an electron is excited to the conduction band there is a vacancy left in the valence band. This vacancy is called a 'hole' and has similar properties to the electron except for its charge which is positive. The electron and hole are known as charge carriers. Insulators may be classified as materials that have a band gap greater than 6 eV.

3.3.1 Effective Mass

The kinetic energy, E of a free electron is given by

$$E = \frac{\vec{p}^2}{2m_o} \tag{3.2}$$

where $\vec{p}$ is the momentum of the electron and m_o is the free-electron mass. In a semiconductor, an electron in the conduction band is similar to a free electron in that it is relatively free to move around in the crystal. However because of the periodic potential of the lattice, Equation 2.2 is not strictly valid for describing the energy of a free electron in a semiconductor. Equation 2.2 can still be used if the free-electron mass is replaced with an effective mass, m_n, of the conduction band electron in the crystal.

$$E = \frac{\vec{p}^2}{2m_n} \tag{3.3}$$

The electron effective mass depends on the properties of the semiconductor. A similar equation for the kinetic energy of holes may be used with the free-electron mass term replaced with m_p, the effective mass of a hole in the valence band. The effective mass may be obtained from the second derivative of E with respect to $\vec{p}$:

$$m_n = \left(\frac{d^2E}{d\vec{p}^2}\right)^{-1} \tag{3.4}$$

If a graph of momentum versus energy is made, then the wider the parabola, corresponding to a smaller second derivative, the larger the effective mass. The effective mass concept allows electrons and holes to be treated as classical charged particles. The actual energy-momentum relationships for semiconductors are much more complex. The energy-momentum relationships for Si and GaAs are shown in Figure 3.6.

For both Si and GaAs, around the minimum of the conduction band and the maximum of the valence band the energy-momentum curves are essentially parabolic. In Si the minimum of the conduction band does not occur at the same crystal momentum as the maximum of the valence band. Therefore when an electron makes a transition from the maximum point in the valence band to the minimum point in the conduction band, it requires

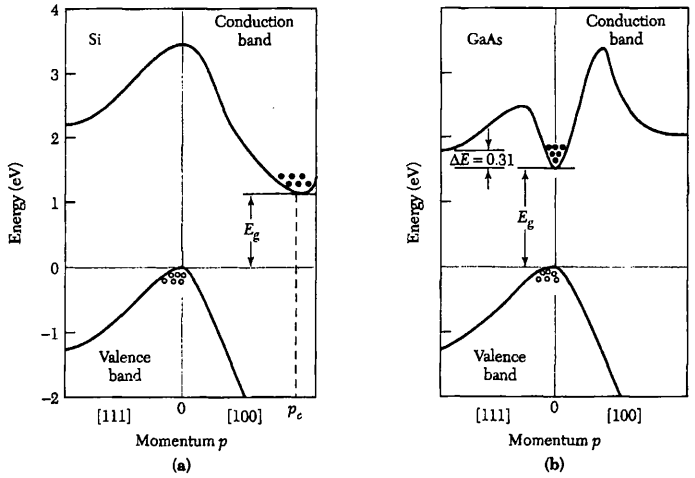

Figure 3.6: Energy band structures of Si and GaAs [31]

not only an energy change but also a momentum change. For GaAs however, the maximum in the valence band and minimum of the conduction band occur at the same momentum. An electron may make the transition from the valence band to the conduction band without a change in momentum. Because of this Si is known as an indirect semiconductor whereas GaAs is a direct semiconductor. Both direct and indirect semiconductors may emit a photon when an electron is transferred from the conduction band to the valence band. However indirect semiconductors must also emit a phonon as well as a photon to account for the difference in crystal momentum. This difference between direct and indirect semiconductors is very important for light-emitting diodes and semiconductor lasers. These devices require direct semiconductors for efficient generation and absorption of photons. GaN,

the material studied in this thesis, is a direct semiconductor and is used to fabricate blue light emitting diodes and lasers. The band structure of GaN will be described in more detail in Chapter 4.

3.4 Intrinsic & Extrinsic Semiconductors

Semiconductors can be broken down into two categories - intrinsic and extrinsic. At any given temperature, continuous thermal agitation results in the excitation of electrons from the valence band to the conduction band. This excitation of electrons leaves an equal number of holes in the valence band. An intrinsic semiconductor is one that contains relatively small amounts of impurities compared with the thermally generated electrons and holes. When a semiconductor is doped with impurities, the semiconductor is said to become extrinsic. The electron density, $n(E)$ in an intrinsic semiconductor is equal to the product of the density of allowed energy states per unit volume, $N(E)$, and the probability $F(E)$ of an electron occupying an energy state in the energy range dE. The electron density in the conduction band is thus given by integrating with respect to E from the top of the conduction band to the bottom of the conduction band as given by,

$$n = \int_{E_c}^{E_{top}} n(E)dE = \int_{E_c}^{E_{top}} N(E)F(E)dE \tag{3.5}$$

The probability of an electron occupying an energy state, E, is given by the Fermi-Dirac distribution function [13],

$$F(E) = \frac{1}{1 + e^{(E-E_f)/kT}} \tag{3.6}$$

where k is the Boltzmann constant and T is the absolute temperature in Kelvin. E_f is the Fermi energy and is defined as the energy level at which the probability of occupation by a charge carrier is exactly one half. The

band structure, the density of states, the occupation probability and the electron/hole densities are shown in Figure 3.7. For an intrinsic semiconduc-

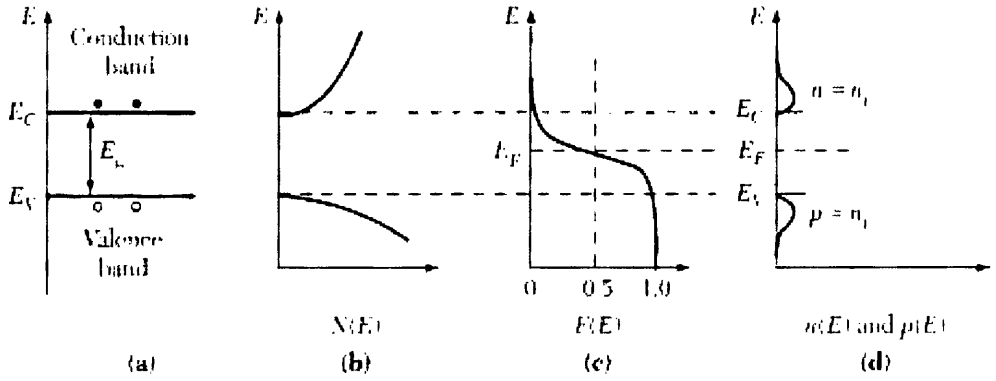

Figure 3.7: The intrinsic semiconductor: (a) band diagram, (b) density of states, (c) occupation probability, and (d) electron/hole densities [13]

tor the number of electrons per unit volume in the conduction band is equal to the number of holes per unit volume in the valence band, i.e. $n = p = n_i$, where n_i is the intrinsic carrier density.

Extrinsic semiconductors contain impurities that are normally introduced intentionally during the growth process or placed in specific regions (e.g. by ion implantation) in later processing steps. Since purity is not an issue with extrinsic semiconductors they are used in more applications than their intrinsic counterparts. Device properties and characteristics can be controlled by the addition of small amounts of impurities in a process known as doping. There are two types of possible dopant: p-type, where additional free holes are available in the valence band, and n-type, where additional electrons are introduced in the conduction band.

The two types of doping may be explored more thoroughly if we consider the doping of Si, which has four valence electrons. Arsenic is typically used to dope Si and make it n-type. A Si atom is replaced, or substituted, by an arsenic atom with five valence electrons. The arsenic atom forms covalent bonds with its four neighbouring Si atoms. This leaves one unbound electron which can be considered as a localised mobile negative charge. The arsenic atom, having a core of charge +5, is considered as an immobile positive charge, since the +5 core is not neutralised by the four electrons that participate in the covalent bonding. Since the positively charged arsenic atom balances the excess electron, the charge neutrality of the crystal is maintained. At low temperatures the negative electrons are attracted to the positive arsenic atoms and are bound tightly. At room temperature however, there is enough thermal energy to break this attraction and the electrons are free to conduct.

If a boron atom is substituted for a Si atom then the Si becomes p-type. Boron has only three valence electrons and so cannot complete the covalent bonds with the Si atom. This creates a hole in one of the bonds to the boron atom which can be filled by an electron from an adjacent atom, allowing the hole to migrate away. This hole may be viewed as a mobile positive charge. The boron atom, since it has accepted an electron to complete its bonds, can be seen as an immobile localised negative charge. Similarly to n-type doping, at low temperatures the negative boron atom attracts the positive hole and they are tightly bound. At higher temperatures there is enough thermal energy to break the bond and the hole is free to move, allowing conduction.

The energy levels for a p-type and an n-type semiconductor are shown in Figure 3.8. Doping creates localised energy levels within the forbidden region of the band gap. The energy levels can be donors or acceptors, denoted E_D

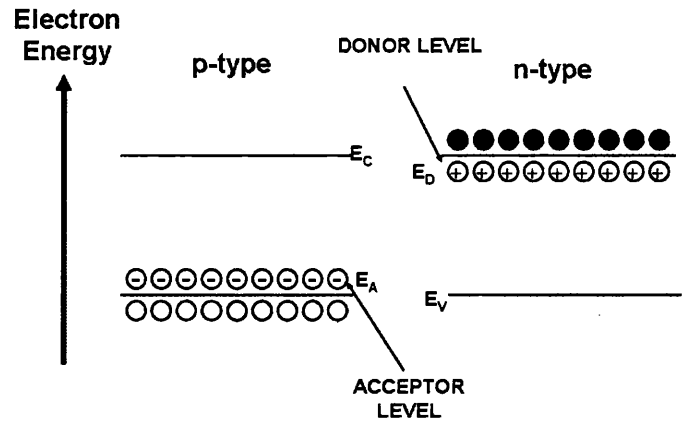

Figure 3.8: Energy levels for a p-type and an n-type semiconductor respectively

and E_A in Figure 3.8. If the donor levels are located close to the conduction band then very little energy is required to excite their electrons into the conduction band. Thus at room temperature these donor levels will be mostly ionised. The same is true for acceptor levels. If the acceptor level sits just above the valence band then it easily accepts electrons and becomes ionised, leaving a hole in the valence band.

3.5 Carrier Transport in Semiconductors

The majority of semiconductor devices operate under nonequilibrium conditions. Nonequilibrium conditions occur when excess carriers are generated in a semiconductor. Excess carriers may be generated by various means, such as ionising radiation or incident light. The mechanism that restores a semiconductor to the equilibrium state is the recombination of the excess minority charge carriers with the majority charge carriers. The theory for carrier drift, diffusion, generation and recombination is discussed in the following section.

3.5.1 Drift Current

Electrons in the conduction band and holes in the valence band can essentially be viewed as free particles. According to the kinetic theory of a free gas, under thermal equilibrium conditions the average kinetic energy of an electron in the conduction band is $1/2\ kT$ per degree of freedom (where k is the Boltzmann and T is the absolute temperature). Since an electron may move in three directions the kinetic energy of an electron in the conduction band is given by:

$$\frac{1}{2}m_n v_{th}^2 = \frac{3}{2}kT \tag{3.7}$$

where m_n is the effective mass of an electron, ν_{th} is the average thermal velocity and k and T are defined previously. The thermal velocity of electrons at room temperature is $\sim 10^7$ cm/s for Si and GaAs. The electrons in a semiconductor move rapidly in all directions. They randomly collide and scatter with lattice atoms, impurity atoms and other scattering centres within the crystal. This random motion of the electrons leads to a zero net displacement of an electron over a sufficiently long time period. The average distance between collisions is called the mean free path, and the average time between collisions is called the mean free time, denoted τ_c. The mean free path of an electron is typically $\sim 10^{-5}$ cm giving a $\tau_c \sim 10^{-12}$ seconds.

When an electric field E is applied to a semiconductor, each electron will experience a force equal to $-qE$, where q is unit charge, and will move in the opposite direction to the electric field vector. The electrons will still randomly collide with lattice and impurity atoms within the crystal but will also undergo displacement due to the presence of the electric field. The velocity of an electron travelling under the influence of an electric field is called the drift velocity and is denoted ν_n.

The drift velocity may be evaluated by equating the momentum applied to the electron during free flight between collisions ($-qE\ \tau_c$) to the momentum gained by the electron in the same period ($m_n\ v_n$) i.e.;

$$-qE\tau_c = m_n v_n \tag{3.8}$$

This equation can be re-arranged to give the expression;

$$v_n = -\left(\frac{q\tau_c}{m_n}\right) E = -\mu_n E \tag{3.9}$$

where μ_n is known as the electron mobility and has units cm^2/Vs. Equation 3.9 shows that the carrier drift velocity is directly proportional to the applied electric field. A similar expression may be found for holes in the valence band,

$$v_p = \left(\frac{q\tau_c}{m_h}\right) E = \mu_p E \tag{3.10}$$

where m_p is the hole effective mass, μ_p is the hole mobility and v_p is the hole drift velocity. The negative sign is removed from Equation 3.9 as the hole drift is in the same direction as the applied electric field vector.

The mobility of electrons and holes is an important parameter for carrier transport in a semiconductor. The mobility depends upon two terms, the effective mass of the carrier and the mean scattering time between collisions τ_c. The mean scattering time is determined by the various scattering mechanisms, the two most important being lattice scattering and impurity scattering. Lattice scattering results from thermal vibrations of the lattice atoms at temperatures above 0 K while impurity scattering occurs when a charge carrier travels past an ionised dopant impurity. At large values of E (around $3V/\mu m$ for silicon), Equations 3.9 and 3.10 become invalid and the drift velocity is independent of the applied field. The mobility values become non-linear and the drift velocities saturate as a function of applied electric field. At very large E fields the process of impact ionisation or avalanche multiplication starts.

3.5.2 Diffusion Current

Diffusion is the process that describes the movement of charge carriers from an area of high concentration to an area of low concentration. The diffusion effect is not related to Coulomb interactions or applied electric fields. It arises due to the fact that it is more probable that a carrier in a high concentration area will move to an area of lower concentration than vice-versa since there are more carriers able to do so. It may be expressed mathematically by the diffusion equation for electrons and holes [13].

$$F_n = -D_n \nabla n \tag{3.11}$$

$$F_p = -D_p \nabla p \tag{3.12}$$

F_n and F_p are the electron and hole flux respectively and ∇ n and ∇ p are their carrier concentration gradients. The diffusion constant, D_n (and also D_p) is related to the carrier mobility by the Einstein equation [13],

$$D_n = \left(\frac{kT}{q}\right) \mu_n \tag{3.13}$$

3.6 Charge Generation in a Semiconductor

The generation of charge carriers within a semiconductor material may occur as a result of:

- the thermal process
- optical excitation by electromagnetic radiation
- passage of ionising radiation e.g. charged particles

3.6.1 Thermal Generation of Charge Carriers

The thermal generation of an electron-hole pair can either occur directly (band to band) or indirectly (via intermediate energy levels within the forbidden region of the band gap). In some direct semiconductors the band gap is small enough compared to the thermal voltage at room temperature ($\frac{kT}{q}$ = 0.00259V) that electrons may be excited directly from the valence band to the conduction band. Si, GaAs, GaN and diamond all have large enough band gaps to allow room temperature operation of these materials as radiation detectors since the probability of direct excitation is very low. Thermal excitation in these materials may occur in two (or more) steps through intermediate local energy levels within the band gap. These intermediate states are created by imperfections within the crystal and by impurities. If the density of these intermediate defect levels is large then the performance of the semiconductor may be significantly degraded due to increased leakage currents. It is also possible to have deep energy levels within the forbidden region of the band gap due to defects or dopants that do not act as shallow donors or acceptors.

3.6.2 Generation of Charge Carriers by Electromagnetic Radiation

A photon incident on a semiconductor can impart enough energy to the lattice that it causes some bonds to be broken. This can be visualised in the band theory of solids as raising an electron from the valence band to the conduction band, creating an electron-hole pair. A schematic diagram of the three principal processes is shown in Figure 3.9.

If the energy of the absorbed photon is equal to the bandgap of the

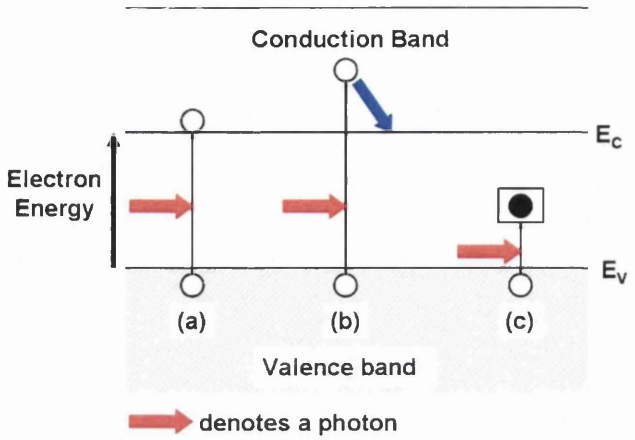

Figure 3.9: Generation of charge carriers due to the absorption of electromagnetic radiation. The three cases are (a) $E_{photon} = E_g$, (b) $E_{photon} > E_g$ and (c) $E_{photon} < E_g$

semiconductor then an electron is excited from the top of the valence band to the bottom of conduction band (process (a)). If the photon energy is greater than the band gap then the electron and hole occupy higher energy states in their respective energy bands. The carriers then make their way to the band edges by losing energy to the lattice via phonon interactions (process (b)). If the photon energy is not large enough to allow a band to band transition than an electron may be excited into a local empty impurity or defect state in the forbidden region of the band gap. This results in the creation of a hole in the valence band and an occupied ionised energy level in the forbidden region (process (c)). The generation of charge carriers by the passage of ionising radiation, e.g. an alpha particle, will be covered in more detail in Section 3.9.

3.7 Charge Recombination in a Semiconductor

An ideal radiation detector is one that collects all of the charge that is liberated in the material. Once the generation of charge carriers has occurred the mechanism that returns the semiconductor back to its equilibrium state is recombination. The minority charge carriers (electrons in a p-type material, holes in an n-type material) combine with the majority charge carriers in the recombination process. The recombination process is significantly different for direct and indirect semiconductors. The two processes are discussed separately in this section and are considered in terms of carrier lifetime.

3.7.1 Direct Recombination

When a semiconductor is in equilibrium, the net generation rate of charge carriers is equal to the rate of recombination of the charge carriers. The recombination rate, R, is proportional to the product of the electron and hole concentrations

$$R = \beta np \tag{3.14}$$

where β is a proportionality factor, n is the electron concentration (cm^{-3}) and p is the hole concentration (cm^{-3}). In thermal equilibrium the generation rate equals the recombination rate and

$$R_{th} = G_{th} = \beta n_o p_o = \beta n_i^2 \tag{3.15}$$

where R_{th} is the recombination rate and G_{th} is the generation rate in thermal equilibrium. The subscript o indicates an equilibrium quantity, while n_i is the intrinsic carrier concentration. The excess carrier recombination rate, U,

can be defined as

$$U = R - R_{th} = \beta(np - n_i^2) \tag{3.16}$$

If ionising radiation loses energy in a semiconductor sample or the sample is illuminated with light so that the thermal equilibrium conditions are upset, then the electron and hole concentrations will be increased by the same amount equal to Δ - since the electrons and holes are produced in pairs. The recombination rate will increase to

$$R = \beta(n_o + \Delta n)(p_o + \Delta n) \tag{3.17}$$

where Δn is excess electron density and Δp is the excess hole density.

If the incident ionising radiation or illumination is constant then the additional generation rate (G_L) is equal to the excess recombination rate and is given by

$$G_L = U = R - R_{th} = \beta \Delta n_L(p_o + n_o + \Delta n_L) \tag{3.18}$$

where Δn_L is the excess minority carrier density generated by the incident ionising radiation or light. If the injected carrier concentration is much less than the majority carrier concentration then Equation 3.18 simplifies to

$$G_L = \frac{\Delta n_L}{\tau_r} \tag{3.19}$$

where

$$\tau_r = \frac{1}{\beta p_o} \tag{3.20}$$

for a p-type semiconductor and

$$\tau_r = \frac{1}{\beta n_o} \tag{3.21}$$

for an n-type semiconductor.

When the ionising radiation is no longer incident on the semiconductor the material returns to its equilibrium state with a time constant τ_r. This

time constant is called the recombination lifetime and the above equations hold for direct semiconductors such as GaAs, GaN and diamond. In a direct semiconductor when an electron recombines with a hole the energy is either released as a photon (radiative recombination) or transferred directly to another electron or hole (known as the Auger process). In a direct semiconductor radiative recombination should dominate, however it will be shown in Chapter 6 that under certain conditions (namely after high levels of irradiation) non-radiative recombination can become significant. In non-radiative recombination the energy liberated by an electron and hole combining is dissipated via lattice vibrations (phonons).

3.7.2 Indirect Recombination

Indirect semiconductors such as Si have a low probability of band to band recombination of charge carriers because the electrons at the bottom of the conduction band and the holes at the top of the valence band have different crystal momenta. The recombination process in indirect semiconductors instead occurs through localised energy levels within the forbidden region of the band gap. These localised energy levels within the band gap are the result of imperfections in the crystal due to impurities or defects and are able to trap charge carriers. The energy levels within the forbidden region are often referred to as trapping centres. These trapping centres can affect the charge collection properties of a detector as deep energy levels within the band gap can hold onto charge for a significant period of time. A defect energy level within the band gap may undergo four basic transitions as shown in Figure 3.10.

Here the before and after conditions of a single defect level are considered. The level can be neutral and become negatively charged by accepting

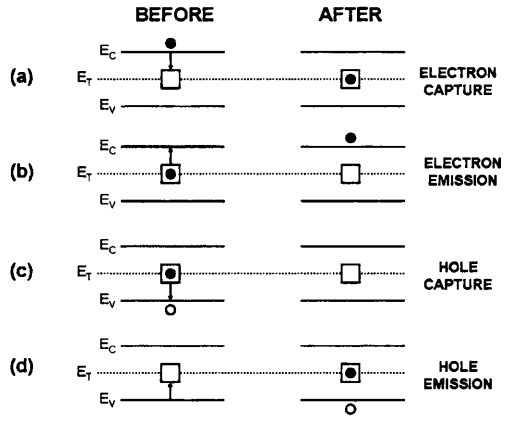

Figure 3.10: Indirect recombination processes at room temperature

an electron from the conduction band. This is shown in (a) and the process is known as electron capture. Conversely the defect level can initially be negatively charged and release an electron into the conduction band. The defect level becomes neutral and the process is known as electron emission (process (b)). In (c) the process of hole capture can be seen. A hole in the valence band recombines with an electron from a charged trapping centre. The final mechanism, hole emission, is shown in (d). An electron is excited from the valence band into the defect level creating a free hole and an occupied trapping site.

In a recombination event processes (a) and (c) occur while a generation event occurs when process (d) follows process (b). Trapping occurs when processes (a) and (b) follow each other (trapping of an electron in a defect energy level followed by re-emission of the electron back to the conduction band at some time later) and when process (d) follows process (c) hole trapping occurs. The four trapping processes are often studied in terms of their emission probabilities and capture cross sections. The derivation of the emission prob-

ability and capture cross section for each of the processes is not covered here, a detailed analysis may be found in [31].

3.8 Metal-Semiconductor Contacts

The charge carriers generated in a semiconductor by the passage of ionising radiation are extracted and collected by electrical contacts. These metal contacts are typically fabricated on opposite sides of the detection material and a potential difference applied between them. This potential difference leads to an internal electric field which separates the charge carriers resulting in an induced charge on the metal electrodes. Metal-semiconductor contacts can be rectifying, i.e. a potential barrier exists between the metal and semiconductor thus limiting current flow, and non-rectifying, i.e. the contact between the metal and semiconductor has negligible resistance and current can flow freely. Rectifying metal-semiconductor contacts are called Schottky contacts while non-rectifying metal-semiconductor contacts are called ohmic contacts. Both Schottky and ohmic contacts were realised on the GaN and diamond material studied in this work. This section will describe the formation of the Schottky barrier, the influence of surface states on the barrier height, and the ideal ohmic contact. Finally the current transport mechanisms across a metal-semiconductor contact will be described.

3.8.1 Formation of the Schottky Barrier

The Schottky contact is due to the difference of work function between a semiconductor and metal. The work function of a material is defined as the energy required to raise an electron from the Fermi level, E_F, to the vacuum state. The quantity is denoted ϕ_m for a metal and ϕ_s for a semiconductor.

A semiconductor also has an electron affinity, χ_s, which is the difference in energy between the bottom of the conduction band and the vacuum state. The work function of a semiconductor may be found using the following equation

$$q\phi_S = q(\chi_s + V_n) \tag{3.22}$$

where q is the charge on an electron and V_n is the energy required to excite an electron from the Fermi level to the bottom of the conduction band. Figure 3.11 shows the energy band diagram of a metal-semiconductor system where the metal and an n-type semiconductor are slowly brought into contact.

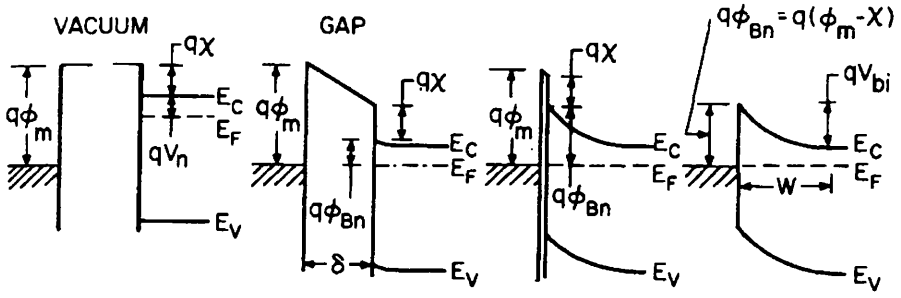

Figure 3.11: The formation of a Schottky barrier [31]

On the far left, the metal and semiconductor are not in contact and the system is not in thermal equilibrium. If a wire of length δ is connected between the metal and the semiconductor then electrons flow from the semiconductor into the metal since $\phi_s < \phi_m$. The Fermi level in the metal is raised by an amount equal to the difference between the work function of the metal and the semiconductor. This alignment of the Fermi levels is attained by the flow of electrons from the semiconductor to the metal. As the distance decreases between the metal and semiconductor an increasing negative charge is built up on the surface of the metal (since electrons flow from the

semiconductor to the metal). An electrostatically balancing positive charge exists on the surface of the semiconductor arising from uncompensated donor ions that have been depleted of electrons. The layer of negative charge on the metal surface is very thin while the corresponding positively charged layer on the surface of the semiconductor is wider because the semiconductor is less conductive. This space-charge region in the semiconductor is known as the depletion layer and has a thickness, W. Due to the removal of electrons, the Fermi level in the semiconductor changes position relative to the conduction and valence bands with the result that the bands are bent upward as the Fermi levels of the metal and semiconductor must remain the same. For electrons to flow out of the semiconductor and into the metal they must surmount a potential barrier, giving the contact rectifying properties. When the gap reaches an inter-atomic spacing, i.e. the metal and semiconductor are in contact, an intimate Schottky contact is formed. The barrier height, ϕ_{Bn}, of the contact for an n-type semiconductor is given by

$$q\phi_{Bn} = q(\phi_m - \chi_s) \tag{3.23}$$

Conversely, when a p-type semiconductor with a work function greater than that of a metal is brought into contact with a metal the bands are bent downward. This forms a p-type Schottky contact which also has rectifying properties. The barrier height, ϕ_{Bp}, for a p-type semiconductor is given by

$$q\phi_{Bp} = E_g - q(\phi_m - \chi_s) \tag{3.24}$$

where E_g is the band gap of the semiconductor.

The band structure of a metal-semiconductor contact may be altered by the application of an external bias. Figure 3.12 shows the energy band diagrams for metals on both n-type and p-type semiconductors under different biasing conditions. If we consider an n-type semiconductor then when

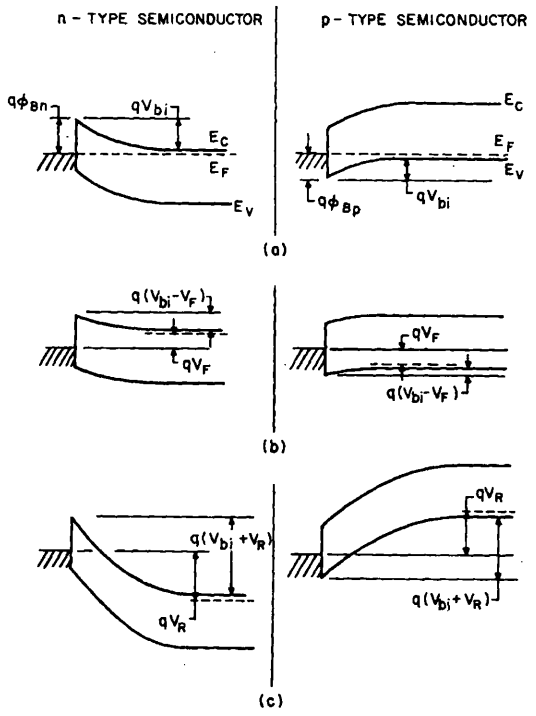

Figure 3.12: Energy band diagram of metal n-type and metal p-type semiconductors under different biasing conditions: (a) thermal equilibrium; (b) forward bias and (c) reverse bias [31]

the applied bias is zero, as in case (a), the band diagram is under thermal equilibrium conditions and the Fermi levels for both the metal and semiconductor are equal. Applying a positive (forward) bias voltage to the metal with respect to the n-type semiconductor results in a decrease of the metal-semiconductor barrier height. When a forward bias is applied electrons can move easily from the semiconductor into the metal because the barrier has been reduced by a voltage V_F. Applying a negative (reverse) bias (as in case (c)) to the metal with respect to the semiconductor results in it being more difficult for the electrons to flow from the semiconductor to the metal.

There are similar results for p-type semiconductors except the polarity of the applied voltage is reversed. The application of an external bias changes the depletion width in the semiconductor. The depletion width, W, is given by [13]

$$W = \sqrt{\frac{2\epsilon_s}{qN_D}(V_{bi} - V)} \tag{3.25}$$

where ϵ_s is the dielectric permittivity of the semiconductor, N_D is the donor density, V_{bi} is the built in potential and V is the applied external bias. The resultant capacitance, C, per unit area of the depletion region is given by [13]

$$C = \sqrt{\frac{q\epsilon_s N_D}{2(V_{bi} - V)}} = \frac{\epsilon_s}{W} \tag{3.26}$$

3.8.2 Surface States

The above treatment is for the idealised case. This assumes that the semiconductor is defect free, the semiconductor surface does not have any impurities and has the same electrical and structural properties as the semiconductor bulk, and there are no chemical reactions between the metal and semiconductor. In practice surface states play an important role in determining the barrier height of a metal-semiconductor contact. Surface states can act as donors or acceptors. If there are surface states densely distributed within a small energy interval in the forbidden region then the Fermi level must bend at the surface to align with their position. This decreases the amount of band bending possible and the Fermi level becomes relatively fixed at the surface, introducing the concept of Fermi level pinning. When surface states are present the Fermi levels of the semiconductor and metal will realign, as in the case of the idealised Schottky model but the charge exchange is now made between the metal and the surface states (see Figure 3.13). The density of surface states may be so large that the Fermi level is fixed even before the

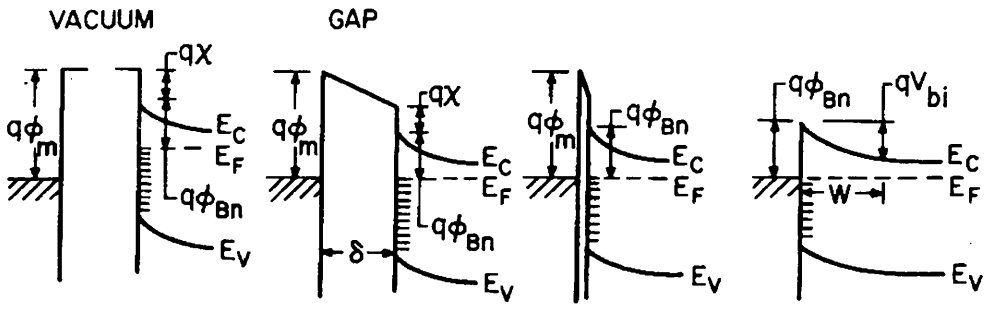

Figure 3.13: The formation of a Schottky barrier with surface states present [31]

metal is brought into contact. Then the Fermi level is said to be pinned and the barrier height is independent of the work function of the metal. GaAs is a material whose Fermi level is believed to be pinned at the mid-gap level due to the presence of deep traps at the surface.

3.8.3 The Ohmic Contact

The second type of electrical contact is the ohmic contact which has a negligible resistance to current flow. The contact resistance is low compared to the resistance of the bulk semiconductor. A good ohmic contact should not significantly degrade device performance and can pass the required current with a voltage drop that is small compared to the drop across the active region of the device. An ohmic contact is formed on an n-type semiconductor when the work function of the metal is less than the work function of the semiconductor. The converse is true for a p-type semiconductor.

3.8.4 Current Transport Mechanisms

Under normal operating conditions, two mechanisms are responsible for the transport of charge carriers across a metal-semiconductor junction. The charge carriers can jump over the barrier in the case of thermionic emission, or the charge carriers can tunnel through the barrier, where field emission (or quantum mechanical tunnelling) is the process. For any given metal-semiconductor junction both mechanisms can assist in the transport of charge carriers across the barrier. The current transport in a Schottky barrier is due mainly to the majority charge carriers, in contrast to a p-n junction where the current transport is due mainly to minority carriers. The dominant transport process for Schottky diodes operated at room temperature is thermionic emission of carriers from the semiconductor over the potential barrier into the metal. The field emission, or quantum mechanical tunnelling current, becomes dominant at low temperatures or if the semiconductor has a high doping concentration. The current-voltage characteristic of a Schottky diode where thermionic emission is the dominant transport mechanism is described by [13]

$$J = J_S \left(\exp^{(\frac{qV}{kT})} - 1 \right) \tag{3.27}$$

where J is the current density, q is the charge, k is the Boltzmann constant, T is the temperature and J_S is given by

$$J_S = A^{**} T^2 \exp^{(\frac{-q\phi_{Bn}}{kT})} \tag{3.28}$$

J_S is the saturation current density, A^{**} is the effective Richardson constant (equal to 26.4 $\mathrm{cm}^{-2}\mathrm{K}^{-2}$ for n-type GaN) and ϕ_{Bn} is the barrier height. The applied voltage, V, is positive for forward bias and negative for reverse bias. It is possible to calculate the barrier height from the I-V characteristic of a

device using the following equation:

$$\phi_{Bn} = \frac{kT}{q} \ln\left(\frac{J_S}{A^{**}T^2}\right) \tag{3.29}$$

J_S may be found experimentally by plotting a graph of current density versus voltage and extrapolating back to V = 0. In addition to the majority carrier current, a minority carrier current also exists. This current is as a result of minority carriers being injected from the metal contact into the semiconductor. Typically the minority carrier current is orders of magnitude smaller than the majority carrier current and can be neglected.

3.9 Principles of Radiation Detection Theory

Semiconductor radiation detectors are utilised in many applications such as; imaging tools in medicine, spectroscopic devices in industry and as particle detectors in high energy physics experiments. The principle of operation of a semiconductor radiation detector is that any incident radiation, for example a charged particle, loses energy as it passes through a semiconductor material. The number of electron-hole pairs created within the detection medium is proportional to the energy lost by the incident radiation. The generated charge carriers may be separated by applying an electric field and collected by electrodes.

The way in which incident radiation loses energy in a semiconductor detector is strongly dependent on the type and the energy of radiation. The three types of radiation of interest are:

- Charged particles e.g. α particles, electrons
- Photons e.g. x-rays and gamma rays

- Neutrons

Both heavy charged particles and fast electrons, due to the electric charge carried by these particles, continuously interact via the Coulomb force with the electrons present in the detection material. The uncharged radiations, photons and neutrons, do not interact with the electrons or nuclei in the detection medium through the Coulomb force. The uncharged radiations must undergo a catastrophic interaction, such as a collision with a nucleus or electron, that radically alters the properties of the incident radiation.

3.9.1 Charged Particle Interactions

Charged particles, such as an alpha particle, interact with matter primarily through Coulomb forces between their charge and the negative charge of the orbital electrons within the atoms of the semiconductor medium. When the particle enters the detector material it simultaneously reacts with several electrons. The electrons can either be raised to a higher orbital energy state within the absorber atom (excitation) or they can be liberated from the atom, creating an electron-hole pair (ionisation). The energy gained by the electrons comes at the expense of the charged particle and its energy is decreased as a result of these encounters. The charged particle continually interacts with the orbital electrons until it eventually loses all of its kinetic energy and is stopped. The linear stopping power, S, of an absorber is defined as the differential energy loss (dE) divided by the differential path length (dx) [30]:

$$S = -\frac{dE}{dx} \tag{3.30}$$

For particles with a given charge state, S increases as the particle velocity decreases. The rate of energy loss over an incremental distance for a charged

particle with a known velocity is given by Bethe-Block formula [30]:

$$-\frac{dE}{dx} = \frac{4\pi e^4 Z^2}{m_0 v^2} NB \tag{3.31}$$

where ν is the velocity of a particle of charge e, interacting in an absorber that has a density of atoms, N, and an atomic number Z. The electrons in the absorber have a rest mass m_0 and a charge e. B is given by [30]:

$$B = Z\left[ln\frac{2m_0v^2}{I} - ln\left(1 - \frac{v^2}{c^2}\right) - \frac{v^2}{c^2}\right] \tag{3.32}$$

where c is the speed of light and the parameter I represents the average excitation and ionisation potential of the absorber. For non-relativistic particles only the first term in Equation 3.32 is significant. It can be seen that for a given (non-relativistic) charged particle the linear stopping power varies with $1/\nu^2$, or inversely with particle energy. A particle with a lower incident energy spends more time near the orbital electrons in the absorber and loses energy more rapidly than a particle with a higher incident energy. The linear stopping power also depends on the magnitude of the charge of the particle. The greater the charge on the incident particle the greater the energy loss within the absorbing material. It is also seen from Equation 3.31 that detector materials with a large atomic number have a large linear stopping power.

The plot of specific energy loss along the track of a charged particle as it travels through the detection medium is known as the Bragg curve. Figure 3.14 shows the specific energy loss of a 5.48 MeV α particle as it passes through 40 μm of Si. The graph was calculated using the SRIM simulation package [33]. For the majority of the track, the specific energy loss increases as $1/E$ as predicted by Equation 3.31. Near the end of the track the charge on the alpha particle is reduced through electron pickup and the curve falls off to zero. From Figure 3.14 it can be seen that a 5.48 MeV alpha particle

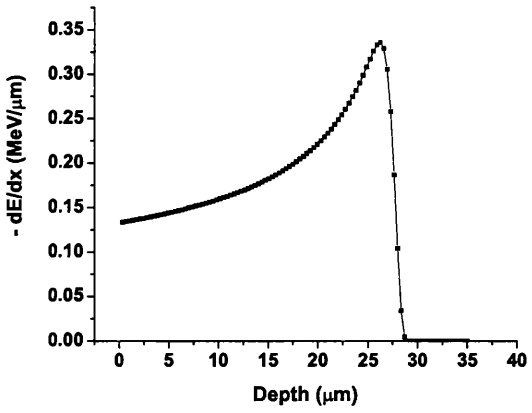

Figure 3.14: Bragg curve for a 5.48 MeV α particle in 40 um of Si

loses all of its energy in Si after travelling a distance of around 30 μm. Two papers that discuss the energy loss for various particles in an absorber may be found in [34], [35].

3.9.2 X-ray & gamma-ray Interactions

There are three main mechanisms by which a photon can interact with an absorber. These are:

- The photoelectric effect
- Compton Scattering
- Pair production

These three processes lead to the partial or full transfer of the photon energy to electron energy. The processes result in sudden and abrupt changes in the photon history in that, the incident photon either disappears completely or is scattered through a significant angle. This behaviour is in stark

contrast to charged particles which slow down gradually through continuous, simultaneous interactions with many absorber atoms.

Photoelectric Effect

In the photoelectric process a photon interacts with an atom in the detection medium with the result that an energetic photoelectron is ejected by the atom from one of its bound energy shells. The interaction is with the atom as a whole and cannot take place with free electrons. The most probable origin of the photoelectron is from the most tightly bound shell of the atom, the K shell. The photoelectron is ejected with an energy ($E_{photoelectron}$) given by:

$$E_{photoelectron} = E_{\gamma} - E_{binding} \tag{3.33}$$

where E_{γ} is the energy of the incident photon and $E_{binding}$ is the binding energy of the electron with its associated atom. The ejected photoelectron undergoes multiple scattering in the surrounding material where it loses energy by two processes. One process is electron-phonon scattering where the electron scatters off ions within the lattice. The second process occurs when a photoelectron collides with an electron in the valence band and excites it to a higher energy level, creating an electron-hole pair in the process. The probability of a photoelectron interaction increases with the atomic number (Z) of the absorber material and is given by [30];

$$\tau \sim constant \times \frac{Z^n}{E_{\gamma}^{3.5}} \tag{3.34}$$

where $4 < n < 5$ depending on the energy of the photon.

Compton Effect

Compton scattering occurs between an incident photon and an electron in the detector material. The incoming photon is deflected through an angle θ with respect to its original direction. The photon transfers a portion of its energy to the electron (assumed to be initially at rest), which is then known as the recoil electron. All angles of scattering are feasible and the energy transferred to the electron can vary from zero to a large fraction of the photon energy. The Compton scattering process is illustrated in Figure 3.15. The energy of the scattered photon is related to the scattering angle

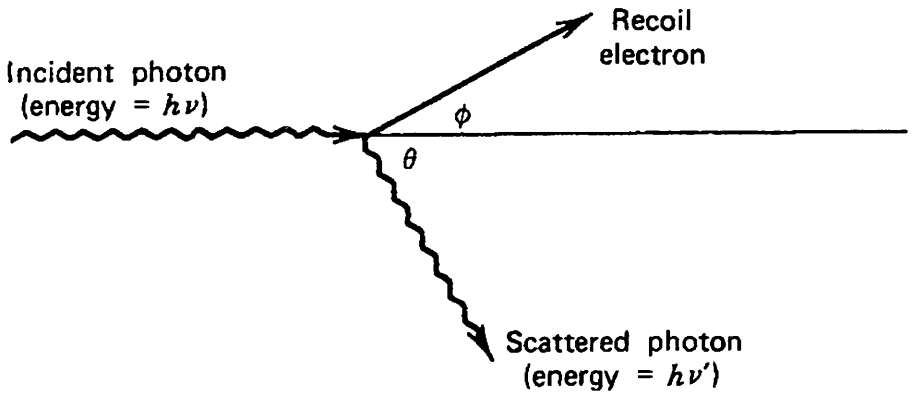

Figure 3.15: Compton scattering process [30]

by the equation

$$h\nu' = \frac{h\nu}{1 + \frac{h\nu}{m_0c^2}(1 - cos\theta)} \tag{3.35}$$

where $h\nu'$ is the energy of the scattered photon, $h\nu$ is the energy of the incident photon and m_0c^2 is the rest-mass energy of the electron (0.511 MeV). The recoil electron is scattered through an angle ϕ and the scattered photon through an angle θ.

Pair Production

If an incident photon has an energy twice that of the rest-mass energy of an electron (i.e. 1.02 MeV) then the process of pair production is possible. In this interaction a photon enters the Coulomb field of a nucleus and disappears through the creation of an electron-positron pair. Any excess energy carried by a photon above the 1.02 MeV required to create an electron-positron is transferred into kinetic energy which is shared between the electron and positron. The positron eventually annihilates with an electron in the detection medium and two annihilation photons are produced as secondary products of the interaction [30]. The probability of pair production is very small at low photon energies and is generally confined to high energy gamma rays.

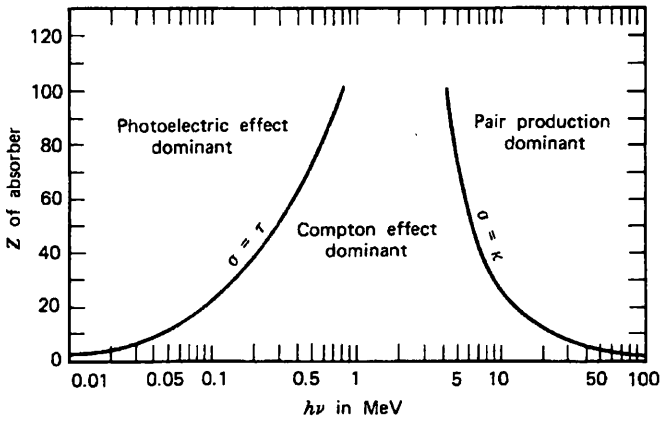

Figure 3.16: The dominant processes for photon interactions as a function of photon energy in various absorbers [30]

Figure 3.16 shows the relative importance of the photoelectric effect, Compton scattering and pair production for different absorber materials and photon energies. Photoelectric absorption is the dominant process at photon

energies less than 100 keV when detection media with a large atomic number ($Z \geq 20$) are considered. Compton scattering starts to become significant at energies greater than 100 keV, while pair production is the dominant process at photon energies greater than 10 MeV.

3.9.3 Neutrons

Neutrons, as with photons, carry no electric charge and therefore do not interact in an absorber by means of the Coulomb force. Incident neutrons can travel through many centimetres of material without any type of interaction. A neutron may however, interact with a nucleus of the absorbing material. This interaction may result in either the neutron completely disappearing, being replaced by one or more more secondary radiations, or else the energy or direction of the neutron is changed significantly. Products of neutron interactions almost always result in the creation of heavy charged particles. These particles may be produced either as a result of neutron induced nuclear reactions or they may be the nuclei of the detector medium itself which have gained energy as a result of nuclear collisions.

Chapter 4

GaN as a Radiation Hard Detector

4.1 Introduction

The properties of GaN, such as its wide band gap and large displacement energy, may result in it being more resistant to radiation damage than current materials. The proposed upgrade of the Large Hadron Collider (LHC) at CERN, the so called Super-LHC (SLHC), is one example where ultra radiation hard semiconductor tracking detectors will be required. This chapter describes the radiation damage mechanisms that occur in a semiconductor and outlines the effects of radiation damage on detector performance. Samples from three epitaxial GaN wafers were irradiated to anticipated SLHC radiation levels with protons of energy 24 GeV/c and reactor neutrons (all neutron fluences are given as 1 MeV equivalent). The effects of the irradiations on detector performance were assessed through evaluation of the detector macroscopic properties, such as leakage current and charge collection efficiency. The chapter concludes by comparing the radiation hardness

properties of the GaN material studied with the most promising results reported on other detector media such as oxygenated Si, epitaxial Si and SiC.

4.2 GaN Background & Growth Techniques

The development of the first commercial high-brightness GaN light emitting diodes (LEDs) by Shuji Nakamura in 1993 sparked worldwide interest in GaN and its related ternary compounds [36]. Until 1993, the only blue light emitting devices commercially available were based on silicon carbide which, because of its indirect band gap, is not capable of emitting light of sufficient intensity to be of wide interest. GaN blue LEDs completed the range of primary colours and made possible applications such as daylight visible full-colour LED displays and white LEDs [37]. Nitride based blue LEDs coated with a fluorescent layer of yttrium aluminium garnet (YAG) produce bright white light and represent a viable competitor to incandescent bulbs. In recent years blue laser diodes (LDs), which have a shorter wavelength than the present technology, have successfully been fabricated on GaN. This shorter wavelength makes it possible to read and write more data on the same disk area than is possible with the current technology.

Other applications of GaN and its related compounds include microwave power devices, ultra-high power switches and High Electron Mobility Transistors (HEMTs) [38] . These applications make use of the direct wide band gaps, good thermal stability, and ability to withstand high temperature, properties of GaN and its related compounds.

4.2.1 Growth of GaN

GaN does not exist in nature and must be synthesised through chemical processes. As a result of its high melting temperature and high dissociation pressure no classical method can be expected to be successful for bulk crystal growth of GaN. Below 950°C gallium does not react with molecular nitrogen and so higher temperatures have to be used. Bulk GaN crystals are generally grown at high temperatures (1200°C-1600°C) under high nitrogen pressures in order to prevent GaN decomposition [39]. The difficulty of growing bulk GaN crystals has led to extensive research into the growth of thin GaN layers on foreign substrates. Nearly every possible crystal growth technique, substrate type and substrate orientation has been tried in an effort to grow high quality epitaxial GaN films.

The four main techniques that are currently used to grow thin films of GaN are Hydride Vapour Phase Epitaxy (HVPE) [40], Metal Organic Vapour Phase Epitaxy (MOVPE) [41], Molecular Beam Epitaxy (MBE) [42], [43] and Metal Organic Chemical Vapour Deposition (MOCVD). The most successful growth technique of epitaxial GaN films is MOCVD and was the method used to grow the three epitaxial GaN wafers studied in this chapter. A typical two flow MOCVD reactor is shown in Figure 4.1.

The main flow composed of reactant gases with a high velocity is directed through the nozzle across the surface of the rotating substrate. The sub-flow, composed of nitrogen, is directed perpendicular to the surface of the substrate. The purpose of this sub-flow is to bring the reactant gases into contact with the substrate. Hydrogen is used as a carrier gas.

Suitable precursors for the MOCVD growth must exhibit sufficient volatility and stability to be transported to the surface. These precursors should also have appropriate reactivity to decompose thermally into the desired solid

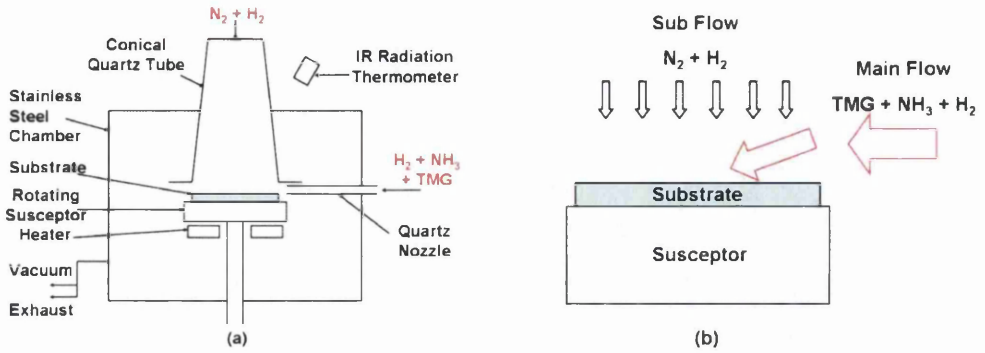

Figure 4.1: (a) Schematic diagram of an MOCVD reactor [36], (b) Gas flow close to the substrate

and to generate readily removable gaseous by-products. Ideally the precursors should be water and oxygen insensitive, nontoxic and noncorrosive. Typically the trialkyls, trimethylgallium (TMG), trimethylaluminium (TMA) and trimethylindium (TMI) are used as Ga-metal, Al-metal and In-metal precursors respectively. Ammonia (NH_3), hydrazine (N_2H_4), monomethylhydrazine $(CH_3)N_2H_2$ and dimethylhydrazine $(CH_3)_2N_2H_2$ serve as nitrogen precursors. Although the trialkyl compounds are extremely water and oxygen insensitive, and ammonia is highly corrosive, the majority of the best material grown today is produced by reacting these compounds with NH_3 at substrate temperatures in the region of 1000°C [44] - [46].

Temperatures in excess of 800°C are required to obtain single crystalline high-quality GaN films, and the GaN films with the best optical and electrical properties are grown at 1050°C. When substrate temperatures greater than 1100°C are used the dissociation of GaN results in voids in the growth layer. The high growth temperatures in the MOCVD process restrict the choice of substrates that can be used and have a contradictory effect on the crystal

quality. On one hand, at higher temperatures the surface mobility of atoms is larger and the quality of the grown film is higher. On the other hand if high temperatures are used during growth then the post growth cooling process introduces greater strain (than if lower temperatures were used) between GaN and the substrate material. This strain creates more structural defects in the GaN film and results in poorer quality material.

4.2.2 Substrates and Buffer Layers

As discussed earlier, the high melting temperature and dissociation pressure are the two main obstacles to growing large single crystals of GaN. Single crystalline GaN films have been grown heteroepitaxially on a number of substrates that have similar lattice constants and thermal expansion coefficients to GaN. There is no ideal substrate for heteroepitaxy of GaN and, as a consequence, there has been intense research into finding the most suitable substrate material. Table 4.1 shows the lattice constants and thermal expansion coefficients of various substrates that have been used for GaN epitaxy.

Sapphire is the most frequently used substrate for GaN growth due to its relatively low price, the availability of large area crystals of good quality, its transparent nature, stability at high temperature and fairly mature growth technology. If GaN is grown directly onto sapphire the crystal quality is poor due to the large lattice and thermal expansion mismatch between the two materials and also due to non-ideal nucleation. To improve the quality of the GaN layer an AlN or GaN buffer layer is usually grown [47], [48]. The GaN buffer layer is grown at relatively low temperatures ($\sim 500^{o}$C) and its thickness can vary from tens of nanometres to a few microns. It has been found that with other growth conditions being equal, the epilayers with the best crystallinity are grown on buffer layers with the worst crystallinity [29]. The

Crystal	Symmetry	Lattice constant (nm)	Thermal expansion coefficient (a,c) ($x10^{-6}K^{-1}$)
GaN	W	(0.3189; 0.5185)	(5.59; 3.17)
Sapphire	H	(0.4758; 1.299)	(7.5; 8.5)
6H-SiC	W	(0.308; 1.512)	(4.2; 4.86)
ZnO	W	(0.3250; 0.5213)	(8.25; 4.75)
Si	C	0.54301	3.59
AlN	W	(0.3112; 0.4982)	(4.2; 5.3)

Table 4.1: Lattice parameters and thermal expansion coefficients of various substrates that have been used for GaN epitaxy. W - Wurtzite, H - Hexagonal, C - Cubic

large defect density of these GaN buffer layers is thought to accommodate the large lattice mismatch between GaN and sapphire. Other substrates that are commonly used for the heteroepitaxial growth of GaN are 6H-SiC, ZnO and Si.

4.3 GaN for harsh radiation environments

The Large Hadron Collider (LHC) [4] is a particle accelerator and collider located at CERN, near Geneva, Switzerland. There are five detectors that are currently being constructed at the LHC; two of them, ATLAS [3] and CMS [51] are large, general purpose particle detectors, the other three; LHCb [52], ALICE [53] and TOTEM [54] are smaller and more specialised. A sixth additional detector, fp420 [55], is scheduled to be installed in 2009. The fp420 detector is an extension of the ATLAS detector and will be used for proton tagging. The high collision and event rates of the LHC will result

in the tracking detectors of these experiments receiving unprecedented levels of radiation. It has been calculated that at the LHC design luminosity of 10^{34} $cm^{-2}s^{-1}$, the innermost pixel detectors (4 cm from the interaction point) of the ATLAS detector will receive a total 1 MeV neutron equivalent accumulated particle fluence of 3x10 ^{15} cm^{-2} after 10 years of operation [5]. The radiation is a direct result of the proton-proton collisions themselves and from background neutrons created as backsplash from the calorimeters of the ATLAS detector. The hadronic radiation resulting from the proton-proton collisions creates bulk damage within the semiconductor tracking medium, leading to an increase in the detector leakage current, full depletion voltage and a decrease in the detector charge collection efficiency.

The proposed machine upgrade of the LHC, the SLHC [56], presents significant challenges for designers of radiation detectors. The SLHC is proposed to operate at 10 times the luminosity of the LHC, i.e 10^{35} $cm^{-2}s^{-1}$, and will require detectors that are able to withstand 1MeV neutron equivalent fluences greater than $1x10^{16}$ cm^{-2} after 5 years of operation. Figure 4.2 shows the accumulated hadron fluences expected in the SUPER-ATLAS inner detector after 5 years operation [5]. It should be noted that these values are calculated using data, found in [57], for the ATLAS detector and scaled to the SUPER-ATLAS integrated luminosity. The exact geometry of the SUPER-ATLAS detector is not yet decided but the data may be used as an illustration of the expected radiation levels and challenges faced. As well as these extremely high radiation levels the increase in luminosity will lead to an increase in track density and therefore detectors with finer granularity will be required. If these requirements are to be met then pixel detectors will have to cover the tracking volume up to higher radii and the microstrip detectors will have to be made with shorter strip lengths compared to the

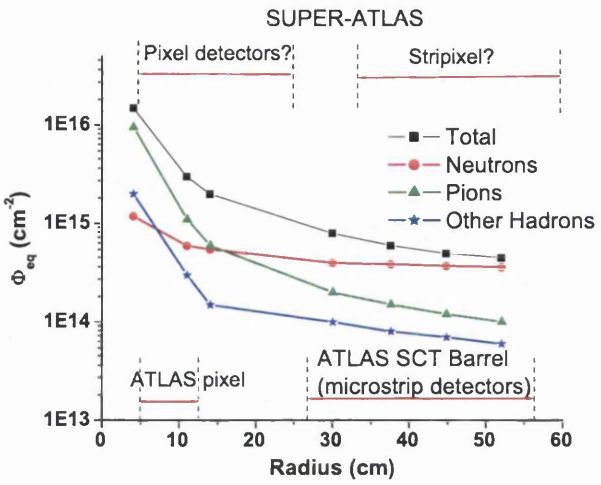

Figure 4.2: Hadron fluences expected in the SUPER-ATLAS inner detector after 5 years of operation. All fluences are 1 MeV neutron equivalent fluences [5].

present ATLAS detector (see Figure 4.2).

The current Si pixel and microstrip detector technology would not be able to withstand the radiation fluences expected at the SLHC [56]. The RD50 collaboration "Development of Radiation Hard Semiconductor Devices for Very High Luminosity Colliders" [8] was formed in 2002 with the aim of developing semiconductor sensors capable of operating in the SLHC environment. There are two main strategies followed within the RD50 collaboration aimed at improving the radiation tolerance of systems placed in harsh environments; material engineering and device engineering. The material engineering category covers the defect engineering of Si by using enhanced levels of oxygen in the Si substrate and also the use of other semiconductors such as SiC and GaN as radiation detectors. The standard Si material used as tracking detector bulk material is n-type Float Zone (FZ) Si. There have been several approaches undertaken to defect engineer FZ Si in order to make it more

radiation tolerant. One approach was to enrich FZ Si by putting an oxygen jet on the melting zone of a FZ ingot and diffusing oxygen into the Si wafer at high temperatures (1100°C - 1200°C) over long time periods (several hours to 10 days) [58]. This technique, Diffusion Oxygenated Float Zone (DOFZ) Si, produced wafers with oxygen concentrations as high as $4x10^{17}$ O cm^{-3}. FZ Si has also been enriched with other elements such as nitrogen, carbon, germanium, and tin and the radiation tolerance of these enriched materials assessed [59]. Other defect engineering techniques include irradiating FZ Si with electrons in order to increase the oxygen dimer content [60] and exposing FZ Si to a hydrogen plasma in order to increase the hydrogen content of the detector [61]. A further way of increasing the oxygen content in Si is by growing Czochralski (CZ) and Magnetic Czochralksi (MCZ) Si. Both CZ and MCZ have a much higher oxygen content than FZ Si or even DOFZ Si [62]. Epitaxial Si detectors have also been studied with a view to understanding their radiation tolerance. The oxygen enriched epitaxial Si is typically grown to a thickness between 25 μm and 50 μm on a low resistivity MCZ substrate [63] however 150 μm epitaxial Si has recently become available . There have been extensive radiation damage studies of the aforementioned defect engineered Si detectors. Some of the results reported will be discussed in Section 4.7 and compared to the findings in this work.

The device engineering branch of the RD50 collaboration investigates improved radiation tolerance by utilising novel detector structures such as full 3D detectors, semi-3D detectors [64] and single type column 3D detectors. 3-D detectors were first proposed by Sherwood-Parker in 1997 [9]. The electrodes of a 3D detector are an array of columns of diameter $\sim$ 5-10 μm placed a distance of around 30-100 μm apart. The columns are filled alternately with p^+- or n^+- electrode material. Since the electric field evolves

laterally from column to column, the depletion distance is only 30-100 μm while the charge created by an ionising particle is still that of a 300 μm thick detector. The smaller distance between the electrodes results in much shorter charge collection times compared to standard 300 μm thick planar Si detectors. This attribute of 3D detectors is extremely important for devices irradiated to very high fluences where the drift length for charge carriers and the depletion depth for any given bias voltage are severely reduced (more will be said on the effects of radiation damage in Si detectors in the following section). Simpler 3D designs such as the single type column (STC) detector have also been fabricated and characterised [65]. In the case of the STC detector instead of the electrodes penetrating the full length of the bulk material they stop short, $\sim$ 50 μm, from the opposite surface of the 300 μm thick Si material.

Also investigated within the RD50 collaboration are the radiation hardness properties of other semiconductor materials, such as SiC and GaN. Table 4.2 shows the important electrical and mechanical properties of a range of semiconductor materials that are either currently used for ionising radiation detection or are potential candidates for future use as ionising radiation detectors. The 4H-SiC polytype is the preferred SiC polytype for radiation detection applications due to its high electron mobility.

The main advantage of SiC and GaN is that the large band gaps of both materials, compared to Si, lead to very low leakage currents which would allow room temperature operation of devices fabricated on these materials. A possible second advantage is that is that both materials may be more resistant to radiation damage compared to Si on account of their relatively large displacement threshold energies. GaN in particular, is of interest for use as a radiation hard ionising radiation detector due to the high ionic

Property	Si	GaN	4H-SiC	Diamond	Ge	GaAs
Z	14	31/7	14/6	6	32	31/33
E_g (eV)	1.12	3.39	3.3	5.5	0.66	1.42
Density (g/cm^3)	2.3	6.15	3.2	3.5	5.32	5.32
μ_e (cm^2/Vs)	1450	1000	800-1000	1800-2200	3900	9200
μ_h (cm^2/Vs)	450	30	50-115	1200-1600	1800	320
Dielectric constant	11.9	8.9	9.7	5.7	16.2	12.4
e-h pair creation energy (eV)	3.6	8.9	8.4	13.1	2.96	4.35
e-h pairs/μm (eV)	81	$\sim$ 65	51	36	247	130
Displacement (eV)	13-25	10-20	20-35	43	28	10
Radiation length χ_0 (cm)	9.36	2.56	8.7	12.15	2.30	2.3

Table 4.2: Properties of various semiconductors [5]

bond strength and large crystal density which again should result in GaN exhibiting a greater degree of radiation hardness than other semiconductors.

SiC, because of its greater commercial availability, has been the more heavily studied of the two materials for use in future radiation hard detector devices. The difference between the various SiC polytypes is the stacking order between succeeding double layers of carbon and silicon atoms. Radiation detectors have been realised on both bulk and epitaxial, 50 μm thick, 4H-SiC. Bulk 4H-SiC is currently the only route to produce thick wafers (e.g. 100-500 μm) however the quality of the material has been poor. Conversely, epitaxial 4H-SiC grown on a substrate produces high purity material but the maximum achievable thickness is only 50 μm. The radiation hardness properties of irradiated bulk and epitaxial 4H-SiC will be discussed in Section 4.7.

There has been very little data reported on radiation hardness properties of GaN. One of the main objectives of this thesis is to evaluate GaN's radiation hardness for use as a tracking detector medium at the proposed SLHC.

4.4 Radiation Damage in a Semiconductor Detector

There is very little information on the radiation damage process within GaN, however extensive literature exists on the process within Si detectors. In this section, the radiation damage processes and resultant effects on the macroscopic properties will be discussed as it is understood to affect Si.

Radiation damage is the detrimental alteration of the operational and detection properties of a detector due to high levels of irradiation. The severity of radiation damage is dependent on the energy and the charge of the incident particle. High-energy particles produce three main types of effects within a semiconductor device;

- Long term Ionisation - This is surface damage of the semiconductor. In the case of Si, positive charge is trapped in SiO_2 on the surface of the semiconductor and surface states are created.
- Displacements - These are displacements of atoms from their normal sites in the crystal lattice, producing less ordered structures, with long term effects on the semiconductor properties
- Transient Ionisation - This effect produces electron-hole pairs and has no degrading effect of detector performance

4.4.1 Long Term Ionisation

Long term ionisation produces surface damage which influences the detector capacitance, increases the detector noise and can have a negative impact on the breakdown behaviour of the detector. This surface damage is caused by ionising energy loss (IEL) of the incident particle. Positive charge accumulates in the SiO_2 and interface states at the Si/SiO_2 are built up. Non Ionising Energy Loss (NIEL), resulting in the displacement of atoms from their normal sites in the lattice, causes the creation of crystal detects in the semiconductor bulk. This bulk damage of the semiconductor is the main cause of the degradation in performance of a semiconductor radiation detector.

4.4.2 Displacements

The bulk damage in semiconductor detectors caused by hadrons (neutrons, pions, protons etc.) or energetic leptons is primarily due to the incoming particle displacing a Primary Knock on Atom (PKA) from its lattice site. The displacement of this atom creates an interstitial and a vacancy (Frenkel defect) in the lattice. Both can migrate through the semiconductor crystal lattice and form complex point defects or defect clusters. However the original PKA can only be displaced if there is enough energy to break the binding energy of the atoms in the lattice. For Si the displacement energy is $\sim$ 13-25 eV, whereas for GaN the displacement energy of the Ga atom has been reported to be 19.2 eV [66].

The energy of a recoil PKA or any other atom resulting from a nuclear reaction can of course be much higher. Along the path of these recoils the energy loss consists of two competing contributions, one being due to ionisa-

tion and the other due to further displacements of atoms in the crystal. At the end of any heavy recoil range the non-ionising interactions prevail and a dense agglomeration of defects (disordered region) is formed. Both point defects along the particle paths and the clusters at the end of their range are responsible for the various damage effects in the bulk of the semiconductor detector but ionising losses will not lead to any significant changes in the semiconductor lattice.

A Frenkel pair may be generated in Si if incident neutrons have an energy above 175 eV and if electrons have an energy above 260 keV [57]. Low energy recoils above these energies usually create point defects, however recoils with energies greater than 5 keV create cluster defects at the end of its track. The kinematic lower limits for the production of clusters are $\sim$ 35 keV for neutrons and $\sim$ 8 MeV for electrons.

4.4.3 NIEL Hypothesis

The non-energy ionising loss (NIEL) hypothesis allows a comparison to be made between the bulk displacement damage caused by various hadronic particles (protons, pions, electrons, neutrons) of different energies. According to this NIEL hypothesis the radiation damage of the bulk semiconductor material depends only on this non-ionising energy loss of the irradiating particle. The hypothesis has been experimentally demonstrated for protons, neutrons and pions [67]-[70]. The NIEL hypothesis states that displacement damage induced change in the material properties scales with the amount of energy imparted in displacing collisions, irrespective of the spatial distribution of the introduced displacement defects in a PKA cascade and irrespective of the various annealing sequences that take place after the initial radiation damage. The displacement damage cross section, measured in MeVmb, is

given by the so called damage function D(E) where

$$D(E) = \sum_{v} \sigma_(v)(E) \int_0^{E_R^{Max}} f_v(E, E_R) P(E_R) dE_R \tag{4.1}$$

v denotes every possible interaction of an incoming particle with energy E leading to a displacement within the lattice. The symbol σ_v is the corresponding cross-section for interaction v to occur. $f_v(E, E_R)$ is the probability that an incoming particle of energy E will produce a primary a PKA with recoil energy E_R in the reaction v. The integration is performed over all possible PKA recoil energies E_R. Figure 4.3 shows the displacement damage cross-section versus particle energy for protons, neutron, pions and electrons in Si.

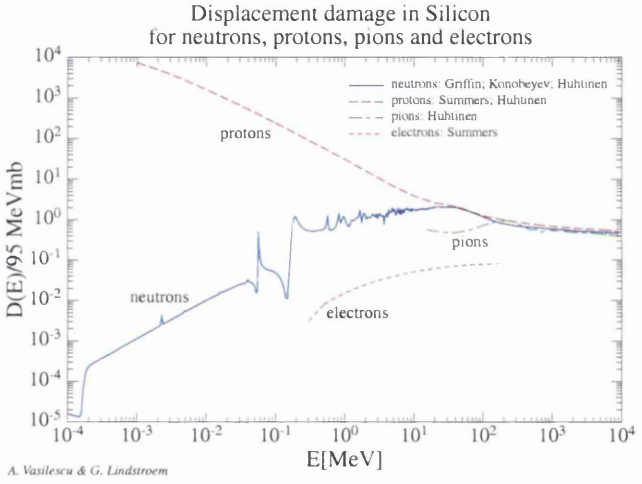

Figure 4.3: Displacement damage in Si for various hadrons [57]

The damage caused by different particles is usually compared to the damage caused by neutrons. The damage function depends on neutron energy and by convention the NIEL of 1 MeV neutrons is taken as a standard reference point. Therefore any hadronic fluence, ϕ_h may be converted to a 1

MeV neutron equivalent fluence ϕ_{eq} if the hardness factor, κ of the incident particle is known using the equation

$$\phi_h = \frac{\phi_{eq}}{\kappa} \tag{4.2}$$

Recently it has been shown that the NIEL hypothesis is violated if oxygen enriched silicon materials are irradiated. In DOFZ Si appreciably less damage is caused by high energy protons or pions than that due to neutrons if normalised to the NIEL equivalent fluence [67]. Additionally it has been reported that 1.8 MeV electrons are 40 times less damaging than hadrons [72].

4.4.4 Effect of Radiation Damage on Detector Operation

Both point defects and clusters can have severe effects on the detector performance, depending on their concentration, energy level and the respective electron and hole capture densities. There are three main macroscopic effects of radiation damage to a semiconductor detector [5]:

- An increase in leakage current proportional to the fluence, increasing the electronic noise and the power consumption
- A change of the effective doping concentration with consequences for the electric field profile and the operating voltage required for full depletion
- An increase of the charge carrier trapping leading to a reduction of the effective drift length for both electrons and holes and leading to a reduction of the charge collection efficiency of the detector

Each of these effects influences the signal-to-noise ratio of a detector which is the most important figure of merit when deciding on the tracking capabilities of an irradiated detector.

Radiation induced defects with deep energy levels in the forbidden region of the band gap act as recombination/generation centres and are responsible for an increase in the leakage current of the detector. This increase in leakage current lowers the signal-to-noise-ratio of the detector reducing its tracking capabilities.

One of the most serious radiation induced effects is the change in the effective doping concentration. Irradiating FZ Si to large hadron fluences introduces shallow and deep acceptor levels within the band gap. This ultimately leads to "type-inversion" where n-type bulk FZ Si becomes p-type. This means that for a type inverted p^+-n Si detector the depletion region grows from the unstructured rear electrode, the n^+-contact, and results in a significant increase of the detector bias to achieve reasonable charge collection. The full depletion voltage dependence on the effective doping concentration is given by

$$V_{FD} = \frac{q_o}{2\epsilon\epsilon_0}|N_{eff}|W^2 \tag{4.3}$$

where V_{FD} is the full depletion voltage, ϵ is the permittivity of the semiconductor, ϵ_0 is the permittivity of free space, N_{eff} is the doping concentration and W is the width of the depletion zone. From the equation it is seen that any increase in N_{eff} leads to a corresponding increase of the full depletion voltage. In certain irradiated silicon devices the formation of the electric field is not as simple as stated above. A so-called "double-junction" can appear, where the electric field grows from the front and the rear contact [73],[74].

The increase of charge carrier trapping in an irradiated device leads to a reduction in charge carrier drift length and thus a reduction of the charge

collection efficiency. Increasing the bias voltage can generally recover some lost signal amplitude by reducing the drift time of the carriers through the device. However, this is only practical if the detector leakage current remains at a reasonable level, since increasing the bias voltage will ultimately cause an unacceptable signal-to-noise ratio or even device breakdown.

The primary defects are subject to change after long-term storage at room temperature, in annealing processes. Such annealing effects may be due to the dissolution of cluster defects releasing migrating vacancies and interstitials. For irradiated Si detectors the leakage current and the electron trapping anneals in a beneficial way, while the hole trapping anneals in a detrimental fashion [72]. The effective trapping probability for electrons and holes at a given temperature, T and time, t after irradiation may be parameterised as:

$$\frac{1}{\tau_{eff_{e,h}}} = \beta_{e,h}(t,T)\phi_{eq} \tag{4.4}$$

where $\tau_{eff_{e,h}}$ is the trapping time for electrons and holes, $\beta_{e,h}$ is the trapping parameter for electrons and holes and ϕ_{eq}, is the 1 MeV equivalent fluence. By plotting a graph of trapping probability versus irradiating fluence β may be evaluated for electrons and holes. In irradiated Si detectors there is initial short term beneficial annealing of the effective doping concentration however over long annealing times the effective doping concentration increases [5].

In summary, the extent to which a detector suffers from radiation damage depends not only on the energy and type of the irradiating particle or photon, but also on the operational bias, temperature and the annealing history of the detector.

4.5 Materials Studied & Detector Characterisation

In this chapter the radiation hardness properties of three semi-insulating (SI) epitaxial GaN wafers were examined. All three SI epitaxial GaN wafers were grown by MOCVD on (0001) sapphire substrates. Two 2 inch diameter, 2.5 μm thick epitaxial GaN wafers were obtained from Tokushima University, Japan [75], and one 2 inch diameter, 12 μm thick epitaxial GaN wafer was obtained from Lumilog, France [76]. The two 2.5 μm thick epitaxial GaN wafers were both grown under different conditions, the details of which were not supplied by the manufacturer. Table 1.3 (see Chapter One) details how these three GaN wafers are referred to in this chapter.

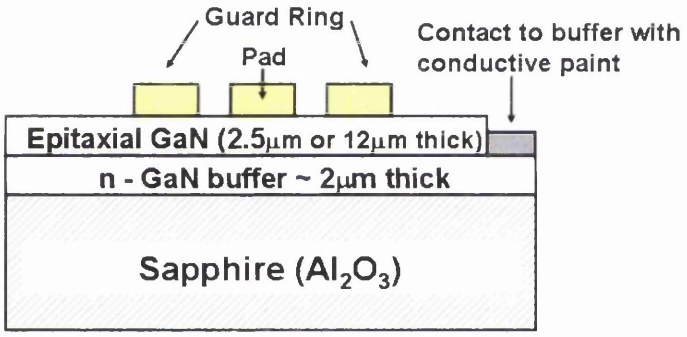

Figure 4.4: Cross-sectional diagram of the GaN material studied

A cross-sectional diagram of the different GaN layers grown on the sapphire substrates is shown in Figure 4.4. An n-GaN buffer layer was grown at a low temperature ($\sim$ 400^{o}C) before growth of the SI epitaxial layer to account for the lattice and thermal expansion coefficient mismatch between GaN and (0001) sapphire. As discussed in Section 4.2.2, GaN grown directly

onto sapphire contains a large density of dislocations resulting in poor crystal quality and detection efficiency. The SI epitaxial layers were grown to a thickness of 2.5 μm or 12 μm and are slightly n-type. The exact values of the carrier concentrations are not known but previous studies have shown that SI GaN layers grown by Tokushima University exhibit a carrier concentration of $\sim$ 3x10^{16} cm^{-3} [77].

The wafers were diced using a mechanical saw into sections of dimension 10 mm by 5 mm in order to fabricate simple test structures. Photolithographic techniques (see Section 2.2.1) were used to define pad and guard ring structures. Schottky contacts were realised by depositing 50 nm of Pd followed by 200 nm of Au using a Plassys 450 MEB evaporator at a pressure of $\leq$ 2x10^{-6} mbar. The Schottky contact was formed between the SI GaN and Pd; while the Au evaporated on top of the Pd facilitated subsequent wire bonding. Before the metal evaporation procedure the samples were placed in a beaker of hydrochloric acid (HCl) for one minute in order to remove the native oxide from the GaN surface. Studies have shown that hydrofluoric acid (HF) is best at removing carbon contamination while HCl is best at removing surface oxide. It was found that re-oxidation of the processed surface is inhibited because it becomes F and Cl terminated [78]. Using Equation 3.23, the theoretical value of the Schottky barrier formed for Pd on SI GaN is 1.02 eV.

Figure 4.5 shows a metalised pad and guard ring test structure. The pad diameter is 1 mm, the guard ring is 500 μm wide and there is a 50 μm isolation gap between the pad and the guard ring. Two sets of pad and guard ring structures were fabricated on each sample. A further contact was made to the n-GaN buffer using conductive silver paint (see Figure 4.6). This enabled a bias to be applied between the pad and the n-GaN buffer contact

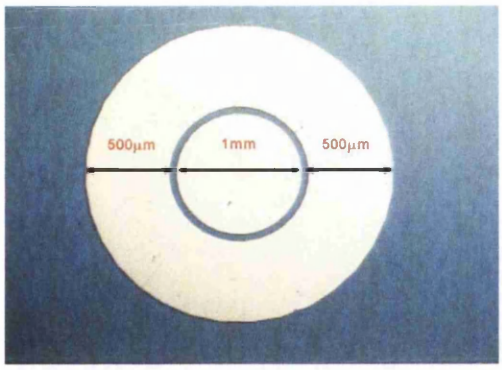

Figure 4.5: Pad and guard ring structures fabricated using photolithographic techniques

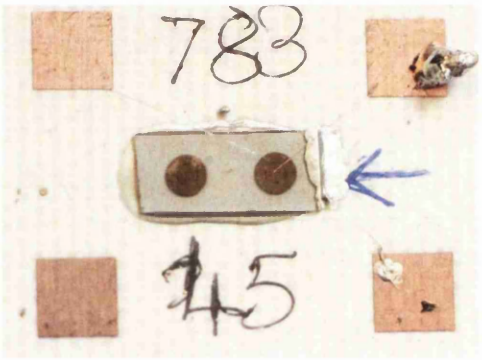

Figure 4.6: A fully fabricated test diode with pad and guard ring structures. Contact was made to the n-GaN buffer with silver conductive paint (on right of sample).

and ensured the epitaxial GaN depletes downward, utilising the full thickness of the epitaxial region. The guard ring was fabricated in order to minimise surface leakage currents. The completed devices were wire bonded to chip carriers for characterisation.

4.5.1 Irradiation Details

Fabricated detectors were irradiated with 24 GeV/c protons at CERN and with reactor neutrons at the TRIGA reactor in Ljubljana, Slovenia [79]. Fluences of up to $3x10^{14}$ $pcm^{-2}s^{-1}$ are achievable at the IRRAD-1 irradiation facility at CERN [80]. The neutron source at the TRIGA reactor can provide a flux of fast neutrons (E > 100 keV) up to $5x10^{12}$ $ncm^{-2}s^{-1}$ (see Figure 4.7). The flux ratio of thermal neutrons (E < 0.5 eV) to fast neutrons (E > 100

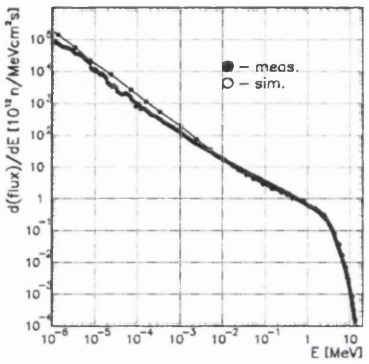

Figure 4.7: Neutron flux versus neutron energy at the TRIGA reactor [79]

keV) is approximately two. Devices were irradiated with protons and neutrons to five fluences; $1x10^{14}$ cm^{-2}, $1x10^{15}$ cm^{-2}, $2x10^{15}$ cm^{-2}, $5x10^{15}$ cm^{-2} and $1x10^{16}$ cm^{-2} and the effects of the irradiations on detector performance assessed. All quoted fluence values are subject to errors of approximately 10% and neutron fluences are 1 MeV equivalent.

4.5.2 Characterisation Techniques

The detectors were electrically characterised pre-and post-irradiation by performing current-voltage (I-V), capacitance-voltage (C-V) and charge collection efficiency (CCE) measurements. All three techniques were performed

with the pad and guard ring kept at the same potential and the n-GaN buffer contact grounded. As stated earlier, the guard ring served to minimise surface leakage currents.

Room temperature (295 K +/- 2 K) I-V measurements were performed using a Keithley 237 electrometer controlled by LABVIEW [81] software. The device under test was housed in a light tight Faraday box that also shielded the device from outside electronic noise. C-V measurements were also performed at room temperature using a Hewlett Packard 4274A multi-frequency LCR meter again controlled via the LABVIEW software. DC bias was supplied from the Keithley 237 via the high output of the LCR meter in order to deplete the device under test. A milli volt A.C. signal from the LCR machine was used to determine the reactance of the device and hence the capacitance. It is assumed that the capacitance is the only element in the circuit so that when a small signal bias is applied the current that flows is phase shifted by 90°C. It is this current that is measured by the LCR meter. The current and applied voltage are related by:

$$I = \frac{V}{Z} = jwVC \tag{4.5}$$

where Z is the capacitor impedance and V is the small A.C. signal of angular frequency w. Therefore from the current measurement the capacitance can be determined. It was possible to measure the capacitance of the device under test at eleven different frequencies ranging from 100 Hz to 100 kHz. The LCR meter not only displayed the capacitance but also gave the Q value of the capacitance measurement. The Q value is used to establish the reliability of the measured capacitance value. In this thesis, if the Q value of the capacitance measurement was smaller than 10 then the capacitance measurement was said to be unreliable. From herein all measured capacitances had Q values greater than 10. All C-V measurements were performed at

room temperature (295 K +/- 2K) and a two second delay was used between frequency steps while a five second delay was used between voltage steps. The frequency dependence of the capacitance can reveal deep defect levels.

CCE measurements are ideally performed using minimum ionising particles (MIPs), e.g. β particles emitted from a ^{90}Sr source. In a standard 300 μm thick Si detector a MIP will produce $\sim$ 24000 e-h pairs, however in 2.5 μm and 12 μm of GaN a MIP will produce only $\sim$ 163 e-h pairs and $\sim$ 780 e-h pairs respectively. The number of e-h pairs produced by a MIP in thin GaN detectors is lower than the electronic noise measured by a typical CCE experimental set-up and so MIPs are not suitable for measuring the CCE of the GaN detectors studied here. Instead the CCE of the GaN detectors was measured using α particles emitted from an ^{241}Am source. Two different ^{241}Am sources were used; one spectroscopic source emitting 5.48 MeV α particles and a second thicker source that emitted α particles with an average energy of 3.82 MeV. The lower energy of the α particles emitted from this second source is due to energy loss of the particles as they travel from the back to the front of the source.

Figure 4.8 shows the Bragg ionisation curve for a 3.82 MeV α particle and 5.48 MeV α particle as they travel in GaN. The data was calculated using the SRIM simulation package [33] and also took into account the thickness of the metal contacts of the detector (50 nm Pd/ 200 nm Au). Integrating under the curve it is found that a 5.48 MeV α particle deposits 722 keV in 2.5 μm of GaN and 4.501 MeV in 12 μm of GaN whereas a 3.82 MeV α particle deposits 909 keV in 2.5 μm of GaN and 3.72 MeV in 12 μm of GaN.

The CCE experimental set-up is shown in Figure 4.9. The detector and alpha particle source were housed in a cylindrical vacuum chamber at a pressure of $\sim$ 23 mbar to ensure negligible energy loss. The measurement set-up

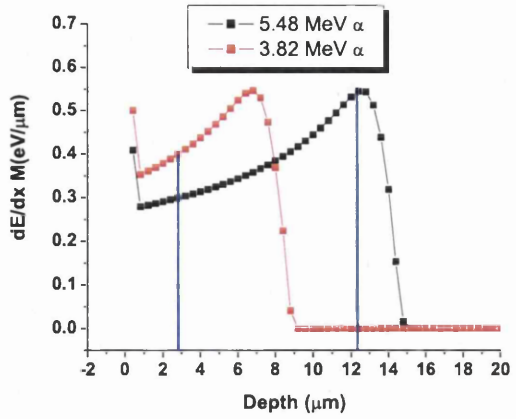

Figure 4.8: Bragg ionisation curves for a 3.82 MeV and 5.48 MeV α particle in GaN. The calculation takes into account the thickness of the metal contact.

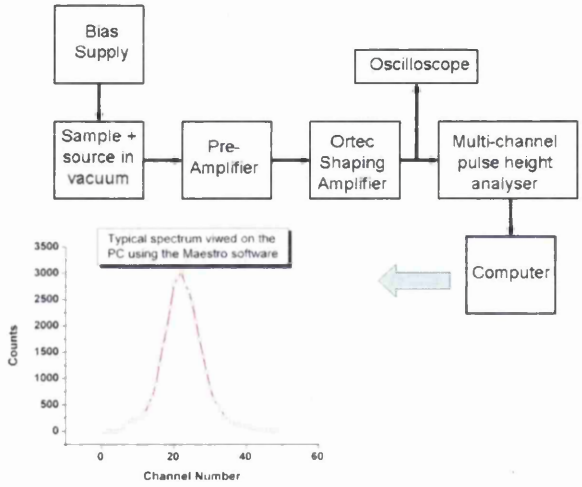

Figure 4.9: CCE experimental set-up

consisted of an Ortec 141 charge-sensitive pre-amplifier and an Ortec shaping amplifier connected to a multi-channel pulse height analyser. The resultant spectrum of counts versus channel number was viewed on the PC using the Maestro software programme [82] and the data saved to disk for off-line anal-

ysis. The shaping time of the Ortec 141 amplifier could be set between 0.5 μs and 10 μs (shaping time of 0.5 μs was used for all the CCE measurements presented here) and the sample could be biased to 1000 V using the voltage supply. The oscilloscope was used to display the α-induced signals from the detector. All CCE measurements were performed at room temperature.

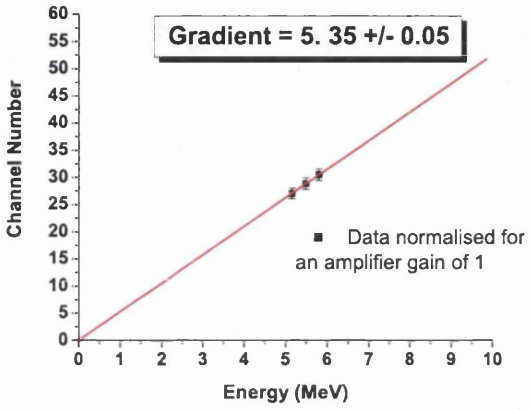

Figure 4.10: Calibration of energy versus channel number scale using three mono-energetic spectroscopic sources

As stated earlier, the Maestro programme bins the data into channel numbers that correspond to energies. In order to determine the CCE of a detector it was necessary to establish the relationship between channel number and energy. To do this a Si surface barrier diode, assumed to have 100% CCE, was used to take spectra of a number of mono-energetic spectroscopic sources; namely ^{241}Am, ^{239}Pu and ^{244}Cm. The energy of the α particles emitted from these three sources is well known and a linear plot may be made of energy versus channel number (see Figure 4.10). The gradient of this plot can then be used to convert directly from a channel number to an energy. The gradient was found to be 5.35 (see Figure 4.10). To calculate the CCE

of the GaN detectors it was also necessary to introduce a scaling factor to account for the difference in electron-hole pair creation energy between silicon (3.6 eV) and GaN (8.9 eV) [5]. The measured energy, E_M, is then found using the equation:

$$E_M = \frac{\frac{Ch_P}{G} \times \frac{\delta_{GaN}}{\delta_{Si}}}{5.35} \tag{4.6}$$

where Ch_P is the channel number of alpha peak, G is the amplifier gain, δ_{GaN} and δ_{Si} are the electron-hole pair creation energies for GaN and Si respectively. The CCE of the detector may then be found using the equation:

$$CCE(\%) = \frac{E_M}{E_D} \times 100 \tag{4.7}$$

where E_D is the energy deposited in the detector by a 5.48 MeV alpha particle.

4.6 I-V, C-V & CCE Results

The first results reported on the radiation hardness of GaN were detectors fabricated on MOCVD 2.5 μm epitaxial GaN grown by Tokushima University [19]. These detectors were irradiated with protons, neutrons and x-rays to various fluences. The 36GaN and 45GaN material studied in this thesis (see Table 1.3) both have a similar epitaxial thickness and were also grown by MOCVD at Tokushima University and serve to establish the radiation hardness of very thin epitaxial GaN material.

4.6.1 36GaN material

The I-V characteristics of the unirradiated 36GaN detector up to a reverse bias of 40 V are shown in Figure 4.11. The detector exhibits the typical

behaviour of a reverse biased Schottky detector with a slow breakdown of the device occurring at a reverse bias of $\sim$ 20 V. It should be noted that

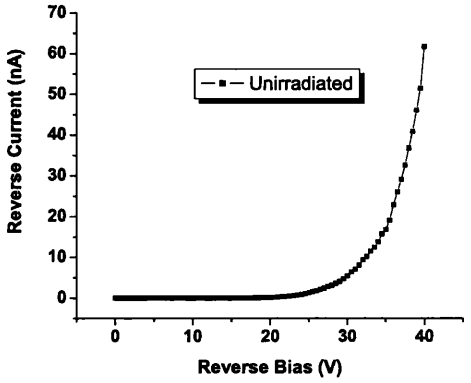

Figure 4.11: Reverse leakage current of unirradiated 36GaN detector

the I-V curves of all the proton and neutron irradiated detectors on all three GaN materials exhibit this same slow breakdown behaviour of the Schottky barrier. The leakage current of the detector increases from $\sim$ 20 fA at an applied reverse bias of 0 V to $\sim$ 60 nA at the maximum applied bias.

Figure 4.12 shows the reverse leakage current characteristics of the 36GaN detectors irradiated to five proton fluences ranging from 10^{14} p cm^{-2} to 10^{16} p cm^{-2}. At an applied bias of 0 V all of the proton irradiated detectors show an increase in leakage current compared to the unirradiated detector (see Table 4.3) At all bias voltages the leakage current of the detector irradiated to the lowest fluence of 10^{14} pcm^{-2} is greater than that of the unirradiated detector and the four other proton irradiated detectors. At reverse bias voltages greater than 20V the leakage currents of the detectors irradiated to $\geq 10^{15}$ pcm^{-2} are several orders of magnitude smaller than the leakage current of the unirradiated detector. At reverse biases $\geq$ 10V the 36GaN detectors

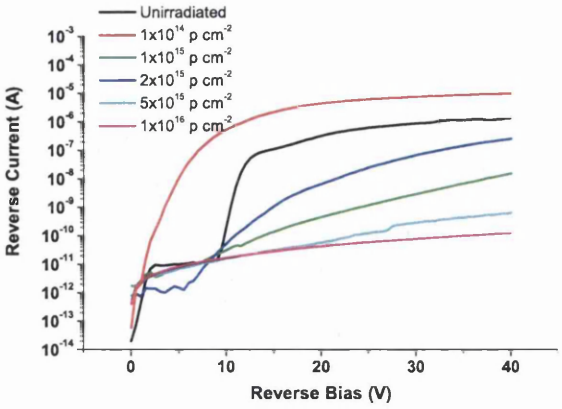

Figure 4.12: Reverse leakage currents of the proton irradiated 36GaN detectors

	I_L at 0 V	I_L at -20 V	I_L at -40V
Unirradiated	-20 fA	-326 pA	-1.36 μA
10^{14} p cm^{-2}	-60 fA	-4.51 μA	-9.98 μA
10^{15} p cm^{-2}	-1.6 pA	-445 pA	-14.8 nA
2x10^{15} p cm^{-2}	-770 fA	-53.5 pA	-24.8 nA
5x10^{15} p cm^{-2}	-560 fA	-55.4 pA	-609 pA
10^{16} p cm^{-2}	-410 fA	-16.7 pA	-122 pA

Table 4.3: Leakage currents of the proton irradiated 36GaN detectors at applied reverse biases of 0V, 20 V and 40 V

irradiated to the two highest fluences have much lower leakage currents than the detectors irradiated to the lower proton fluences and the unirradiated detector.

The I-V curves of the neutron irradiated 36GaN detectors up to a maximum applied reverse bias of 100 V are seen in Figure 4.13. The I-V curves of the irradiated neutron detectors show a similar behaviour to the proton

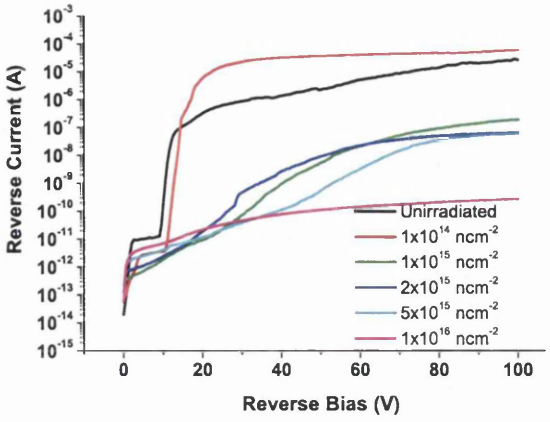

Figure 4.13: Reverse leakage currents of the neutron irradiated 36GaN detectors

irradiated detectors. Again, the detector irradiated to 10^{14} ncm^{-2} has in general, a larger leakage current than the unirradiated detector. It is also seen that, as exhibited by the proton irradiated detectors, there is a non-linear increase in leakage current with increasing neutron fluence and at the maximum applied reverse bias the leakage current of the most highly irradiated detector (10^{16} ncm^{-2}) is several orders of magnitude smaller than that of the unirradiated detector (see Table 4.4).

Figure 4.14 shows a plot of leakage current versus fluence at an applied reverse bias of 20 V for the proton and neutron irradiated devices. It can be seen that the leakage current generally decreases with increasing proton fluence. This behaviour is in contrast to that seen in irradiated Si detectors where the leakage current increases linearly with increasing irradiation fluence.

Figure 4.15 shows a C-V plot of the unirradiated 36GaN detector at frequencies of 10, 20, 40 and 100 kHz (the RD50 collaboration suggests performing C-V measurements at 10 kHz [83]). C-V measurements are useful for

	I_L at 0 V	I_L at -50 V	I_L at -100 V
Unirradiated	-20 fA	-2.26 μA	-26.3 μA
10^{14} n cm^{-2}	-90 fA	-36.8 μA	-58.3 μA
10^{15} n cm^{-2}	-210 fA	-5.49 nA	-184 nA
2x10^{15} n cm^{-2}	-130 fA	-9.33 pA	-63 nA
5x10^{15} n cm^{-2}	-210 fA	-566 pA	-54 nA
10^{16} n cm^{-2}	-60 fA	-114 pA	-273 pA

Table 4.4: Leakage currents of the neutron irradiated 36GaN detectors at applied reverse biases of 0 V, 50 V and 100 V

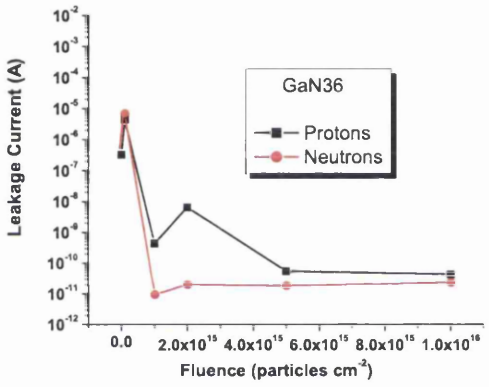

Figure 4.14: 36GaN Leakage current versus fluence plot of the irradiated 36GaN detectors at an applied bias of 20V

determining the carrier concentration, full depletion voltage and the internal bias, V_{bi}, of a detector. The carrier concentration, N_D is found using the following equation,

$$N_D = \frac{2}{q\epsilon\epsilon_0 A^2 d(1/C^2)/dv} \tag{4.8}$$

where ϵ is the dielectric constant for GaN , ϵ_0 is the dielectric constant of free space, A is the contact area and $d(1/C^2)/dv$ is taken from the gradient of a graph of $1/C^2$ versus V. The intercept the fit lines makes with the x-axis gives the internal bias, V_{bi}, of the device. The capacitance of a planar

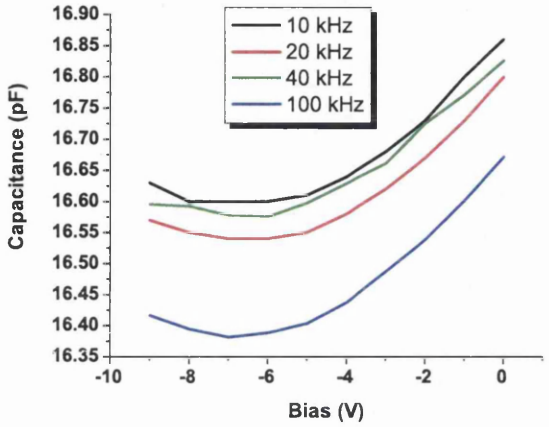

Figure 4.15: C-V curve of the unirradiated 36GaN detector at 10, 20, 40 and 100 kHz

detector should decrease with increasing bias voltage until the device is fully depleted and the capacitance decreases no further. This behaviour is not seen for the unirradiated 36GaN detector where the capacitance decreases slightly from between 0 V and -8 V. This decrease in capacitance however is extremely small. The expected full depletion capacitance for this device is 25 pF. There are several explanations for the C-V behaviour of this device. The most likely is that with such a thin epitaxial layer of GaN (2.5 μm) there are very few free carriers and so it could be that the device is in effect fully depleted at 0 V. Another possible explanation for the C-V behaviour of the unirradiated 36GaN device is that there is poor contact made to the n-GaN buffer with the silver conductive paint resulting in little or no depletion of

the detector with increasing reverse bias. The irradiated 36GaN devices show similar C-V properties to the unirradiated detector.

Figure 4.16 shows α particle pulse height spectra of the unirradiated 36GaN detector for several bias voltages. For all detectors the bias was increased until the detector noise became too large and swamped the signal. As the applied bias is increased the position of the α peak moves as a result

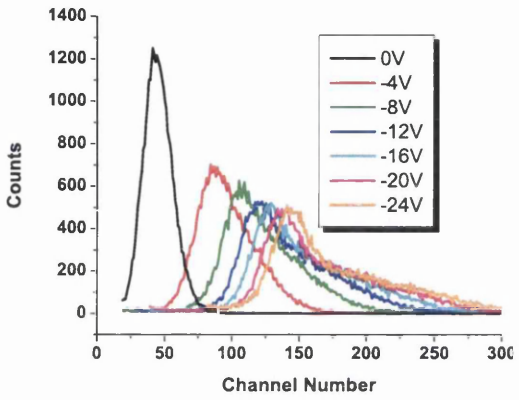

Figure 4.16: ^{241}Am *spectra of the unirradiated 36GaN detector taken at various bias voltages*

of an increase in the amount of charge being collected. Typically the CCE increases linearly with applied bias voltage until either 100% CCE is attained or until an increase in bias voltage results in no change in the CCE of the detector, i.e. there is a plateau of the CCE. In Figure 4.16 the CCE gradually increases with applied voltage and there is no plateau suggesting that increasing the bias voltage or increasing the magnitude of the electric field within the device still further may produce higher CCE values than those observed. This behaviour of the CCE spectra is typical of all the unirradiated and irradiated 36GaN, 45GaN and 12GaN detectors.

The CCE versus applied bias voltage curves for the proton irradiated 36GaN detectors are shown in Figure 4.17. The CCE of the unirradiated

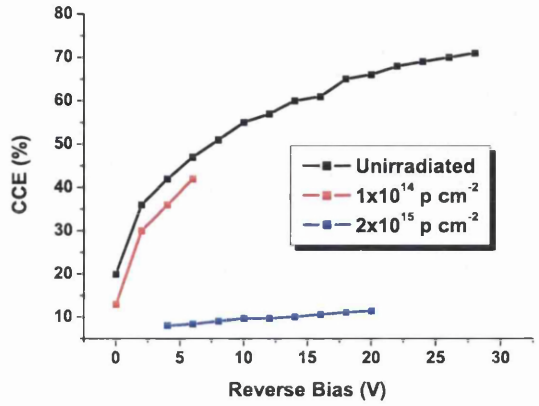

Figure 4.17: CCE versus bias curves of the proton irradiated 36GaN detectors

detector increases with applied voltage until the maximum CCE of 70% is achieved at an applied reverse bias of -28 V. For all reverse bias voltages the CCEs of the proton irradiated detectors are smaller in comparison to the unirradiated detector. The maximum CCE of the detector irradiated to 10^{14} pcm^{-2} is 42% at a reverse bias of 6V while the detector irradiated to 2x10^{15} pcm^{-2} exhibits a CCE of 12% at a reverse bias of 20V. It was not possible to obtain the peak position of the α signals from the three other proton irradiated detectors as either the α signals were too small or the leakage current of these devices was too high. Figure 4.18 shows the CCE versus bias plots for the neutron irradiated 36GaN detectors. The maximum CCEs of the detectors irradiated to 10^{14} ncm^{-2}, 2x10^{15} ncm^{-2} and 5x10^{15} ncm^{-2} are 61%, 20% and 40% respectively. The CCE results seem to suggest that for this GaN material, proton induced damage to the GaN bulk has a more detrimental effect on detector performance than neutron induced damage.

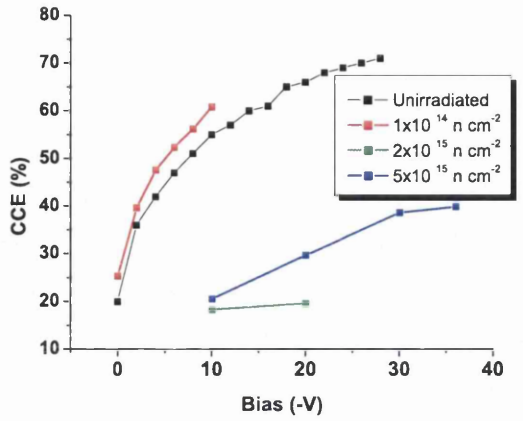

Figure 4.18: CCE versus bias curves of the neutron irradiated 36 GaN detectors

4.6.2 45GaN material

Figure 4.19 shows the I-V curves of the 45GaN detectors irradiated with 24 GeV/c protons to various fluences. The leakage current of the unirradiated

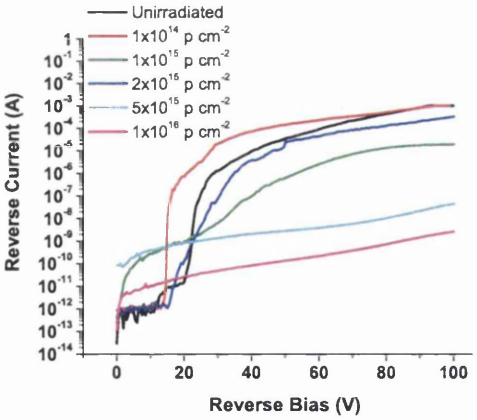

Figure 4.19: I-V curves of the unirradiated and proton irradiated 45GaN detectors

45GaN detector is $\sim$ -30 fA at 0 V and rises to $\sim$ -34 μA at an applied bias of -50 V. It is seen that the Schottky barrier of the unirradiated device begins

to breakdown at an applied reverse bias of 20 V. This breakdown may be viewed as carrier injection through the contact and leads to a sharp increase in the detector leakage current. Table 4.5 shows the leakage currents of the unirradiated and proton irradiated 45GaN detectors at reverse bias voltages of 0 V, 50 V and 100 V. The I-V curves of the proton irradiated 45GaN de-

	I_L at 0 V	I_L at -50 V	I_L at -100 V
Unirradiated	-30 fA	-34 μA	-1 mA
10^{14} p cm^{-2}	-960 fA	-146 μA	-1 mA
10^{15} p cm^{-2}	-230 fA	-628 nA	-18.5 μA
2x10^{15} p cm^{-2}	-450 fA	-25.6 μA	-318 μA
5x10^{15} p cm^{-2}	-858 pA	-2.7 nA	-43 nA
10^{16} p cm^{-2}	-110 fA	-141 pA	-2.68 nA

Table 4.5: Leakage currents of the proton irradiated 45GaN detectors at reverse biases of 0 V, 50 V and 100 V

tectors behave remarkably similarly to those of the proton irradiated 36GaN detectors. Again it is seen that at 0 V the leakage currents of all the irradiated detectors are larger than the unirradiated detector and that at large reverse bias voltages, > 20 V, the leakage current of the 10^{14} pcm^{-2} irradiated detector is larger than that of the unirradiated detector. However all the other proton irradiated 45GaN detectors exhibit leakage currents smaller than the leakage current of the unirradiated detector at reverse biases > 25V.

Figure 4.20 shows the leakage current versus bias curves for the neutron irradiated 45GaN detectors. The leakage current of the detector irradiated to 10^{14} ncm^{-2} is roughly the same as the unirradiated detector for bias voltages > 30 V. At bias voltages > 20 V, the leakage currents of the detectors irradiated to $\geq 10^{15}$ ncm^{-2} are all lower than the unirradiated detector. Ta-

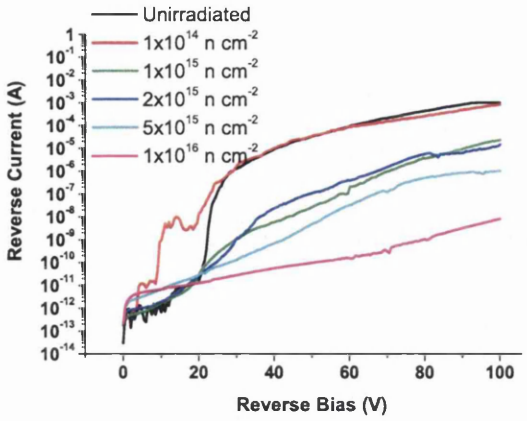

Figure 4.20: I-V curves of the neutron irradiated 45GaN detectors

ble 4.6 summaries the leakage currents of the neutron irradiated detectors at reverse bias voltages of 0 V, 50 V and 100 V. A plot of leakage current versus

	I_L at 0 V	I_L at -50 V	I_L at -100 V
Unirradiated	-30 fA	-34 μA	-1 mA
10^{14} n cm^{-2}	-260 fA	-34.5 μA	-816 μA
10^{15} n cm^{-2}	-260 fA	-26 nA	-22.7 μA
2x10^{15} n cm^{-2}	-180 fA	-110 nA	-14.2 μA
5x10^{15} n cm^{-2}	-280 pA	-4.97 nA	-9.94 nA
10^{16} n cm^{-2}	-220 fA	-102 pA	-8.3 nA

Table 4.6: Leakage currents of the neutron irradiated 45GaN detectors at applied reverse biases of 0 V, 50 V and 100 V

fluence for the proton and neutron irradiated 45GaN detectors at a reverse bias of 40 V is shown in Figure 4.21. As with the irradiated 36GaN detectors, there is a non-linear increase in leakage current with increasing fluence. The most heavily irradiated detector exhibits a leakage current $\sim$ six orders of

magnitude smaller than the unirradiated detector at the maximum reverse bias.

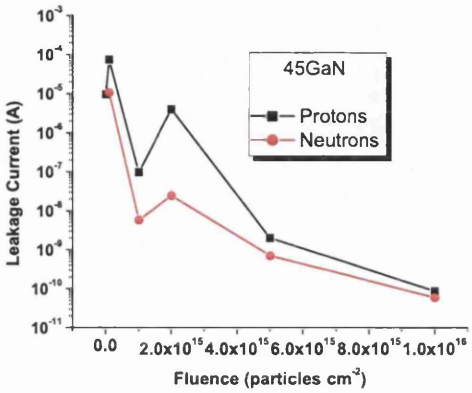

Figure 4.21: Leakage current versus fluence plot of the irradiated 45GaN detectors at a reverse bias of 40 V

The C-V plot of the unirradiated 45GaN detector at 10, 20, 40 and 100 kHz up to a reverse bias of 10 V is shown in Figure 4.22. The C-V curves show similar properties to those of the unirradiated 36GaN detector. The expected full depletion capacitance for this device is 25 pF. The capacitance remains relatively constant at $\sim$ 16 pF and does not appreciably decrease with increasing reverse bias as expected of a planar detector.

The maximum CCE of the unirradiated 45GaN detector is 97% at an applied bias voltage of -12 V and the detector CCE generally drops with increasing neutron fluence (see Figure 4.23). The relatively low leakage currents of the detectors irradiated to 10^{15} pcm^{-2}, 5x10^{15} pcm^{-2} and 10^{16} pcm^{-2} allowed CCE measurements up to larger bias voltages. Detectors irradiated to $\leq$ 2x10^{15} pcm^{-2} show a maximum CCE greater than 60%, however the maximum CCEs of the two most heavily irradiated detectors are $\leq$ 20%.

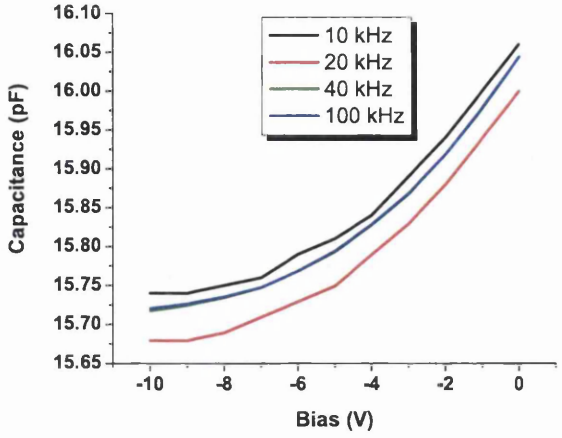

Figure 4.22: C-V curve of the unirradiated 45GaN detector at 10, 20, 40 and 100 kHz

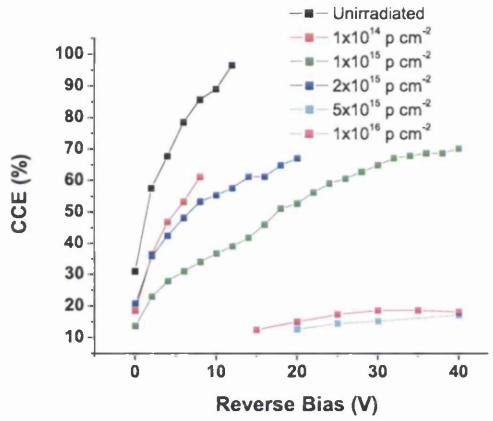

Figure 4.23: CCE versus bias plots of the proton irradiated 45GaN detectors

Figure 4.24 shows the CCE versus bias data for the neutron irradiated 45GaN detectors. All detectors, with the exception of the 10^{16} ncm^{-2} irradiated detector, have CCEs $\geq$ 60%. The detector irradiated to 10^{14} ncm^{-2} has a maximum CCE of 94% at an applied bias of -16 V which is very close to the maximum CCE of the unirradiated detector. The maximum CCE falls

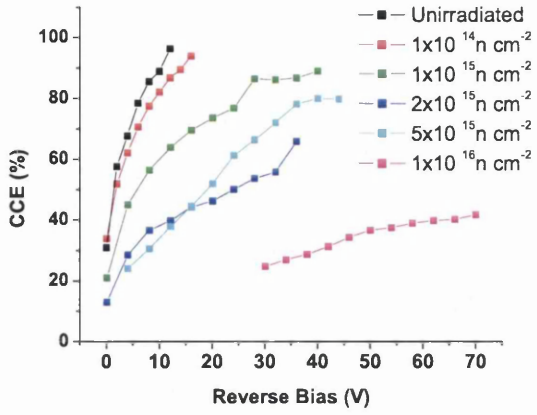

Figure 4.24: CCE versus bias plots of the neutron irradiated 45GaN detectors

to 89% after irradiation to 10^{15} ncm^{-2}, to 66% after irradiation to 2x10^{15} n cm^{-2} and increases to 80% after irradiation to 5x10^{15} ncm^{-2} .

The I-V and CCE data for the irradiated 45GaN detectors again show that the proton irradiations have a more detrimental effect on detector performance compared to neutron induced damage. It is also clearly apparent that the 45GaN material is more radiation hard than the 36GaN material since the 45GaN detectors irradiated to anticipated SLHC fluences exhibit CCEs significantly higher than the 36GaN detectors irradiated to the same fluence levels. As previously stated, Tokushima University did not supply the growth conditions of the 36GaN and 45GaN material. However it is well known that the TMG flow rate, substrate growth temperature, chamber pressure and the Ga/N ratio (typically an N rich growth environment results in higher quality material) significantly affect the crystal quality of the epitaxial GaN layer. It can be assumed that one or more of these growth parameters differ between the 36GaN and 45GaN material.

4.6.3 12GaN material

As previously stated, not enough charge is generated in 2.5 μm epitaxial GaN for it to be of practical use as a detection material for future high energy physics experiments. For GaN to be considered seriously for use as a tracking detector medium in future particle physics experiments the radiation hardness of thicker epitaxial layers must be assessed. In this thesis, the first investigations of the radiation hardness of GaN material with an epitaxial thickness > 2.5 μm have been performed (see Table 1.3).

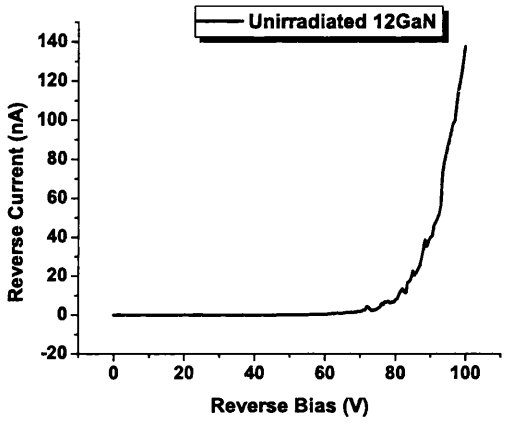

Figure 4.25: I-V curve of the unirradiated 12GaN detector

The I-V characteristics of the unirradiated 12GaN detector up to a reverse bias of 100 V are shown in Figure 4.25. The curve shows typical Schottky diode behaviour with a slow breakdown occurring at a reverse bias voltage of 70 V.

Figure 4.26 shows the reverse bias I-V characteristics of the 12GaN detectors irradiated to various proton fluences. The detector irradiated to 10^{14} pcm^{-2} was destroyed in transit so there is no I-V or CCE data for this sample. At reverse bias voltages lower than 40 V the leakage currents of all

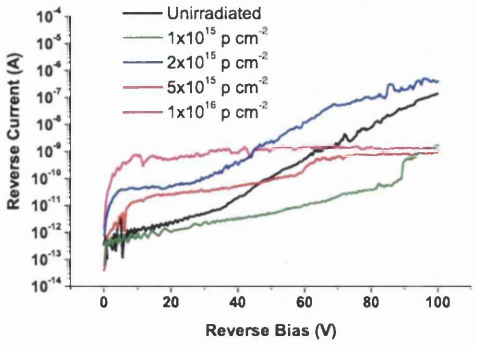

Figure 4.26: Leakage currents of the proton irradiated 12GaN detectors

proton irradiated detectors, with the exception of the detector irradiated to 10^{15} p cm^{-2}, are greater than the unirradiated detector. This behaviour is in contrast to the proton irradiation results on the thinner epitaxial GaN material. A comparison of the leakage currents at 0 V, -50 V and -100 V of the proton irradiated 12GaN detectors is given in Table 4.7. At the largest

	I_L at 0 V	I_L at -50 V	I_L at -100 V
Unirradiated	-360 fA	-114 pA	137 nA
10^{14} p cm^{-2}	no data	-no data	no data
10^{15} p cm^{-2}	-60 fA	-5 pA	-1.61 nA
2x10^{15} p cm^{-2}	-180 fA	-2.43 nA	-374 nA
5x10^{15} p cm^{-2}	-40 pA	-93 pA	-875 pA
10^{16} p cm^{-2}	-1.4 pA	-1.22 nA	-1.13 nA

Table 4.7: Leakage currents of the proton irradiated 12GaN detectors at an applied bias of 0 V, -50 V and -100 V

reverse bias the leakage currents of the detectors irradiated to 10^{15} pcm^{-2}, 5x10^{15} pcm^{-2} and 10^{16} pcm^{-2} exhibit leakage currents $\sim$ 100 times smaller

than the unirradiated detector. As previously seen with the irradiated thin epitaxial GaN detectors there is no increase in leakage current with increasing proton fluence.

Figure 4.27 shows the I-V plots of the neutron irradiated 12GaN detectors up to a reverse bias of 100 V. The leakage currents of the detectors irradiated

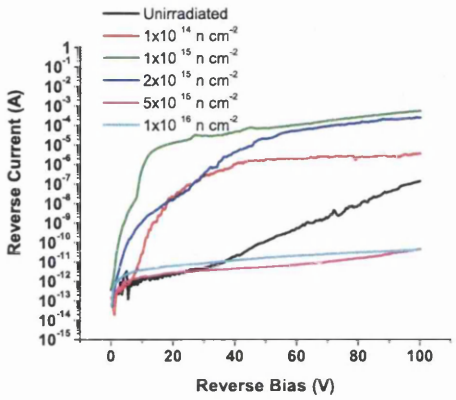

Figure 4.27: I-V curves of the neutron irradiated 12GaN detectors

to 10^{14} ncm^{-2}, 10^{15} ncm^{-2} and 2x10^{15} ncm^{-2} are all larger than that of the unirradiated detector whereas the detectors irradiated to 5x10^{15} ncm^{-2} and 10^{16} ncm^{-2} have much lower leakage currents compared to the unirradiated detector. Table 4.8 gives a comparison of the leakage currents at various bias voltages of the neutron irradiated detectors. A plot of leakage current versus fluence for the proton and neutron irradiated detectors is shown in Figure 4.28 The measured leakage current for each detector is that obtained at a reverse bias of 100 V. The figure again explicitly shows the drastic reduction in leakage current of the detectors irradiated to greater than 5x10^{15} particles cm^{-2} compared to the unirradiated detector.

The leakage currents of the detectors irradiated to 10^{15} ncm^{-2}, 2x10^{15}

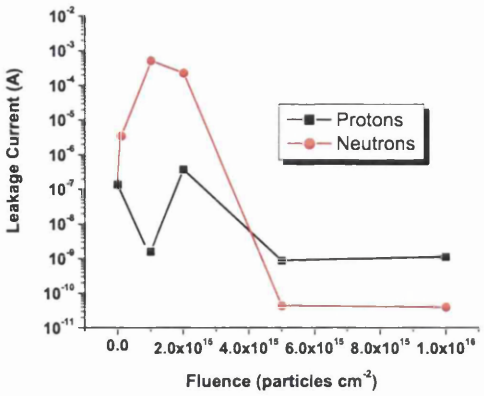

Figure 4.28: Leakage current versus fluence plot of the irradiated 12GaN detectors at a reverse bias of 100 V

	I_L at 0 V	I_L at -50 V	I_L at -100 V
Unirradiated	-360 fA	-114 pA	137 nA
10^{14} n cm^{-2}	-150 fA	-1.8 μA	-3.51 μA
10^{15} n cm^{-2}	-510 fA	-69.5 μA	-515 μA
2x10^{15} n cm^{-2}	-60 fA	-20.1 μA	-234 μA
5x10^{15} n cm^{-2}	-70 fA	-5.48 pA	-44.8 pA
10^{16} n cm^{-2}	-50 fA	-16.3 pA	-40.8 pA

Table 4.8: Leakage currents of the neutron irradiated 12GaN detectors at an applied bias of 0 V, -50 V and -100 V

ncm^{-2} are significantly larger than the leakage currents of the detectors irradiated to corresponding proton fluences. It can be said that in terms of leakage current after irradiation to these fluences neutron damage is more detrimental to detector performance than proton damage. This is in contrast to the leakage current characteristics of the thin epitaxial GaN material

where proton damage is more detrimental to device performance than neutron damage. Figure 4.29 shows the C-V curve of the unirradiated 12GaN detector at a frequencies of 10, 20, 40 and 100 kHz. These C-V curves of

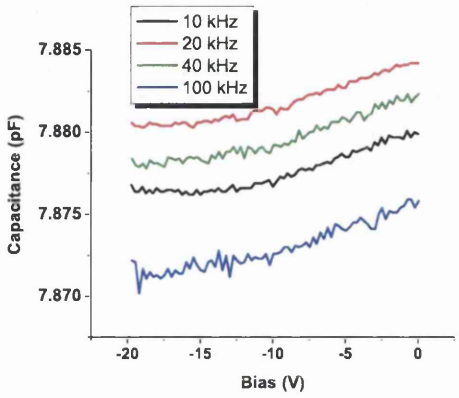

Figure 4.29: C-V data of the unirradiated 12GaN detector

the unirradiated 12GaN detector are similar in shape to the C-V curves of the unirradiated 36GaN and 45GaN detectors. The expected full depletion capacitance for this device is 5 pF. The detector exhibits a relatively flat capacitance of $\sim$ 7.8 pF up to a bias of -20 V suggesting that the device is essentially fully depleted at 0 V.

The CCE versus bias plots for the proton irradiated 12GaN detectors are shown in Figure 4.30. A maximum CCE of 54% is shown by the unirradiated detector at a reverse bias voltage of -140 V. This maximum CCE value is lower than the that of both the unirradiated 36GaN and 45GaN detectors. After irradiation to 10^{15} pcm^{-2} the maximum CCE drops to only 20% at an applied bias of -90 V. The very small leakage currents of the detectors irradiated to 5x10^{15} pcm^{-2} and 10^{16} pcm^{-2} enabled CCE measurements up to large reverse bias voltages. The 5x10^{15} pcm^{-2} irradiated detector exhibits

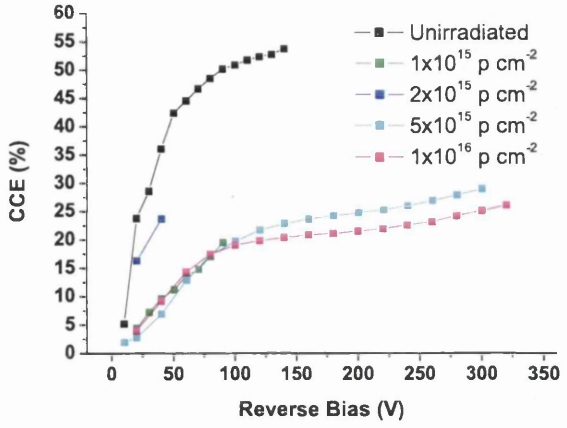

Figure 4.30: CCE versus bias plots of the proton irradiated 12GaN detectors

a maximum CCE of 29% at a bias of -300 V while the maximum CCE of the detector irradiated to 10^{16} pcm^{-2} is 26% at a reverse bias of -320 V.

Figure 4.31 shows the CCE versus bias plots of the neutron irradiated 12GaN detectors. The large leakage currents of the detectors irradiated to 10^{14} ncm^{-2}, 10^{15} ncm^{-2} and 2x10^{15} ncm^{-2} result in CCE measurements being possible only up to bias voltages of -24 V. The maximum CCEs for these detectors are 17% (at -12 V) , 12% (at -6 V) and 16% (at -24 V) respectively. As seen with the proton irradiated detectors, the 12GaN detectors irradiated to neutron fluences of 5x10^{15} ncm^{-2} and 10^{16} ncm^{-2} exhibit extremely low leakage currents enabling CCE measurements up to large bias voltages. The maximum CCE of the 5x10^{15} ncm^{-2} irradiated detector is 26% achieved at -250 V, while the detector irradiated to 10^{16} ncm^{-2} shows a maximum CCE of 20% at an applied bias of -350 V.

Scanning electron microscope (SEM) images of the 12GaN material were taken to establish the exact thickness of the epitaxial layer and the n-GaN buffer layer. The epitaxial and n-GaN buffer regions are not able to be dif-

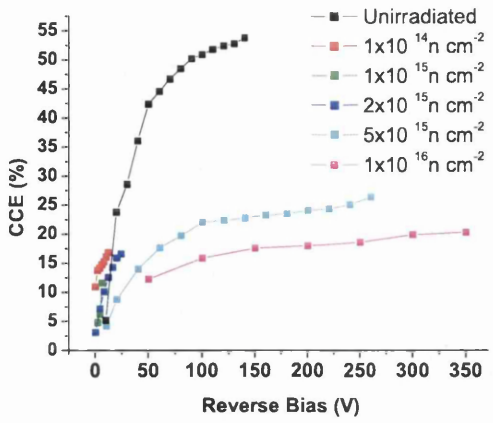

Figure 4.31: CCE versus bias plots of the neutron irradiated 12GaN detectors

ferentiated from each other using an SEM as they have the same crystal structure. However an image taken using an SEM will clearly show the difference between the GaN material and the sapphire substrate. The suppliers of the 12GaN material state that the n-GaN buffer has a thickness of ~ 2.5 μm and the epitaxial layer has a thickness of 12 μm. The SEM image on the

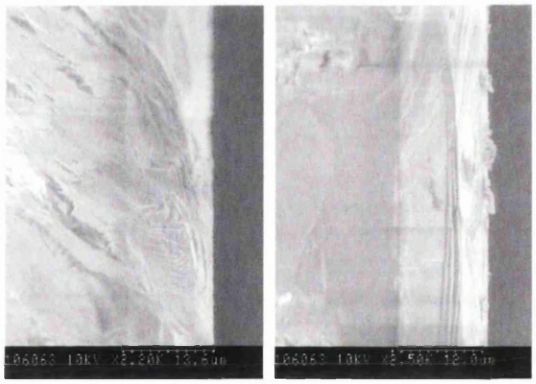

Figure 4.32: Left - SEM image of 12GaN sample. The epitaxial and n-GaN buffer thickness is $\sim$ 13μm, Right - SEM of a second 12GaN sample. The epitaxial and n-GaN buffer thickness in this sample is $\sim$ 8μm

left of Figure 4.32 clearly shows the interface region between the sapphire substrate and the GaN. The thickness of the epitaxial and n-GaN layer is $\sim$ 13 μm. The SEM image on the right of Figure 4.32 was taken from a different sample cut from the 12GaN wafer. In this sample the combined thickness of the epitaxial and buffer layers is only $\sim$ 8 μm. These SEM images suggest that the thickness of the GaN epitaxial and buffer layers vary across the 2 inch wafer. When GaN layers are grown on a two inch sapphire substrate it is common that there is a dome effect from the edge of the wafer to the middle. Samples cut from the middle of the wafer will have thicker GaN layers than samples cut from the edge of the wafer.

The significance of the large variation in thickness of the GaN layers is that the CCE calculations are made assuming a uniform epitaxial thickness of 12 μm across the GaN wafer. It appears that the epitaxial thickness in some samples is significantly less than 12 μm and the actual CCEs of many detectors may be significantly higher than those calculated. This could explain the low maximum CCE of 53% of the unirradiated 12GaN detector compared to the unirradiated thin epitaxial GaN detectors.

4.7 Comparison of GaN Results with Other Materials

The I-V results of the irradiated detectors of all three GaN materials show a non-linear increase in leakage current with increasing fluence. This behaviour is in contrast to I-V data reported on irradiated Si detectors where the damage induced increase in leakage current is dependent on the irradiating particle type and fluence. If normalised to the sensitive volume, V, and to room temperature, the increase in leakage current is strictly proportional

to the 1 MeV NIEL neutron equivalent fluence, Φ_{eq}, and a current related damage constant, α,

$$\Delta I = \alpha \Phi_{eq} V \tag{4.9}$$

At any given temperature and annealing time, the damage parameter α, if normalised to temperature, is a constant independent of Si material type (n- or p- type, CZ, FZ, DOFZ, epi) or irradiating particle type. The same cannot be said of the leakage current behaviour of the irradiated GaN detectors studied in this thesis. Indeed for all three GaN materials, the leakage currents of the most heavily irradiated detectors, those irradiated to 5x10^{15} cm^{-2} and 10^{16} cm^{-2} protons/neutrons are several orders of magnitude lower than the corresponding unirradiated detectors. This type of leakage current behaviour has also been observed in another wide band gap semiconductor, SiC. Bulk, 100 μm thick vanadium doped 4H-SiC Schottky detectors were irradiated to fluences of 5x10^{14} pions cm^{-2} and a non-linear decrease of leakage current with increasing irradiation fluence dependence was observed [84].

The maximum CCEs of the irradiated 36GaN, 45GaN and 12GaN detectors decrease with increasing fluence. It is possible that irradiation of the GaN detectors to high proton and neutron fluences ($\geq$ 5x10^{15} cm^{-2}) result in the generation of deep acceptor states within the forbidden region of the band gap. These acceptor levels trap free electrons reducing the detector leakage current. These acceptor states also trap any free electrons generated by ionising radiation in the material bulk, therefore reducing the CCE of the detector. This compensation of material after irradiation to expected SLHC fluences has also been reported on 25 μm thick epitaxial 4H-SiC detectors [85]. The epitaxial 4H-SiC studied was n-type before irradiation but became intrinsic after irradiation to $\sim$ 10^{15} cm^{-2}.

The most promising radiation hardness results have been reported on CZ, MCZ and epitaxial Si detectors. Detectors fabricated on these materials typically have much lower depletion voltages post-irradiation compared to detectors fabricated on FZ Si and DOFZ. A summary of the maximum CCEs of the 12GaN detectors studied here, DOFZ Si, p-type MCZ Si, epitaxial Si and epitaxial SiC is given in Table 4.9 (irradiations were done using 24 GeV/c protons and 1 MeV NIEL equivalent neutrons). Also shown in the far right hand column of the table is the theoretical maximum number of collected electrons obtainable using a MIP. The p-type MCZ and DOFZ n-in-n devices were 300 μm thick whereas the epitaxial Si devices were only 25 μm thick. As can be seen from the table a larger electric field could be applied to the epitaxial Si than could be applied to the p-type MCZ or the DOFZ n-in-n devices.

Perhaps the most problematic consequence of irradiating Si to large hadron fluences is the increase of charge carrier trapping. Increased trapping leads to a reduction of collected charge therefore lowering the signal to noise ratio of any radiation detector. From Table 4.9 it can be seen that in terms of charge collection efficiency, n-type epitaxial Si is the most radiation hard material currently available. Detectors fabricated on this material exhibit a maximum CCE of 100% before irradiation and 86% after irradiation to 10^{16} ncm^{-2}. However p-type MCZ and DOFZ Si n-in-n detectors may be more suitable for use as tracking detectors at the SLHC as despite their lower charge collection efficiencies after irradiation to large hadron fluences compared to epitaxial Si, more electrons may be collected than 25 μm epitaxial Si. The 12GaN material studied here exhibits the same degree of radiation hardness compared to the epitaxial 4H-SiC reported by Sciortino et al. [85]. The epitaxial 4H-SiC detector irradiated to 10^{16} pcm^{-2} shows a maximum

Detector material	Irradiation fluence	CCE_{MAX} (%)	V@CCE_{MAX} (V)	No. electrons collected from a MIP signal
GaN12	Unirradiated	54	140	421
GaN12	10^{15} p cm^{-2}	20	90	156
GaN12	2x10^{15} p cm^{-2}	24	40	187
GaN12	5x10^{15} p cm^{-2}	29	300	226
GaN12	10^{16} p cm^{-2}	26	320	203
GaN12	10^{14} n cm^{-2}	17	12	132
GaN12	10^{15} n cm^{-2}	12	6	93
GaN12	2x10^{15} n cm^{-2}	17	24	132
GaN12	5x10^{15} n cm^{-2}	26	260	203
GaN12	10^{16} n cm^{-2}	20	350	156
DOFZ Si n-in-n	Unirradiated	100	75	24300
DOFZ Si n-in-n	10^{15} p cm^{-2}	75	800	18225
DOFZ Si n-in-n	4x10^{15} n cm^{-2}	30	850	7290
25 μm epi Si n-type	Unirradiated	100	50	2025
25 μm epi Si n-type	6x10^{15} p cm^{-2}	82	130	1660
25 μm epi Si n-type	10^{16} n cm^{-2}	86	95	1741
MCZ p-type	Unirradiated	100	300	24300
MCZ p-type	10^{15} p cm^{-2}	55	500	13365
MCZ p-type	9x10^{15} p cm^{-2}	8	500	1944
45 μm epi 4H-SiC n-type	Unirradiated	100	250	2295
45 μm epi 4H-SiC n-type	10^{16} p cm^{-2}	25	800	573
45 μm epi 4H-SiC n-type	7x10^{15} n cm^{-2}	23	800	527

Table 4.9: Maximum CCE comparison of irradiated 12GaN detectors, DOFZ, MCZ, epitaxial Si and SiC detectors (DOFZ data [86], epi Si data [87], MCZ data [88], epi 4H-SiC data [85])

CCE of 25% compared to a maximum CCE of 26% of the 12GaN detector irradiated to the same proton fluence. However this maximum CCE of

the irradiated 12GaN detector was achieved at a lower bias voltage than the maximum CCE of the irradiated epitaxial 4H-SiC detector (-300 V compared to -800 V).

4.8 Summary and Future Possibilities

The macroscopic properties and radiation hardness of three GaN wafers were studied in this chapter. The two thin, 2.5 μm thick, epitaxial GaN wafers, 36GaN and 45GaN, obtained from Tokushima University show low leakage currents before irradiation and the 45GaN material exhibits a maximum CCE of 97% at an applied bias of -12V. Both the 36GaN and 45GaN detectors exhibit a non-linear increase in leakage current with increasing irradiation fluence. The 45GaN material can be said to be more radiation hard than the 36GaN material and the detector irradiated to the largest neutron fluence, 10^{16} ncm^{-2}, has a maximum CCE of $\sim$ 40%. The first results of the radiation hardness properties of thicker epitaxial GaN material were also reported in this work. Detectors fabricated on 12 μm epitaxial GaN obtained from Lumilog also exhibited a non-linear increase in leakage current with increasing irradiation fluence. The unirradiated 12GaN detector has a maximum CCE of 54% pre-irradiation and a maximum CCE of 26% and 20% after irradiation to 10^{16} pcm^{-2} and 10^{16} ncm^{-2} respectively. These CCE results are similar to those reported on irradiated detectors that were fabricated on another wide band gap material, epitaxial 4H-SiC, but are not as promising as the results reported on irradiated epitaxial Si detectors.

It is also important to consider how the SLHC operating conditions affect the macroscopic properties of any detector. Over the operational lifetime of the SLHC (5-10 years) there will be significant periods where the beam will

be shut off and the detectors will anneal at room temperature. Silicon detectors generally anneal in a detrimental manner with time, resulting in a change in the effective doping concentration and a significant increase in the full depletion voltage. Detailed research is required into the annealing characteristics of unirradiated and irradiated GaN detectors in order to further assess the suitability of GaN as a radiation hard detection medium.

The main challenge for GaN is the availability of high quality thick SI epitaxial layers. Currently, SI epitaxial layers are only commercially available with thicknesses ≤ 12 μm. The purest GaN material is grown by the MOCVD method however it is not currently feasible to growth thick epitaxial layers using this method because of the slow rate of growth. At Lumilog, it takes 24 hours to grow a 12 μm thick epitaxial layer of GaN onto a sapphire substrate. However, free-standing conductive GaN wafers grown by HVPE are now available. This growth method can achieve growth rates of up to 150 μm/h with laser assisted separation of the GaN film from the sapphire substrate. Commercial suppliers, such as Lumilog, are now offering 400 μm thick two inch wafers of n-type GaN and similar SI free standing wafers will be soon be available.

A further limitation of GaN is, as with the majority of compound semiconductors, there is a large density of as-grown defects. Dislocation densities of 10^{10} cm^{-2} are common, however by fine tuning the growth parameters dislocation densities as low as 10^{6} cm^{-2} have been reported [89]. In order to improve the intrinsic material properties of GaN, for example the hole mobility, the dislocation density must continue to be reduced. It should be remembered that GaN is a relatively young material in comparison with the current semiconductor of choice Si. It is possible that with continuing improvements in growth technology that GaN will be more suitable than Si for

certain applications.

Chapter 5

Etching Studies of GaN

5.1 Introduction

The etching of GaN may be carried out using several techniques which can be broadly classified as either wet or dry etching. In this thesis the 36GaN, 45GaN and 12GaN materials were dry etched in an Inductively Coupled Plasma (ICP) etch tool in order to realise ohmic contacts to the n-GaN buffer layer. This chapter describes the various processes that are commonly used to wet etch GaN and outlines the ICP etch parameters used to dry etch the GaN materials studied in this thesis. I-V, C-V and CCE measurements were performed on the ICP etched GaN samples and the results compared to those made on the devices studied in Chapter 4.

5.2 Motivation for Etching GaN

Etching of GaN and its related ternary alloys plays an essential role in the fabrication of blue, green and ultraviolet LEDs and laser diodes. In this work dry etching techniques were used to remove epitaxial GaN material in order

to define ohmic contacts onto the n-GaN buffer layer. This was done for two main reasons:

1. To make a proper electrical contact to the n-GaN buffer producing better electric field definition compared to the detectors studied in Chapter 4.

2. To produce an Ohmic/Schottky detector, enabling extraction of the ideality factor and Schottky barrier height from I-V characteristics.

In Chapter four, Schottky contacts were made to the SI epitaxial GaN and a further contact was made to the n-GaN buffer using conductive silver paint (see Figure 4.4). This structure enabled a potential difference to be applied between the Schottky contacts on the surface of the epitaxial GaN and the n-GaN buffer. However, this detector structure is not ideal since the electric field and the associated charge path within the device are not well defined. It was thought that fabricating a well-defined ohmic contact to the n-GaN buffer layer would improve the detector performance resulting in an increased CCE compared to the devices discussed in Chapter 4.

The second reason for etching the SI epitaxial GaN layer and fabricating an ohmic contact to the n-GaN buffer layer was to realise an Ohmic/Schottky detector. The ideality factor and barrier height of the Schottky contact and also the carrier concentration of the SI epitaxial GaN layer could then be extracted from the I-V and C-V curves of the etched device.

Development and Characterisation of Ohmic Contacts

Attempts were made at fabricating ohmic contacts to the surface of the three SI epitaxial GaN materials in order to measure fundamental material parameters of the 36GaN, 45GaN and 12GaN SI epitaxial layers. Ohmic contacts of

dimension 200 μm square were placed at the four corners of square samples of dimension 5 mm by 5 mm cut from the three GaN wafers. Hall measurements and the van der Pauw technique were to be used to evaluate the sheet carrier density, n_S, the sheet resistance, R_S, the electron mobility, μ_n, the carrier concentration, N_D, and the bulk resistivity, ρ, of the SI epitaxial layers of the 36GaN, 45GaN and 12GaN materials. Obtaining values of the electron mobility for the three GaN materials was of particular interest as previous studies have shown that the electron mobility of SI epitaxial GaN is as low as 20-40 cm^2/Vs [90]. This value is much lower than the typical electron mobility of conductive GaN epilayers which is $\sim$ 1000 cm^2/Vs (see Table 4.2). Standard photolithographic techniques were used to define the squares at the corners of the samples. A Ti/Au/Pd/Au multilayer of thickness 20 nm/60 nm/40 nm/50 nm was evaporated using a Plassys 450 MEB evaporator and the metalised samples annealed for 30 seconds at 850°C in a rapid thermal annealer (RTA). This metal multilayer, annealing time and temperature were chosen after reviewing the relevant literature [91], [92] and taking into consideration the available metals. The best ohmic contacts, exhibiting the lowest contact resistance, fabricated on GaN consist of a multi-layer of Au, Mo and Ni. However Mo was not available in the Plassys 450 MEB evaporator therefore the Ti/Au/Pd/Au multilayer was evaporated instead.

Transmission line measurement (TLM) structures of 100 μm, 200 μm and 300 μm squares were also patterned using photolithography onto samples diced from the 36GaN, 45GaN and 12GaN wafers in order to establish the contact resistance. The same metal multilayer, annealing temperature and time used to form the contacts for the van der Pauw were also used to form the contacts for the TLM structures. The distances between the squares were 1, 2, 4, 6, 8, 10, 12, 14, 16, 18, 20 , 30, 40 and 50 μm. Images of

100 μm square TLM structures before and after annealing are shown in Figure 5.1. TLM involve performing I-V measurements of adjacent square pads

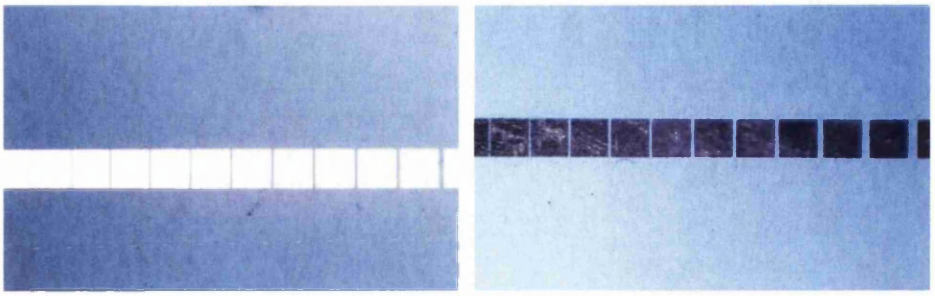

Figure 5.1: 100 μm square TLM structures before annealing (left) and after annealing (right)

and calculating the sheet resistance using Ohm's law. As the distance between adjacent square pads increases then the sheet resistance also increases (a full description of the TLM technique may be found in [93]). A plot of measured sheet resistance versus gap spacing with a linear fit made to the data yields the intersection point of the y-axis with the linear fit as twice the contact resistance. Typically the contact resistance depends on the carrier concentration N_D, the annealing time and temperature, and the measurement temperature. It may also be dependant on interface effects between the GaN material and the metal multi-layer.

Unfortunately, on all three GaN materials, the annealed TLM contacts exhibited Schottky diode behaviour with a slow breakdown of the barrier. Figure 5.2 shows the I-V characteristics before and after annealing of 100 μm and 200 μm square pads fabricated on the 12GaN material. The distance between the pads is 50 μm. The I-V curves clearly show that for both pad sizes the conductivity does improve after the annealing treatment however the contacts are not ohmic after annealing at 850^{o}C for 30 seconds. Similar

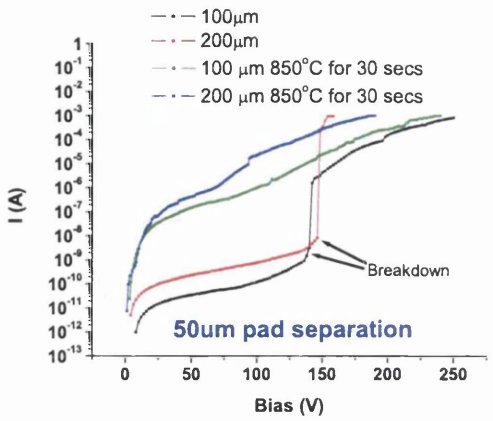

Figure 5.2: I-V curves before and after annealing at 850°C for 30 seconds of 100 μm and 200 μm square pads with a gap distance of 50 μm between adjacent pads

Schottky diode like I-V behaviour was also seen for TLM structures with various gap spacings for all three GaN materials. It can be assumed that the low carrier concentration of the SI GaN materials ($\leq 10^{16}$ cm^{-3}) prevents the formation of ohmic contacts. Studies have shown that it is extremely difficult to achieve contact resistivities $< 10^{-2}$ cm $^{-2}$ for GaN epilayers with a carrier concentration of 10^{17} cm^{-3} [91], [92]. Hall measurements and the van der Pauw technique rely on good ohmic contacts in order to extract the relevant material parameters. Since it was not possible to fabricate low resistance ohmic contacts on the 36GaN, 45GaN and 12GaN materials, Hall and van der Pauw measurements could not be performed.

5.3 Wet Etching of GaN

Wet chemical etching is typically fast and highly selective with minimal damage to the remaining material. However, wet etching is often difficult to control, isotropic and has poor resolution thereby limiting the critical dimension

of the etched features. Wet etching of GaN has generally been unsuccessful due to its low chemical reactivity, believed to be due to its wide band gap, and its high bonding energy [94]. Only a few chemicals have been found to etch GaN (see Table 5.1). A significant limitation of wet-etching is that it

Chemical	Temperature (^{O}C)	Etched Planes	Etch Rate (nm/min)
Potassium hydroxide (KOH) molten	150-247	$\{10\bar{1}0\}$, $\{10\bar{1}\bar{1}\}$	3-2300
10%-50% KOH in ethylene glycol	90-182	$\{10\bar{1}0\}$	1.5-1300
6M KOH in water	30-80	$\{10\bar{1}n\}$	1-50
50% KOH in water	83	none	< 1nm
Phosphoric acid (H_3PO_4)	108-195	$\{10\bar{1}2\}$, $\{10\bar{1}3\}$	13-3200
20% NaOH in ethylene glycol	178	none	670-1000
Photo-enhanced 0.5M KOH in water	20	-	400

Table 5.1: Etched planes and etch rates of GaN for various chemicals [95]

can only be used to etch GaN material that has a nitrogen polar surface [96]. It is believed that KOH can dissolve the initial oxide layer on the surface of a $\{000\bar{1}\}$ Ga polar surface but cannot attack the remaining N-terminated atoms because of the large repulsion between the OH^- ions and three occupied dangling bonds of nitrogen. In contrast, a $\{000\bar{1}\}$ N-terminated GaN surface has only one upward dangling bond and so it is possible for the OH^- ions to attack the back bonds of the Ga atoms. Studies have also shown that the etching process is enhanced along GaN dislocations because the atoms around these dislocations have a lower bonding energy [97].

5.4 Dry etching of GaN

As a consequence of the limited success of the wet etching of GaN there has been a significant amount of research into the dry etching of GaN. The

most developed GaN etching techniques are RIE and ICP etching, details of which were given in Chapter 2. Various plasma chemistries have been used to etch GaN, the most successful being halogen based, using chlorine (Cl_2, $SiCl_4$, BCl, $CHCl_3$) [98]-[100], fluorine (SF_6, CHF_3, CCl_2F_2, C_2ClF_5) [101], [102], iodine (ICl, BI_3) [103] and bromine (IBr, BBr_3) [103]. All are typically combined with a physical etching component such as Ar, N_2, H_2 or O_2.

The physical etching component of the plasma is used to avoid redeposition of the etched material and to increase the anisotropy of the etch. The etch rate is a linear function of chamber pressure and plasma power, with the etch rate decreasing with increasing chamber pressure and increasing with increased plasma power. The etch rate is also dependent on the flow rate of the reaction gas(es). Plasma etching has a significant influence on the electrical characteristics of the resulting metal/GaN contacts because it can not only remove surface oxide and GaN crystal layers but it can also introduce a significant degree of structural damage [105]. Non-stoichiometric surfaces may also be created by the preferential removal of either Ga or N atoms by the etchant gases. Under extreme conditions of high ion energy deep acceptor states may be created, reducing the carrier mobility and increasing the sheet resistance of n-type GaN [103].

In this thesis, an ICP reactor was used to etch the 36GaN, 45GaN and 12GaN material. Wet etching of the three GaN epilayers was considered unsuitable for the reasons previously discussed. The GaN samples were etched at the EPSRC National Centre for III-V Technologies, Sheffield [104] in an ICP Plasma Lab System 100 supplied by Oxford Plasma Technologies. The gases used were $SiCl_4/Cl_2$ mixed with Ar. Table 5.2 describes the ICP parameters used to etch the three SI epitaxial GaN materials. The Ar gas was required to ensure vertical sidewalls of the etched GaN material.

Parameter	Value
$SiCl_4$ flow rate (sccm)	1.5
Cl_2 flow rate (sccm)	15
Ar flow rate (sccm)	4
ICP Power (W)	450
RF Power (W)	150
Chamber pressure (mTorr)	4
He cooling pressure (Torr)	8
Etch rate (nm/min)	180

Table 5.2: ICP etch parameters used for 36GaN, 45GaN and 12GaN materials

Samples of dimension 10 mm by 5 mm were cut from the 36GaN, 45GaN and 12GaN wafers. Photolithographic techniques using S1818 and AZ4562 resist (see Section 2.2.1) were used to pattern ring structures onto the samples. These ring structures have the same dimensions as the guard rings fabricated on the GaN material in Chapter 4 (see also Figure 5.3). The 36GaN and 45GaN samples that were to be etched were patterned using AZ4562 resist spun at 1500rpm, giving a resist thickness of $\sim$ 15 μm. The 12GaN sample that was etched was patterned using S1818 resist as this was the only resist available in the clean room at Sheffield University that was suitable for etching. The samples were etched in the ICP etch tool until the epitaxial layer was removed and the n-GaN buffer layer was reached. Due to the Ar present in the etch gas the selectivity of the S1818 photoresist and GaN was only 1:2. This meant that to etch the 12GaN material six consecutive etches were performed as fresh S1818 photoresist had to be spun onto the GaN material once the old photoresist mask had been etched away.

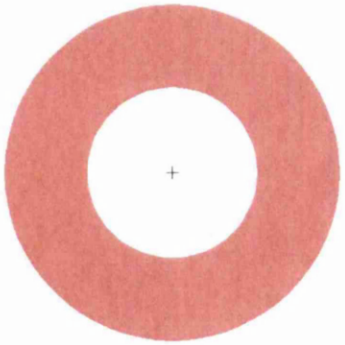

Figure 5.3: L-Edit image of the ring structure patterned onto the three GaN materials for subsequent ICP etching. The ring width is 500 μm.

5.5 ICP Etching Results

5.5.1 Proof of Principle - ICP etched 45GaN sample

Preliminary tests were carried out on a sample cut from the 45GaN material. Figure 5.4 shows an image of an etched 45GaN sample taken using a WKYO NT1100 surface profiler. The profiler uses white light interferometry to measure the surface features on a sample. The bottom image of Figure 5.4 is a 3D plot of the etched sample while the top image is a line trace of the sample in the x-direction. It is clearly seen from the line trace that the average etch depth is $\sim$ 3.5 μm. The manufacturers of the 45GaN material report that the epitaxial thickness is 2.5 μm and the n-GaN buffer is of similar thickness. An etch depth of 3.5 μm implies that there is $\sim$ 1.5 μm of n-GaN buffer material remaining.

The etched samples were subsequently patterned using S1818 resist with pad and guard ring structures as in in Chapter 4. The pad diameter was 1 mm, the guard ring 500 μm wide and the gap distance between the pad and guard ring was 50 μm. Contacts were formed by depositing 50 nm/250 nm

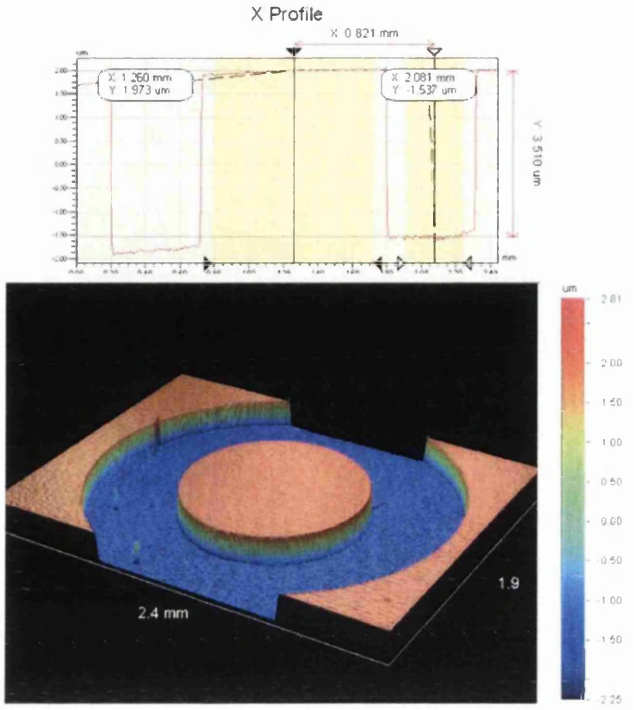

Figure 5.4: Bottom - 3D plot of the etched region on the 45GaN material. Top - A line plot in the x-direction of the etched sample. The measured etch depth is ~ 3.5 μm

of Pd/Au using the Plassys 450 MEB evaporator. This formed a Schottky pad contact to the SI epitaxial GaN and due to the highly conductive nature of the n-GaN buffer layer, an Ohmic ring contact to the n-GaN buffer layer. Before metalisation samples were de-oxidised in HCl. Figure 5.5 is a picture of the bonded ICP etched 45GaN device.

I-V, C-V and CCE measurements were made on the ICP etched 45GaN detector. All three techniques were performed with the bias applied to the pad contact and the ground connection made to the etched ring contact. The I-V plot of the ICP etched 45GaN detector shows characteristics typical of

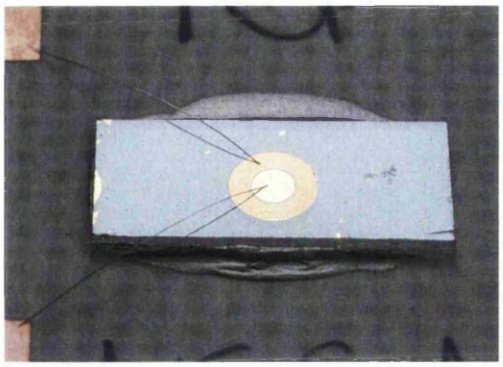

Figure 5.5: Bonded ICP etched 45GaN detector.

an Ohmic/Schottky detector (see Figure 5.6).

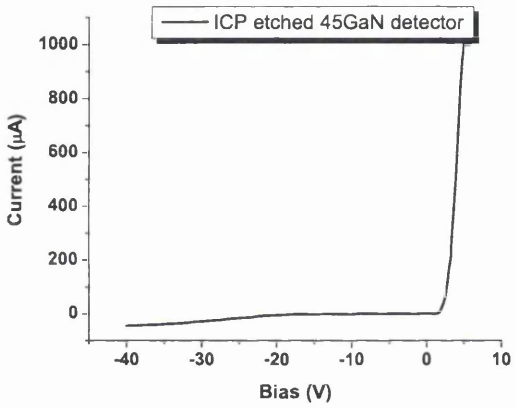

Figure 5.6: Forward and reverse I-V characteristics of the ICP etched 45GaN detector

Figure 5.7 shows the reverse bias I-V plots of the ICP etched 45GaN detector compared to the unetched 45GaN detector studied in Chapter 4.

At small reverse bias voltages the leakage current of the unetched GaN device is similar in magnitude to that of the ICP etched 45GaN device (region a). As the bias voltage increases the leakage current of the ICP etched device

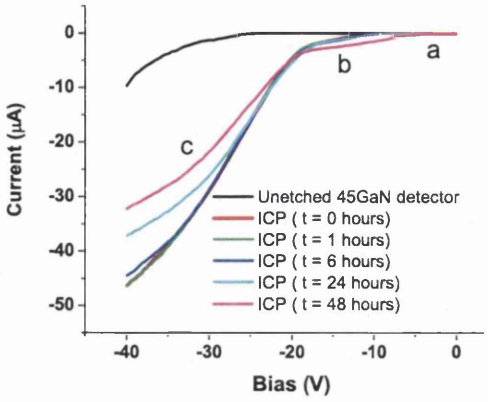

Figure 5.7: I-V curves of the ICP etched and the unetched 45GaN detectors. Also shown are the I-V plots of the ICP etched detector after 1, 6, 24 and 48 hours in the dark.

grows larger than that of the unetched device (region b). This is ascribed to the depletion region spreading laterally, since there is no guard ring on the SI 45GaN surface of the ICP etched device, as well as vertically downward from the 1 mm circular pad. At even larger reverse bias voltages the leakage current of the ICP etched device grows much larger than the unetched device (region c). This large increase in leakage current is probably due to surface leakage as a consequence of the ICP etching. This surface leakage current could be minimised if a guard ring was employed on the surface of the SI 45GaN. A plot of leakage current at a reverse bias of 40 V versus time detector is kept in the dark of the ICP etched device is shown in Figure 5.8.

The Schottky barrier height (SBH) and ideality factor can also be extracted from the I-V characteristics of an Ohmic/Schottky diode. These parameters are evaluated using the ideal diode equation governed by thermionic emission theory (see Equation 3.27). A linear fit to the data points in the forward small voltage region, where series resistance can be neglected, gives

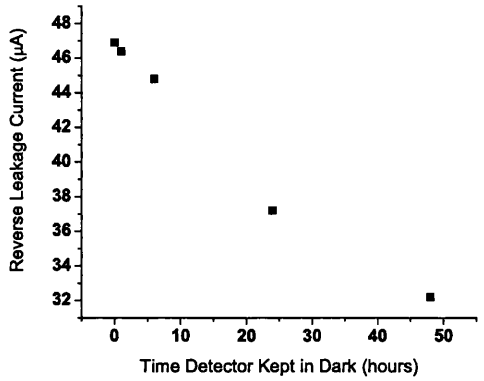

Figure 5.8: Evolution of the reverse leakage current with time the ICP etched detector was kept in the dark. All leakage current values were obtained at a reverse bias of 40 V.

the ideality factor,

$$n = \frac{q}{ckT} \tag{5.1}$$

where c is the gradient of the slope of the $ln(J)$ versus V_F graph. The value J_S is derived from the ln(J) intercept of the fitted line at V = 0 and the barrier height ϕ_b found using Equation 3.29.

Figure 5.9 shows the lnJ versus forward bias plot of the ICP etched 45GaN detector. The measured ideality factor and SBH calculated using the fit to region 1 of the data is 0.94 and 1.06 (+/- 0.02) eV respectively. This measured SBH is in reasonable agreement with the theoretical SBH of a Pd/GaN diode which is 1.02 eV while the calculated value of the ideality factor is in general agreement with those reported on Schottky diodes fabricated on n-GaN [106], [107], [108].

The C-V characteristics at 10 kHz of the ICP etched 45GaN detector at

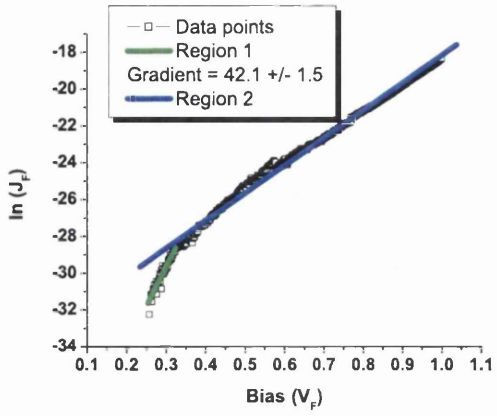

Figure 5.9: $\ln J_F$ *versus* V_F *plot of the ICP etched 45GaN detector.*

room temperature are shown in Figure 5.10. This curve is that typical of a

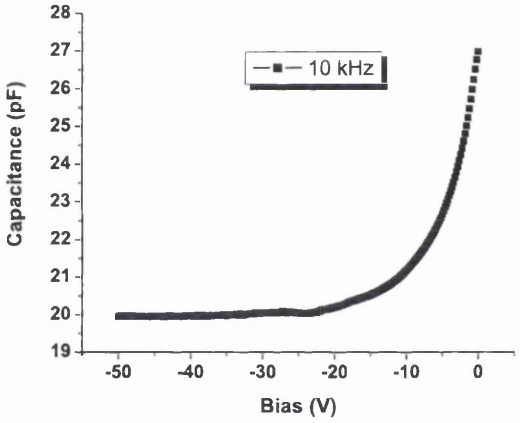

Figure 5.10: C-V plot of the ICP etched 45GaN detector at 10 kHz

planar diode structure and the equation

$$C = \frac{\epsilon \epsilon_0 A}{d} \tag{5.2}$$

where C is the capacitance, ϵ is the dielectric constant for GaN , ϵ_0 is the dielectric constant of free space, A is the contact area and d is the depletion

thickness, can be used to evaluate the depletion depth from the measured capacitance. The voltage at which the C-V curve flattens gives the full depletion voltage of the device. A depletion depth of 2.5 μm gives a theoretical capacitance of 25pF while the measured capacitance is $\sim$ 20 pF. The calculation was made taking the area to be the that of the circular pad contact fabricated on top of the SI GaN layer.

The $1/C^2$ versus V plot for the ICP etched 45GaN detector is shown in Figure 5.11. The gradient of this plot was found to be 1.420 $F^{-2}V^{-1}$

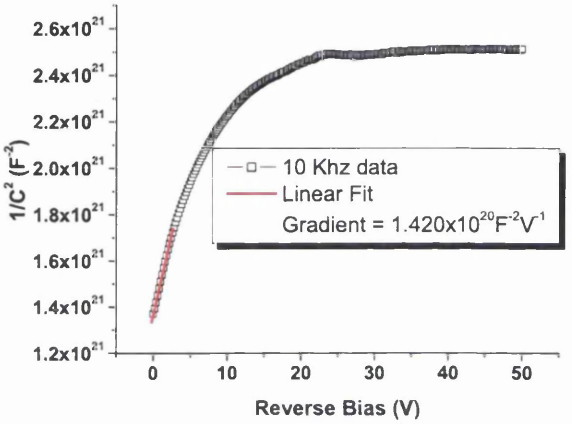

Figure 5.11: $1/C^2$ versus V plot of the ICP etched 45GaN detector

giving the carrier concentration of the SI GaN layer as 1.8x10^{15} cm^{-3} using Equation 4.8. This measured value of the carrier concentration is close to that of 1.4x10^{15} cm^{-3} reported by Sellin. et al. [109] on similar 2 μm thick SI epitaxial GaN grown by Tokushima University.

The CCE was measured to deduce changes caused by the ICP etching. Figure 5.12 shows the CCE versus bias plots for the ICP etched 45GaN detector and the unetched 45GaN detector. For all bias voltages the CCE of the ICP etched device is larger than the unetched device. Both devices

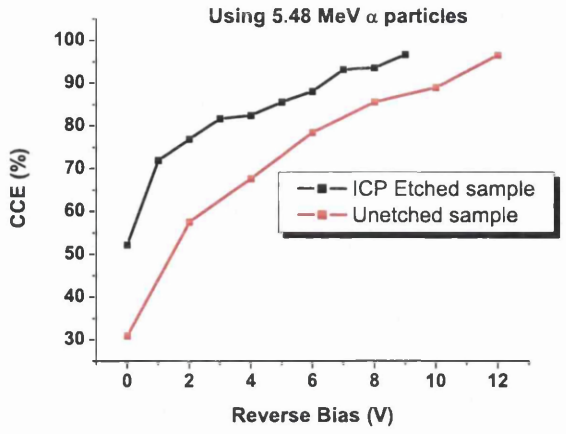

Figure 5.12: CCE versus bias curves for the ICP etched and unetched 45GaN devices

achieve a maximum CCE of 97%, however the etched device attains this CCE at a lower applied bias voltage than the unetched device (-9 V compared to -12 V). The CCE improvement of the etched 45GaN detector may be explained by better definition of the electric field within this device compared to the unetched detector.

5.5.2 Results of ICP etched 36GaN and 45GaN samples

After completion of the preliminary tests of the ICP etched 45GaN sample, a new mask design was produced for further experiments on etched 36GaN, 45GaN and 12GaN samples. This new mask included a further guard ring to be realised on the surface of the SI GaN to reduce the effect of etch damaged sidewalls. Figure 5.13 shows a metalised ICP etched 12GaN detector with a pad and guard ring fabricated on the SI epitaxial GaN surface and an etched ring contact to the n-GaN buffer. The pad diameter is 0.5 mm, there is a

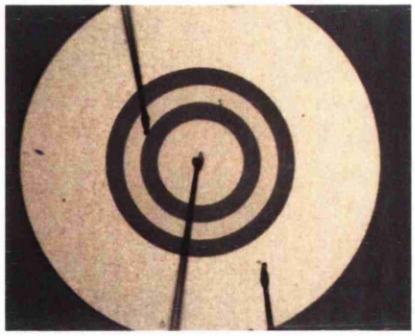

Figure 5.13: Pad, guard ring and etched ring structures fabricated on the ICP etched 12GaN material

100 μm gap between the pad and guard ring, the guard ring is 100 μm wide and there is a further 100 μm gap between the guard ring and the etched ring. The etched ring is 500 μm wide as was the case with the original mask design for ICP etching. Contacts were formed by evaporating 50 nm/200 nm of Pd/Au. A second set of 36GaN and 45GaN samples were metalised by evaporating 100 nm/150 nm of Ti/Au. This enabled a comparison of the ideality factors and measured SBHs between the Pd Schottky devices and the Ti Schottky devices. I-V, C-V and CCE measurements were made of the ICP etched samples with the pad and guard ring kept at the same potential and the etched ring contact connected to ground.

The etched 36GaN and 45GaN devices metalised with Ti contacts exhibited Schottky like forward bias I-V characteristics until breakdown of the contact occurred at $\sim$ 8 V (see Figure 5.14). The reason for this behaviour is not known however it could be attributed to an insulating interface formed between the GaN and the Ti metal. It was not possible to extract the ideality factor and SBH values from these detectors due to the poor quality of the Ohmic contact.

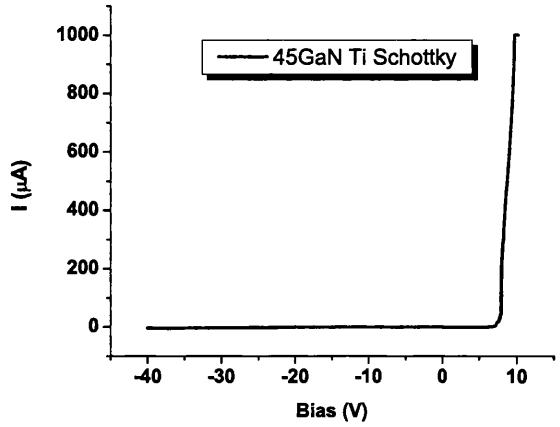

Figure 5.14: I-V characteristics of the ICP etched 45GaN detector with Ti contacts. The detector exhibits Schottky/Schottky instead of the desired Ohmic/Schottky behaviour.

The ICP etched 36GaN and 45GaN detectors metalised with Pd contacts exhibited good Ohmic/Schottky I-V characteristics (see Figure 5.15). Figure

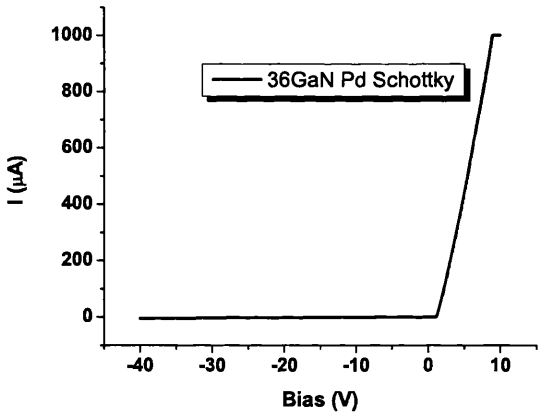

Figure 5.15: I-V characteristics of the ICP etched 36GaN detector with Pd contacts.

5.16 shows the lnJ_F versus forward bias plot of the ICP etched 36GaN Pd

Schottky detector. The calculated ideality factor was 0.42 and the measured

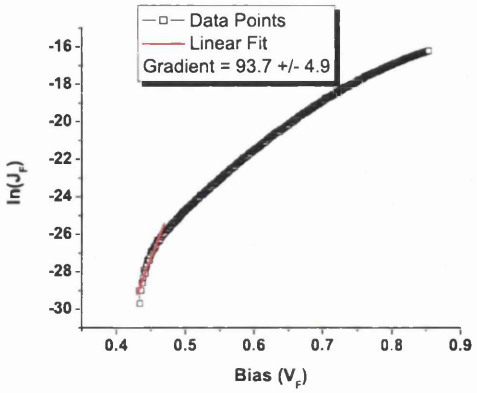

Figure 5.16: $\ln J_F$ *versus* V_F *plot of the ICP etched 36GaN detector. Pd metal was used to form the Schottky contact.*

SBH was 1.78 eV. This value for the ideality factor is very low (should be between 1 and 2) while the barrier height is very large (theoretical value of ϕ_{Bn} = 1.02 eV). The measured carrier concentration calculated from a plot of $1/C^2$ against V of the ICP etched 36GaN detector is 1.33x10^{15} cm^{-3}.

From Figure 5.17 it can be seen that the ICP etched 36GaN detector exhibits much improved CCE values compared to the unetched 36GaN detector. The maximum CCE of the etched detector is 76% at an applied bias of -8 V whereas the maximum CCE of the unetched detector is 71% at an applied bias of -28 V. This improvement in the CCE of the ICP etched 36GaN device is again attributed to better definition of the electric field within the SI epitaxial GaN material.

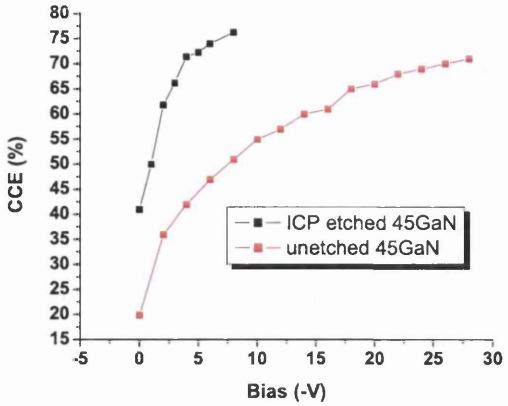

Figure 5.17: Comparison of the CCE versus bias plots of the ICP etched and unetched 36GaN detectors

5.5.3 ICP etched 12GaN Results

Figure 5.18 shows an image taken using the WYKO NT1100 surface profiler of the ICP etched 12GaN sample. The line trace taken in the x direction of the sample shows an average measured etch depth of $\sim$ 12.5 μm. The manufacturers of the 12GaN material state that the SI epitaxial GaN is 12 μm thick so it was assumed that the sample has been etched down to the n-GaN buffer layer. To verify that the n-GaN buffer had indeed been reached two probes were placed on the etched region and a small bias applied. Due to the conductive nature of the n-GaN region applying a small bias between the two probes should result in the Keithley 237 registering a μA current (this was the case for the ICP etched 36GaN and 45GaN samples). However, the current recorded by the Keithley 237 was $\sim$ 100 pA and a similar current was found when two probes were placed on the surface of the SI GaN. This indicated that either the n-GaN buffer was not very conductive, the SI GaN had not been fully etched or that the sample had been etched not only through the SI

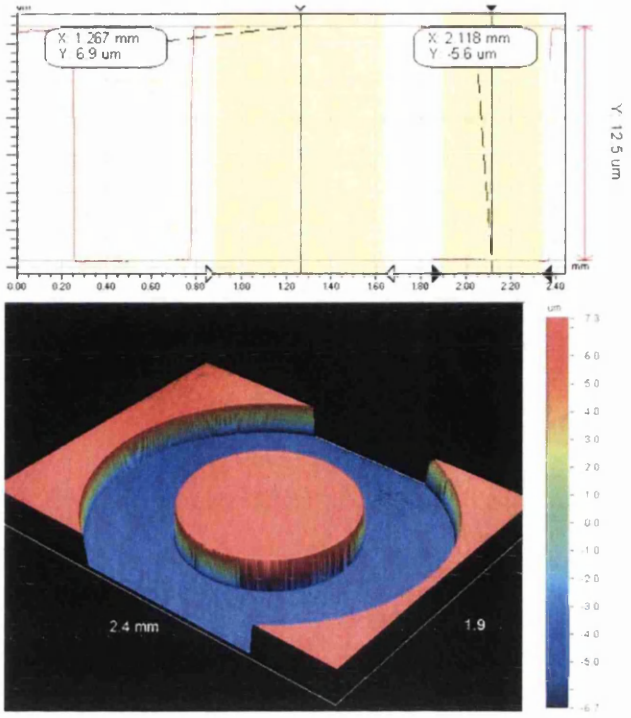

Figure 5.18: Bottom - 3D plot of the etched region on the 12GaN sample. Top - A line plot in the x-direction of the etched sample. The measured etch depth is ~ 12.5 μm

GaN but also through the n-GaN buffer layer and into the sapphire substrate. The latter is more likely since it was established in Section 4.6.3 that the SI GaN epitaxial layer was not uniformly 12 μm thick across the wafer. Indeed the SEM image of one of the 12GaN samples (see Figure 4.32) shows the SI epitaxial GaN and n-GaN buffer having a combined epitaxial thickness of ~ 8 μm. Despite the possibility that the n-GaN buffer had been fully etched the 12GaN sample was metalised and the detector characterised through I-V, C-V and CCE measurements. The forward and reverse I-V properties of the etched sample are shown in Figure 5.19. The detector shows Schottky

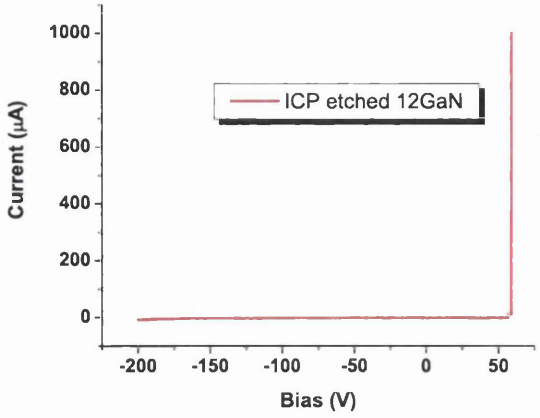

Figure 5.19: I-V characteristics of the ICP etched 12GaN sample

behaviour for both voltage polarities indicating that the etched ring contact is made with the sapphire substrate rather than the n-GaN buffer. A log plot of the reverse current versus reverse bias is shown in Figure 5.20. The

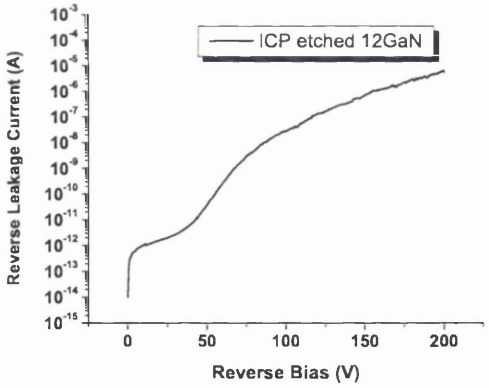

Figure 5.20: Reverse leakage current characteristics of the ICP etched 12GaN sample

lack of a good quality ohmic contact meant that the ideality factor and SBH

of the Pd Schottky contact could not be extracted. C-V characteristics of the ICP etched 12GaN detector are shown in Figure 5.21. The capacitance essentially remains constant up to an applied reverse bias of 200 V.

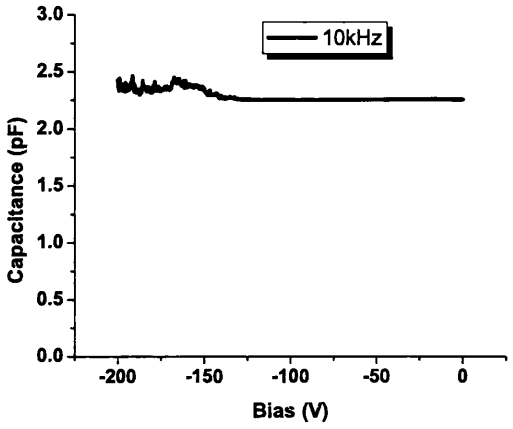

Figure 5.21: C-V characteristics of the ICP etched 12GaN sample

CCE measurements of the ICP etched 12GaN detector were performed using 5.48 MeV α particles. The CCE versus bias plot for the etched 12GaN detector is shown in Figure 5.22 and compared to the CCE data obtained from the unetched 12GaN device. The ICP etched 12GaN device exhibits improved CCE properties in comparison to the unetched 12GaN device. The CCE of the etched device is larger than the CCE of the unetched device at all bias voltages. The maximum CCE of the etched detector is 68% achieved at a bias of -80 V whereas the unetched detector has a maximum CCE of 54% at a bias of -140 V. The CCE data suggests that better definition of the electric field within the SI material increases the CCE of the detector. However taking into consideration the SEM images of the 12GaN material (see Figure 4.29), it could also be the case that the SI epitaxial GaN region is thicker in the ICP etched 12GaN sample than in the unetched sample. If the

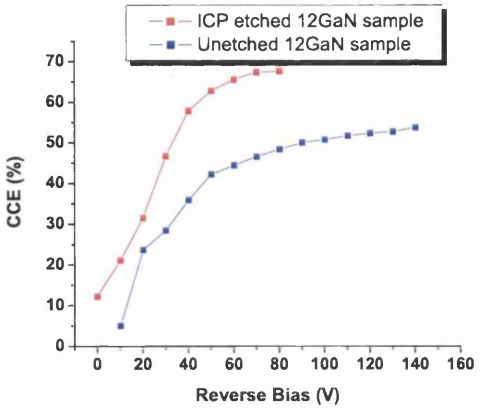

Figure 5.22: CCE versus bias characteristics of the ICP etched and unetched 12GaN samples

etched 12GaN material had a thicker SI epitaxial region than the unetched material then more charge would be deposited by an incident α particle in the SI epitaxial GaN region and the CCE would appear higher.

Due to time constraints the etched devices were not irradiated therefore there is no data on whether or not the revised detector geometry resulted in increased radiation hardness.

5.6 Summary and Conclusions

The geometry of the detectors studied in Chapter 4 was not the optimal configuration for operation as an ionising radiation detector. These detectors had contacts made to the n-GaN buffer layers by coating the side of the sample with silver conductive paint. By using ICP etching it was possible to produce patterned contacts to the n-GaN buffer layer of the 36GaN, 45GaN and 12GaN materials.

Well-defined ohmic ring contacts were realised onto the n-GaN buffer

layers and Schottky pad contacts were fabricated on the surface of the SI epitaxial GaN layers. The ideality factor and SBH of the Schottky contact as well as the carrier concentration were extracted from I-V and C-V characteristics of ICP etched devices. The carrier concentration of the SI epitaxial 36GaN material was found to be 1.33×10^{15} cm^{-3} while the carrier concentration of the SI epitaxial 45GaN material was 1.8×10^{15} cm^{-3}. For all three GaN materials the ICP etched devices exhibited superior charge collection efficiencies than the unetched devices. This is attributed to better definition of the electric field within the etched devices resulting in improved charge transport. The results extracted from the ICP etched detectors strengthen the viewpoint that for GaN to be extensively used as an ionising radiation detector it must be possible to define contacts to both the front and back of GaN material. For this to occur, the detector material must either be $\sim$ 300 μm thick free standing GaN or alternatively epitaxial GaN grown on a conductive substrate such as Si or SiC.

Chapter 6

Defect Characterisation of Irradiated GaN Detectors

6.1 Introduction

Defects, both as-grown and radiation induced, generally degrade the performance of a semiconductor detector. Several techniques have been developed aimed at investigating the microscopic defects that determine the macroscopic properties of a semiconductor device. Of particular interest is the correlation between the radiation induced macroscopic deterioration effects of a detector and the microscopic defects responsible for this degradation in performance. Common techniques that are used in defect spectroscopy are; deep level transient spectroscopy (DLTS), thermally stimulated current (TSC), photoluminescence (PL), microwave absorption (MWA), contact photoconductivity (CPC) and transient current technique (TCT). The DLTS method is the most sensitive for obtaining knowledge on specific defect concentrations, their energy level and capture cross sections. However, a major shortcoming of the DLTS technique is that it can only be used to charac-

terise detectors irradiated to a maximum 1 MeV neutron equivalent fluence of 10^{11} cm^{-2} [110]. This is because application of the DLTS technique on high resistivity material requires that;

$$\frac{N_t}{N_s} << 1 \tag{6.1}$$

where N_t is the concentration of deep defect levels and N_s is the net doping concentration. In this chapter PL, CPC and TSC techniques were used to evaluate the microscopic defect properties of the unirradiated and irradiated 36GaN, 45GaN and 12GaN detectors. The GaN detectors were fabricated at Glasgow University and the PL, CPC and TSC measurements were performed by researchers at Vilnius University.

6.2 Types of Defects

The formation of structural and chemical defects during growth of a semiconductor is unavoidable. Crystal lattice defects are normally classified by their dimensionality:

- 0-D defects encompassing point defects, antisites, interstitials, interstitial and substitutional impurities and complexes of these defects
- 1-D defects such as dislocations
- 2-D defects on the surface of the semiconductor, stacking faults and cracks
- 3-D defects forming cluster defects and micro-voids etc.

All of the above defect types can influence doping directly, forming shallow or deep levels in the band gap. The presence of 2 and 3-D defects may influence

the doping indirectly, changing the doping efficiency through gettering of dopant atoms at these defects.

Various types of point defects are shown in Figure 6.1. The absence

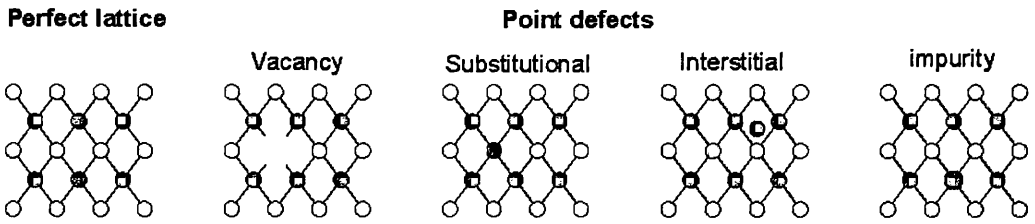

Figure 6.1: Various types of point defects in a compound semiconductor [19]

of an atom from its usual position in the lattice creates a vacancy defect, while substitutional defects occur in compound semiconductors when atoms are switched in the crystal, e.g. in the case of GaAs, a Ga atom is found where an As atom should be present. The appearance of an atom between the allowed positions in the crystal lattice results in an interstitial point defect. Interstitial defects may be self-interstitials or they may be impurity interstitials. An impurity substitutional defect occurs when an impurity atom is located on a lattice site in the place of an constituent atom, e.g. in the case of GaAs, a C atom resides where an As should be present.

There are two primary types of 1D defects that may occur within a crystal structure during growth; edge dislocations and screw dislocations (see Figure 6.2). A mixed dislocation is an intermediate combination of an edge and screw dislocation. Edge dislocations can be visualised as being formed by adding an extra half-plane of atoms to a perfect crystal, so that a defect is created in the regular crystal structure along the line where the extra half-

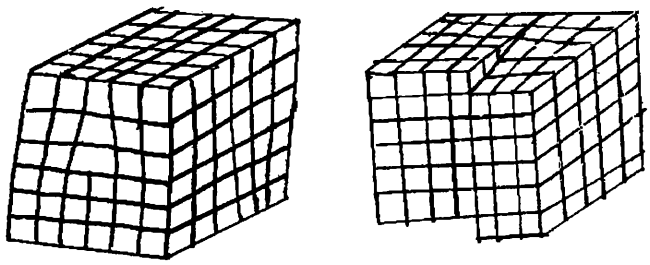

Figure 6.2: An edge dislocation (left) and a screw dislocation (right) [19]

plane ends. Screw dislocations are more difficult to visualise but occur when columns of atoms twist during the growth process.

2D or area defects represent a large area discontinuity in the lattice. Examples include grain boundaries and twins. A grain boundary is a transition between crystals having no particular oriental relationship to one another. These grain boundaries appear during the crystal growth stage. Twinning is a change in the crystal orientation across a plane. Another 2D defect is the stacking fault. In this defect, the stacking sequence of an atomic layer is interrupted. Stacking faults can either be intrinsic or extrinsic stacking faults. Intrinsic stacking faults occur when a part of the crystal layer is missing while extrinsic stacking faults occur when an extra layer is inserted between two crystal layers.

The results in Chapter 4 suggest that the degradation of CCE and the unusual leakage current characteristics under irradiation of the GaN detectors were due to radiation induced defects. However it is important to understand the as-grown defects of GaN before any attempt is made at evaluating radiation induced defects.

6.3 Defects in GaN

The formation of defect levels in GaN is strongly dependent on the growth conditions, temperature, Ga to N ratio and growth technique. Unintentionally doped GaN is nominally n-type and can have electron concentrations as high as 10^{18} cm^{-3}. This auto-doping of GaN is attributed to the formation of shallow donor levels with activation energies ranging from 30-40 meV [111]-[113]. Theoretical calculations have shown that nitrogen vacancies may be shallow hydrogen like donors in GaN [113], [114]. These nitrogen vacancies are thought to be responsible for the unintentional n-type doping of GaN. A further deeper V_N level is also believed to exist with an energy level $\sim$ 120 meV from the conduction band. The Ga vacancy forms a shallow acceptor level 0.14 eV above the valence band.

There are more than 30 recognised defect levels in GaN, some of which are shown in Figure 6.3. All native defects in GaN, with the exception of the N vacancy and Ga vacancy create deep defect levels in the band gap. The nitrogen antisite, N on Ga site, and gallium antisite, Ga on N site, introduce levels close to the middle of the band gap. Both antisites occur in low concentrations as a result of the high energy required to form them [115], [116]. A deep level at 0.5 eV above the valence band is formed by the neutral Ga interstitial while the neutral N interstitial introduces two closely spaced deep acceptor levels at an energy level $\sim$ 1 eV separated by $\sim$ 0.06 eV [118]. Unintentional impurities such as oxygen, carbon, and hydrogen, present during the growth of GaN also introduce deep levels within the band gap.

N-type conductivity in GaN is usually achieved by Si doping. Si substitutes for Ga atoms in the lattice, providing a loosely bound electron. P-type conductivity in GaN has been successfully achieved by Mg doping. Ther-

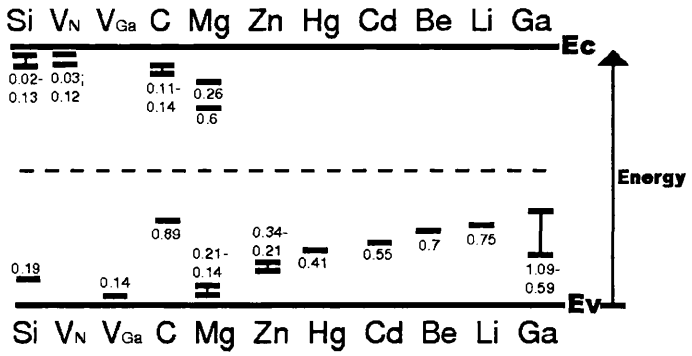

Figure 6.3: Selected defect levels in GaN. V_{Ga} and V_N denote Ga and N vacancies respectively. Ga is a Ga atom on an N atom site (that is a Ga antisite) [117]

mal annealing or electron beam irradiation is required to activate the Mg acceptors.

Threading dislocations (TDs) in GaN also have an important role to play in crystal growth. As already stated the densities of TDs for GaN epilayers grown on sapphire can be as high as 10^{10} cm^{-2}. These threading dislocations are a direct result of the lattice and thermal expansion coefficient mismatch between sapphire and GaN. There has been a range of conflicting theoretical and experimental results reported on the electrical activity and role of TDs in GaN. A good review is given by Reshchikov et al. [119]. First principle calculations suggest that edge TDs are electrically inactive while other theoretical predictions suggest that different types of edge TDs (open core, full core, Ga and N vacancy structures) introduce numerous electronic states in the band gap.

Progress of understanding the electrical activity of both edge and screw TDs in GaN has been limited because of the difficulty in distinguishing the effects of impurities and point defects from the intrinsic properties of the dislocation core. These effects have probably led to the conflicting results

reported on the electrical activity of edge and screw TDs in GaN.

6.4 Photoluminescence

Photoluminescence (PL) spectroscopy is a powerful non-invasive, non-destructive tool for detection and identification of point defects in semiconductors. A monochromatic laser illuminates the material under investigation and imparts excess energy to the material in a process called photo-excitation. Photo-excitation causes electrons within the material to move into permitted excited states. When these electrons de-excite to their equilibrium states, the excess energy is released and may include the emission of light (a radiative process) or may not (a non-radiative process). The energy of the emitted light, or photoluminescence, is related to the difference in energy levels between the two electron states involved in the transition, i.e. between the excited state and the equilibrium state. This energy difference may be equal to the band gap of the material or it could reveal a defect level.

The three main applications of PL spectroscopy are band gap determination, defect level detection and establishing the recombination mechanisms of a material. The return to equilibrium, also known as recombination, can involve both radiative and non-radiative processes. The amount of photoluminescence and its dependence on the level of photo-excitation and temperature are directly related to the dominant recombination process. Luminescence is associated with radiative recombination while non-radiative recombination occurs in two cases;

(a) If there is a strong electron-phonon coupling. This interaction, where energy is transferred from the excited electron to the lattice, may be preferable to luminescence

(b) If there exist disordered regions in the semiconductor (e.g. after irradiation) that allow multi-step recombination involving many defect levels at different energy states.

6.4.1 Experimental set-up

PL spectroscopy measurements of the unirradiated and irradiated 36GaN, 45GaN and 12GaN detectors were carried out at the University of Vilnius, Lithuania. A schematic diagram of the Vilnius PL set-up is shown in Figure 6.4. The illuminating source used was a continuous wave (cw) He-Cd laser

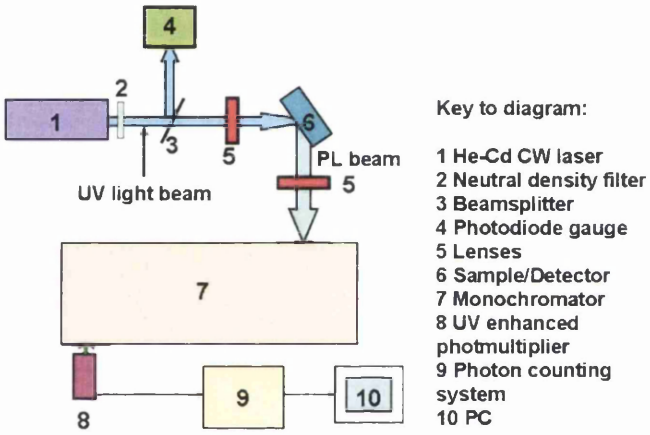

Figure 6.4: Schematic of the PL set-up at Vilnius University

(1) operating at a wavelength of 325 nm. The laser light passed through a neutral density filter (2) and a series of lenses (5). The laser light was split using a beamsplitter (3) and the photodiode gauge (4) employed to measure the intensity of the laser light. The PL signal emanating from the sample (6) was dispersed by a monochromator (7) and the intensity measured using a UV enhanced photomultiplier tube (8) and single photon counter (9). The measured PL intensity at each wavelength was transferred to the computer

(10) and the data saved for off-line analysis. All PL measurements of the irradiated GaN samples were performed at room temperature.

6.4.2 Typical GaN PL Spectrum

Typical PL spectra obtained for two different excitation powers of an unintentionally doped GaN sample are shown in Figure 6.5. The observed PL

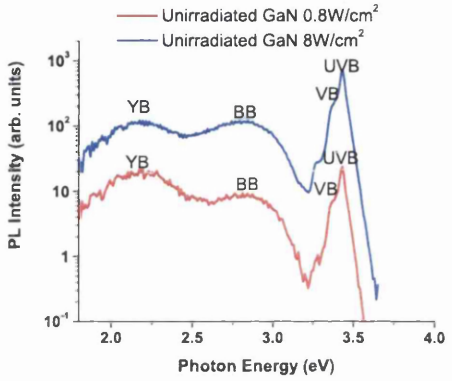

Figure 6.5: Typical PL spectra of an unirradiated GaN sample

spectra show four distinct bands typical of unintentionally doped GaN; the ultra-violet band (UVB), the violet band (VB), the blue band (BB) and the yellow band (YB). The UVB peaks at a photon energy of approximately 3.4 eV, the VB at 3.36 eV, the BB at 2.85 eV and the YB at 2.15 eV. An excellent review of the luminescence properties of GaN may be found in [18]. This review attempts to correlate these observed PL bands and the type of defect (e.g. impurity atoms, Ga or N vacancies, complexes etc.) thought to accountable for them. The UVB is attributed to band to band recombination while the VB is attributed to shallow donor-acceptor recombination. The BB and YB have attracted substantial attention due to the controversial

assignment of their origin and the role that the related defects plays in GaN. The BB is due to transitions from the conduction band or a shallow donor to a relatively deep acceptor having an energy between $\sim$ 0.3 eV and 0.4 eV. This BB PL is related to the threading dislocations discussed earlier that can be present in significant numbers in GaN. The stress field of these TDs are likely to trap Ga vacancies, oxygen and their complexes. These defect complexes form the acceptor like levels 0.3-0.4 eV from the edge of the valence band. It has also been shown that under high excitation power there is a blue shift of the BB peak. The YB peak in GaN is always broad, nearly Gaussian, with a FWHM of 350-400 meV and appears structureless even at the lowest measurement temperature. The origin of the YB is disputed, with contradictory results reported in the relevant literature [120]. The common consensus however is that the YB is due to transitions from a shallow donor to a deep acceptor 0.86 eV from the valence band edge. This deep acceptor level is ascribed to complexes involving C and Ga vacancies.

6.4.3 Results of 36GaN material

PL measurements were performed at room temperature (approximately 295K) using excitation powers of 0.8 W/cm^2 and 8 W/cm^2. However the PL spectra for the most heavily irradiated GaN detectors were only detectable using the higher excitation power. Figure 6.6 shows the PL spectra of the proton and neutron irradiated 36GaN detectors. All spectra exhibit the four bands that are typical of unintentionally doped GaN. Figure 6.7 shows the evolution of PL intensity versus irradiation fluence of the YB, BB, VB and UVB of the irradiated 36GaN detectors. Both Figure 6.6 and Figure 6.7 show that after irradiation with both protons and neutrons the PL intensity of the four bands generally decreases compared to the PL from the unirradiated detector.

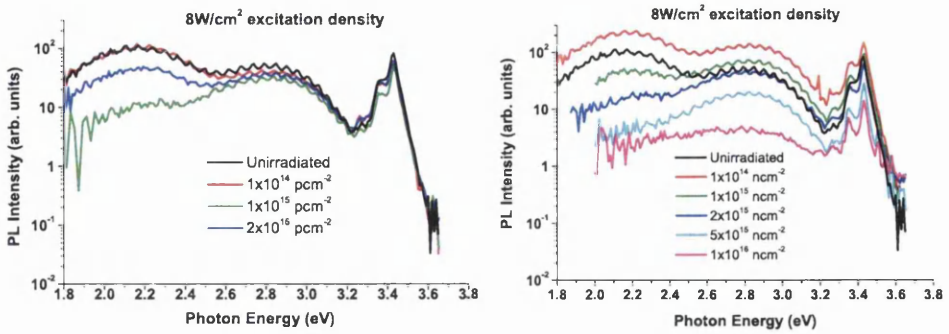

Figure 6.6: PL spectra of the proton irradiated (left) and neutron irradiated (right) 36GaN detectors

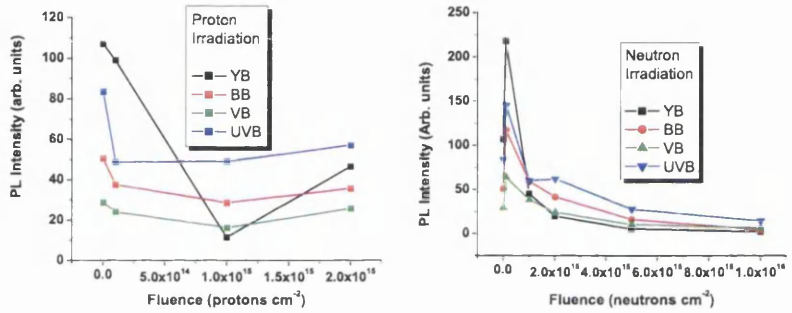

Figure 6.7: PL intensity versus fluence plots of the YB, BB, VB and UVB for the irradiated 36GaN detectors. Proton irradiations are on the left, neutron irradiations on the right.

6.4.4 Results of 45GaN material

The PL spectra of the proton and neutron irradiated 45GaN detectors are seen in Figure 6.8. Again it was found that the intensities of the 4 peaks generally decreased with irradiation fluence (see Figure 6.9).

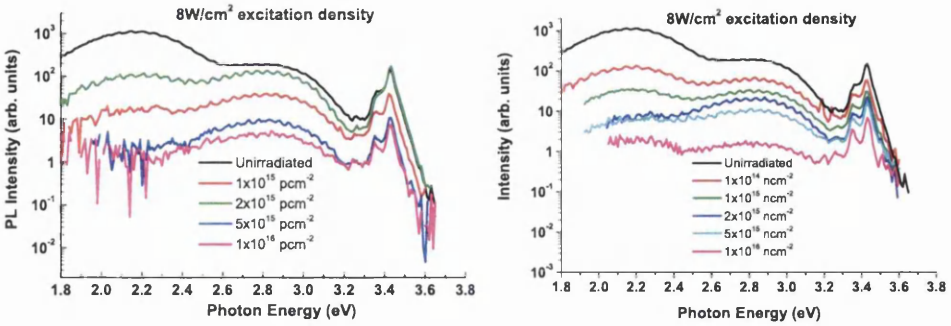

Figure 6.8: PL spectra of the proton irradiated (left) and neutron irradiated (right) 45GaN detectors

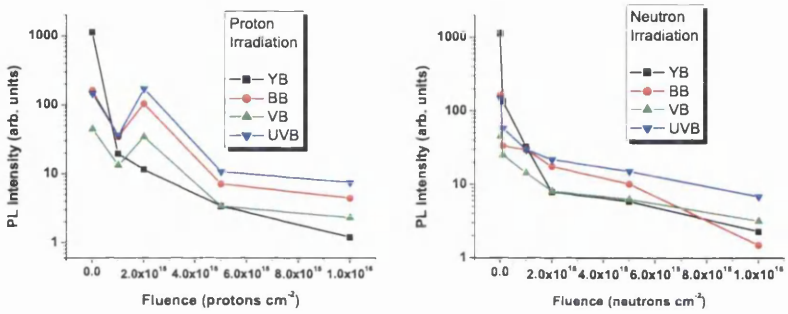

Figure 6.9: PL intensity versus fluence plots of the YB, BB, VB and UVB for the irradiated 45GaN detectors. Proton irradiations are on the left, neutron irradiations on the right.

6.4.5 Results of 12GaN material

The PL spectra of the neutron irradiated 12GaN detectors are shown in Figure 6.10. The PL intensities of peaks the four bands decrease with increasing neutron fluence (see Figure 6.11).

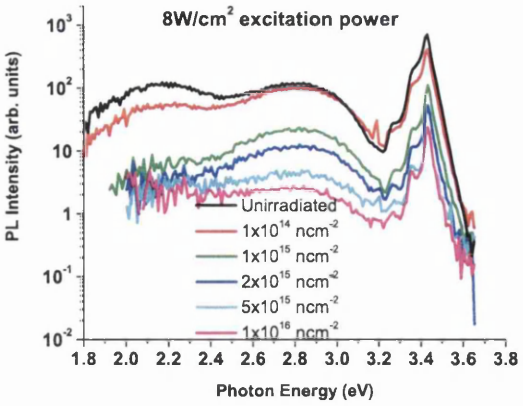

Figure 6.10: PL spectra of the neutron irradiated 12GaN detectors

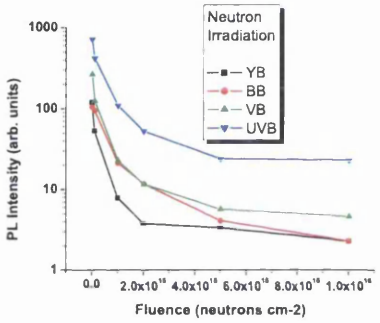

Figure 6.11: PL intensity versus fluence plots of the YB, BB, VB and UVB for the neutron irradiated 12GaN detectors

6.4.6 Discussion of PL Results

For all three GaN materials the PL intensity of the four bands generally decreases with increasing fluence compared to the PL intensity of the unirradiated detector. A decrease of PL intensity means that the photo-induced excess carriers disappear from PL active centres due to competing non-radiative recombination centres through the introduction of radiation induced point

and cluster defects. The luminescence of the exciton region (UVB) and the VB region are only slightly reduced after irradiation whereas both the YB and BB show a substantial reduction in PL intensity.

In particular the YB luminescence for all three GaN materials undergoes a drastic reduction in intensity after irradiation to SLHC fluences ($\geq$ 5x10^{15} cm^{-2}) compared to the YB PL of the unirradiated detector. It can be said that non-radiative recombination becomes the dominant recombination mechanism after irradiation to SLHC fluences. Free charge carriers once captured by a non-radiative recombination centre effectively disappear from charge transport. This would explain the reduction in CCE of the 36GaN, 45GaN and 12 GaN detectors studied in Chapter 4 after irradiation to fluences $\geq$ 5x10^{15} cm^{-2}.

6.5 Contact Photoconductivity

Microwave absorption (MWA) and contact photoconductivity (CPC) are two techniques commonly used to monitor the recombination and trapping processes of excess charge carriers in a semiconductor material. MWA is a non-invasive method based on the pump-probe technique with optical generation and microwave absorption by the free charge carriers [121]-[122], while the CPC technique relies on measuring induced photocurrent decays. For geometric and contact reasons the MWA technique could not be used to investigate the current decays of the GaN samples.

6.5.1 Experimental set-up

In the CPC technique the increase in conductivity of the semiconductor due to the photo-generated current is recorded through the drop in voltage across

a resistor. The photocurrent transient decay gives an indication of the recombination time and trapping properties of the semiconductor material.

Figure 6.12 shows the experimental set-up used for the CPC measurements. The excitation source used was a pulsed (either 30 ps or 10 ns) infra-

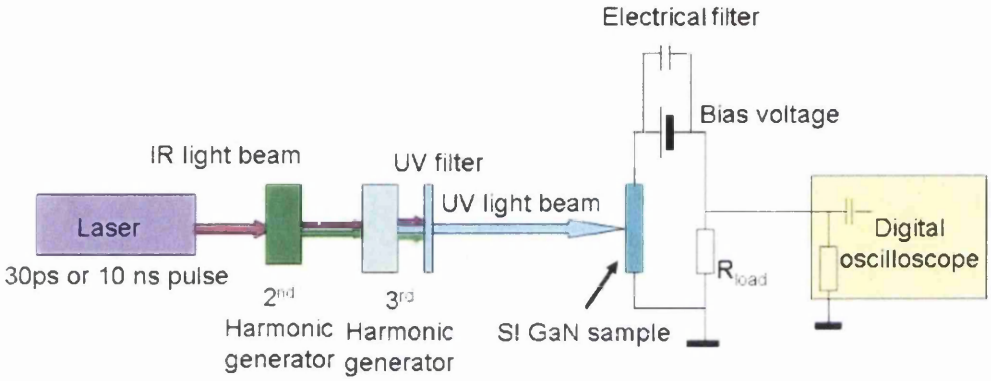

Figure 6.12: CPC experimental set-up

red (IR) YAG:Nd^{+3} laser. UV light of wavelength 355 nm was produced by passing the IR light through 2nd and 3rd harmonic oscillators. The SI GaN sample could be biased from 1 to 10 V and the photo-response of the device was measured through the voltage drop on a load resistor. The output signal was transferred by coaxial cable to the Tektronix TDS-5104 digital oscilloscope and the photo-response transient recorded. The photo-induced excess carrier decay curve could then be analysed off-line.

6.5.2 Typical CPC Decay Transient of SI GaN Sample

Figure 6.13 shows a typical CPC decay spectrum of the SI GaN samples studied. The high density of dislocations associated with SI GaN makes it almost

impossible to establish an analytical solution of the transient decay curve. This is due to randomised carrier diffusion trapping processes in the disordered structure of the dislocations. The decay process can only be analysed by segments and measured using different decay scales, from nanoseconds to milliseconds. For the SI GaN samples studied here the decay is characterised by a fast non-exponential part (region 1) and an asymptotic exponential part (region 2). The initial fast non-exponential decay component is determined

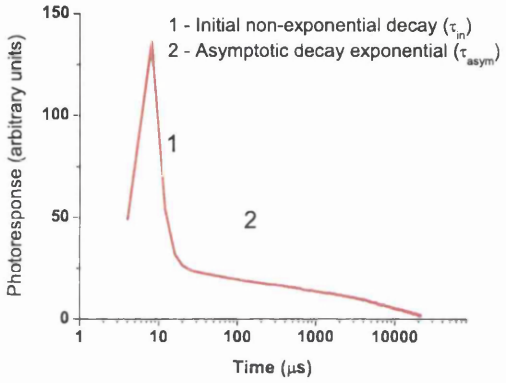

Figure 6.13: Typical CPC decay transient of SI GaN sample. The plot is shown on a semi-log scale in order to show the two transient decay regions more clearly.

by the non-radiative recombination and carrier capture processes while the asymptotic exponential component is ascribed to excess carrier trapping processes at dislocations and point defect clusters within the SI epitaxial GaN layer [123]-[124].

For the fast decay component, the instantaneous decay time (τ_{in}), is approximated by the intersection of the tangent to the data at t = 0s and the horizontal line at e^{-1} (see Figure 6.14). This method of extracting τ_{in} was developed by Vilnius University and has been used in several papers [121]-[124]. It should be noted however that other strategies may be used

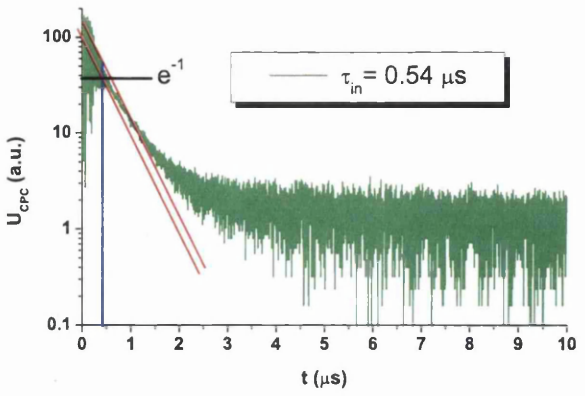

Figure 6.14: The technique used to approximate the instantaneous decay time of the SI GaN detectors.

to evaluate τ_{in}. The asymptotic exponential decay time constant, τ_{asym}, is approximated in a similar manner except the tangent is drawn where the decay curve approaches the noise level of the measurement set-up. These approaches allow a qualitative comparison of the τ_{in} and τ_{asym} decay constants for the irradiated 36GaN, 45GaN and 12GaN detectors.

6.5.3 Results of 36GaN material

Figure 6.15 shows the non-exponential regions of the decay transients of the proton irradiated 36GaN detectors. It can be seen that the photo-response decay is faster for more heavily irradiated 36GaN detectors. Figure 6.16 shows the τ_{in} and τ_{asym} decay lifetimes of the irradiated 36GaN detectors. Both the instantaneous and asymptotic decay lifetimes generally decrease with increasing irradiation fluence. From the figure it can also be seen that proton irradiation results in a similar reduction of the τ_{in} and τ_{asym} components. In the extreme case the 10^{16} ncm^{-2} irradiated detector exhibits a τ_{asym} lifetime $\sim 10^3$ times smaller than that of the 10^{14} ncm^{-2} irradiated

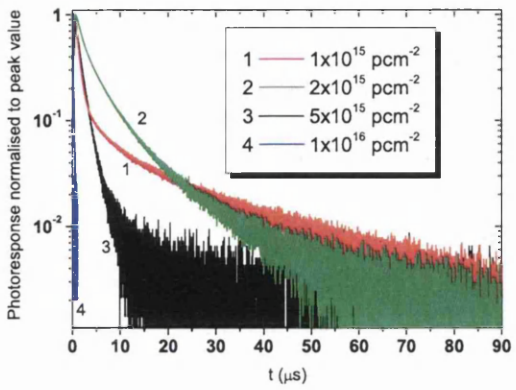

Figure 6.15: Transient decay spectra of the proton irradiated 36GaN detectors

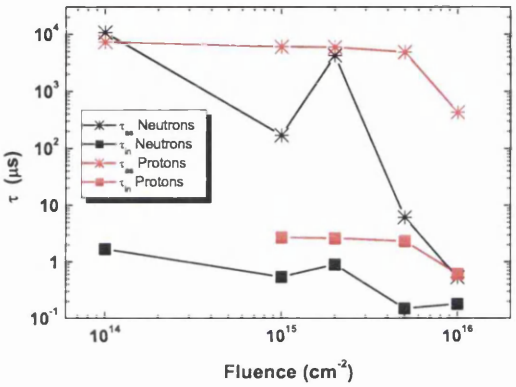

Figure 6.16: τ_{in} and τ_{asym} lifetimes of the proton and neutron irradiated 36GaN detectors

detector.

6.5.4 Results of 45GaN material

The measured τ_{in} and τ_{asym} decay lifetimes of the proton irradiated 45GaN detectors are shown in Figure 6.17. As with the irradiated 36GaN detectors both the instantaneous and asymptotic lifetimes of the 45GaN detectors

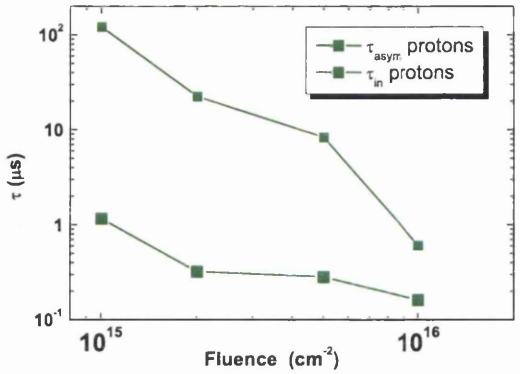

Figure 6.17: τ_{in} and τ_{asym} lifetimes of the proton irradiated 45GaN detectors

decrease with increasing proton fluence. Due to time limitations lifetime measurements of the neutron irradiated 45GaN samples were not performed.

6.5.5 Results of 12GaN material

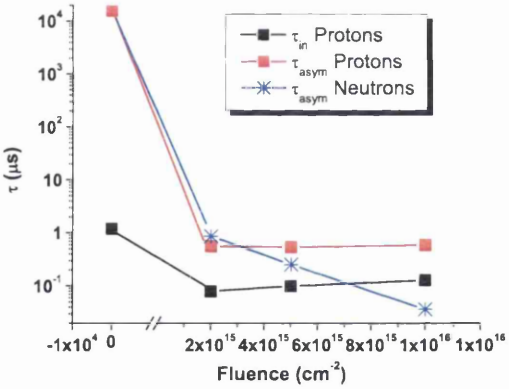

Figure 6.18: τ_{in} and τ_{asym} lifetimes of the unirradiated and irradiated 12GaN detectors

Figure 6.18 shows the τ_{in} and τ_{asym} decay lifetimes of the unirradiated

and proton/neutron irradiated 12GaN detectors. Both lifetimes decrease after irradiation with the 10^{16} ncm^{-2} irradiated detector exhibiting a τ_{asym} lifetime $\sim 10^5$ smaller than the unirradiated detector.

6.5.6 Discussion of CPC Results

The instantaneous and asymptotic lifetime values extracted from CPC measurements on the GaN detectors generally decrease with increasing irradiation fluence. The decrease in τ_{in} lifetime with increasing fluence together with the PL results indicate a significant increase in non-radiative recombination. This increase in non-radiative recombination results in more trapping of generated charge carriers and a reduction in the maximum charge collection efficiency. The irradiation of the GaN detectors also results in more disorder of the SI GaN material, enhancing the carrier decay rate which is observed by the shortened τ_{asym} lifetime. Disorder facilitates capture of charge carriers into relatively shallow levels, reducing the occupation of the recombination active centres and affecting the efficiency of radiative recombination [123].

6.6 Thermally Stimulated Current

Another method of investigating both as-grown and radiation induced deep levels in GaN is the thermally stimulated current (TSC) technique. The device under test (DUT) is cooled in the dark to a low temperature and then excited using a light source (typically white light is used) or an external bias. The DUT is then left to relax to the equilibrium state in the dark. This process fills the defect levels in the semiconductor with charge carriers. Heating the sample empties the defect levels at specific temperatures resulting in an increase in current. The activation energy of the defect levels revealed by

TSC may be found using either the initial rise method, which was the approach used in this work [125], or by the maximal position of the TSC curve [126].

6.6.1 Experimental set-up

The TSC measurement set-up is shown in Figure 6.19. The sample (2) was

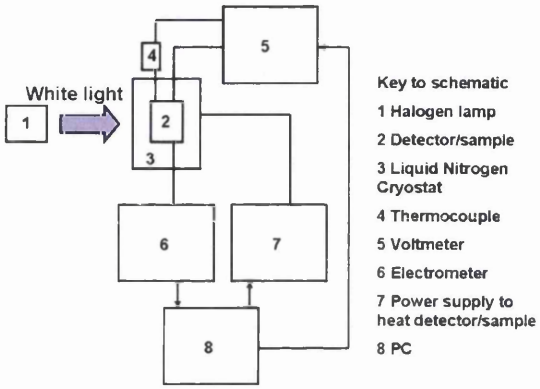

Figure 6.19: A schematic diagram of the TSC measurement set-up

housed in a liquid nitrogen cryostat (3) that allowed measurements to be made in the temperature range 100K to 350K. The sample temperature was determined from the output voltage of a calibrated thermocouple (4) attached to a voltmeter (5) and the sample heated using the power supply (7). A heating rate of 10K/min was used. An electrometer (6) measured the TSC and illumination of the sample was provided using a halogen lamp (1). The current measured by the electrometer was passed to the PC (8) where the data could be saved for off-line analysis.

6.6.2 TSC Results

Unirradiated Sample

Figure 6.20 shows the dependence of TSC and dark current on temperature of the unirradiated 45GaN sample. The TSC technique can be used to establish defects states with activation energies of 0.9 eV above the valence band and below the conduction band. No structure of the TSC spectra is observed in

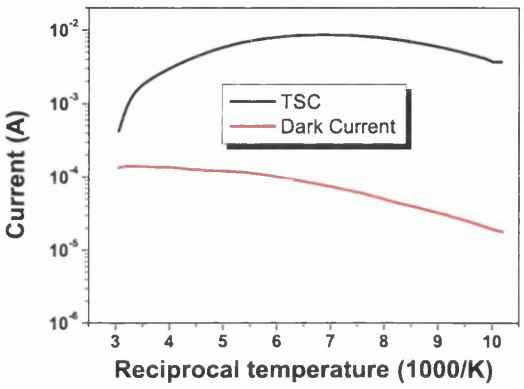

Figure 6.20: TSC and dark current spectra of the unirradiated 45GaN sample

the temperature range 100K to 350K that could be typical of thermal carrier generation from defect levels. Instead there is only one broad maximum in the TSC curve. The unirradiated 36GaN and 12GaN detectors showed qualitatively similar TSC characteristics.

In order to reveal possible single defect levels of this maximum the multiple heating technique was applied. This multiple heating technique is a powerful tool for the discrimination of overlapping thermally stimulated processes in materials with many defect levels in the band gap [125]. The multiple heating enables the sequential emptying of the initially filled shallower defect levels (light excitation fills the defect levels) and gives information

about deeper defect levels in the repetitive temperature scans. The heating cycles were performed by heating and cooling the sample in 10K steps.

Using the multiple heating technique, however, did not change the shape of the TSC spectra, as is shown in Figure 6.21. This implies that the mea-

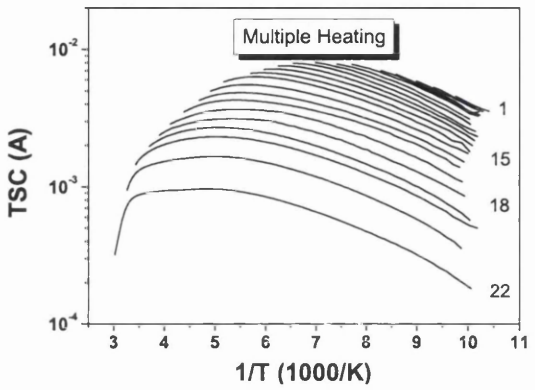

Figure 6.21: TSC spectra of the unirradiated 45GaN detector obtained using the multiple heating technique. The figures on the right hand side of the plot indicate the number of the repetitive heating and cooling cycles made during the measurement.

sured TSC dependence is not caused by thermal carrier generation but rather by variation in carrier mobility. Similar conclusions have been reported in [127], [128] where mobility increases with decreasing temperature until a maximum is reached at approximately 150K. A model is proposed in [128] in which the effect of potential fluctuations due to crystal inhomogeneities is involved causing percolation charge carrier transport in GaN. At low temperatures charge carriers generated by light, fill potential wells screening impurities and smoothing the potential distribution within the unirradiated 45GaN sample. During subsequent heating thermally released carriers recombine causing defect inhomogeneities to act as scattering centres. Such

defect inhomogeneities are rife in compound semiconductors such as SI GaN. This model may also be used to explain the TSC spectra of the unirradiated GaN detectors studied in this thesis.

6.6.3 Irradiated Samples

The irradiated GaN detectors showed different TSC structure compared to the unirradiated GaN detectors. The current values decreased by several orders of magnitude. Figure 6.22 shows the TSC curves of the 10^{14} ncm^{-2} irradiated 45GaN detector at several applied biases. The TSC spectra remain relatively flat for all temperatures and have no characteristic features even though light excitation caused a current increase by up to one order of magnitude. Figure 6.23 shows the TSC spectra for the 10^{15} ncm^{-2} irradi-

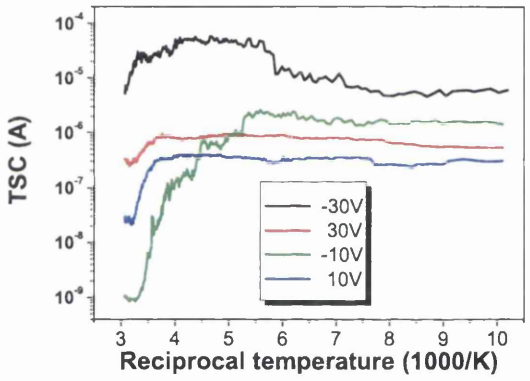

Figure 6.22: TSC spectra of the 10^{14} ncm^{-2} irradiated 45GaN detector using the single heating technique

ated 45GaN detector at two applied bias voltages. Again the spectra have no characteristic features that can be resolved and trap activation energies cannot be extracted.

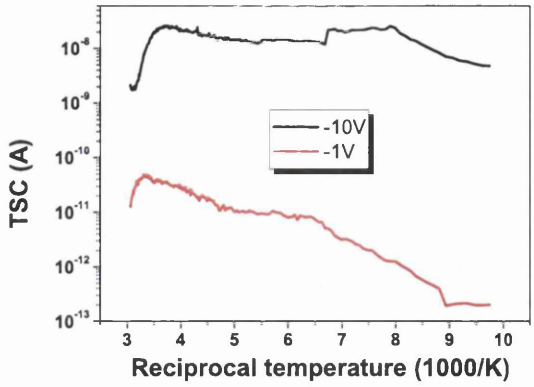

Figure 6.23: TSC spectra of the 10^{15} ncm^{-2} irradiated 45GaN detector using the single heating technique

The TSC spectra of the 10^{14} ncm^{-2} and 10^{15} ncm^{-2} irradiated 45GaN detectors could be explained by radiation induced defects that act as scattering centres or traps. This explanation would fit the model proposed in the previous section. Current instabilities were also observed in these two detectors which could be caused by the random change of carrier drift paths in highly disordered material. In the disordered material defective regions of higher resistivity might appear that are inaccessible to the charge carriers forcing them to move in percolation paths around such high resistivity inclusions.

By using the multiple heating technique on the 45GaN sample irradiated to 10^{15} ncm^{-2} a set of defect levels could be identified (see Figure 6.24). The most clearest defect levels are at energy levels of 0.15, 0.17-0.20, 0.27-0.32 and 0.46 eV.

The increase in irradiation fluence to 10^{16} ncm^{-2} resulted in a further growth of the material resistivity and a TSC structure that could be attributed to a whole collection of different defects and inhomogeneities (see Figure 6.25). The figure also shows that the TSC structure gradually van-

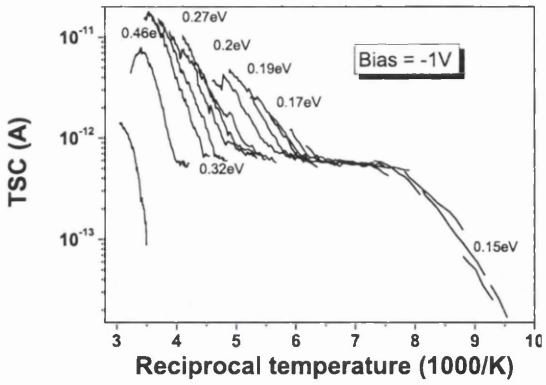

Figure 6.24: TSC spectra of the 10^{15} ncm^{-2} irradiated 45GaN detector using the multiple heating technique. The effective thermal activation energy values are located nearby the curves.

ishes with increasing bias voltage. This can be explained by the growing role of the high injection field over the potential barrier at the Schottky contact. Thermal activation energy values of 0.16-0.2, 0.27-0.32, 0.36-0.45 and

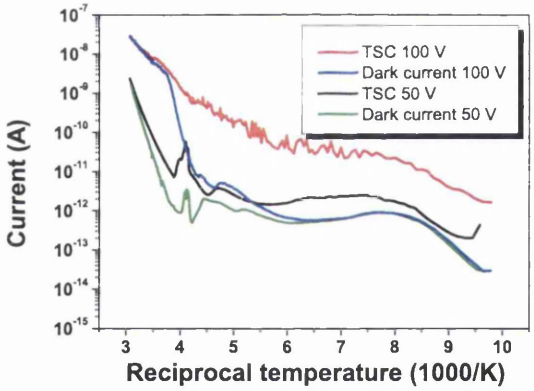

Figure 6.25: TSC spectra of the 10^{16} ncm^{-2} irradiated 45GaN detector using the single heating technique

0.73-0.74 eV were obtained using the multiple heating technique (see Figure

6.26). These energy values are similar to those obtained from the detector

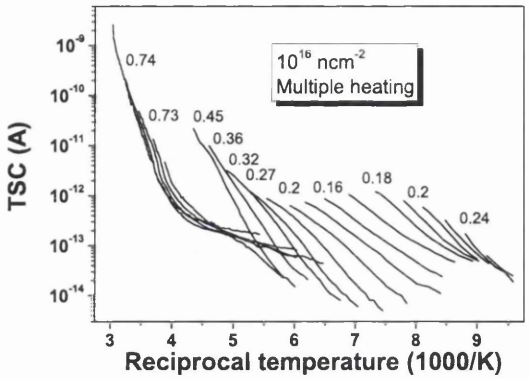

Figure 6.26: TSC spectra of the 10^{16} ncm^{-2} irradiated 45GaN detector using the multiple heating technique. The effective thermal activation energy values are located nearby the curves.

irradiated to 10^{15} ncm^{-2} with the addition of a new level with an activation energy of 0.73-0.74 eV.

6.6.4 Discussion of TSC Results

The TSC results show that there are several competing complicated transport mechanisms in both the unirradiated and irradiated SI GaN detectors. A broad maximum was exhibited by the unirradiated 45GaN detector using both the single and multiple heating techniques. This TSC behaviour is not caused by thermal carrier generation but by mobility variation. Several thermal activation energy values were found for defect levels in the neutron irradiated 45GaN samples. For the most highly irradiated 45GaN detector activation energies of 0.16-0.2, 0.27-0.32, 0.36-0.45 and 0.73-0.74 eV were found (see Table 6.4). However, due to the complicated current transport mechanisms in both the unirradiated and irradiated 45GaN detectors it is

Irradiation fluence	Activation Energies (eV)
10^{15} ncm^{-2}	0.15, 0.17-0.2, 0.27-0.32, 0.46
10^{16} ncm^{-2}	0.16-0.2, 0.27-0.32, 0.36-0.45, 0.73-0.74

Table 6.1: Trap activation energies of neutron irradiated 45GaN detectors

difficult to determine the radiation induced defect levels from the as-grown defect levels.

6.7 Conclusions and Summary

The microscopic properties of unirradiated and irradiated SI GaN detectors were investigated using photoluminescence, contact photoconductivity and thermally stimulated current techniques. PL measurements revealed the UVB, VB, BB and YB structure that are typical of undoped n-type GaN. The PL intensity of these four bands generally decreases with increasing fluence compared to the unirradiated detector indicating an increase in non-radiative recombination. The YB luminescence in particular underwent a large reduction in intensity after irradiation to SLHC fluences. It can be said that non-radiative recombination becomes the dominant recombination mechanism after irradiation to SLHC fluences. This dramatic increase in non-radiative recombination would explain the reduction in CCE of the 36GaN, 45GaN and 12 GaN detectors studied in Chapter 4 after irradiation to fluences $\geq$ 5x10^{15} cm^{-2}.

CPC measurements of the irradiated GaN detectors revealed two decay processes of the induced photo-current; a non-exponential region ascribed to fast carrier recombination and an asymptotic region ascribed to excess carrier trapping. The CPC measurements revealed an increase in non-radiative

recombination with increasing fluence observed through the reduction in τ_{in} corroborating the PL results. The irradiation of the GaN detectors resulted in more disorder of the SI GaN material, enhancing the carrier decay rate which was observed by the shortened asymptotic lifetime.

TSC measurements of the GaN detectors revealed several competing complicated transport mechanisms. The TSC curve of the unirradiated GaN detector was caused not by thermal carrier generation but by variation of the charge carrier mobility. Thermal activation energies of 0.16-0.2, 0.27-0.32, 0.36-0.45 and 0.73-0.74 eV were extracted from neutron irradiated 45GaN detectors.

Chapter 7

GaN as an UV Detector

7.1 Introduction

The research area of ultraviolet (UV) photodetection has drawn a great deal of attention in recent years. Both civil and military industries demand better UV instrumentation for applications such as engine control, solar UV monitoring, UV source calibration, UV astronomy, flame sensors, detection of missile plumes and secure space-to space communications [129], [130]. Due to their compactness, high stability and low cost, solid state semiconductor detectors are the best choice for UV photodetectors. The well-established Si technology offers cheap and efficient solutions for UV detection, although Si photodetectors are sensitive to infra-red and visible radiation and require optical filters to block these lower energy photons.

Photodetectors based on wide band gap semiconductors, such as diamond, SiC and III-nitride semiconductors, can achieve UV selectivity without the use of optical filters. Moreover as mentioned in Chapter 4, wide band gap semiconductors are chemically, mechanical and thermally stable which are advantageous when used in harsh environments. GaN in particular has been

extensively studied since the properties of the first GaN UV photodetectors were reported in 1992 by Khan et al. [131]. GaN's wide direct band gap (3.39 eV) makes it an ideal material for UV photon detection. The band gap of GaN (and therefore the cut-off wavelength) can also be tuned by the addition of Al, forming the ternary alloy AlGaN. Cut-off wavelengths ranging from 365 nm (GaN) to 200 nm (AlN) may be realised by varying the molar fraction of Al (see Table 7.1). Selective UV photodetectors are also required

$Al_xGa_{1-x}N$	E_g (eV)	λ_c (nm)
x = 0	3.4	365
x = 0.23	3.88	320
x = 0.25	4.0	310
x = 0.35	4.28	290
x = 1	6.2	200

Table 7.1: Band gaps (E_g) and cut-off wavelengths (λ_c) of AlGaN materials with varying Al mole fraction

in biological applications such as protein folding experiments. An example of an experiment that is used to study the secondary structure of a protein is Circular Dichroism (CD) [143], [144]. CD will be discussed further later in this chapter.

This chapter describes the development and optimisation of metal-semiconductor-metal (MSM) photodetectors on several GaN/AlGaN materials. The optimal material, diode geometry and metalisation scheme was established and incorporated into the design of a 46 channel position sensitive diode array detector to be used in a CD experiment at Daresbury Laboratory.

7.2 Background and Motivation

7.2.1 GaN/AlGaN UV Photodetectors

A photodetector can be treated as a device that is capable of detecting an optical signal and producing an electrical signal proportional to the optical signal. If the energy of a photon is larger than the band gap of the semiconductor then an electron-hole pair is produced. The generated electron-hole pairs are collected by applying a bias to metal contacts that are usually fabricated on the semiconductor surface.

Figure 7.1 shows schematic diagrams of the basic photodetector structures fabricated on GaN/AlGaN epitaxial layers. UV photodetectors are typically

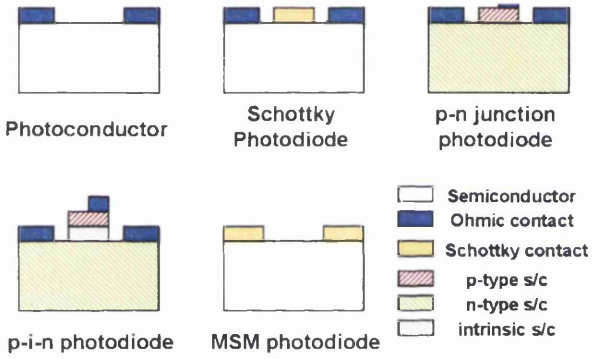

Figure 7.1: Schematic structures of a photoconductor, Schottky photodiode, p-n photodiode, p-i-n photodiode and a metal-semiconductor-metal (MSM) photodiode

compared in terms of their quantum efficiency, responsivity, power linearity, spectral response, bandwidth, UV/visible contrast and detectivity.

Photoconductive detectors are the simplest photodetector structure, consisting of two metal contacts on a semiconductor layer. These devices exhibit high responsivities however they are also associated with significant

photoresponse for photons below the band gap and temperature dependant characteristics [131]-[133]. This below band gap photoresponse results in photoconductors having low UV/visible contrasts. A further problem with photoconductive detectors fabricated on GaN/AlGaN is that they suffer from persistent photoconductivity (PPC) effects, i.e. the photoinduced increase of the device conductance remains for a long period of time after removal of the light source [134].

Photodiodes consist of an ohmic contact and a Schottky contact that is transparent to UV light. They typically have a flat responsivity for excitation above the band gap and have a UV/visible contrast of order 10^3 [135], [136]. Their time response is RC limited (resistance and capacitance of the device) with minimum time constants in the nanosecond range [137]. Photodiodes have been widely used in environmental applications [138].

P-n and p-i-n photodiodes fabricated on GaN/AlGaN show good linearity with optical power and can have UV/visible contrasts as high as 10^4 [139]. However their time response is usually limited by the behaviour of the p-dopants (typically Mg related centres). There has also been great difficulty in fabricating AlGaN p-n and p-i-n photodiodes with high molar fractions of Al. This is due to difficulties in obtaining low resistivity p-type regions and forming good ohmic contacts.

Metal-semiconductor-metal (MSM) photodiodes consist of two interdigitated Schottky metal contacts deposited on highly resistive material. These devices show very low dark currents, good linearity with optical power, and can have UV/visible contrasts as high as 10^4 [140],[141]. Their responsivity is related to the finger separation and the nature of the metal contact (full metal or semi-transparent). These photodetectors also exhibit excellent transient characteristics with response times of the order of 100 picoseconds [142].

MSM photodiodes also exhibit large bandwidth and low noise characteristics making them a good choice for solar-blind communications.

7.2.2 Circular Dichroism

All human proteins are polymers built up from amino acids linked end to end by peptide bonds. For a protein to be soluble in water it must be able to fold up into a ball whose surface is hydrophilic - water loving. However the peptide bonds in the backbone of the protein molecule are themselves hydrophilic. For folding to occur each of these peptide sites has to be neutralised by forming hydrogen bonds with other peptides in the chain rather than with the surrounding water molecules. This is achieved by the formation of a regular secondary structure within the interior of the polymer molecule. The most common types of secondary structure are α-helices and β sheets. Some amino acids promote α-helix formation whereas others hinder their formation and favour a β-sheet structure.

All amino acids are chiral molecules, that is, they cannot be superimposed on their mirror image and are therefore said to possess "handedness". One of the properties arising from this asymmetry is that their interaction with right and left handed circularly polarised light differs. Circular Dichroism (CD) is defined as the difference in absorption between left hand and right hand circularly polarised light as it passes through a solution of an optically active molecule, for example a protein (see Figure 7.2). The resultant dichroic spectrum has a shape that is specific to the protein's conformation. The CD spectrum therefore acts as a signature for the adopted conformation of the secondary structure of the protein.

CD measurements are performed in the UV region (180 nm to 240 nm) of the electromagnetic spectrum. Absorption in this region of the spectrum

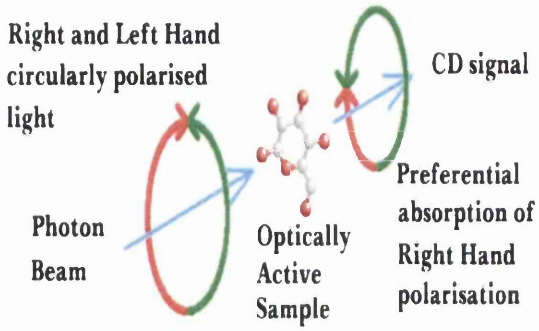

Figure 7.2: A schematic diagram of Circular Dichroism

arises from electron transitions that can occur in the peptide bonds that hold the protein molecule together. There are clear distinctions between the spectrum obtained from an α-helix and that from a β-sheet (see Figure 7.3). It is not possible to obtain good CD data below 190 nm using conventional

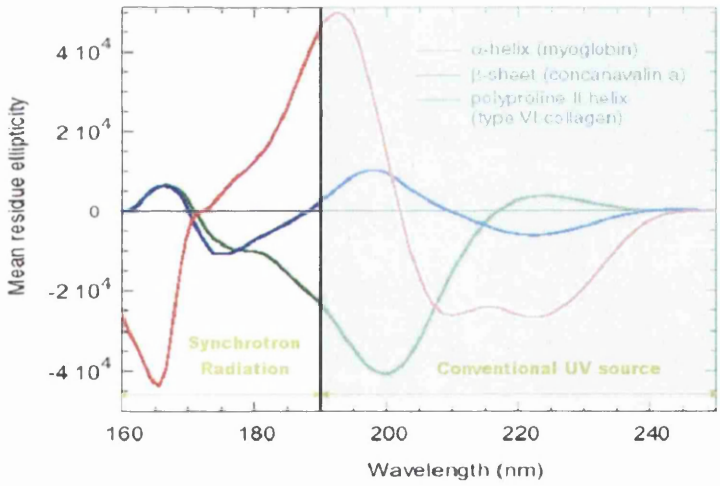

Figure 7.3: CD spectrum of an α-helix and CD spectrum of a β-sheet in the 180 nm to 240 nm range [16]

UV sources such as deuterium lamps or xenon arc lamps due to strong UV absorption by both the protein sample and by oxygen in the air. However the high brightness offered by synchrotron radiation overcomes this limitation and enables CD measurements to be performed below 190 nm. Figure 7.4 shows the photon intensity versus wavelength plots for conventional CD instrumentation, such as a deuterium source (pink line), and for synchrotron radiation at Daresbury SRS Station 12 (green line). The unshaded region of

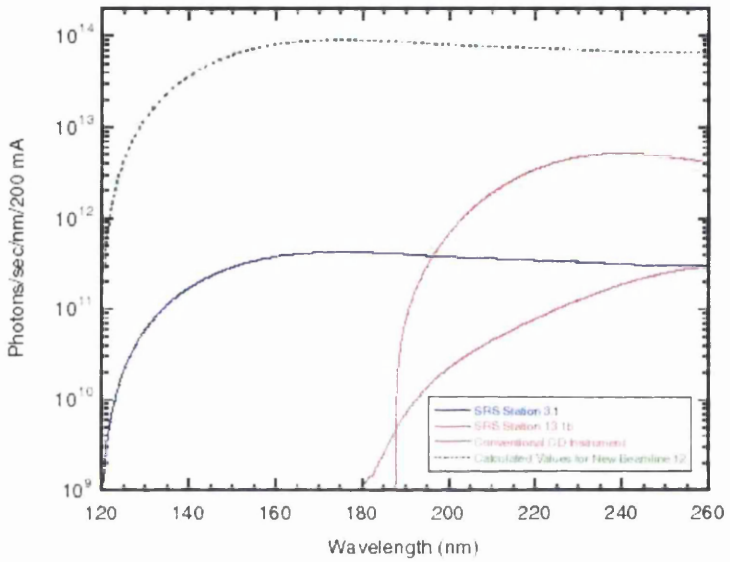

Figure 7.4: Intensity versus wavelength plots for synchrotron radiation (green dotted line) and conventional CD instrumentation (pink line)

Figure 7.3 gives an indication of the greater CD information available using synchrotron radiation instead of a conventional UV source.

Neuro-degenerative diseases such as Alzheimer's and Creutzfeldt-Jakob disease occur when certain proteins in the brain do not fold in the conventional way. Normally the structure of these proteins is dominated by α-helices which make them soluble in the water inside the brain. If however,

their structure changes to one dominated by β-sheets, filaments can form which are no longer water soluble. It is believed that neuro-degenerative diseases are caused when proteins adopt this filament conformation. Knowing exactly how proteins fold and examining the misfolding of proteins could help both in understanding neuro-degenerative diseases and in designing drugs to treat them.

7.2.3 Energy Dispersive Circular Dichroism

CD measurements are typically performed using a photomultiplier tube (PMT) connected to a lock-in amplifier, which is phase locked to a photoelastic modulator that provides the circularly polarised light [145], [146]. The lock-in amplifier has a relatively slow response with time constants of ~ 0.5 ms and moreover is limited to a single channel input. CD measurements performed in this way require sequential scanning across the wavelength spectrum and are useful for secondary structure determination but not for time-resolved measurements and the observation of structural changes. It is also time consuming, with a typical scan of one protein taking hundreds of seconds [16].

An improved CD measurement set-up that renders the need for scanning unnecessary has been proposed by a team at the Rutherford Appleton Laboratory (RAL) [16]. This Energy Dispersive Synchrotron Radiation (EDSR) CD set-up, shown in Figure 7.5, would enable the user to simultaneously measure the CD signal at 46 wavelengths. UV radiation is directed onto a protein sample and then dispersed by a grating onto a 46 channel diode array detector. Each channel of the array detector maps one wavelength allowing 46 wavelengths to be sampled in one measurement. Special dedicated electronics would also be incorporated for the parallel read-out of the detection elements, followed by a data acquisition system that processes the data and

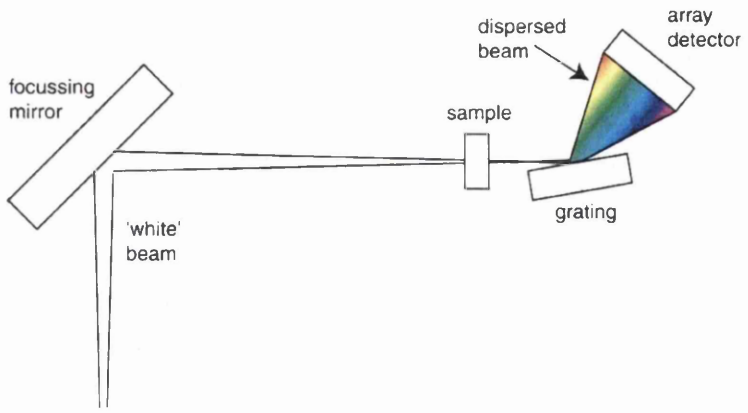

Figure 7.5: The proposed Energy Dispersive Synchrotron Radiation (EDSR) CD set-up

calculates the CD signal [147]. This obviates the need for lock-in amplifiers for each channel. It was also proposed that the 46 channel diode array detector should be a photodiode and that if possible this detector should be solar blind or ideally tailored to the detection of light with wavelengths only in the region of interest so that optical filters are not required.

A prototype 16 channel EDSR CD set-up was initially developed at RAL. A scheme based on transimpedance amplifiers with variable filters and a high-frequency filter for the de-coupling of the AC and DC components of the signal was used for each individual diode's read-out. This de-coupling is necessary to enable the calculation of the CD signal. A field programmable gate array (FPGA) based data acquisition (DAQ) system was used for the on-line calculation of CD and temporary storage. In this prototype version, known as "16-pix" the front end read-out electronics were manufactured using discrete components. 16-pix operates at a frequency of 20 MHz and has a maximum AC signal gain of 6 and a maximum DC signal gain of 150 [147].

The aim in this chapter was to fabricate a 46 channel diode array detector on the most suitable GaN material to be used in a CD experiment utilising the prototype "16-pix" electronic read-out. The following section describes the fabrication and optimisation of GaN MSM detectors on four GaN materials and one AlGaN material. A 46 channel diode array detector was then fabricated on the material that showed the best characteristics.

7.3 Fabrication and Characterisation of GaN UV Detectors

MSM interdigitating finger test structures were fabricated on the various GaN and AlGaN materials. The details of three of the GaN wafers, known as 36GaN, 45GaN and 12GaN were given in Chapter 4. The fourth GaN wafer was obtained from Emcore [148] and had an epitaxial thickness of 2 μm. This epitaxial layer was grown on an n-GaN buffer layer and a sapphire substrate. A two inch diameter, AlGaN wafer was also obtained from Emcore however the epitaxial thickness and Al content of the material were not divulged by the manufacturer. PL measurements revealed that the Al molar fraction of the AlGaN wafer was 10% [19].

The MSM photodetector structure was chosen for the following reasons:

- The low hole mobility of GaN (see Table 4.2) means that the distance between collecting electrodes must be relatively small. MSM photodetectors can be tailored so that the finger separation distance is of the order of the hole drift length. This reduces the collection time for photogenerated e-h pairs and the probability of generated charge being trapped before it is collected.

- Despite the electrodes being close together the interleaving finger geometry means that the active area of the device is not significantly compromised.

- Time resolved CD measurements require fast photodetectors. As discussed in Section 7.2.1 response times of MSM detectors are of the order of 100 picoseconds.

Two different MSM photodiode geometries were fabricated on the GaN/AlGaN materials using photolithography techniques outlined in Chapter 2. These test structures were designed using the L-Edit CAD drawing software and written onto a photolithographic mask. One geometry had a finger pitch of 10 μm and a finger width of 5 μm (i.e. a finger separation of 5 μm) while the second geometry had a finger pitch of 20 μm and a finger width of 10 μm (i.e. a finger separation of 10 μm). These finger separations and widths were chosen in accordance with the results of Monroy et al. [149] and Blue et al. [150], who showed that finger separations and widths $\leq$ 10 μm are required to maximise the measurable quantum efficiency of a MSM photodetector. Before metal deposition the samples were de-oxidised in HCl for one minute. Schottky contacts were realised by evaporating 50 nm/200 nm of Pd/Au metal and the fabricated devices were wire bonded to chip carriers for characterisation. The theoretical Schottky Barrier Height (SBH) of this Pd-GaN contact is 1.02 eV. Figure 7.6 shows fabricated MSM test structures with a finger separation/width of 5μm (left) and 10μm (right). The overall dimensions of each diode was 400 μm by 590 μm. The 5 μm finger spacing design had an active area of 0.120 mm^2 while the 10 μm finger spacing design had a slightly smaller active area of 0.116 mm^2. From herein the 5 μm finger spacing design will be referred to as "5 μm design" and the 10 μm finger spacing design will be referred to as "10 μm design".

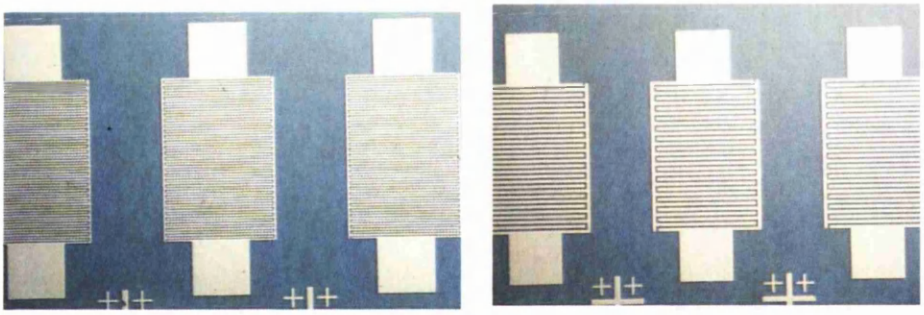

Figure 7.6: Left - Interdigitated MSM finger diodes with a finger separation/width of 5 μm (left) and 10 μm (right) fabricated on the various GaN/AlGaN materials

7.3.1 Characterisation of MSM photodiodes

Fabricated devices were characterised by performing current-voltage (I-V) and spectral response measurements. For I-V measurements a Keithley 237 electrometer was used. One set of fingers was biased while the second set was kept at ground. All I-V measurements were performed in a dark environment at room temperature.

The spectral response measurement set-up is shown in Figure 7.7. A Hamamatsu L7893-01 deuterium lamp was used as the UV light source. A Jobin Yvon monochromator was used and controlled by LABVIEW software. It was possible to select wavelengths ranging from 180 nm to 800 nm. A fibre optic cable of diameter 0.8 mm was connected to the output of the monochromator and positioned directly in front of the MSM photodiode. The MSM photodiode was soldered into a BNC box and housed in a light tight Faraday box. The photocurrent was measured by a Keithley 237 electrometer which could also be used to apply a bias to the photodetector. A motorised x-y stage, controlled by LABVIEW software enabled accurate alignment (to a precision of approximately 5 μm) of the fibre optic cable and

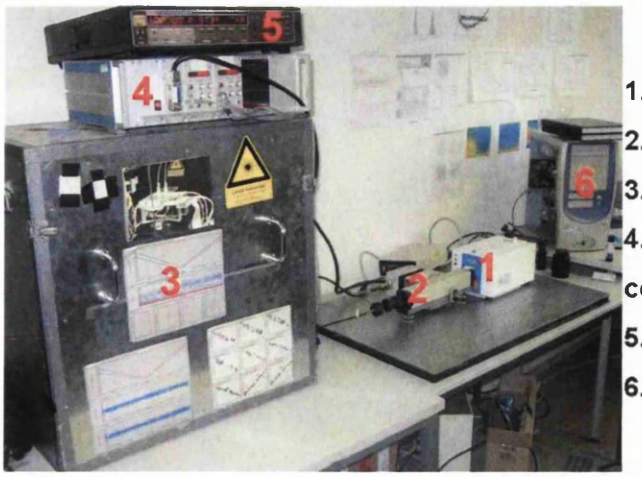

Figure 7.7: Spectral response measurement set-up

the MSM photodiode. In order for the device to attain equilibrium a delay of 5 seconds between each wavelength step was used for all spectral response measurements.

A plot of radiant intensity versus wavelength of the Hamamatsu L7893-01 deuterium lamp was supplied by the manufacturer (see Figure 7.8). In order to calibrate the spectral response measurement set-up a UV sensitive S1336-5BQ Si photodiode was purchased from Hamamatsu. The manufacturer provided a responsivity versus wavelength plot for the S1336-5BQ Si photodiode. Using this data the theoretical photocurrent from the Si photodiode was calculated using the equation:

$$I_P = R \times P_{OUT} \tag{7.1}$$

where I_P is the photocurrent, R is the responsivity (units of A/W) and P_{OUT} is the output power of the deuterium lamp (shown in Figure 7.8). Figure 7.9

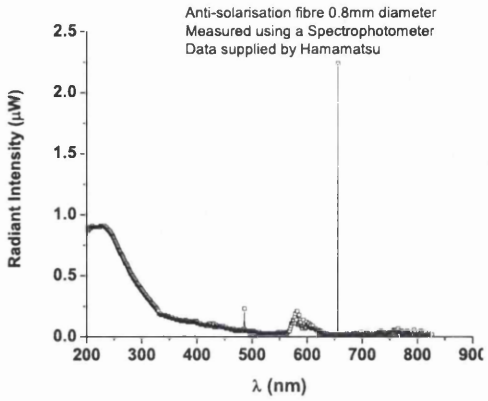

Figure 7.8: Power output versus wavelength as measured by a spectrophotometer for the Hamamatsu L7893-01 deuterium lamp.

shows the theoretical photocurrent versus wavelength data of the Si photodiode compared to the measured photocurrent versus wavelength values. It can

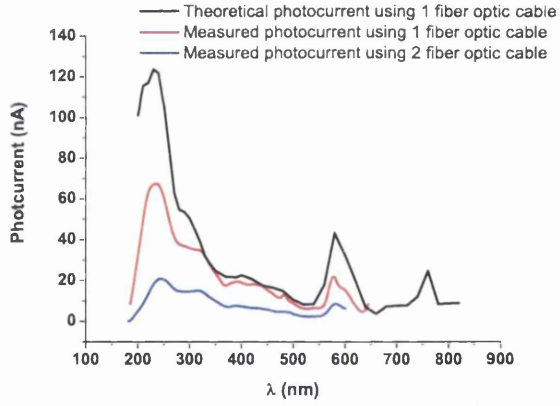

Figure 7.9: Theoretical and measured photocurrents of the Hamamatsu S1336-5BQ Si photodiode

be seen that the theoretical (black line) and measured photocurrent (red line) curves are qualitatively similar however there is some unexplained attenua-

tion of the measured photocurrent signal that is more pronounced at shorter wavelengths. Also shown on the plot is the photocurrent measured from the Si photodiode when a second fibre optic cable is inserted between the output of the deuterium lamp and the monochromator. There is a marked decrease in signal magnitude compared to when only one fibre optic cable is used. The maximum photocurrent for all three curves occurs at a wavelength of $\sim$ 235 nm.

In any spectral response measurement it is essential to establish whether the area of the detector is greater or smaller than the area of the beam of incident light. The beam area was measured using the "Startracker" active pixel sensor (APS) which is currently being characterised by the MI^3 collaboration [151]. The "Startracker" is sensitive to visible radiation and the MI^3 collaboration's remit is to develop the sensor for detection of light across the entire electromagnetic spectrum, in particular for UV, x-rays and γ rays. There are 525 by 525 pixels on the "Startracker" and each pixel is a 25 μm by 25 μm square. The distance between the fibre optic and the sensor was varied and the area of the beam calculated. Figure 7.10 shows images taken at 450 nm using the "Startracker" at distances of 2 mm, 4 mm and 8 mm between the sensor and the fibre optic cable. Table 7.2 gives a summary of the beam radius and the beam area at distances of 2 mm, 4 mm and 8 mm between the fibre optic cable and the sensor. Using the data obtained by the "Startracker" sensor it can be seen that for all distances between the sensor and the fibre optic cable the area of the beam is larger than the area of the 400 μm by 590 μm MSM photodiodes. The spectral response measurements for the GaN/AlGaN MSM photodiodes were performed with a distance of 2 mm between the fibre optic cable and the detector.

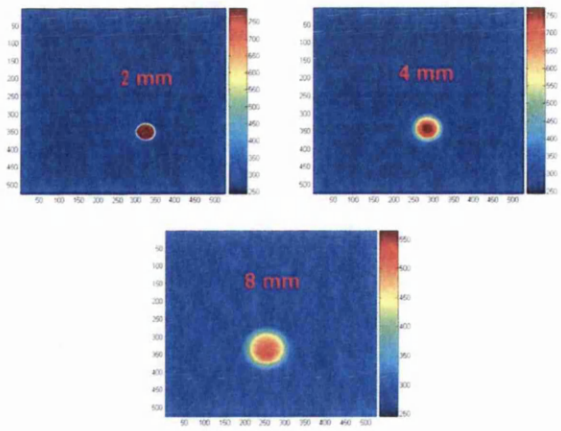

Figure 7.10: Images of the beam profile at 450 nm taken using the "Startracker" sensor. The distance between the fibre optic cable and the sensor was varied between 2 mm (top left), 4 mm (top right) and 8 mm (bottom).

Distance (mm)	Radius (pixels)	Radius (mm)	Beam Area (mm^2)
2	25	0.625	1.227
4	35	0.875	2.405
8	50	1.250	4.909

Table 7.2: Beam profile parameters at a distance of 2 mm, 4 mm and 8 mm between the sensor and fibre optic cable

7.4 Leakage Current and Spectral Response Results

7.4.1 Leakage Current

Leakage/dark current measurements of the fabricated MSM GaN photodiodes were performed up to a bias of +/- 25V. Figure 7.11 shows the typical I-V characteristics of the interdigitated MSM photodiodes. As expected, the

detectors exhibited Schottky behaviour with a slow breakdown occurring, in this case after +/- 20V. The voltage at which this slow breakdown of the detector started varied from device to device.

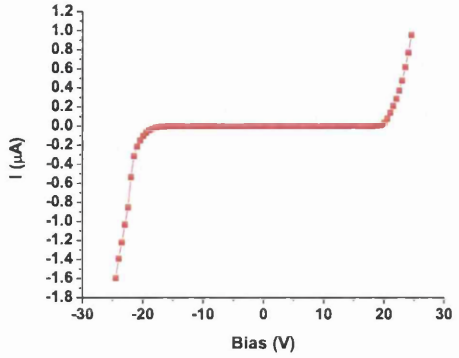

Figure 7.11: Typical I-V curve of the MSM photodiodes fabricated on the GaN/AlGaN materials

The I-V curves of the MSM photodiodes with the 5 μm design are shown in Figure 7.12. There was several difficulties fabricating the 5 μm design 12GaN device and as a consequence there is no data curve for this device. The MSM photodiode fabricated on the 45GaN material has the lowest leakage current while the AlGaN MSM photodiode exhibits the largest leakage current, reaching the compliance value of the measurement set-up, 1 mA, after application of only +/- 0.4 V. The MSM photodiodes fabricated on the 36GaN and Emcore GaN also show typical MSM photodiode behaviour.

I-V curves of the 10 μm design MSM photodiodes fabricated on the various materials are shown in Figure 7.13. The I-V curves are similar to those of the 5 μm design MSM photodiodes with the AlGaN MSM photodiode again showing the largest leakage current and the 45GaN MSM photodiode exhibiting the smallest. The 10 μm design MSM photodiodes fabricated on

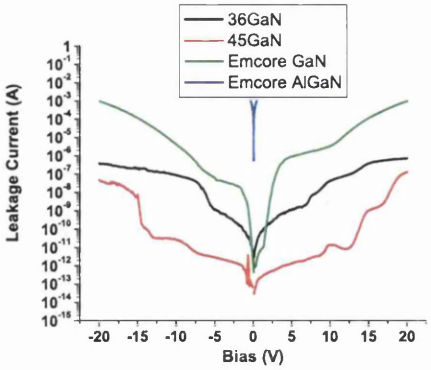

Figure 7.12: I-V curves of MSM photodiodes with the 5 μm design fabricated on various GaN/AlGaN materials

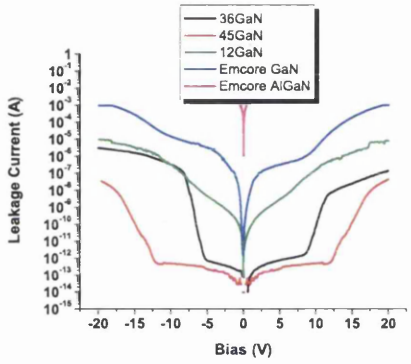

Figure 7.13: I-V curves of MSM photodiodes with the 10 μm design fabricated on various GaN/AlGaN materials

the 36GaN, 12GaN and Emcore GaN materials also show good leakage current characteristics. The fact that both designs fabricated on the Emcore AlGaN material have extremely large leakage currents implies that this is a material rather than a fabrication effect.

A comparison of the leakage currents of the MSM photodiodes with the

5 μm design and the 10 μm design fabricated on the 36GaN, 45GaN and Emcore GaN is shown in Figure 7.14. Both diode designs fabricated on the 45GaN and Emcore GaN have similar leakage current characteristics. The 10 μm design fabricated on the 36GaN material however, at bias voltages $\leq$ +/-5 V, exhibits leakage currents several orders of magnitude smaller than the 5 μm design fabricated on the same material.

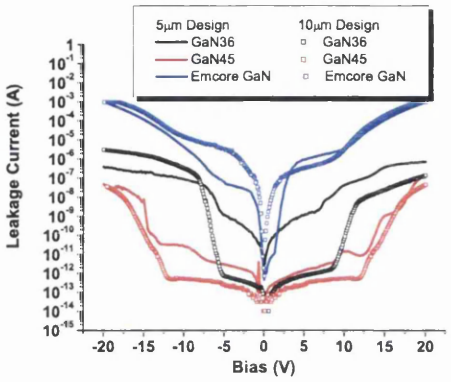

Figure 7.14: Leakage current comparison of the two different diode designs

7.4.2 Spectral Response at 0V

All spectral response measurements were performed by scanning the detector in the x and y directions using the motorised stage until the maximum photocurrent at a wavelength of 235 nm was found. Spectral response scans were then made from 180 nm to 500 nm in 1 nm steps by changing the wavelength with the monochromator. Figure 7.15 shows the spectral response curves of the MSM GaN photodiodes at an applied bias of 0 V. The plot on the left compares the spectral responses of the 5 μm design fabricated on the various GaN materials while the plot on the right compares the spectral responses of the 10 μm design. Due to the large leakage current of the MSM AlGaN

diodes ($\sim$ 1 μA at 0 V) there was no observable change in the total current due to the photocurrent. All the spectral response curves exhibit a photo-

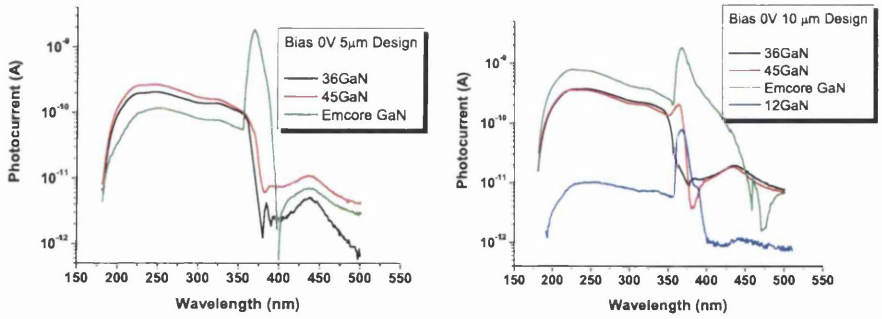

Figure 7.15: Spectral response curves at 0V of the 5 μm design (left) and 10 μm design (right) MSM GaN diodes fabricated on the 36GaN, 45GaN, 12GaN and Emcore GaN. A semi-log scale is used for clarity.

peak between 220 nm and 240 nm. This peak is expected and is typical of a deuterium source. However both the 5 μm design and 10 μm design MSM Emcore diodes exhibited a further unexpected peak at a wavelength of 365 nm. This wavelength corresponds to the cut-off wavelength (λ_c) of GaN, so called because for wavelengths longer than λ_c the photocurrent drops several orders of magnitude and the response of the detector is "cut-off". It will be shown that the 36GaN and 45GaN MSM diodes also exhibit a large photocurrent peak at 365 nm when placed under bias. This unusual peak at 365 nm has also been reported by Ferguson et. al [152] who fabricated MSM detectors on highly resistive GaN. The material make-up was similar to that studied in this thesis; a conductive n-GaN buffer was grown on top of a sapphire substrate and the highly resistive 2 μm thick GaN layer was grown on top. No explanation for the origin of this photo-peak at 365 nm is given by the authors.

One possible explanation for the appearance of this unexpected photo-peak is related to the influence of the 2 μm thick n-GaN buffer layer on the charge transport properties of the photo-generated carriers. Figure 7.16(a) shows the structure of GaN material that is typically used for MSM photo-diodes. A thin nucleaton layer, approximately 30 nm thick, is grown on top

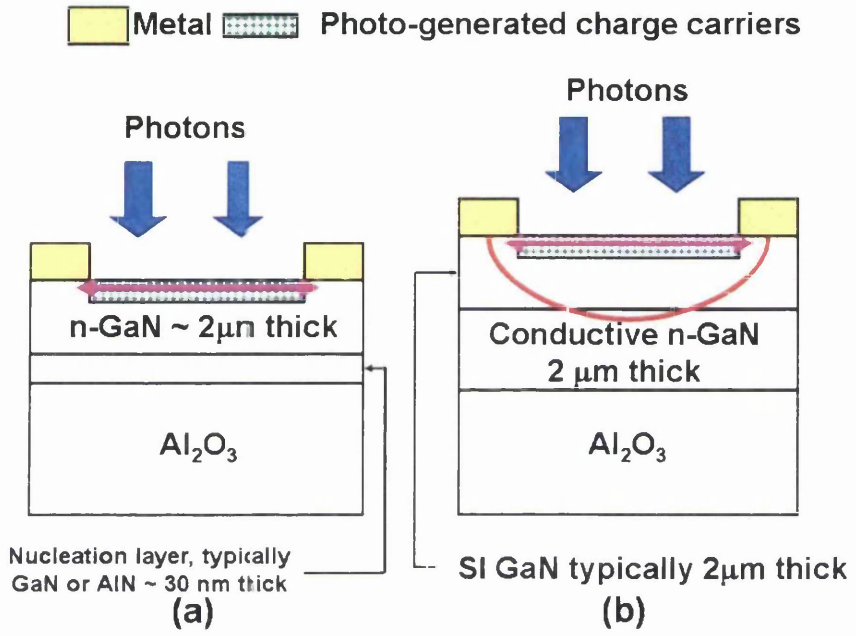

Figure 7.16: Transport routes of photo-generated charge carriers in SI GaN grown on a thin nucleation layer (a) and SI GaN grown on a conductive buffer layer (b)

of a sapphire substrate and the GaN material (typical carrier concentration $\geq 10^{16}$ cm^{-3}) is grown on top of the nucleation layer. The nucleation layers used are typically of a low conductivity. A plot of absorption coefficient versus wavelength for GaN is shown in Figure 7.17. The plot data shows that photons with an energy greater than 3.39 eV are absorbed within approximately 100 nm of GaN (using the general relationship that absorption

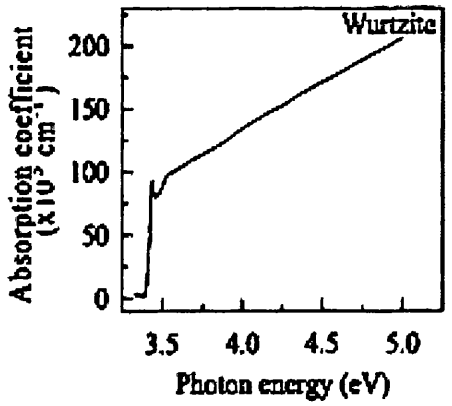

Figure 7.17: Absorption spectrum for GaN at room temperature [153]

depth = 1/absorption coefficient). This means that the surface and sub-surface properties of the GaN material play an extremely important role in transport of the photo-generated carriers. When UV light is incident on the detector charge carriers are generated in the thin region close to the surface of the material (green and white checkered region). A bias is applied to the metal electrodes and the charge carriers are extracted towards the contacts (pink line).

However, as shown in Figure 7.16(b), the GaN material studied in this thesis has a 2 μm thick conductive buffer layer which has an influence on the electric field within the device. The horizontal mobility of the photo-generated carriers, parallel to the surface (pink line), is much less than in the direction of crystallite growth which is perpendicular to the surface. It is also likely that there exist percolative charge transport channels in the SI GaN material which promote the vertical transport of charge carriers, instead of lateral transport. Moreover, the distance between the electrodes, i.e the finger spacing, is at least twice that of the SI epitaxial GaN thickness. Therefore it is possible that the photo-generated charge carriers will prefer to

travel vertically downwards through a percoation channel, along the buffer layer and then back up towards an electrode via another percolation channel instead of horizontally traversing the SI GaN layer to be collected by the electrode. The net result is that the current path through the red line of Figure 7.16(b) may exceed or be comparable to that of the pink line.

The photocurrent is therefore dependent on whether or not the UV light penetrates deep enough into the SI GaN to reach the percolative transport channels. These percolative channels are likely to begin several tens of nanometres below the surface (there will be some crystal re-arrangement at the surface). Photons with an energy greater than 3.39 eV are absorbed very close to the surface of the GaN material and the photo-generated charge carriers travel horizontally towards the electrodes (pink line) instead of through percolative channels. In GaN the surface carrier lifetime is much shorter than the bulk carrier lifetime. This is a result of the large number of defects within the surface layers that are able to trap any charge carriers. Therefore the induced photocurrent is dependant on the surface quality of the SI GaN. Any inhomogeneities or roughness of the surface significantly reduces the detector photocurrent.

However as the photon energy decreases, the penetration depth into the SI GaN material increases. At a photon energy of 3.39 eV the generated charge carriers are able to reach the percolative channels and the photocurrent increases since carrier lifetime is greater in the bulk GaN than in the surface regions. This is one possible, albeit non-analytical, explanation for the unexpected large photocurrent peak at 365 nm. In terms of this thesis this artefact can effectively be disregarded as the region of interest for circular dichroism is for wavelengths below 240 nm. From here on only the wavelength range 180-240 nm is considered when comparing the maximum

photocurrents, responsivities and UV/visible contrasts of the various MSM GaN photodetectors.

For the 5 μm design it can be seen from Figure 7.15 that between 180 nm and 240 nm the 45GaN detector exhibits the largest photocurrent and the Emcore GaN detector exhibits the lowest photocurrent. However the right hand plot of figure 7.15 shows that for the 10 μm design the photocurrent from the Emcore GaN device is larger than the photocurrents of the other three materials. The 10 μm design 36GaN and 45GaN devices have similar photocurrents while the 12GaN device has a photocurrent two orders of magnitude smaller than the Emcore GaN device.

Figure 7.18 is a plot comparing the photocurrents of the 5 μm design and 10 μm design fabricated on the 36GaN, 45GaN and Emcore GaN materials. It can be seen that for all three GaN materials the photocurrent of the MSM

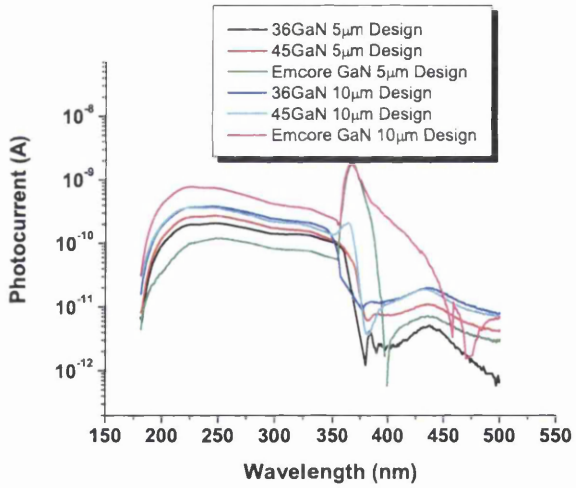

Figure 7.18: Plot comparing the spectral responses of the 5 μm design and 10 μm design

diodes with the 10 μm design is larger than that of the 5 μm design. These re-

sults contradict the findings of Monroyet. al [149] who state that the smaller the finger separation, the larger the photocurrent. However the epitaxial GaN material Monroy studied was grown on a thin AlN nucleation layer. Figure 7.18 further supports the theory that the photo-generated charge carriers follow percolation paths on their way to the collecting electrodes. If this was not the case then doubling the distance between the electrodes would reduce the electric field by half and therefore reduce the photocurrent - an effect which is not seen.

Table 7.3 compares the responsivities and UV/visible contrasts of the MSM photodetectors. The responsivity is calculated using Equation 7.1 and evaluated at 235 nm. The UV/Visible contrast is calculated as a ratio of the photocurrent at 235 nm divided by the photocurrent at 500 nm.

Material/Design	Responsivity x 10^{-4} (A/W)	UV/visible contrast
36GaN 5 μm	2.50	281
36GaN 10 μm	4.63	47
45GaN 5 μm	3.30	69
45GaN 10 μm	4.43	47
Emcore GaN 5 μm	1.34	38
Emcore GaN 10 μm	9.45	110
12GaN 10 μm	0.12	14

Table 7.3: Responsivities and UV/visible contrasts of the MSM photodetectors fabricated on the various GaN materials

7.4.3 Effect of Applied Bias

Spectral response measurements of the MSM photodiodes were performed at several bias voltages between -9 V and 9 V. The spectral response plots subsequently shown are for negative bias voltages. Both the 5 μm design and 10 μm design detectors fabricated on the Emcore GaN material have large leakage currents even at small applied bias voltages (+/- 0.1 V). For these devices there was no observable difference between the photocurrent and leakage current.

The spectral response curves of the 5 μm design (left) and the 10 μm design (right) MSM 36GaN detectors at several applied bias voltages are shown in Figure 7.19. For both detectors, as expected when studying MSM

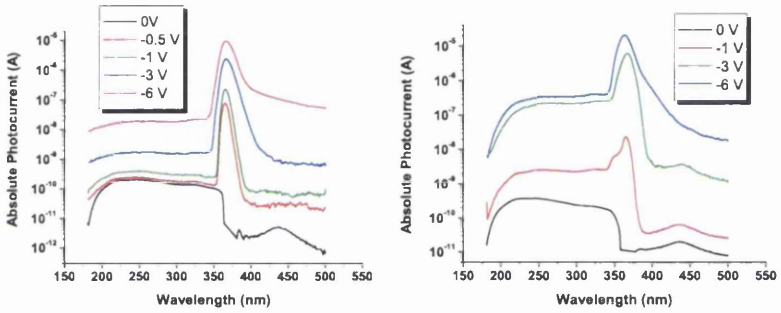

Figure 7.19: Spectral response of the 5 μm (left) and 10 μm (right) design 36GaN devices at several bias voltages

devices, the photocurrent increases with increasing applied bias. This is due to faster extraction of the charge carriers before they can recombine or be trapped in defect levels. The maximum responsivity of the 5 μm design 36GaN detector is 20 mA/W at 235 nm while the 10 μm design 36GaN detector exhibits a maximum responsivity of 300 mA/W at the same wavelength.

Figure 7.20 shows the spectral response curves of the MSM 45GaN detector at various bias voltages. The response curves of the 5 μm design 45GaN device are on the left while the response curves of the 10 μm design 45GaN device are on the right. Again it is seen that as the bias voltage between the

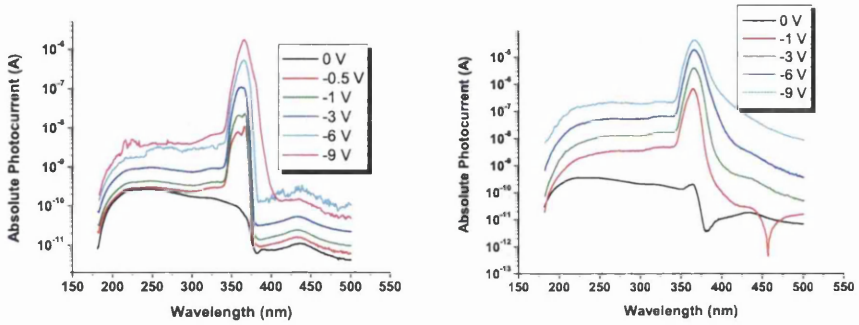

Figure 7.20: Spectral response of the 5 μm and 10 μm design 45GaN devices at several bias voltages

sets of fingers is increased there is an increase in the measured photocurrent. At an applied bias of -9 V the 5 μm design 45GaN device exhibits a responsivity of 3.7 mA/W while at the same bias the 10 μm design 45GaN device exhibits a responsivity of 175 mA/W.

The spectral response curves of the 10 μm design 12GaN detector at various bias voltages are shown in Figure 7.21. The photo-peak observed at 365 nm in the spectral response curves of the biased MSM detectors fabricated on the thin SI epitaxial GaN is not present in the spectral response curves of the 10 μm design 12GaN detector (except at 0 V). This property supports the theory that the conductive n-GaN buffer layer has an important effect on the charge transport path of the photo-generated charge carriers. The distance between the collecting electrodes of the 10 μm design 12GaN detector is comparable to the epitaxial thickness. Therefore it is probable that

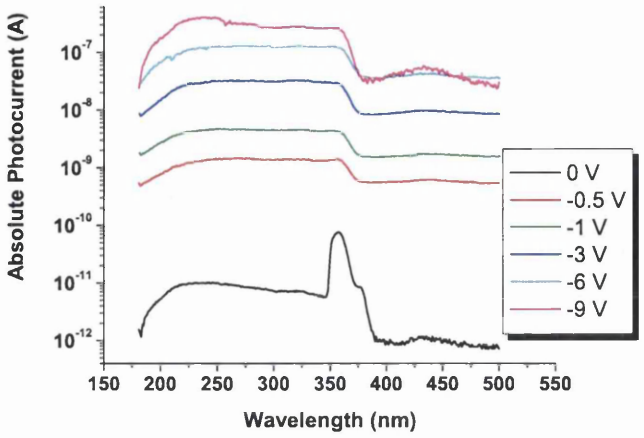

Figure 7.21: Spectral response data of the 10 μm design 12GaN device at bias voltages of 0 V, -0.5 V, -1 V, -3 V, -6 V and -9 V

the preferential route of the photo-generated carriers is directly towards the electrodes instead of via percolation paths. At 235 nm the responsivity of the 10 μm design 12GaN detector at an applied bias of -9 V is 433 mA/W.

A comparison of the spectral response curves between the 5 μm design and 10 μm design 36GaN detectors at bias voltages of -1 V, -3 V and -6 V is shown in Figure 7.22. It can be seen that for all applied bias voltages the photocurrent of the 10 μm design 36GaN detector is one or two orders of magnitude greater than that of the 5 μm design 36GaN detector. A similar trend is also observed of the 5 μm design and 10 μm design 45GaN detectors (see Figure 7.23). Table 7.4 summarises the maximum responsivities and UV/visible contrasts of the various MSM GaN test structures at 235 nm. The results clearly indicate that a finger separation/width of 10 μm should be used as the preferred diode geometry of the 46 channel diode array detector. The results also show that at a bias voltage of 0 V the MSM diodes fabricated

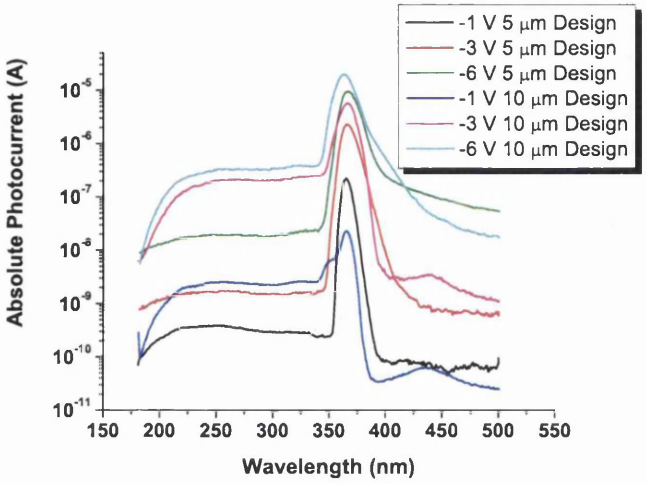

Figure 7.22: Spectral response curves of the 5 μm design and 10 μm design 36GaN detectors at bias voltages of -1 V, -3 V and -6 V

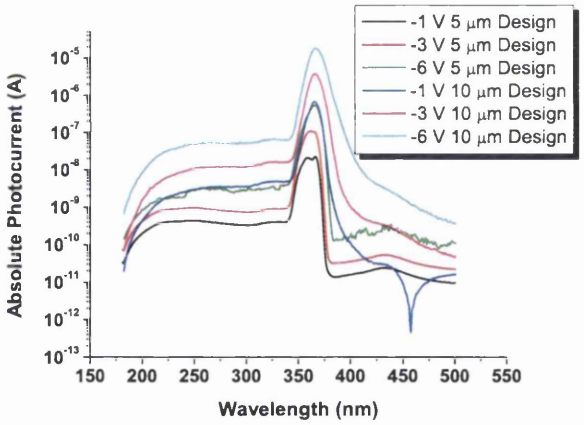

Figure 7.23: Spectral Response curves of the 5 μm design and 10 μm design 45GaN detectors at bias voltages of -1 V, -3 V and -6 V

Material/Design	Responsivity (mA/W)	UV/visible contrast	Bias (V)
36GaN 5 μm	20	0.35	-6
36GaN 10 μm	414	23	-6
45GaN 5 μm	1.9	14	-6
45GaN 5 μm	3.7	67	-9
45GaN 10 μm	44	112	-6
45GaN 10 μm	177	20	-9
12GaN 10 μm	122	3.3	-6
12GaN 10 μm	436	13	-9
Emcore GaN 5 μm	0.134	38	0
Emcore GaN 10 μm	0.945	110	0

Table 7.4: Maximum Responsivities and UV/visible contrasts of the MSM photodetectors fabricated on the various GaN materials

on the Emcore GaN material exhibit the maximum responsivity (see Table 7.3). However at 0 V the maximum responsivities of the 36GaN and 45GaN detectors are roughly comparable to the responsivity of the Emcore GaN. At an applied bias of -6 V and using the 10 μm design it can be seen that the 12GaN detector has a maximum responsivity of 436 mA/W, the 36GaN detector a maximum responsivity of 414 mA/W and the 45GaN detector a maximum responsivity of 44 mA/W. On examining the results, if the 46 channel diode array detector is to operate unbiased, the optimal material to use is the Emcore GaN. If the array detector is to be biased then 12GaN should be the better material to use.

However a lack of suitable material meant that is was not possible to fabricate the 46 channel diode array detector on either the Emcore GaN or

the 12GaN material. Several attempts were made at fabricating the array detector structure on the 36GaN and 45GaN materials. As a result of several fabrication difficulties, namely poor pattern transfer and lift-off failure, it was only possible to fabricate the array detector on the 45GaN material. The following section describes the specific fabrication details and initial characterisation of the 45GaN array detector.

7.5 Fabrication and Characterisation of GaN Array Detector

Photolithographic techniques were used to fabricate a 46 channel MSM diode array detector on the 45GaN material. Schottky contacts were realised by evaporating 50 nm/ 200 nm of Pd/Au and each MSM diode had a finger separation/width of 10 μm. The size of each individual diode was 400 μm by 590 μm and the pitch between two adjacent diodes was 500 μm. One set of fingers of each diode is linked to a central common electrode for biasing purposes. A picture of the left hand section of the array detector is shown in Figure 7.24. The common bias line connecting each of the diodes can be seen as can the square bond pads for the second set of fingers of each diode.

The 16-pix set-up relies on the ability to plug the UV light array detector into a commercial 'female' Dual-in-Pin (DIP) socket. It was therefore necessary to design and produce a PCB that was compatible with a commercial 'male' DIP socket so that the GaN array detector could be used in the 16-pix set-up. Figure 7.25 shows an exported image of the PCB design. The smaller square copper pads were of dimension 0.5 mm on each side while the larger square copper pads were of dimension 1.5 mm on each side. The pitch of these larger square copper pads was 2.54 mm, matching the pitch

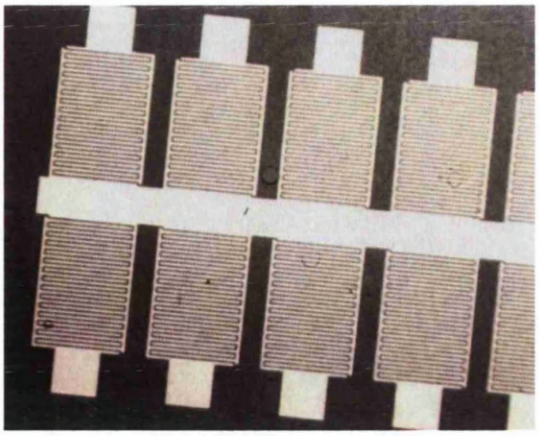

Figure 7.24: Optical image of a section of the 46 channel diode array detector fabricated on the 45GaN material. The central strip connecting the diodes is for biasing purposes.

Figure 7.25: PCB design for the read-out of the GaN array detector. The track width is 200 μm.

between the pins of the open frame male DIP socket purchased from E-tec Interconnect Limited. Figure 7.26 shows an image taken of the bonded 46 channel diode array detector.

A second PCB was designed and fabricated for the purpose of performing dark current and spectral response measurements on the 45GaN array detector. This PCB design is shown in Figure 7.27. The track width is 300 μm,

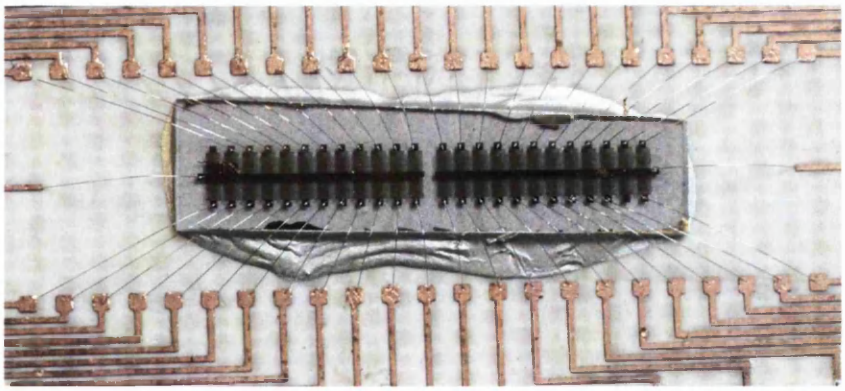

Figure 7.26: Picture of the 45GaN array detector. There are 48 wire bonds in total; 46 for the individual diodes and two for the central ground lines.

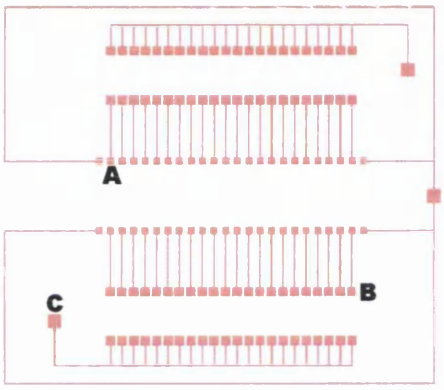

Figure 7.27: PCB designed to evaluate the dark current and spectral response of the 45GaN array detector

copper pads A are of dimension 1.5 mm by 1.5 mm, pads B are of dimension 2 mm by 2 mm and pads C are of dimension 3 mm by 3 mm. Holes were drilled in the centre of the smaller square pads (pads A) and a female DIP socket placed into the board. The completed test board is shown in Figure 7.28. Electrical switches were soldered between the copper tracks and three

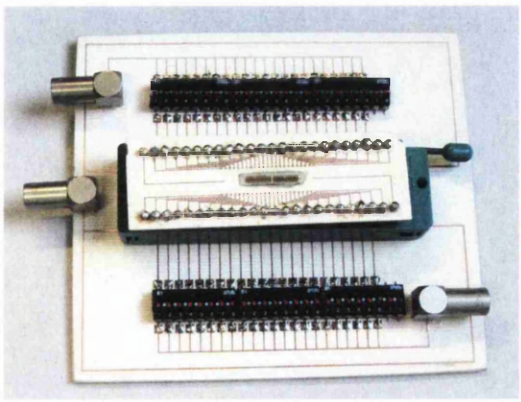

Figure 7.28: Picture of the completed test board with the GaN detector and male DIP socket plugged into the test board.

lemo connectors were soldered on top of pads C. The board enabled the user to apply a bias to the device and to turn individual MSM GaN diodes on and off.

7.5.1 Dark Current and Spectral Response Results

I-V measurements were performed in order to assess the dark current characteristics of the 45GaN array detector and to establish if there were any defective or shorted channels. The following convention was used in order to identify individual MSM diodes. In Figure 7.26 channels 2-23 correspond to the top set of MSM diodes going from left to right. Channels 24-47 correspond to the bottom set of MSM diodes again with channel 24 being the bottom left MSM diode and channel 47 the bottom right MSM diode. Channels 1 and 48 are bias lines. Figure 7.29 shows the I-V characteristics of 6 selected channels up to an applied bias of +/-10 V. The other 40 channels exhibited I-V properties similar to the six shown in Figure 7.29 with the exception of channels 2 and 46 that were shorted. This represented a functional

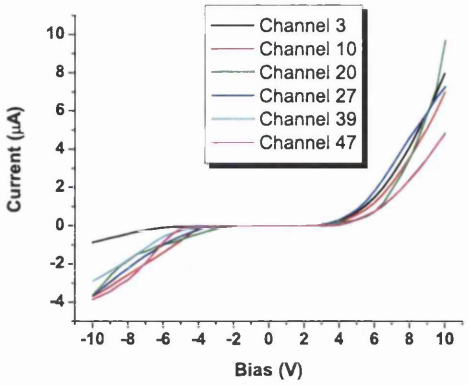

Figure 7.29: Dark current characteristics of six channels. I-V measurements were performed on all 46 channel channels however for clarity only six channels are shown in this plot.

channel yield of 96.5%.

Figure 7.30 shows the spectral response curves at an applied bias of 0 V of several channels of the 45GaN array detector. Again a delay time of 5 seconds was used between each wavelength increment. It can be seen that

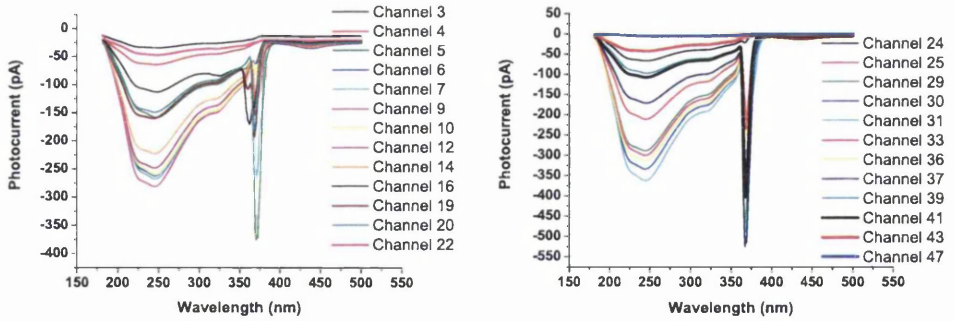

Figure 7.30: Spectral response curves of selected channels of the 45GaN array detector at an applied bias of 0 V

the channels located in the centre of the GaN sample exhibited the largest

photocurrent (e.g. channels 7-14 and 29-35). Indeed there is a definite trend where the photocurrent decreases the further the MSM diode is from the centre of the GaN sample. This is confirmed by the fact that the channels at the extreme edges of the array (channels 3,22, 24 and 27) have far lower photocurrents compared to the other channels. An explanation of this observed property of the 45GaN array detector could be that the dicing procedure created stress within the GaN material. This stress is more pronounced at the edges of the GaN sample and as a result the material here is of poorer quality and more defective compared to the GaN material in the central region of the cut sample. The majority of channels also exhibited the photoresponse peak at around 360-370 nm that was also observed in the 45GaN test structures.

7.5.2 Initial Tests of 45GaN Array Detector Using 16-pix Set-up

After initial characterisation of the 46 channel diode array detector further spectral response measurements were performed at the Rutherford Appleton Laboratory using the 16-pix set-up. The measurement set-up consisted of a blue LED, a Bentham TMC 300 monochromator, a photoelastic modulator operating at 50 kHz (used to polarise light from the protein sample), the 46 channel 45GaN array detector, the 16-pix read-out system and a PC. The electronics of the 16-pix set-up are such that a high frequency filter is used for separation of the AC and DC components of the photocurrent signal. The AC and DC values are measured at a rate of 20 MHz and averaged over every half period of the photoelastic modulator frequency, i.e. every 25 kHz. A further superaveraging is performed by the software and the superaveraged DC, AC_{high} and AC_{low} values are calculated, displayed onscreen to the user and stored to disk. The number of superaverages could be varied between 1

and 10000. A superaverage of one results in data being stored every 20 μs while a superaverage of 10000 results in a measurement being stored every 200 ms. The CD signal is calculated using the equation:

$$CD = \frac{AC_{high} - AC_{low}}{DC} \tag{7.2}$$

Figure 7.31 shows the DC photoresponse of 3 channels of the 45GaN array detector when the LED is turned on and turned off. All three channels show

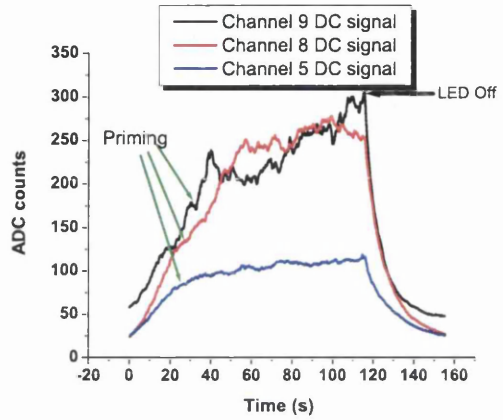

Figure 7.31: DC photoresponse of channels 5, 8 and 9 of the 45GaN array detector

a slow rise in photocurrent after the LED is turned on, taking approximately 110 seconds for the photocurrent to level-off. This so called 'priming' effect is attributed to photo-generated carriers filling defect traps in the SI 45GaN material therefore increasing the photoconductivity of the device (since carrier lifetime is increased). The photoconductivity slowly increases with constant illumination until all of the traps are filled and equilibrium is reached. The priming effect is clearly due to the SI GaN material and not the geometry of the MSM detector since, as explained in Section 7.2.1, one of the properties of MSM photodetectors is their fast response times.

The CD signal at any wavelength is very weak and is approximately 10^{-3}-10^{-5} of the initial beam. This is one reason why synchrotron radiation, with its large photon flux, is used for CD experiments. This also means that any small changes in the detector significantly affects the measured CD signal and in the worst instance could completely mask the CD signal. These small changes include unwanted fluctuations in the photocurrent through for example trapping or de-trapping of charge or priming. It is almost certain that the significant priming exhibited by channels 5,8 and 9 of array detector would result in severe distortions of the CD spectrum of any protein. It was also found that the difference between the AC_{high} and AC_{low} values of channels 5, 8, 9 of the GaN array were too low for an accurate measurement of CD.

The conclusion of these tests with the 16-pix set-up was that is was extremely unlikely that the 46 channel 45GaN array detector would produce the CD spectrum expected if it were used in a protein CD experiment. This is due to the priming effect of the device and also because the difference between the AC_{high} and AC_{low} signals was extremely small. It was decided to try to maximise the photoresponse of the MSM diode by increasing the active area of the device. The following section describes how the active area of the MSM detector was increased and gives the spectral response measurements of these new devices.

7.6 New Diode Design and Semi-Transparent Contacts

Two strategies were pursued to increase the active area of the MSM diode.

- The physical area of the device was increased.

- Semi-transparent contacts instead of full metal contacts were employed.

The previous dimensions of the GaN MSM photodetectors were 400 μm by 590 μm. The dimensions were increased to 900 μm by 2500 μm resulting in over a ten-fold increase in the active area of the detector. In order to further increase the active area, a slight alteration was also made to the geometry of the MSM diode. This involved keeping a finger separation of 10 μm and reducing the finger width to 5 μm. The finger separation was chosen in accordance with the results shown earlier in this chapter where the MSM devices with a finger separation of 10 μm exhibited larger photocurrents than those with a 5 μm finger separation.

The second approach used to increase the active area was to employ semi-transparent contacts (approximately 10 nm thick) instead of full metal contacts. Ni, Au, Pt, Pd, indium-tin-oxide (ITO) have all been been used to realise semi-transparent contacts to n-GaN [154]. Of these metals Pd has the highest light transmittance of 70% [155] in the wavelength region 200 nm to 350 nm. Table 7.5 compares the active areas of the smaller area diode design (studied earlier in this chapter), the revised larger area full metal contact design and the larger area semi-transparent metal contact design. These designs are referred to as "design A", "full metal" and "semi-transparent metal" respectively for the remainder of this thesis.

Design	Active Area (mm^2)
A	0.116
Full Metal	1.27
Semi-transparent metal	1.94

Table 7.5: Active areas of designs A, full metal and semi-transparent metal

7.6.1 Fabrication of Full Metal and semi-transparent metal Designs

Four channel and eight channel MSM diode designs were drawn and subsequently patterned onto a photolithographic mask. For the semi-contact structure two designs were required, one for the interdigitated fingers that were to be metalised with 10 nm Pd and a second design for the bond pads that were to be metalised with 200 nm of Au. Alignment marks, consisting of crosses of various dimensions, were also drawn for subsequent registration of the thin and thick metal layers. A central electrode connected the MSM diodes together enabled biasing of the device. Figure 7.32 shows an image of the 4 channel array diode design.

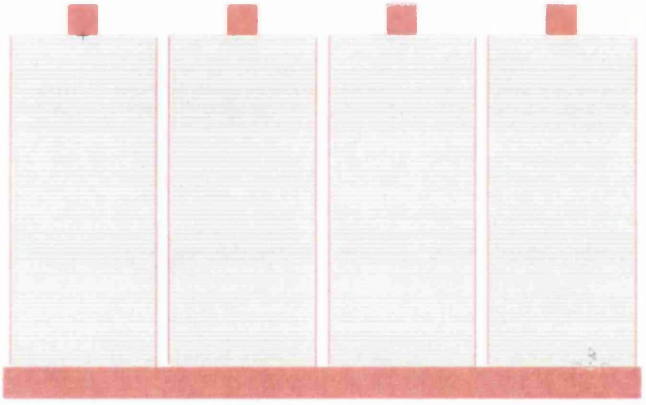

Figure 7.32: L-Edit image of the full-metal 4 channel MSM diode design. The central bar at the bottom connects the diodes together

Several attempts were made using photolithographic techniques at fabricating the 4 channel and 8 channel diode designs onto the 36GaN and 45GaN materials. However there were significant problems such as poor pattern transfer and failed lift-off (see Figure 7.33) that prevented successful

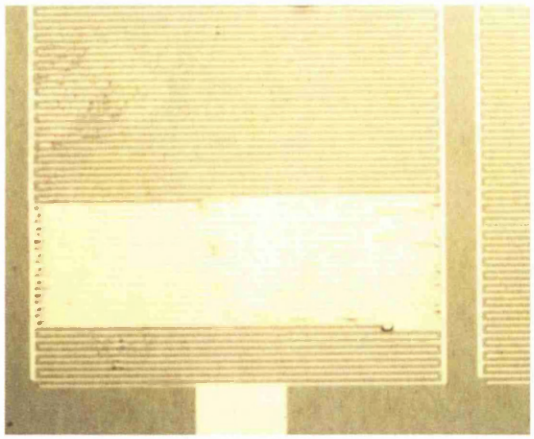

Figure 7.33: Lift-off failure

fabrication of these larger area diode devices. It is likely that the large area and dense nature of the structures to be patterned were the causes for the this failure to produce working devices.

It was subsequently decided that e-beam lithography should be used to fabricate the 4 channel and 8 channel full metal and semi-transparent metal devices. Dose tests were made on bi-layers of PMMA resist in order to establish the optimal exposure dose for successful pattern transfer. Once the optimal dose was established e-beam lithography techniques, described in Chapter 2, were used to pattern the samples. A bi-layer of PMMA resist was used in order to assist metal lift-off. In the case of the semi-transparent metal design, the e-beam was used to write the areas that were to be evaporated with 10 nm of Pd. Photolithography techniques were then used to pattern the areas for the deposition of 200 nm of Au for bonding purposes. There proved to be no difficulty in aligning the thin metal layer and the thick metal layer. Figure 7.34 shows optical images of a full-metal MSM diode (left) and a semi-transparent metal MSM diode (right). It is easy to differentiate

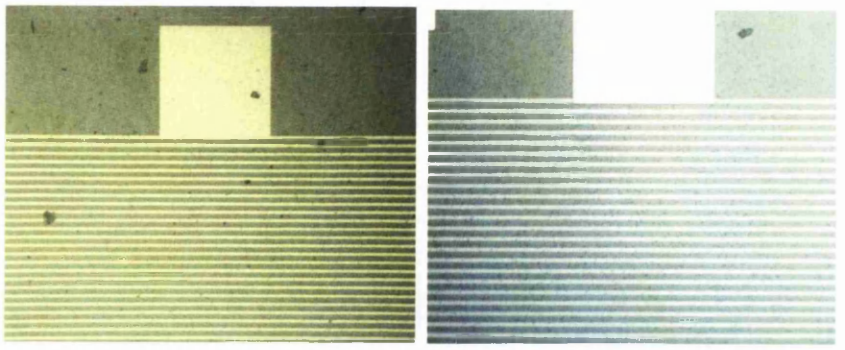

Figure 7.34: Optical images of the full-metal MSM diode (left) and semi-transparent metal MSM diode (right)

between the thin metal and thick metal regions of the semi-transparent metal MSM diode. It can also be seen that there is excellent alignment of the bond pad and the top semi-transparent finger.

Both the full metal and semi-transparent metal structures were fabricated on the 36GaN and 45GaN materials. I-V and spectral response measurements were performed and the effect of the new diode design and metalisation scheme assessed. It should be noted that at a distance of 2 mm between the detector and the fibre optic cable the area of the MSM device is now larger than the beam area. All spectral response measurements were performed with the detector a distance of 2 mm from the fibre optic cable.

7.6.2 I-V and Spectral Response Results of New Devices

The dark current versus voltage characteristics of the full metal and semi-transparent metal designs fabricated on the 36GaN and 45GaN showed typical Schottky/Schottky characteristics and leakage currents of approximately

10^{-7} A up to an applied bias of +/- 20 V. As with the smaller area MSM diodes a slow breakdown of the Schottky contact was observed after certain bias voltages.

Figure 7.35 shows the spectral response curves of the 4 channel full metal design MSM arrays fabricated on the 36GaN material (left) and 45GaN material (right). All spectral response curves were obtained at 0 V applied bias.

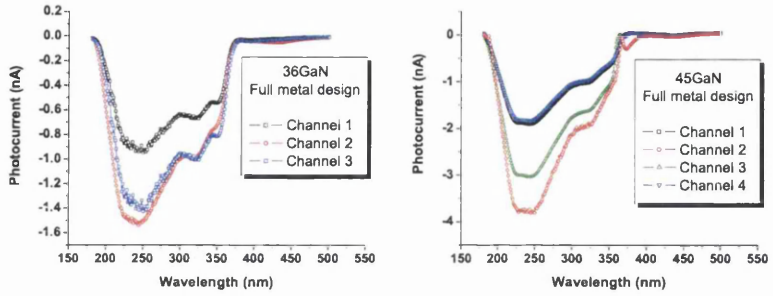

Figure 7.35: Spectral responses curves of the full metal design MSM diodes fabricated on the 36GaN and 45GaN materials

In Figure 7.32 channel 1 corresponds to the far left diode and the channel number increases sequentially from left to right. Channel 4 of the 36GaN array detector was shorted. It was observed that the channels situated in the centre of the array exhibited larger photocurrents than the channels at the edge of the array. This can be attributed to edge effects discussed in Section 7.5.1. At 235 nm the maximum photocurrent of the full metal 36GaN design was approximately 1.5 nA whereas the maximum photocurrent of the full metal 45GaN design was 3.75 nA.

The spectral response curves of the 4 channel semi-transparent metal design MSM arrays fabricated on the 36GaN and 45GaN materials are shown in Figure 7.36. All spectral response curves were obtained at 0 V. For both

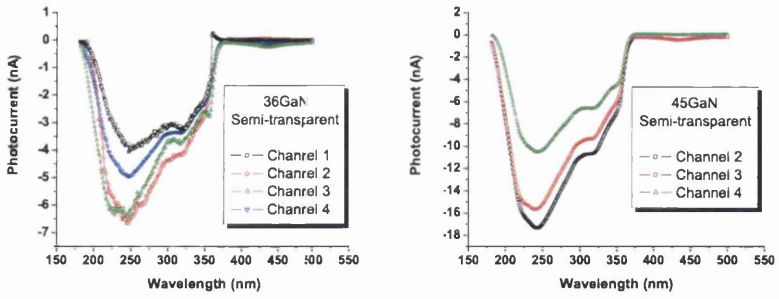

Figure 7.36: Spectral responses curves of the semi-transparent metal MSM diodes fabricated on the 36GaN and 45GaN materials

devices and all channels the photocurrent peaked at 240 nm instead of the expected 235 nm. This is probably due to increased priming since the active area of the semi-transparent metal diode design is larger than that of the full metal design. At 235 nm the maximum photocurrent exhibited by the semi-transparent metal 36GaN design was 6 nA while the maximum photocurrent exhibited by the semi-transparent metal 45GaN design was 17 nA.

Figure 7.37 compares the spectral responses of the initial diode design (design A), the full metal design and the semi-transparent metal design fabricated on the 36GaN and 45GaN materials. All response curves were obtained at 0 V and the chosen curves for the full metal and semi-transparent metal designs were those from the channels that exhibited the largest photocurrent at 235 nm. For example the spectral response curve of channel 3 of the semi-transparent metal 36GaN array detector is used for comparison with the other two diode designs. As expected an increase of the diode active area results in an increase in the photocurrent. Table 7.6 summarises the responsivity and UV/visible contrasts of the different MSM diode designs and contact schemes fabricated on the 36GaN and 45GaN materials. The maximum responsivities

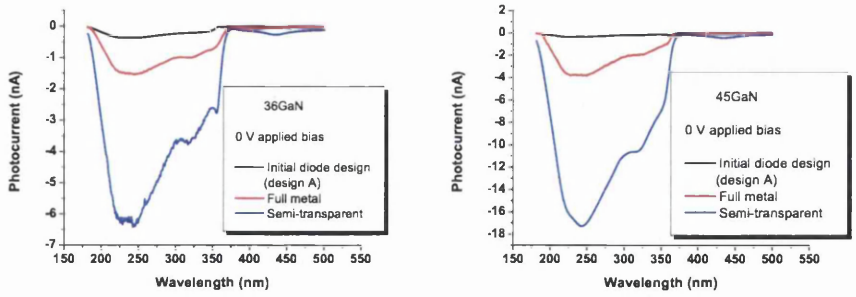

Figure 7.37: Spectral response comparison of the three diode configurations studied in this thesis. Response curves of the designs fabricated on the 36GaN material are on the left and the response curves for the 45GaN material are on the right.

Material/Design	Responsivity (mA/W)	UV/visible contrast
36GaN design A	0.46	47
36GaN full metal	1.6	105
36GaN semi-transparent metal	6.9	50
45GaN design A	0.43	47
45GaN full metal	4.1	219
45GaN semi-transparent metal	18.8	85

Table 7.6: Responsivities and UV/visible contrasts of design A, semi-transparent metal and full-metal device fabricated on 36GaN and 45GaN

at 235 nm of the full metal and semi-transparent metal designs fabricated on the 45GaN material are larger than the maximum responsivities of the corresponding designs fabricated on the 36GaN material. For example the semi-transparent metal 45GaN device has a maximum responsivity of 18.8 mA/W which is more than twice the maximum responsivity exhibited by the semi-transparent metal 36GaN device (6.9 mA/W).

I-V measurements up to an applied reverse bias of 20 V were performed with 235 nm light incident on the full metal and semi-transparent metal MSM devices. Photocurrent versus bias plots for the full metal 36GaN and 45GaN devices are shown in Figure 7.38. Also shown on the plots are the dark current measurements. A bias step of -0.1 V and a delay time of 10 seconds between each measurement was set in order to minimise priming effects on the measured detector photocurrent. The photocurrent of the full-

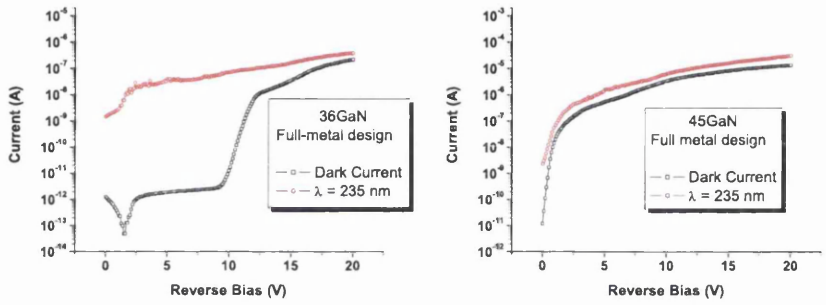

Figure 7.38: Photocurrent and dark current plots for the full metal 36GaN and 45GaN detectors

metal 36GaN device is at least three orders of magnitude greater than the leakage current up to a reverse bias of 10 V. For reverse biases greater than 1 V the photocurrent of the full metal 45GaN device is approximately three times that of the leakage current.

Figure 7.39 shows the photocurrent and dark current plots up to a reverse bias of 20 V for the semi-transparent metal design 36GaN and 45GaN detectors. The photocurrent/dark current ratio decreases for the semi-transparent metal 36GaN device with increasing applied bias. For both the full metal and semi-transparent metal 36GaN and 45GaN detectors the maximum responsivity occurs at a reverse bias of 20 V while the maximum photocurrent/dark

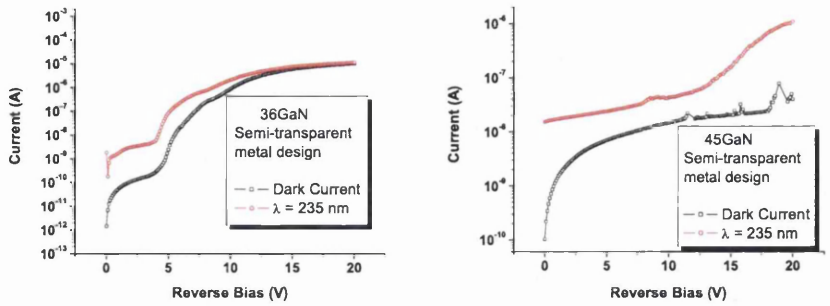

Figure 7.39: Photocurrent and dark current plots for the semi-transparent metal 36GaN and 45GaN detectors

current contrast occurs at 0 V. Table 7.7. shows the responsivity and photocurrent/dark current contrast values of the 36GaN and 45GaN detectors for applied biases of 0 V and -20 V. At 0 V the semi-transparent metal 45GaN

Material/Design	Resp. (mA/W)	Photo/dark contrast	Bias (V)
36GaN full metal	1.6	1102	0
36GaN semi-transparent metal	6.9	1736	0
45GaN full metal	4.1	330	0
45GaN semi-transparent metal	18.8	148	0
36GaN full metal	430	1.7	-20
36GaN semi-transparent metal	12700	1.1	-20
45GaN full metal	22220	1.48	-20
45GaN semi-transparent metal	1177	27	-20

Table 7.7: Comparison of the responsivities and photocurrent/dark current contrasts of the full metal and semi-transparent metal 36GaN and 45GaN devices at reverse biases of 0 V and 20 V. The photocurrent was measured at a wavelength of 235 nm.

detector has the largest responsivity compared to the other devices. The largest photocurrent/dark current contrast is shown by the semi-transparent metal 36GaN device at a bias of 0 V. At a reverse bias of 20 V the full metal 45GaN detector has a responsivity of 22.2 A/W.

This section has shown that the responsivity of an MSM GaN detector can be maximised through increasing the physical size of the device and by using semi-transparent contacts rather than full metal contacts. In order to maximise the responsivity of a MSM GaN detector semi-transparent contacts should always be employed where possible.

7.7 Summary and Conclusions

The aim of this chapter was to establish the optimal GaN/AlGaN material and diode geometry for the subsequent fabrication of a 46 channel diode array detector. Two MSM diode geometries were investigated; one with a finger separation/width of 5 μm and a second with a finger separation/width of 10 μm. It was found that 10 μm design MSM detectors exhibited larger photocurrents than the 5 μm design detectors and that for a number of devices a photo-peak was present at 365 nm. Both these results were unexpected and are attributed to the influence of the conductive buffer layer on the photo-generated charge carriers and also to percolation charge paths within the SI GaN material. A 46 channel diode array detector was fabricated on the 45GaN material with each MSM diode having a finger separation/width of 10 μm. Photoresponse tests using the 16-pix set-up at RAL showed that the channels of the array detector exhibited substantial priming. This priming is attributed to photo-generated carriers filling defect traps in the SI 45GaN material therefore increasing the photoconductivity of the device. It was

thought that as a consequence of this priming the array detector would not produce the expected protein CD spectrum when used in a CD experiment at Daresbury SRS.

It was decided to try and maximise the responsivity by increasing the physical size of the MSM diode and to also use semi-transparent contacts. Laborious work was done fabricating and optimising the large area and semi-transparent contact MSM devices. E-beam lithography techniques were used for the fabrication of these so called full metal and semi-transparent metal designs onto the 36GaN and 45GaN materials. The semi-transparent contacts were realised by evaporating 10 nm of Pd. As expected the larger active areas of the full-metal and semi-transparent metal detectors compared to the original MSM diode devices resulted in an increase in photocurrent. The semi-transparent metal design 36GaN and 45GaN devices exhibited larger photocurrents at an applied bias of 0 V than the full-metal diode design devices. At zero applied bias photocurrent/dark current contrasts of over 1000 were exhibited by the full metal and semi-transparent metal 36GaN devices.

Chapter 8

Synchrotron Studies

8.1 Introduction

Synchrotron light is the electromagnetic radiation emitted when charged particles, usually electrons or positrons, moving at velocities close to the speed of light, are forced to change direction under the action of a magnetic field. The electromagnetic radiation is emitted in a narrow cone in the forward direction, at a tangent to the particle's orbit. Synchrotron light is unique in its intensity and brilliance and it can be generated across the range of the electromagnetic spectrum; from infra-red to x-rays. Applications that make use of synchrotron radiation include x-ray absorption spectroscopy, powder diffraction, protein crystallography, lithography for integrated circuits and protein folding experiments.

At Daresbury SRS there is a dedicated CD set-up for the measurement of vacuum-ultraviolet CD on biological materials such as proteins and carbohydrates. This chapter describes the CD station 12 set-up at Daresbury SRS and compares the CD data obtained from a Hamamatsu Si array photodiode and from the semi-transparent metal 45GaN array photodiode detector

characterised in the previous chapter. Also described in this chapter is the fabrication and characterisation of chemical vapour deposition (CVD) single crystal diamond detectors for use as an in-situ synchrotron beam position monitor (BPM).

8.2 CD at Daresbury Station 12

Station 12 Set-up

The SRS at Daresbury is a 2 GeV electron storage ring, operated solely for the provision of synchrotron radiation for multiple simultaneous user experiments. It routinely operates at high circulating currents (150-250 mA) and long lifetimes ($\geq$ 24 hours), typically providing 4500 hours per year of user beam time with high stability and reproducibility.

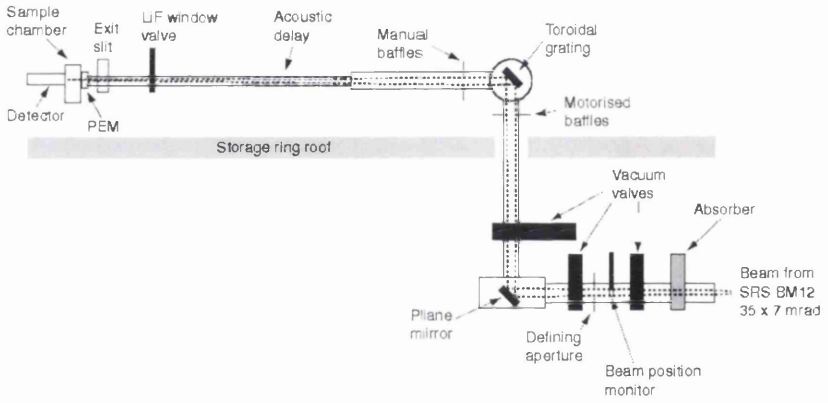

Figure 8.1: Layout of the CD12 beamline showing the major components

CD measurements are typically made on general-purpose vacuum ultraviolet (VUV) spectroscopy beamlines not optimised for the specific requirements of CD. However beamline station 12 at Daresbury SRS, known as

"CD12", has been designed for the optimal performance for CD measurements in the wavelength range from 120 nm to 1000 nm. CD12 was commissioned in 2003 and initial characterisation showed the high photon flux, linearity, good spatial resolution and low stray light properties of the beamline [156]. The general layout and components of CD12 are shown in Figure 8.1.

The main components of the front end are the water cooled beam absorber, defining apertures, two vacuum valves and a motorised scanning tungsten vane monitor for measurement of the beam position. The apertures accept almost all of the UV radiation from the bending magnet. Beam baffles are used to minimise the stray light component incident on the detector and to allow control of the part of the beam that is selected in order to optimise the polarisation characteristics.

The monochromator has the facility to hold up to three diffraction gratings or mirrors simultaneously however only one grating element is currently installed. This is a toroidal diffraction grating designed for peak output at 200 nm. The grating radii were chosen to give vertical focusing at the exit slit (7.8 metres from the monochromator) and horizontal focusing at the sample (0.2 metres from the exit slit), at a wavelength of 200 nm. This configuration results in a horizontal beam size of approximately 5 mm at the sample. The beam size at the sample position does not significantly change throughout the wavelength range of 180 nm to 280 nm used for CD spectroscopy.

The exit slit width is manually adjustable from zero to 10 mm. The sample environment consists of an optical table placed at the end of the beamline, after the lithium fluoride exit window. For CD spectroscopy the photoelastic modulator (PEM) is located in a light tight nitrogen purged chamber mounted on the optical table. The sample stage, where the protein

is located, is housed in a second nitrogen purged chamber. Nitrogen is used in order to purge oxygen molecules that absorb the VUV light.

The semiconductor array detector, which is plugged into the 16-pix system, is positioned as close as physically possible to the end of the sample chamber. The 16-pix read-out system has already been described in Chapter 7. Pre-acquisition settings such as the number of superaverages taken and the DC level multiplier could be modified using the C-Vision software on the PC. During an acquisition the C-Vision software can display the AC_{high}, AC_{low} and DC signals of all 16 channels. From these values the measured CD signal could be evaluated.

8.2.1 CD Results

In order to check that the set-up was working as expected a calibration CD spectrum of 10 mg ml^{-1} camphorsulphonic acid (CSA) [157] was obtained using a sixteen pixel silicon photodiode array. The Si photodiode array was based on Hamamatsu's S411 UV photodiode series with a UV response down to at least 200 nm and a sensitive area of 1.3 mm^2 per pixel. The pitch of each individual pixel was 1 mm. CSA is commonly used as a calibration standard for CD instruments because of its CD minima at 192.5 nm and maxima at 290.5 nm (see Figure 8.2)[157] . The value reported for the ratio of the two bands varies between 2 and 2.2 with the general consensus being around 2.1 [158].

Figure 8.3 shows the DC signal versus wavelength response of CSA obtained using the Si photodiode array. Scans were performed in 1 nm steps starting at 320 nm and ending at 180 nm. The slit width was opened to its maximum in order to get as much light as possible incident on the detector.

Figure 8.4 shows the AC_{high}-AC_{low} versus wavelengths response of CSA

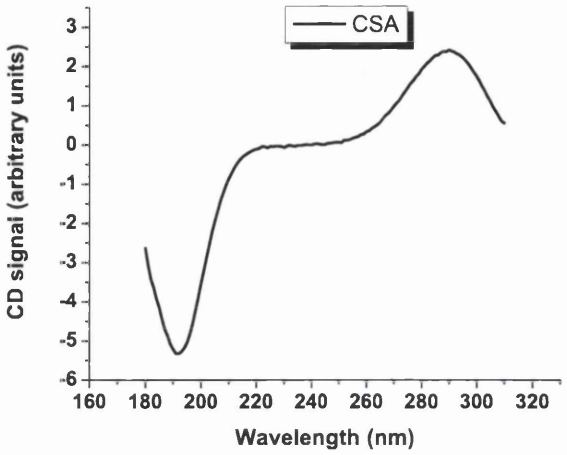

Figure 8.2: Typical CSA CD spectrum. This spectrum was taken using a photomultiplier tube to detect the signal (standard CD measurement technique).

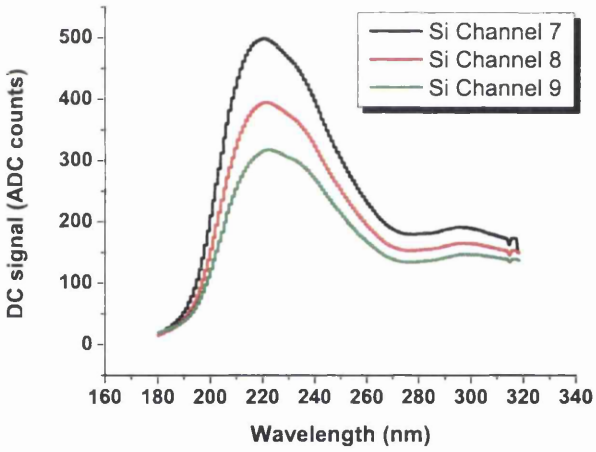

Figure 8.3: CSA static CD spectrum taken using channels 7, 8 and 9 of the Si photodiode

obtained from the Si photodiode array. It is this AC signal that determines the "handedness" of the material at a particular wavelength. These AC

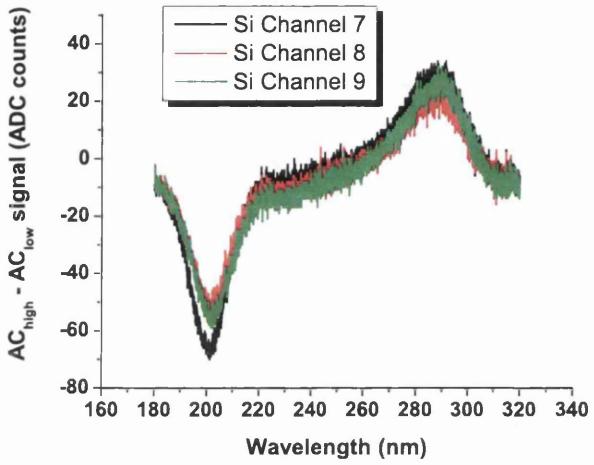

Figure 8.4: CSA static AC_{high}-AC_{low} spectrum taken using channels 7, 8 and 9 of the Si photodiode

spectra of CSA shows a maximum at approximately 290 nm and a minimum at approximately 200 nm. This minimum occurs at a longer wavelength than expected however due to time constraints it was not possible to examine the origin of this artefact. The ratio of the maxima and minima is approximately 2.2 for channel 7, 2.1 for channel 8 and 2.1 for channel 9. These values are in good agreement with the accepted ratio of 2.1.

Figure 8.5 shows the CD spectrum of CSA obtained from the Si photodiode array. The CD signal is calculated by dividing the AC_{high}-AC_{low} signal by the DC signal (see Equation 7.2). The CD spectrum exhibits the maxima at 290 nm however no minima is observed at 192 nm. This can be explained by strong absorption of short wavelength light ($\leq$ 200 nm) by both the CSA sample and more significantly by oxygen present between the exit slit and the

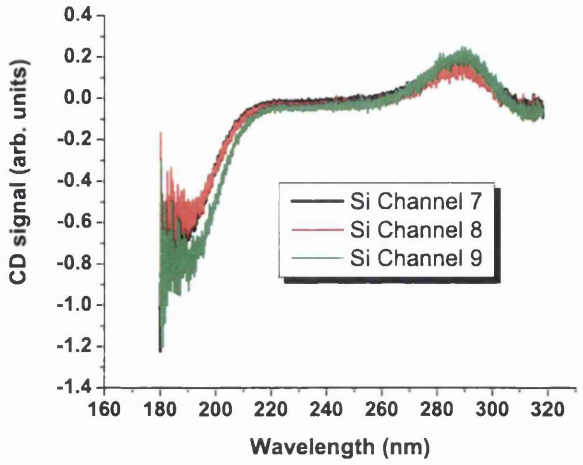

Figure 8.5: CD spectrum of CSA taken using channels 7, 8 and 9 of the Si photodiode

detector. As mentioned earlier the detector is positioned as close as possible to the exit slit however air exists in this gap region. The presence of residual oxygen strongly absorbs UV light, dramatically reducing the intensity. Therefore it can be said that this CD spectrum is only reliable down to a wavelength of 200 nm.

Due to time limitations, (there was less than one full day of beamtime available) it was only possible to investigate the CSA CD data of one GaN array detector. It was decided that the semi-transparent metal 45GaN device should be used since at 0 V, the MSM diodes of this detector exhibited the largest photoresponse between 180 and 240 nm compared to the other GaN array devices. Figure 8.6 shows the DC signal versus wavelength spectrum of CSA obtained from two channels of the semi-transparent metal 45GaN array detector. The spectrum is extremely unusual and totally unexpected in that the photoresponse increases with increasing wavelength. Repeat scans

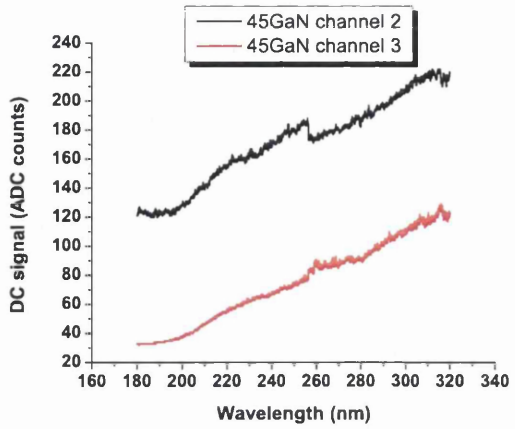

Figure 8.6: CSA static CD spectrum taken using channels 2 and 3 of the semi-transparent metal 45GaN array device

from 320 nm to 180 nm were made and similar spectra were observed. It could be that the observed spectrum is a result of the slow de-trapping of photo-generated charge carriers. When setting the starting wavelength of the scan (i.e. at 320 nm) there is backsplash of the monochromator (i.e. the monochromator overshoots the desired wavelength). It is possible that the backsplash was so large that for a short time the grating was positioned such that 365 nm light was incident on the 45GaN array detector. As discussed in Chapter 7, at 365 nm, the MSM GaN detectors exhibited an extremely large photoresponse, several orders of magnitude greater than at 320 nm. If when starting a wavelength scan at 320 nm there already exists a large number of photo-generated carriers which are trapped in defect states, these carriers may slowly de-trap and lead to the spectrum exhibited in Figure 8.6.

The AC_{high}-AC_{low} versus wavelength spectrum of CSA obtained from two channels of the semi-transparent metal 45GaN array detector did not exhibit the expected maxima at 290 nm and minima at 192 nm (see Figure 8.7).

Figure 8.8 shows the CD spectrum of CSA obtained from channels 2 and 3 of

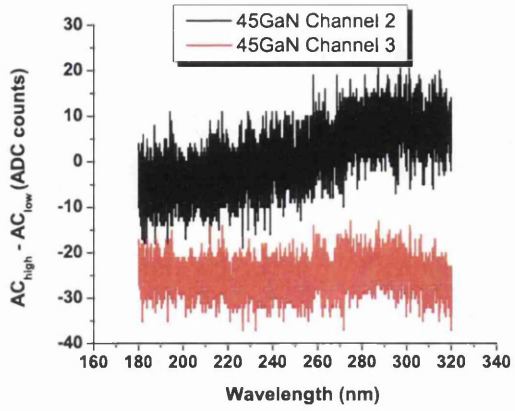

Figure 8.7: CSA static AC_{high}-AC_{low} spectrum taken using channels 2 and 3 of the semi-transparent metal 45GaN array device

the semi-transparent metal 45GaN array detector. Both figures 8.7 and 8.8

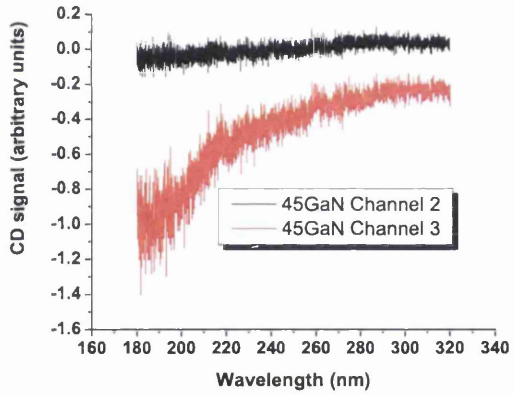

Figure 8.8: CSA static CD spectrum taken using channels 2 and 3 of the semi-transparent metal 45GaN array device

are included for completeness and serve to show that the semi-transparent metal 45GaN device does not resolve the CD features expected of CSA.

It can be concluded that poor material quality, hampered by priming, is to blame for the failure of the semi-transparent metal 45GaN device exhibiting a CD spectrum that is characteristic of CSA. As priming was also observed in the other MSM GaN array detectors it is likely that they would have also exhibited similar CD CSA spectra as that of the semi-transparent metal 45GaN detector.

8.3 CVD Diamond for Beam Monitoring

For the past decade diamond has been of interest to physicists across the globe. Its large band gap (E_g = 5.5 eV), large displacement energy and high charge carrier mobility (see Table 4.2) compared to Si have caught the attention of particle physicists who seek a detector material able to withstand high radiation environments [159].

Diamond has also been investigated for use as a permanent in-line x-ray beam position monitor (BPM) in the energy range 4 keV to 25 keV. Third generation synchrotron x-ray beams may presently be focussed to < 1 μm and devices with similar spatial precision are required to monitor the beam position or provide real-time information for position control. Conventional BPMs based on semiconductor photodetectors, mainly Si, typically involve the complete absorption of incoming radiation. To make in-line devices for measuring the beam characteristics without significant attenuation of the x-ray flux, a detector material with a low absorption cross-section is desirable. Hence for the x-ray energy range of 4 keV to 25 keV a low atomic number semiconductor, such as diamond, is required. Figure 8.9 graphically shows the advantage of using diamond instead of silicon as the detection medium for an in-line low-energy x-ray BPM.

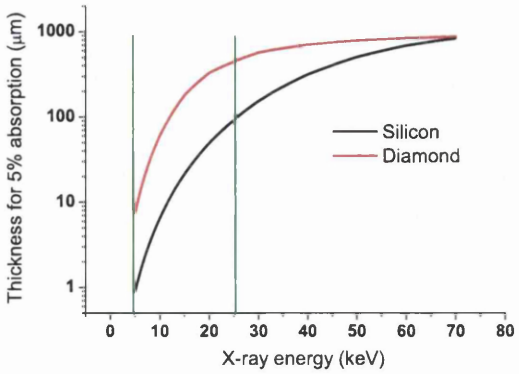

Figure 8.9: Plot comparing the thickness for 5% absorption versus x-ray energy between diamond and silicon

The first studies of diamond as a semi-transparent BPM were performed using polycrystalline CVD diamond [160]. A 20 μm thick polycrystalline diamond layer was grown on top of a silicon wafer. A circular hole was back-etched in the silicon and 50 nm thick Au contacts evaporated onto both sides of the material. The electrical contact on one side of the membrane was divided into four sections separated by a narrow gap resulting in four quadrant beam position monitors. The promising initial results led to further studies of polycrystalline CVD diamond as a BPM (a review may be found in [161]) and commercial devices have been made available [162]. However, one inherent drawback of these BPMs is that the material is polycrystalline, with grain sizes typically of the order of 10-20% of the deposited material thickness. Regions of degraded charge transport and carrier lifetime properties have been observed within these grain boundaries and result in non-uniformity of the detector x-ray response [163]. This non-uniformity of the soft x-ray response limits the performance of the BPM and as a consequence there has been sub-

stantial research into growing single crystal CVD diamond. The improved electrical properties of single crystal diamond compared to polycrystalline material were first reported by Isberg et al. [164]. Experimentally determined room temperature values of 4500 and 3800 cm^2/Vs were obtained for the electron and hole mobility respectively. This section describes the I-V, CCE and X-ray response characteristics of a single crystal diamond detector made for potential use as a semi-transparent BPM. The device fabrication, I-V and CCE measurements were performed at the University of Glasgow while the x-ray response measurements were done at the ESRF synchrotron in Grenoble.

8.3.1 Device Fabrication

The single crystal diamond sample was grown by Element Six, Ascot, UK [165]. The charge transport properties of this material were investigated using the transient current technique (TCT) [166] and have been reported in [167]. At room temperature and at an applied field of 0.8 V/μm drift velocities of 5.6x10^6 cm/s and 7.5x10^6 cm/s were obtained for electrons and holes respectively. The saturation velocity obtained for electrons was 9.6x10^6 cm/s and for holes was 14.1x10^6 cm/s. The measured electron and hole lifetimes were tens of nanoseconds and constituted a dramatic improvement over charge carrier lifetimes in high quality polycrystalline material (2-3 times larger in single crystal material than polycrystal material) [168].

First, the 3.5 by 3.5 mm diamond sample (thickness 333 μm) was cleaned using acetone, IPA and rinsed in RO water. A further sulphuric acid/hydrogen peroxide clean ensured that the diamond surface was free of any contamination. Both sides of the sample were then given an oxygen plasma treatment in order to terminate any free dangling bonds at the surface. A metal multi-

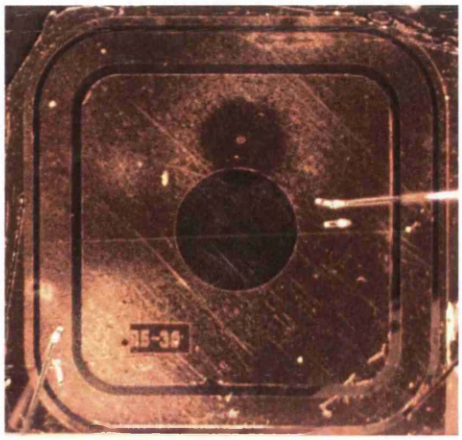

Figure 8.10: Optical image of the front contact of the diamond sample

layer of 10 nm/30 nm/ 130 nm Ti/Pd/Au was evaporated onto one side of the diamond sample and the sample was subsequently annealed in nitrogen at 650^0C for 10 minutes to form a carbide-diamond interface. The front side electrode was processed in two stages utilising photolithographic techniques, (see Chapter 2), to obtain a 10 nm/30 nm/ 130 nm Ni/Pd/Au contact with a thinned central contact area of diameter 0.8 mm of 5 nm/ 5 nm Ni/Au. The fabrication resulted in a Schottky-Ni-Ohmic TiC contact configuration and enabled the device to be operated as a solid state ionisation chamber. Figure 8.10 shows an optical image of the front side electrode on the diamond sample. The diamond was mounted onto a miniature circuit board to enable subsequent I-V and CCE measurements at Glasgow and sub-micron scanning measurements in the beam of the ESRF-ID21 x-ray microscope.

8.3.2 Results

Figure 8.11 shows the leakage current characteristics of the diamond detector. The leakage current between the front and rear electrode contacts was

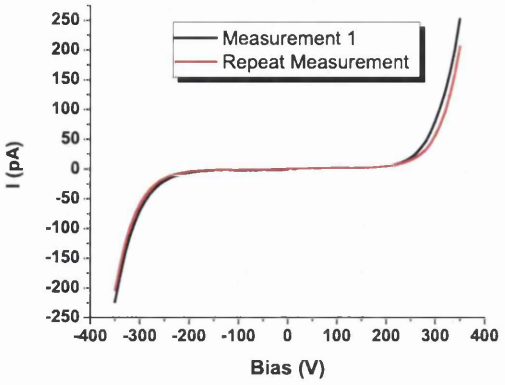

Figure 8.11: Leakage current of the diamond sample

less than 10 pA for an applied field of 0.6 V/μm and showed no obvious dependence on polarity. CCE measurements were also performed using 5.48 MeV alpha particles emanating from an ^{241}Am source. The experimental set-up and calibration has been described in Chapter 4. The device showed excellent charge collection properties for bias voltages between -50 V and -300 V (see Figure 8.12). A further lower energy peak was also observed and is thought be due to charge collected by the guard ring. Similar spectra, with one main peak and one lower energy peak, were obtained using 2 MeV α particles [169].

The preliminary tests served to establish the low leakage current and high charge collection efficiency properties of the diamond device. X-ray response tests were then carried out at the ID21 x-ray Microscopy beamline at ESRF by raster scanning the diamond sample in a submicron (0.4 x 0.12 μm^2 FWHM), monochromatic 7.2 keV x-ray beam at a nominal intensity of $\sim$ 5x10^7 photons/sec. A schematic diagram of the ESRF ID21 X-Ray Microscopy beamline is shown in Figure 8.13 [170]. Figure 8.14 shows the

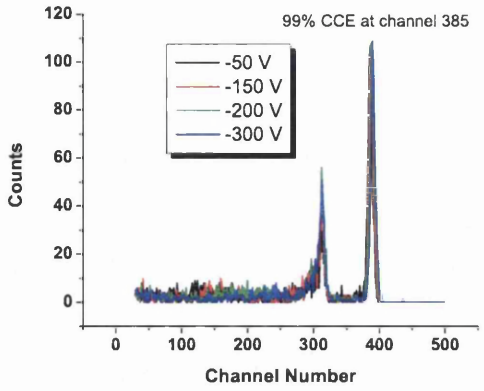

Figure 8.12: Alpha spectrum response of the diamond detector at various bias voltages

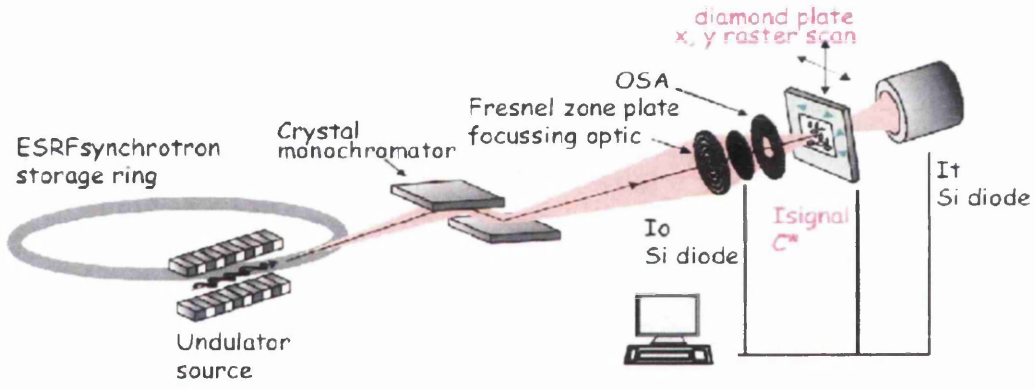

Figure 8.13: The ESRF ID21 X-Ray Microscopy beamline

I-V response measured with the diamond sample in the x-ray beam. The device shows a highly asymmetric I-V response, much in contrast to the dark I-V characteristics. With a negative bias applied to the Ti rear contact and at a field of > 0.1 V/μm the device shows a saturated current response. For forward, positive bias, the measured current exceeded the negative bias

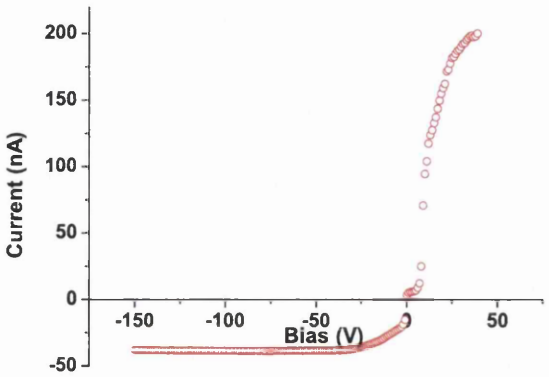

Figure 8.14: I-V curve of the Ni-TiC contacted diamond sample measured in the unfocussed 100 μm x-ray beam

plateau value by a factor of $\sim$ 4 at a field of 0.1 V/μm. This is believed to be result from photoconductive current gain since a similar current gain with bias behaviour was observed in a device fabricated on the same diamond material with annealed Ti contacts on both sides [18].

Figure 8.15 shows the x-ray induced current map of the diamond sample scanned in a 100 μm pin-hole collimated beam. Measurements were performed with a bias of -100 V applied to the carbided Ti rear contact. The 2 mm square front electrode contact and the central 0.8 mm diameter area where the contact is only 10 nm thick both showed a uniform response. A standard deviation in the diamond photocurrent of 0.18% was measured for 225 points at 12.5 μm steps with the sub-micron focussed beam. Signal response for the area under the thin electrode was 8.3 +/- 0.9% higher than that of the surrounding thick electrode area, in agreement with the calculated x-ray beam absorption occurring in these metal layers of these electrode regions of 7.7% and 0.27% respectively. The high area response (yellow/green

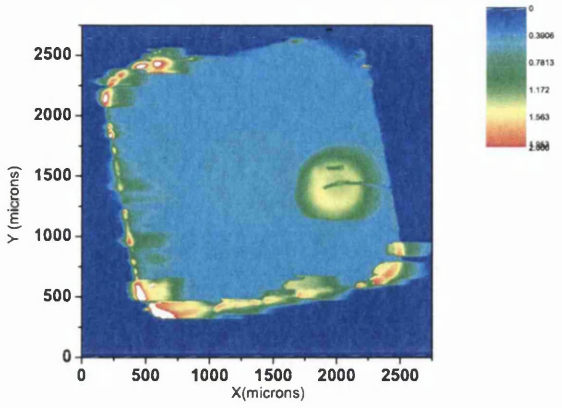

Figure 8.15: Photocurrent map of diamond sample at an applied bias of - 100 V. The image is normalised by a simultaneous map made of the incident x-ray beam intensity

region) of diameter $\sim$ 0.5 mm seen directly centred under the wire bond that was made to contact the front electrode gave a peak signal value of 10.5 nA, which was $\sim$ 3.5 times greater than that for the surrounding uniform area. The explanation of this is unknown but the interface to the diamond underneath the wire bond had presumably been disrupted by the mechanical impact of the wire bonding process to this blocking contact. High current response points are also seen along the edges of the contact area. These contact edge hot spots show decay comet tails (the x-direction scan rate was 100 μm/s) but this was not the case for the excess current region under the wire bond.

Single crystal CVD diamond plates have been shown to have the uniform spatial response necessary for the monitoring of micron and sub-micron X-ray beams. The next step was to fabricate and test diamond BPMs with multi-electrode geometries. Several multi-electrode detector designs were

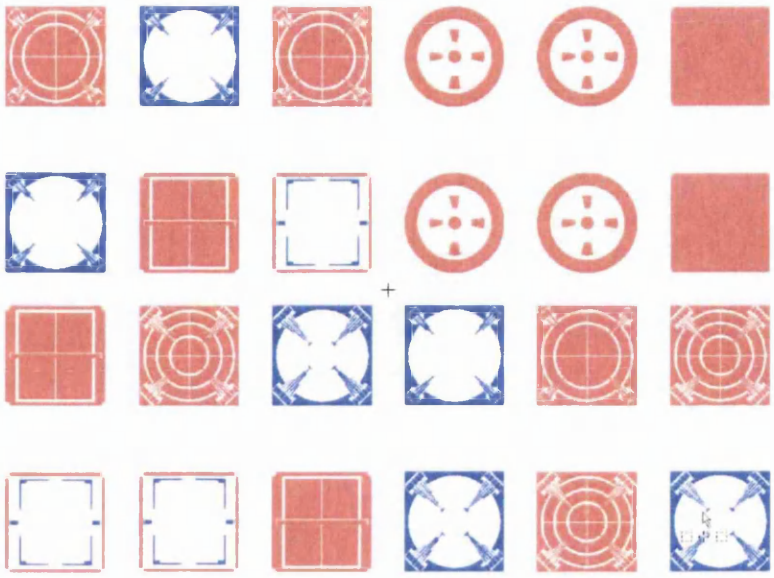

Figure 8.16: Exported L-Edit image of the various designs patterned onto a 2.5 inch mask plate

drawn using the L-Edit CAD package and subsequently written onto 2.5 inch square mask plates. There were nine different designs in all, ranging from a simple quadrant structure to complex multi ring electrode structures and multi-strip patterns. Guard rings are included in all the designs and each design fits into a diamond sample of dimension 3.5 mm by 3.5 mm. Figures 8.16 and 8.17 show images exported from the L-Edit package of the motifs patterned onto the two masks.

For each design there is a thin metal and corresponding thick metal motif. Copies of these two masks have been made and sent to collaborators in Germany and the United States of America. Using these masks parallel processing of more single crystal diamond samples grown by Element Six into radiation detectors is underway both in Germany, the USA and at the University of Glasgow. When these devices are fabricated, x-ray measurements

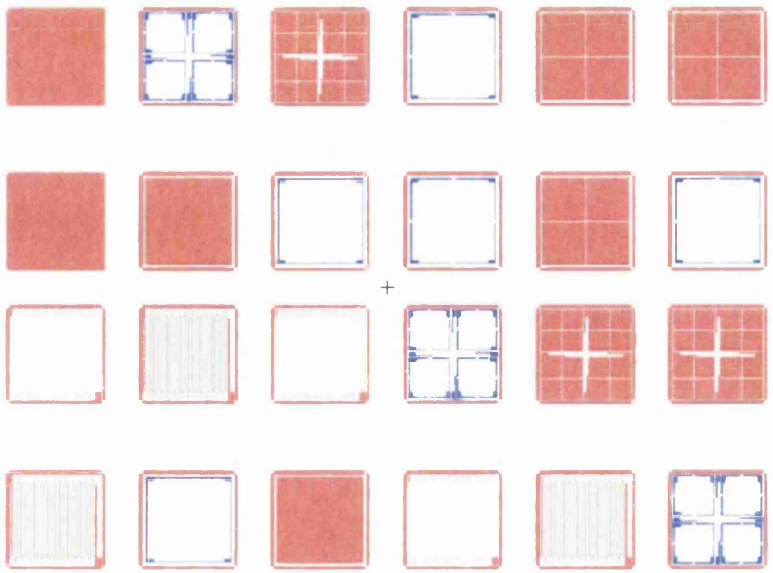

Figure 8.17: Exported L-Edit image of the various designs patterned onto a second 2.5 inch mask plate

will be performed at the ESRF and the suitability of single crystal diamond as an in-situ x-ray beam position monitor will be established.

8.4 Summary and Conclusions

In this chapter the CD spectrum of camphorsulphonic acid (CSA) was measured using the semi-transparent metal 45GaN photodetector array. The observed CD spectrum was not that of the expected CD spectrum of CSA. This is attributed to the poor quality of the 45GaN material, evident through the observed priming of the device. The synchrotron results show that semi-insulating GaN grown on a conductive buffer layer is not a suitable material for energy dispersive circular dichroism measurements. However if high quality, semi-insulating GaN with a low defect density were available then it could

outperform silicon as an UV light detector.

Single crystal diamond was also assessed for its suitability as an in-situ soft x-ray semi-transparent beam position monitor. The fabricated detector exhibited low leakage currents up to an applied field of 0.6 V/μm and $\sim$ 100% CCE at an applied reverse bias of 50 V. X-Ray measurements at the ESRF showed the excellent uniform response of the diamond device. The initial results indicate that single crystal diamond shows great promise as an in-situ semi-transparent position beam monitor. Further single crystal diamond soft x-ray detectors will be fabricated and characterised in the coming months however this work is outwith the scope of this thesis.

Chapter 9

Conclusions and Summary

The work in this thesis centred upon on evaluating GaN as a radiation hard particle detector and as an ultra-violet light detector. Single crystal diamond was also studied for use as an in situ soft X-ray beam position monitor.

Samples from three semi-insulating epitaxial GaN wafers were irradiated with protons and neutrons to anticipated SLHC fluences. Two of these wafers had an epitaxial thickness of 2.5 μm while the third had an epitaxial thickness of 12 μm. The effects of the various irradiations on the macroscopic properties of the GaN detectors were assessed via current-voltage, capacitance-voltage and charge collection efficiency measurements. All three 36GaN, 45GaN and 12GaN unirradiated detectors exhibited low leakage currents and maximum charge collection efficiencies of 70%, 97% and 54% respectively. The 36GaN, 45GaN and 12GaN detectors irradiated with protons and neutrons to 10^{14} particles cm^{-2} all had similar leakage currents to the corresponding unirradiated detectors. However the detectors irradiated to higher fluences exhibited leakage currents significantly smaller than the unirradiated detectors. Indeed, for all three GaN materials, the leakage currents of the detectors irradiated to the highest fluences (10^{16} particles cm^{-2}) were several orders of magnitude

smaller than the unirradiated devices. This unusual leakage current with irradiating fluence dependence has also been observed for other wide band gap semiconductors, namely SiC and diamond. The irradiated devices showed a substantial drop in charge collection efficiency with increasing fluence. After irradiation to 10^{16} pcm^{-2} the 36GaN, 45GaN and 12GaN detectors had maximum charge collection efficiencies of 12%, 17% and 26% respectively. Additionally, these values were obtained at significantly higher bias voltages than the those for the unirradiated devices.

Samples from the 36GaN, 45GaN and 12GaN wafers were also dry etched in an inductively coupled plasma machine for the purpose of defining ohmic contacts to the n-GaN buffer layer and improving the detector geometry. From the current-voltage and capacitance-voltage characteristics of the etched devices the ideality factor, Schottky barrier height and carrier concentration were extracted. The carrier concentration of the 36GaN material was found to be 1.33x10^{15} cm^{-3} while the ideality factor and Schottky barrier height of the Pd-GaN contact was found to be 0.41 and 1.78 eV respectively. An ideality factor of 0.94, a Schottky barrier height of 1.06 eV and a carrier concentration of 1.8x10^{15} cm^{-3} was evaluated for the 45GaN device. Previous SI GaN wafers grown by Tokushima have had similar carrier concentrations as the 36GaN and 45GaN material studied here. The parallel plate capacitor geometry of the etched devices resulted in an increase in charge collection efficiency compared to the unetched devices. This is attributed to better definition of the electric field within the etched devices resulting in significantly improved charge transport.

Attempts were made at understanding and identifying the microscopic as-grown and radiation-induced defects that determine the macroscopic characteristics of the GaN detectors. The microscopic properties of unirradiated

and irradiated SI GaN detectors were evaluated using photoluminescence (PL), contact photoconductivity (CPC) and thermally stimulated current (TSC) techniques. Photoluminescence spectroscopy of all the unirradiated and irradiated GaN devices revealed the yellow, blue, ultra-violet and violet bands typical of unintentionally doped SI GaN. The PL intensity of all four bands decreased with increasing irradiation fluence indicating an increase in non-radiative recombination. For all irradiated GaN detectors the yellow band had the most dramatic reduction in PL intensity. It is extremely likely that these radiation induced non radiative recombination centres are responsible for the drastic reduction in both leakage current and CCE of the irradiated GaN detectors. CPC measurements of the irradiated GaN detectors revealed two decay processes of the induced photo-current; a non-exponential region ascribed to fast carrier recombination and an asymptotic region ascribed to excess carrier trapping. The CPC measurements revealed an increase in non-radiative recombination with increasing fluence, corroborating the findings of the PL spectroscopy measurements. The irradiation of the GaN detectors also resulted in more disorder of the SI GaN material, enhancing the carrier decay rate which was observed by the shortened asymptotic lifetime. TSC measurements of the GaN detectors revealed several competing complicated transport mechanisms. The TSC curve of the unirradiated GaN detector was not due to thermal carrier generation but by mobility variation. Thermal activation energies of 0.16-0.2, 0.27-0.32, 0.36-0.45 and 0.73-0.74 eV were extracted from neutron irradiated 45GaN detectors.

Combining the findings of Chapters 4, 5 and 6 it can be said that the GaN material studied in this thesis is not suitable for the anticipated SLHC environment. Indeed several issues must be addressed before GaN can se-

riously be considered for radiation hard applications. The primary issue is the lack of availability of high quality thick semi-insulating GaN epilayers. The purest GaN material is grown by the MOCVD method however it is not economically viable to grow thick epitaxial layers using this method because of its inherently slow growth rate. Recently free-standing conductive bulk GaN wafers have been grown by hydride vapour phase epitaxy (HVPE). This HVPE technique has the advantage of fast growth rates (150 μm/hr) however the quality of the GaN material has not been fully assessed.

A second issue that must be addressed is material quality. In the past decade the point and dislocation defect densities of epitaxial GaN films have been reduced however further reductions are necessary for GaN to be suitable as a radiation hard detector medium.

Finally, the results of Chapter 4 showed that by employing the planar electrode structure typical of radiation detectors, the charge collection properties of the GaN device improved. This ultimately means that if epitaxial GaN material is to be used as the detection material then a suitable conductive substrate is required on which the epitaxial GaN can be grown. This conductive substrate must have similar thermal expansion coefficients and lattice constants as GaN in order to minimise the lattice mismatch. Si, on account of its low cost and high availability, is currently being investigated as a possible substrate material however the mismatch between it and GaN is very high. One approach could be to grow the high quality epitaxial layer onto a free-standing conductive GaN wafer grown by HPVE.

Chapters 7 and 8 evaluated GaN as a position sensitive MSM UV light detector for the measurement of Circular Dichroism. The aim was to produce a 46 channel diode array detector on GaN capable of recording the CD spectrum of a protein. First the optimal material, MSM diode geome-

try and metalisation contact scheme had to be established. Laborious, time consuming work was spent developing e-beam lithography and photolithography processes for the fabrication of MSM photodiodes on four GaN wafers and one AlGaN wafer. Two MSM diode geometries were investigated; one with a finger separation/width of 5 μm and a second with a finger separation/width of 10 μm. It was found that 10 μm design MSM detectors exhibited larger photocurrents than the 5 μm design detectors and that for a number of devices a photo-peak was present at 365 nm. Both these results were unexpected and are attributed to the influence of the conductive buffer layer on the photo-generated charge carriers and also to percolation charge paths within the SI GaN material. At 0 V the 10 μm design 45GaN, 36GaN, 12GaN and Emcore GaN devices exhibited responsivities of 0.44, 0.46, 0.01 and 0.95 mA/W respectively. Responsivities of 177, 414 and 436 mA/W were measured for the 45GaN, 36GaN and 12GaN devices at applied biases of -6 V. The results indicated that the 46 channel diode array should be fabricated on Emcore GaN if the device is to be operated unbiased and on the 12GaN if the device was to be operated under bias. Due to a lack of available material however, it was not possible to fabricate the array detector on either of these materials. A 46 channel diode array detector was fabricated on the 45GaN material with each MSM diode having a finger separation/width of 10 μm. Photoresponse tests using the 16-pix set-up at RAL showed that the channels of the array detector exhibited substantial priming. This priming is attributed to photo-generated carriers filling defect traps in the SI 45GaN material therefore increasing the photoconductivity of the device.

The photoresponse of the MSM devices was increased by adopting two strategies. The first was to increase the active area of the device by increasing both the number of fingers and the finger length while the second was to use

semi-transparent contacts instead of full-metal contacts. These new MSM diode designs increased the active area of the device by ten and twenty times respectively. Four and eight channel diode arrays were realised on both the 36GaN and 45GaN materials and the devices characterised via current-voltage and spectral response measurements. As expected the larger active areas of the full-metal and semi-transparent metal detectors compared to the original MSM diode devices resulted in an increase in photocurrent. At an applied bias of 0 V, the semi-transparent metal 45GaN detector exhibited the largest responsivity (18 mA/W) of all devices.

In Chapter 8 the CD spectrum of camphorsulphonic acid (CSA) was measured using the semi-transparent metal 45GaN photodiode array detector and compared to the spectrum obtained with a Hamamastu Si photodiode. The typical CSA CD spectrum of a minimum at 192.5 nm and a maximum at 290.5 nm was not recorded by the semi-transparent metal 45GaN device. This is attributed to the priming of the device which leads to unstable photocurrents (device takes over 120 seconds to reach equilibrium). In short, the synchrotron results showed that semi-insulating GaN grown on a conductive substrate is not a suitable material for energy dispersive circular dichroism measurements.

MSM detectors realised on SI GaN grown on AlN have shown high responsivities, large UV/visible contrasts and perhaps more importantly no evidence of priming [171]. This material is eminently appropriate for the realisation of a position sensitive 46 channel diode array detector on GaN. These findings show that the concept of a GaN visible/blind position sensitive UV detector is valid, however the GaN material studied in this work is not suitable. For deep UV applications, AlGaN is preferable to GaN due to its shorter cut-off wavelength. In recent years there have been rapid ad-

vancements in AlGaN material quality and device processing [172]. If this trend continues AlGaN is likely to be the preferred medium for UV and deep UV detection.

Single crystal diamond was also assessed for its suitability as an in-situ soft x-ray semi-transparent beam position monitor. The fabricated detector exhibited low leakage currents up to an applied field of 0.6 V/μm and $\sim$ 100% CCE at an applied reverse bias of 50 V. X-Ray measurements at the ESRF showed the excellent uniform response over the full area of the diamond device. These preliminary investigations indicate that single crystal diamond shows great promise as an in-situ semi-transparent position beam monitor. Further single crystal diamond soft x-ray detectors will be fabricated and characterised in the coming months. The grand ambition is to produce a semi-transparent soft x-ray beam position monitor on 50 μm thick single crystal diamond.

Bibliography

[1] http://www.micron.com/k12/semiconductors/history

[2] http://en.wikipedia.org/wiki/Semiconductor_device

[3] ATLAS : Technical Proposal for a General-Purpose pp Experiment at the Large Hadron Collider at CERN.- Geneva: CERN, 1994.- 272 p.- (LHC Tech. Proposal, 2).- CERN-LHCC-94-43.- LHCC-P-2, (*CERN Document Server*

[4] LHC webpage, http://lhc-new-homepage.web.cern.ch/lhc-new-homepage/

[5] M. Moll, *Nucl. Instr. and Meth. A 546, pp 202-211, 2006*

[6] M. Rahman, *IEE Transactions on Nuclear Science, Vol. 50, No. 6, December 2003*

[7] RD48 collaboration, http://rd48.web.cern.ch/RD48/

[8] The RD50 collaboration, http://cern.ch/rd50/

[9] S.I. Parker, C.J. Kenney, J. Segal, *Nucl. Instr. and Meth. A 395, (1997), pp 328-343*

[10] J. Kemmer, *Nucl. Instr. and Meth. 169, pp 499, 1980*

[11] R. Juza, H. Hahn, Z. Anorg, *Anng. Chem. 234, pp 248, 1938*

[12] J. Kemmer, *Appl. Phys. Lett. 185, pp 327, 1967*

[13] S.M Sze, " Semiconductor Devices, Physics and Technology" (2nd Edition), Wiley, New York

[14] J. Hochedez et. al., Innovative Telescopes and Instrumentation for Solar Astrophysics. Edited by Stephen L. Keil, Sergey V. Avakyan . *Proceedings of the SPIE, Volume 4853, pp. 419-426 (2003).*

[15] G. Colangelo, O. Pace, R. Marsden, B. Fleck, "Solar Orbiter: A Challenging Mission Design for Near Sun Observations", *ESA bulletin 104 - November 2000*

[16] S. Manolopoulos, D. Clarke, G. Derbyshire, G. Jones, P. Read, M. Torbert, *Nucl. Instr. and Meth. A 531, p 302-306, 2003*

[17] RD42 collaboration, "Development of Diamond Tracking Detectors for High Luminosity Experiments at LHC", LHCC-RD-012; CERN-LHCC-2007-002.- Geneva : CERN, 12 Jan 2007

[18] J Morse, M Salome, E Berdermann, M Pomorski, W Cunningham, J Grant, *Diam. Rel. Mat., Jan 2007*

[19] A. Blue thesis, *"New Materials and Processes for Radiation Detection" 2005*

[20] S.A. Campbell, "The Science and Engineering of Microelectronic Fabrication", Oxford University Press, New York, 2001

[21] Course notes for "E-Beam Lithography", by Dr. Stephen Thoms, Department of Electronic and Electrical Engineering, University of Glasgow 2005

[22] http://www.microchem.com/products/lor.htm

[23] www.astp.com/plasma/pl_examples.html

[24] J. Reece Roth "Industrial Plasma Engineering Vol. 1: Principles", IOP Publishing, Bristol 1995

[25] J. Reece Roth "Industrial Plasma Engineering Vol. 2: Principles", IOP Publishing, Bristol 2001

[26] J. Bhardwaj, A. Ashraf, A. McQuarrie, Surface Technology Systems, Internal Publication

[27] S. J. Pearton, "GaN and Related Materials II", Gordon and Breach Science Publishers, 2000

[28] E.H. Rhoderick, "Metal Semiconductor Contacts" (2nd Edition), Oxford University Press 1988

[29] S. J. Pearton, "Optoelectronic Properties of Semiconductors and Superlattices: GaN and Related Materials II", Gordon and Breach Science Publishers 2000

[30] G.F Knoll, "Radiation Detection and Measurement" (3rd Edition), Wiley, New York 1999

[31] S.M. Sze "Physics of Semiconductor Devices", (2nd Edition), Wiley, New York 1981

[32] C. Y. Yeh, Z. W. Lu, S. Froyen, A. Zunger *Phs. Rev. B, 46, 100086, 1992*

[33] SRIM software, http://www.srim.org/

[34] S. Hancock, F. James, J. Movchet, P.G. Rancoita, L. Vanrossum, *Phs. Rev. B 28, vol 2, pp 615-620, 1983*

[35] S. Hancock, F. James, J. Movchet, P.G. Rancoita, L. Vanrossum, *Nucl. Instr. and Meth. B, 1 pp 615-620, 1984*

[36] S. Nakamura, T. Mukai, M. Senoh, *Appl. Phys. Lett. 64, 1687, 1994*

[37] S. Nakamura, G. Fasol, "The Blue Laser Diode. GaN Based Light Emitters and Lasers", Springer, Berlin, 1997

[38] J. Wurfl, V. Abrosimova, J. Hilsenbeck, E. Nebauer, W. Rieger, G. Trankle, "Review paper: Reliability considerations of III-nitride microelectronic devices", Microelectronic Reliability, 39, pp 1737-1757, 1999

[39] S. Porowski, J.M. Baranowski, M. Leszzynski, J. Jun, M. Bockowski, I. Gregory, S. Krukowski, M. Wroblewskiw, B. Lucznik, G. Nowak, K. Pakula, W. Wysmolek, K.P. Corona, R. Stepniewski, "Physical prperties of GaN single crystalline substrates and homoepitaxial layers", International Symposium on Blue Lasers and Light Emitting Diodes, Chiba Univ., Japan, March 5-7, pp 38-41, 1996

[40] X. Zu, R.P. Vaudo, C. Loria, A. Salant. G.R. Brandes, J. Chaudhuri *J. Cryst. Growth, 246, 243, 2002*

[41] G. B. Stringfellow, "Organometallic Vapor Phase Epitaxy Theory and Practice", Academic Press, New York, 1989

[42] G. Popovici, H. Morkoc, "Deposition and Properties of III-Nitrides by Molecular Beam Epitaxy in Physics and applications of group III semiconductors", 0xford University, 1998

[43] S.N Mohammad, H. Morkoc, "Progress and Prospects of Group III-Nitride Semiconductors", *Progress in Quantum Electronics, Elsevier Press, 1996*

[44] M.A. Khan, R. A. Skogman, R. G. Schulze, M. Gershenzon, *Appl. Phys. Lett. 58. 430, 1983*

[45] M. Hashimoto, H. Amano, N. Sawaki, I. Akasaki, *J. Cryst. Growth, 68, 163, 1984*

[46] S. Nakamura, T. Mukai, M. Senoh, *Appl. Phys. Lett. 58, 2021, 1991*

[47] H. Amano, I. Akasaki, K. Hiramatsu, N. Sawaki, *Thin Solid Films, 163, 415, 1988*

[48] I. Akasaki, H. Amano, Y. Koide, K. Hiramatsu, N. Sawaki, *J. Cryst. Growth, 98, 209, 1989*

[49] K. Yokouchi, T. Araki, T. Nagatomo, O. Omoto, *Inst. Phys. Conf. Ser. v. 142, 867, 1996*

[50] A. Ohtani, K.S. Stevens, R. Beresford, *MRS Symp. Proc. v. 339, pp 471-476, 1994*

[51] Technical proposal.- Geneva: CERN, 1994.- 254 p.- (LHC Tech. Proposal, 1).- CERN-LHCC-94-38.- LHCC-P-1, *CERN Document Server*

[52] LHCb : Technical Proposal. - Geneva: CERN, 1998.- 170 p.- (Tech. Proposal).- CERN-LHCC-98-004.- LHCC-P-4, *CERN Document Server*

[53] ALICE: Technical Pproposal for a Large Ion collider Experiment at the CERN LHC.- Geneva: CERN, 1995.- 237 p.- (LHC Tech. Proposal, 3).- CERN-LHCC-95-71.- LHCC-P-3, *CERN Document Server*

[54] TOTEM, Total Cross Section, Elastic Scattering and Diffraction Dissociation at the LHC: Technical Proposal (CERN Document Server)

[55] FP420: An R&D Proposal to Investigate the Feasibility of Installing Proton Tagging Detectors in the 420 m Region of the LHC, FP420: CERN-LHCC-2005-025; LHCC-I-015.- Geneva : CERN, 21 Jun 2005 . - 17 p, *CERN Document Server*

[56] F. Gianotti, M.L. Mangano, T. Virdee *"Physics potential and experimental challenges of the LHC luminosity upgrade"*, hep-ph/0204087; April 2002.

[57] G.Lindstrom, *Nucl. Instr. and Meth. A 512, pp 30-43, 2003*

[58] G. Lindtrom on behalf of the CERN RD48 collaboration, *Nucl. Instr. and Meth. A 466 pp 308-326, 2001*

[59] RD48,"2nd Status Report", CERN LHCC 98-39, LEB Status Report/RD48, 21 October 1998.

[60] V. Boisvert, J.L. Lindstrom, M. Moll, L.I. Murin, I. Pintilie, *Nucl. Instr. and Meth. A 552, pp 49-55, 2005*

[61] L.F. Makarenko, F.P. Korshunov, S.B. Lastovski, N.M. Kazuchits, M.S. Rusetsky, E. Fretwurst, G. Lindstrom, M. Moll, I. Pintilie, N.I. Zamiatin, *Nucl. Instr. and Meth. A 552, pp 77-81, 2005*

[62] A.Barcz, M.Zielinski, E.Nossarzewska, G. Lindstrm, *Appl. Surf. Sci. 203-204, pp 396-399, 2003*

[63] I.Pintilie, M.Buda, E.Fretwurst, G.Lindstrom, J.Stahl, *Nucl. Instr. and Meth. A 556 pp 197-208, 2006*

[64] Z. Li, R. Beuttenmuller, W. Chen, D. Elliott, V. Radeka, J. Takahashi, W. C. Zhang, *Nucl. Instr. and Meth. A 478, pp 303-310, 2002*

[65] C.Piemonte, M.Boscardin, G.-F. Dalla Betta, S. Ronchin, N. Zorzi, *Nucl. Instr. and Meth. A 541, pp 441-448, 2005*

[66] A. Ionascut-Nedelcescu, C. Carlone, A. Houdayer, H.J. von Bardeleben, J.L. Cantin, S. Raymond *IEEE Trans. Nucl. Sci. 49, 2733, 2002*

[67] RD48, "1st Status Repoer", *CERN LHCC 97-39, Status Report/RD48, 20 June 1997*

[68] A. Chilingarov et. al, *Nucl. Instr. and Meth. A 360, pp 432, 1995*

[69] S.J. Bates et. al, "Pion Induced Damage in Silison Detectors", *CERN-ECP/95-96, 1995*

[70] P.A. Aarnio et. al, *Nucl. Instr. and Meth. A 360, pp 521, 1995*

[71] M. Moll, E. Fretwurst, M. Kuhnke G. Lindstrom, *Nucl. Instr. and Meth. B 186, pp 100-110, 2002*

[72] G. Kramberger, V. Cindro, I. Mandic, M. Mikuz, M. Zavrtanik *Nucl. Instr. and Meth. A 481, pp 297-305, 2002*

[73] V. Eremin, E. Verbitskaya, Z. Li, *Nucl. Instr. and Meth. A 476, pp 556-564, 2002*

[74] M. Swartz *Nucl. Instr. and Meth. A 565, pp 212-220, 2006*

[75] Tokushima University, http://www.tokushima-u.ac.jp/English/englishtop.html

[76] LUMILOG company, http://www.lumilog.com/

[77] T. Wang, T. Shirahama, H.B. Sun, H.X. Wang, T. Bai, S. Sakai, *Appl. Phys. Lett. 76, pp 2220-2222, 2000*

[78] G. Moldovan thesis, "Optimisation of metallic contacts to n-type gallium nitride", University of Nottingham, 2003

[79] Neutron Irradiation Facility at jozef Stefan Institute, Ljubljana, http://www-f9.ijs.si/ mandic/ReacSetup.html

[80] IRRAD 1 Irradiation Facility at CERN, http://irradiation.web.cern.ch/irradiation/irrad1.htm

[81] National Instruments LABVIEW software, http://www.ni.com/labview/

[82] Maestro MCA software, http://www.ortec-online.com/maest.htm

[83] RD50 Internal Document, http://rd50.web.cern.ch/rd50/doc/Internal/rd50_2003_003_version_15-10-2004.doc

[84] W. Cunningham, J. Melone, M. Horn, V. Kazukauskas, P. Roy, F. Doherty, M. Glaser, J. Vaitkus, M. Rahman *Nucl. Instr. and Meth. A 509 (2003) pp 127-131*

[85] S. Sciortino, F. Hartjes, S. Lagomarsino, F. Nava, M. Brianzi, V. Cindro, C. Lanzieri, M. Moll, P. Vanni, *Nucl. Instr. and Meth. A 546, pp 138-145, 2005*

[86] G. Casse, LHCb UK Collaboration Board Meeting, July 2004

[87] E. Fretwurst, Talk given at the 6th RD50 Workshop, Helsinki, June 2005

[88] H. Hoedlmoser, Talk given at the 8th RD50 Workshop, Prague, June 2006

[89] J.L. Pau, C. Rivera, E. Munoz, E. Calleja, U. Schuhle, E. Frassyinet, B. Beaumont, J.P. Faurie, P. Gibart, *J. Appl. Phys. 95, pp8275-8279, 2004*

[90] J. Vaitkus, E. Gaubas, T. Shirahama, S. Sakai, T. Wang, K.M. Smith, W. Cunningham *Nucl. Instr. and Meth. A 514, pp 141-145, 2003*

[91] C. Lu, H. Chen, X. Lv, X. Xie, S. Noor Mohammad, *J. Appl. Phys. 91, pp 9218-9224, 2002*

[92] S. Noor Mohammad, *J. Appl. Phys. 95, pp 7940-7953, 2004*

[93] T.C. Shen, G.B. Gao, H. Morkoc, *J. Vac. Sci. Technol. B 10, pp 2113-2131, 1992*

[94] S.J. Pearton, J.C. Zolper, R.J Shul, F. Ren, *J. Appl. Phys. 86, pp 1-78, 1999*

[95] D.A. Stocker, E.F. Schubert, J.M. Redwing, *Appl. Phys. Lett. 73, pp 2654-2656, 1998*

[96] D. Li, M. Sumiya, S. Fuke, D. Yang, D. Que, Y. Suziki, Y. Fukuda, *J. Appl. Phys. 90, pp 4219-4223, 2001*

[97] K. Shiojima, *Journal of Vacuum Science and Technology B. 18, pp 37-40, 2000*

[98] T.G. Zhu, D.J.H. Lambert, B.S. Shelton, M.M. Wong, U. Chowdhury, R.D. Dupuis, *Appl. Phys. Lett. 77. pp 2918-2920, 2000*

[99] D. Basak, O. Fareed, K. Nishino, S. Sakai, *Journal of Vacuum Science and Technology B. 18, pp 2491-2494, 2000*

[100] I. Adesida, A. Mahajan, E. Andideh, M. Asif Khan, D.T. Olsen, J.N. Kuznia *Appl. Phys. Lett. 63, pp 2777-2779, 1993*

[101] F. Karouta, J.L. Weyher, B. Jacobs, G. Nowak, A. Presz, I. Gregory, L.M.F. Kaufmann, *J. Elec. Mat. 28, pp 1448-1451, 1999*

[102] H. Lee, J.S. Harris, *J. Elec. Mat. 27, pp 185-189, 1998*

[103] S.J. Pearton, R.J Shul, F. Ren,, *MRS Internet Journal of NSR, 5, article 11, 2000*

[104] EPSRC National Centre for III-V Technologies, *http://www.sheffield.ac.uk/eee/research/nc35t*

[105] F. Karouta, B. Jacobs, O. Schoen, M. Heuken, *Physics Status Solidi A, 176, pp 755-758, 1999*

[106] H.J. Wang, L. He *J. Elec. Mat. 27, pp 1272-1278 ,1998*

[107] C.K. Ramesh, V. Rajagopal Reddy, Chel-Jong Choi, *J. Mat. Sci. and Engin. B, 112, pp 30-33, 2004*

[108] B. Akkal, Z. Benamara, H. Abid, A. Talbi, B. Gruzza *Mat. Chem. and Phys., 85, pp 27-41, 2004*

[109] P.J. Sellin, D. Hoxley, A. Lohstroh, A. Simon, W. Cunningham, M. Rahman, J. Vaitkus, E. Gaubas *Nucl. Instr. and Meth. A, 531, pp 82-86, 2004*

[110] E. Fretwurst, C. Dehn, H. Feick, P. Heydarpoor, G. Linstrom, M. Moll, C, Schutze, T. Schulz *Nucl. Instr. and Meth. A 377, pp 258-264, 1996*

[111] J.I. Pankove, S. Bloom, G. Harbeke, *RCA Review, 36, pp 163, 1995*

[112] R. Dingle, I. Ilegems, *Solid State Commun. 9, pp 175, 1971*

[113] R. J. Molnar, T. Lei, T.D. Moustakas, *Appl. Phys. Lett. 62, pp 72, 1993*

[114] P. Boguslavski, E.L. Briggs, J. Bernholc, *Phys. Rev. B 51, pp 17255, 1995*

[115] T.L. Tansley, R.J. Egan, *Phys. Rev. B, 45, pp 10942, 1992*

[116] T.L. Tansley, R.J. Egan, *Physica B, 185, pp 190, 1993*

[117] V. Bougrov, M.E. Levinshtein, S.I. Rumyanstev, A. Zubrilov, "Properties of Advanced Semiconductor Materials: GaN, AlN, InN, BN, SiC, SiGe", John Wiley and sons, New York, 2001

[118] P. Boguslavski, E.L. Briggs, J. Bernholc, *MRS, Symp. Proc. v.339, pp 693-698, 1994*

[119] M. A. Reshchikov, D. Huang, L. He, H. Morkoc, J. Jasinski, Z. Liliental-Weber, S.S. Park, K.Y. Lee *Physica B, 367, pp 35-39, 2005*

[120] M. A. Reshchikov, H. Morkoc, *J. Appl. Phys. 97, 061301, 2005*

[121] E. Gaubas, J. Vaitkus, E. Simoen, C. Claeys, J. Vanhellemont, *Mater. Sci. Semicond. Process. 4, pp 125, 2001*

[122] E. Gaubas, *Lith. J. Physics, 27, pp747, 2003*

[123] E. Gaubas, S. Jursenas, A. Miasojedovas, J. Vaitkus, A. Zukauskas, *J. Appl. Phys. 96, pp4236-4333, 2004*

[124] A. Uleckas, M. Bauza, E. Gaubas, J. Grant, K. Kazlauskas, J. Vaitkus, *International Conference: Radiation Interaction with Material and its use in Technologies, Kaunas, September 2006*

[125] G. Kavaliauskiene, V. Kaukauskas, V. Rinkevicius, J.Storasta, J. V. Vaitkus, R. Bates, V. OShea, K. M. Smith, *Applied Physics A, 69, pp415 - 420, 1999*

[126] Z.C. Huang, K. Xie, R. Wie, *Rev. Sci. Instrum. 62, pp1951, 1991*

[127] G. Li, S.J. Chua, W. Wang, *Solid State Commun. 111, pp 659, 1999*

[128] V. Kazukauskas, V. Kalendra, J. Vaitkus *Nucl. Instr. and Meth. A 508, pp 421-426, 2006*

[129] M. Razeghi, A. Rogalski, *J. Appl. Phys. 79, pp 7433, 1996*

[130] Y.A. Goldberg *Semicond. Sci. Technol. 14, R41, 1999*

[131] M.A. Khan, J.N. Kuznia, D.T. Olson, J.M. Van Hove, M. Blaingame, L.F. Reitz, *Appl. Phys. Lett. 60, pp 2917-2919, 1992*

[132] C.V. Reddy, K. Balakrishnan, H. Okmura, S. Yoshida, *Appl. Phys. Lett. 73, pp 244-246, 1998*

[133] E. Munoz, E. Munroy, F. Calle, M.A. Sanchez, E. Calleja, B. Beaumont, P. Gibart, *Appl. Phys. Lett. 71, pp 870, 1997*

[134] E. Monroy, F. Calle, E. Munoz, F. Omnes, B. Beaumont, P. Gibart, *J. Elect. Mat. 28, pp 238, 1999*

[135] E. Monroy, F. Calle, J.L. Pau, F. J. Sanchez, E. Munoz, F. Omnes, B. Beaumont, P. Gibart, *J. Appl. Phys. 88, pp 2081, 2000*

[136] Q. Chen, J.W. Yang, A. Osinsky, S. Gangopadhyay, B. Lim, M.Z. Anwar, M.A. Khan, D. kuksenkov, H. Temkin, *Appl. Phys. Lett. 70, pp 2277, 1997*

[137] E. Monroy, F. Calle, E. Munoz, B. Beaumont, F. Omnes, P. Gibart, *Electron. Lett. 35, pp 1488, 1999*

[138] E. Monroy, F. Calle, C. Angulo, P. Vila, A. Sanz, J.A. Garrido, E. Calleja, E. Munoz, S. Haffouz, B. Beaumont, F. Omnes, P. Gibart, *Appl. Opt. 37, pp 5058, 1998*

[139] D. Walker, V. kumar, K. Mi, P. Sandvik, P. kung, X.H. Zhang, M. Razeghi *Appl. Phys. Lett. 76, pp 403, 2000*

[140] E. Monroy, F. Calle, E. Munoz, F. Omnes, *Phys. Stat. Sol. A 176, pp 157, 1999*

[141] J.C. Carrano, T. Li, P.A. Grudowski, C. J. Eiting, R.D. Dupuis, J.C. Campbell, *J. Appl. Phys. 83, pp 6148, 1998*

[142] J.C. Carrano, T. Li, D.L. Brown, P.A. Grudowski, C. J. Eiting, R.D. Dupuis, J.C. Campbell, *Appl. Phys. Lett. 73, pp 2405, 1998*

[143] G.D. Fasman, "Circular Dichroism and the Conformational Analysis of Biomolecules", 1996, New York/London, Plenum Press

[144] G.R. Jones, I.H. Munro, "Steucture of Dynamic Molecules", edited by E. Fanchon pp 305-337, 2000, Oxford University Press

[145] B.A. Wallace, *J. Synchrotron Rad. 7, pp 289, 2000*

[146] J.C. Sutherland, P.C. Keck, K.P. Griffin, M.Z. Takacs, *Nucl. Instr. and Meth. 195, pp 375, 1982*

[147] G. Jones, S. Manolopoulos, D. Clarke, P. Read, G. Derbyshire, *UK patent application No. PCT /GB2004/000365*

[148] EMCORE company, http://www.emcore.com/

[149] E. Monroy, T. Palacios, O. Hainout, F. Omnes, F. Calle, J.F. Hochendez, *Appl. Phys. Lett. 80, pp 3198, 2002*

[150] A. Blue, J. Grant, W. Cunningham, F. Quarati, K.M. Smith, M. Rahman, V. O'Shea, S. Manolopoulos *Nuc. Instr. and Meth A. 546, pp 131-134, 2005*

[151] MI3 collaboration homepage http://mi3.shef.ac.uk

[152] I. Ferguson, C.A. Tran, R.F. Karlicek Jr., Z.C. Feng, R. Stall, S. Liang, Y. Lu, C. Joseph, *Mat. Sci. and Engin. B50, pp 311-314, 1997*

[153] J.F.Huth, J.H. Lee, I.K. Shmagin, R.M. Kolbas, H.C. Casey, Jr., B.P. Keller, U.K. Mishra, S.P. DenBaars, *Appl. Phys. Lett. 71 , pp 2572-2574, 1997*

[154] C. Touzi, A. Rebey, B. Elijani, *Microelectronics Journal 33, pp 961-965, 2002*

[155] Q. Chen, J.W.Wang, A. Osinsky, S. Gangopadhyay, B. Lim, M.Z. Anwar, *Appl. Phys. Lett. 70, pp 2277-2279 1997*

[156] D. Clarke, G. Jones, *J. Synchrotron Rad. 11, pp 142-149, 2004*

[157] S.Y. Venyaminov, T.T. Tang, *"Circular Dichroism and the Conformational Analysis of Biomolecules", pp 69-107, New York/London, Plenum Press*

[158] W.C. Johnson, *"Circular Dichroism and the Conformational Analysis of Biomolecules", pp 635-652, New York/London, Plenum Press*

[159] The RD42 Collaboration, *"Development of Diamond Tracking Detectors for High Luminosity Experiments at LHC"*, DRDC/P56, CERN/DRDC 94-21, 1994

[160] P. Bergonzo, A. Brambilla, D. Tromson, R.D. Marshall, C. Jany, F. Foulon, C. Gauthier, V.A. Sole, A. Rogalev, J. Goulon, *J. Synch. Rad. 6, 1, pp 1-5, 1999*

[161] P. Bergonzo, D. Tromson, C. Mer., *J. Synch. Rad. 13-2, 151, 2006*

[162] C. Schulze-Briese, "CVD-Diamond XBPM development at PSI" *Proc. of the 9th Int. Conf. on Synchrotron Radiation Instrumentation, Daegu, Korea, 2006*

[163] D. Tromson, A. Brambilla, F. Foulon, C. Mer, B. Guizard, R. Barrett, P. Bergonzo, *Diam. and Rel. Mat. 9, pp 1850-1855, 2000*

[164] J. Isberg, J. Hammersberg, E. Johansson, T. Wikstrom, D. Twitchen, A. Whitehead, S. Coe, G. Scarsbrook, *Science 297, pp 16701672, 2002*

[165] Element Six Ltd., King's Ride Park, Ascot, Berkshire, SL5 8DP, UK

[166] G. Kramberger, PhD thesis, University of Ljubljana, 2001

[167] H. Pernegger, S. Roe, P. Weilhammer, V. Eremin, H. Frais-Kolbl, E. Griesmayer, H. Kagan, S. Schnetzer, R. Stone, W. Trischuk, D. Twitchen, A Whitehead, *J. Appl. Phys. 97, 073704, 2005*

[168] J. Isberg, J. Hammersberg, H. Bernhoff, D. Twitchen, A.J. Whitehead, *Diamond and Rel. Mater. 13, 4-8, pp 872-875, 2004*

[169] A. Lohstroh, *"IBIC Imaging in synthetic single crystal diamond"*, 3rd Norhdia Workshop, Darmstadt, Sept. 2006

[170] J. Susini, A. Somogy, R. Barrett. M. Salom, S. Bohic, B. Fayard, D. Eichert, O. Dhez, P. Bleuet, G. Martnez-Criado, R. Tucoulou, *AIP Conference Proceedings 716, pp 18-21, 2004*

[171] S. Butun, M. Gokkavas, Y. Hongbo, E. Ozbay, *Appl. Phys. Lett. 89, 073503, 2006*

[172] E. Munoz, E. Munroy, J.L. Pau, F. Calle, F. Omnes, P. Gibart, *J. Phys. Condens. Matter. 13, pp 7115-7137, 2001*